

DOTTORATO DI RICERCA IN

Meccanica e Scienze avanzate dell'Ingegneria:
Disegno e Metodi dell'Ingegneria Industriale e Scienze Aerospaziali

Ciclo XXV

Settore Concorsuale di afferenza: 09 / A3
Progettazione industriale, costruzioni meccaniche e metallurgia

Settore Scientifico Disciplinare: ING / IND 15

*Reverse Engineering tools: development and
experimentation of innovative methods for physical and
geometrical data integration and post-processing*

Presentata da: Francesca Lucchi

Coordinatore Dottorato:
Prof. Vincenzo Parenti Castelli

Relatore:
Prof. Leonardo Seccia

Correlatori:
Prof. Franco Persiani
Ing. Francesca De Crescenzo

Alma Mater Studiorum – Università di Bologna
Tesi di Dottorato
Francesca Lucchi
Ciclo XXV

Abstract

In recent years, the use of Reverse Engineering systems has got a considerable interest for a wide number of applications. Therefore, many research activities are focused on accuracy and precision of the acquired data and post processing phase improvements. In this context, this PhD Thesis deals with the definition of two novel methods for data post processing and data fusion between physical and geometrical information.

In particular a technique has been defined for error definition in 3D points' coordinates acquired by an optical triangulation laser scanner, with the aim to identify adequate correction arrays to apply under different acquisition parameters and operative conditions. Systematic error in data acquired is thus compensated, in order to increase accuracy value.

Moreover, the definition of a 3D thermogram is examined. Object geometrical information and its thermal properties, coming from a thermographic inspection, are combined in order to have a temperature value for each recognizable point. Data acquired by an optical triangulation laser scanner are also used to normalize temperature values and make thermal data independent from thermal-camera point of view.

Key words:

Reverse Engineering; Surface Accuracy; Measuring Uncertainties; Performances Evaluation; Metrological Characterization; Data Fusion; Thermography; 3D Thermography; Data Normalization.

Sommario

L'impiego di tecniche di Ingegneria Inversa si è ampiamente diffuso e consolidato negli ultimi anni, tanto che questi sistemi sono comunemente impiegati in numerose applicazioni. Pertanto, numerose attività di ricerca sono volte all'analisi del dato acquisito in termini di accuratezza e precisione ed alla definizione di tecniche innovative per il post processing. In questo panorama, l'attività di ricerca presentata in questa tesi di dottorato è rivolta alla definizione di due metodologie, l'una finalizzata a facilitare le operazioni di elaborazione del dato e l'altra a permettere un agevole data fusion tra informazioni fisiche e geometriche di uno stesso oggetto.

In particolare, il primo approccio prevede l'individuazione della componente di errore nelle coordinate di punti acquisiti mediante un sistema di scansione a triangolazione ottica. Un'opportuna matrice di correzione della componente sistematica è stata individuata, a seconda delle condizioni operative e dei parametri di acquisizione del sistema. Pertanto, si è raggiunto un miglioramento delle performance del sistema in termini di incremento dell'accuratezza del dato acquisito.

Il secondo tema di ricerca affrontato in questa tesi consiste nell'integrazione tra il dato geometrico proveniente da una scansione 3D e le informazioni sulla temperatura rilevata mediante un'indagine termografica. Si è così ottenuto un termogramma in 3D registrando opportunamente su ogni punto acquisito il relativo valore di temperatura. L'informazione geometrica, proveniente dalla scansione laser, è stata inoltre utilizzata per normalizzare il termogramma, rendendolo indipendente dal punto di vista della presa termografica.

Contents

Abstract.....	iii
Sommario.....	v
Contents.....	vii
List of Tables.....	xiii
List of Figures	xvii
Introduction.....	1
1. Reverse Engineering: systems and processes.....	7
1.1 Reverse Engineering tools	11
1.2 The acquisition pipeline	18
1.2.1 Scans planning and acquisition process.....	18
1.2.2 The registration process.....	19
1.2.3 Range map merge and refining phases.....	20

2. Experimental Error Compensation Procedure	23
2.1 Mathematical analysis of errors.....	26
2.1.1 Resolution, accuracy and precision.....	29
2.2 Error analysis in scanning processes.....	32
2.3 Methodology guidelines	40
2.3.1 Materials and instruments	41
2.3.2 Experimental set up.....	45
2.3.2.1 Laser scanner calibration.....	45
2.3.2.2 Reference surface structure.....	50
2.3.3 Acquisition phase.....	58
2.3.4 Elaboration phase.....	62
2.3.5 Compensation phase	71
2.4 Results: Laser beam perpendicular to the reference surface.....	72
2.5 Results: oblique angle between the laser beam and the reference surface.....	89
2.5.1 Non rectangular frames.....	102
2.5.1.1 Systematic error compensation arrays for non rectangular frames.....	105
 3. Infrared Thermography	 111
3.1 Fundamental Physical principles and theory of operation	112
3.1.1 Emitted and incident radiations	114
3.1.2 Blackbody	121

3.1.3 Planck's Law	123
3.1.4 Wien displacement Law	124
3.1.5 Stephan-Boltzmann Law	125
3.1.6 Radiation emitted in a spectral band	125
3.1.7 Reflection, Absorption and Transmission	126
3.1.8 Emissivity	129
3.2 Thermographic inspection.....	132
3.2.1 Thermography techniques.....	132
3.2.1.1 Active and Passive Thermography	132
3.2.2 Thermography instruments.....	137
3.3 Thermography measurements.....	140
3.3.1 Measuring uncertainties.....	142
3.4 Applications.....	144
3.4.1 Thermography in industrial processes.....	145
3.4.1.1 Active Pulsed thermography.....	146
3.4.1.2 Lock-in and pulsed phase thermography.....	150
3.4.1.3 Passive thermography	152
3.4.2 Medical Imaging.....	156
3.4.3 Architectural and cultural heritage.....	160

4. IR thermography and RE: a data fusion process	165
4.1 Data fusion between surface data and infrared data.....	167
4.2 Data fusion: state of the art.....	168
4.2.1 Integration processes by texture mapping methods	169
4.2.2 Integration processes with marker registration.....	172
4.2.3 Video projection as integration process	173
4.2.4 Integration processes with volumetric RE systems.....	175
4.2.4 Integration processes with calibration procedures.....	176
4.3 Methodology.....	177
4.3.1 The acquisition process.....	180
4.3.2 Infrared system devices.....	187
4.4 Data Registration	189
4.4.1 The registration workflow	191
4.4.2 World and camera coordinates systems	198
4.5 Data correction	204
4.5.1 Non planar geometry inspection	207
4.5.1.1 Point – Source Heating Correction.....	208
4.5.1.2 Video Thermal Stereo Vision.....	208
4.5.1.3 Direct Thermogram Correction.....	209
4.5.1.4 Shape from Heating.....	210
4.5.1.5 Experimental Correction Methods.....	212
4.5.2 Lambert’s Cosine Law.....	213

4.5.3	Temperature correction procedure	215
4.6	Visualization environment	218
4.7	Experimental case study	222
Conclusions.....		229
Appendix A.....		233
	Laser Scanner Konica Minolta Vivid-9i technical notes	233
	Specifications	233
Appendix B.....		237
	Results: Laser beam perpendicular to the reference surface	237
Appendix C.....		251
	Different materials emissivity values	251
Appendix D.....		265
	File format supported by common 3D modeler tools.....	265
Appendix E.....		271
	Thermo camera datasheet	271
	Specifications Flir ThermaCAM™ SC640.....	271
	Technical data Testo 882.....	274
References.....		279

List of Tables

Table 2.1 Konica Minolta Vivid-9i: some instrument information	42
Table 2.2 Laser scanner optics: area acquirable from each lens. All values are in mm. Data are taken from Konica Minolta datasheet.....	43
Table 2.3 Performance parameters of Konica Minolta laser scanner. Data are taken from Konica Minolta datasheet.....	44
Table 2.4 Stored Calibration Values and Design Dimensions (Units: mm)	49
Table 2.5 Angular acquired combinations.....	61
Table 2.6 Theoretical and real values of acquired area for the lenses and at 600 and 900 mm of distance	75
Table 2.7 Mean, Min and max resolution values in X and Y directions, in function of the number of arrays involved in the mean process. Tele lens, 600 mm distance.	78
Table 2.8 Point to remove symmetrically for each row and column in order to have a reduction of point's distances standard deviation	81
Table 2.9 Surface and standard deviation in relation to the number of averaged arrays. Tele lens and 600 mm distance. All values are in mm.....	85
Table 2.10 Comparison between Minolta Data Sheet and experimental data for a specific case with the Tele lens and at a scanning distance of 600mm.....	87
Table 2.11 Correction arrays comparison: evaluation of the mean value and standard deviation of the correction related to some key points.....	88
Table 2.12 Arrays comparison: evaluation of the mean value and standard deviation of the correction related to some key points.....	89

Table 2.13 Acquired range maps with different tilt angles combinations: in green are highlighted rectangular arrays, that is to say, arrays in which all points are acquired; instead in yellow are highlighted arrays where not all points are acquired	91
Table 2.14 Area acquired at 600 mm distance with a Tele lens, in dependence on different geometrical parameters	93
Table 2.15 Points to remove symmetrically in each row and column in order to have a decrease of standard deviation of vectors of distances between two near points.....	97
Table 2.16 Surface and standard deviation and points resolution in relation to the number of averaged arrays. Tele lens, 600 mm distance and (20°, 20°) of angles.....	99
Table 2.17 Comparison between Minolta Data Sheet and experimental data for a specific case with the Tele lens and at a scanning distance of 600mm, tilt angles of 20°	100
Table 2.18 Points distances standard deviation, mean, minimum and maximum resolution values for the first scan of all non rectangular frames.....	103
Table 3.1 Emissivity values for different materials	130
Table 3.2 Focal Plane Arrays Devices	139
Table 4.1 Example of the first ten point of a mesh saved in a pts file format: the first part of the table correspond to point's coordinates in mm, whereas the second part are the normal vector correspond to the respective acquired point. The three coordinates are shown in the column.....	184
Table 4.2 Thermography correction: some notable values	225
Table 0.1 Mean, Min and max resolution values in X and Y directions, in function of the number of arrays involved in the mean process. Tele lens, 900 mm distance.	238
Table 0.2 Mean, Min and max resolution values in X and Y directions, in function of the number of arrays involved in the mean process. Middle lens, 600 mm distance.....	239
Table 0.3 Mean, Min and max resolution values in X and Y directions, in function of the number of arrays involved in the mean process. Middle lens, 900 mm distance.....	240
Table 0.4 Mean, Min and max resolution values in X and Y directions, in function of the number of arrays involved in the mean process. Wide lens, 600 mm distance.	241

Table 0.5 Mean, Min and max resolution values in X and Y directions, in function of the number of arrays involved in the mean process. Wide lens, 900 mm distance.	242
Table 0.6 Surface and standard deviation in relation to the number of averaged arrays. Tele lens and 900 mm distance. All values are in mm.....	246
Table 0.7 Surface and standard deviation in relation to the number of averaged arrays. Middle lens and 600 mm distance. All values are in mm	247
Table 0.8 Surface and standard deviation in relation to the number of averaged arrays. Middle lens and 900 mm distance. All values are in mm	247
Table 0.9 Surface and standard deviation in relation to the number of averaged arrays. Wide lens and 600 mm distance. All values are in mm.....	248
Table 0.10 Surface and standard deviation in relation to the number of averaged arrays. Wide lens and 900 mm distance. All values are in mm.....	249

List of Figures

Figure 1.1 Some representation of a 3D point cloud: a) gray scale image range map; b) 3D point connected as a wire-mesh; c) a mesh artificially shaded; d) representation with returned laser intensity (Beraldin, 2009).....	8
Figure 1.2 Reverse Engineering process and output.....	9
Figure 1.3 Classification of 3D imaging techniques (Sansoni et al, 2009).....	11
Figure 1.4 Volumetric data: an example	13
Figure 1.5 Time of flight laser scanner: the measuring principal	14
Figure 1.6 Triangulation laser scanner: the measuring principal.....	15
Figure 1.7 Example of a structured light scanning technique on an object surface: increasing fringe density is shown from image a) to image d) (Guidi et al, 2010).....	16
Figure 1.8 Comparison between optical range imaging technique (Sansoni et al, 2009) ..	17
Figure 1.9 Two different range maps are first register by the identification of 3 pairs of homologous points	20
Figure 1.10 Filling holes on an acquired mesh	21
Figure 2.1 The same quantity is measured many times: σ is the precision error and it is random; β is the bias error and it is systematic.....	31
Figure 2.2 Error in measurement of a variable in infinite number of readings (Coleman, Steele, 1989).....	32
Figure 2.3 Sphere positions on a stairway (Boehler et al, 2003).....	34

Figure 2.4 The target used for resolution investigation: an example of low (in the middle) and high (on the right) resolution instruments (Boehler et al, 2003).....	34
Figure 2.5 The testing vase (Artenese et al, 2003)	35
Figure 2.6 Test object used in the experiments to evaluate point resolution in Z (a) direction and in x,y one (b). some solids (c) and planes (d) are evaluated to testing accuracy and uncertainty	36
Figure 2.7 Origin of some typical uncertainties in 3D imaging systems (Beraldin, 2009)	37
Figure 2.8 Laser beam diffraction.....	38
Figure 2.9 Noise standard deviation in relation to the variation of (on the top) scanner laser intensity and (on the bottom) of surface distance (Sun et al, 2009).....	39
Figure 2.10 The reference surface used for the acquisition process.....	44
Figure 2.11 The Field Calibration System, parts nomenclature (Vivid manual).....	47
Figure 2.12 The Field Calibration System: the installation space, the calibration area and laser scanner connection (Vivid manual)	48
Figure 2.13 The calibration chart: on the top the calibration of the Wide lens and on the bottom Tele and Middle procedures are shown.....	49
Figure 2.14 Glass sheet degree of freedom.....	51
Figure 2.15 Glass sheet fixing: clamps connections.....	53
Figure 2.16 Upper and lower shafts.....	53
Figure 2.17 Gears: XA 30 100 B3 <i>Tramec S.r.l.</i>	54
Figure 2.18 Bearings and their boxes insert into the frame: on the left the boxes are designed in blue, in green the bearings are sketched. On the right, their position into the up and bottom part of the frame	55
Figure 2.19 Shaft/frame connection.....	56
Figure 2.20 Two goniometers are fixed to measure angular movements.....	57

Figure 2.21 The realized structure and its CAD definition.....	57
Figure 2.22 The scanning process with laser beam perpendicular with the reference surface, a first set up, before the support structure development	59
Figure 2.23 On the left: representation of the acquisition process; on the right: example of real scan.	60
Figure 2.24 An acquisition setting.....	62
Figure 2.25 An example of reduction process: on the left a visualization of the distances between two near points: it is possible to notice a wide dispersion in boundary parts....	65
Figure 2.26 Principal components 3D space	67
Figure 2.27 Last square method: example of application in the bidirectional space.....	67
Figure 2.28 Elaboration phase workflow	70
Figure 2.29 The acquisition process: two acquired frame as seen in PET. Scans are acquired with a Tele lens at a distance of 600 mm (on the left) and 900 (on the right)	73
Figure 2.30 The acquisition process: two acquired frame as seen in PET. Scans are acquired with a Middle lens at a distance of 600 mm (on the left) and 900 (on the right).....	73
Figure 2.31 Area of the acquired frame in relation to scanning and focal distances.....	74
Figure 2.32 3D graph of an acquired surface portion. Point's Z coordinates are view as a color map; coordinate values are in mm.....	76
Figure 2.33 dx and dy distanced between two near points are evaluated, in order to define local points resolution	76
Figure 2.34 3D graph on points distances in x (on the top) and y (on the bottom) directions (all values are in mm)	77
Figure 2.35 Segment lengths in dependence on its position in the frame (column: segment position which runs from 1 to 640): the first image corresponds to the first row, the second one to the meddle row (240) and the last one to the last row (480).....	79

Figure 2.36 Segment lengths in dependence on its position in the frame (row: segment position which runs from 1 to 480): the first image corresponds to the first column, the second one to the middle column (320) and the last one to the last column (640).	80
Figure 2.37 3D graph of the shifting between acquired points and the best fitting plane. All values are in mm	83
Figure 2.38 Standard deviation trend in function of the number of averaged arrays: Tele lens and scanning distance of 600mm	84
Figure 2.39 Acquired and reduced plane: from the difference between the reduced plane and the best fitting plane errors in coordinates' determination are evaluated. Averaged and corrected plane: from the difference between the corrected plane and the best fitting plane errors in coordinates' determination are evaluated.....	86
Figure 2.40 some acquisition frame: Tele lens, 600 mm of scanning distance and changing tilt angles.....	90
Figure 2.41 Only with some angular combination, the whole frame is completely acquired; in all the other conditions only some central points are stored, and in many parts no points are present	92
Figure 2.42 3D representation of points coordinates in <i>Matlab</i> environment. Tele lens 600 mm of distance, $\alpha = 20^\circ$, $\beta = 20^\circ$	93
Figure 2.43 Points resolution in X and Y directions, in function of their location in the frame. Tele lens, 600 mm of acquiring distance and $(20^\circ, 20^\circ)$ of tilt angles.....	94
Figure 2.44 Segment lengths in dependence on its position in the frame (column: segment position which runs from 1 to 640): the first image corresponds to the first row, the second one to the middle row (240) and the last one to the last row (480). Tele lens, 600 mm of scanning distance and tilt angles of 20° each	95
Figure 2.45 Segment lengths in dependence on its position in the frame (row: segment position which runs from 1 to 480): the first image corresponds to the first column, the second one to the middle column (320) and the last one to the last column (640). Tele lens, 600 mm of scanning distance and tilt angles of 20° each.....	96
Figure 2.46 Error representation in pseudo color, in function of points position in the acquired frame. Case study with geometric parameters α and β of 20° each.....	98

Figure 2.47 Error standard deviation in relation to the number of arrays involved in the mean process. Tele lens, 600 mm of acquiring distance and (20°, 20°) of inclination.....	98
Figure 2.48 Correction value (mm) in relation to point index. $\Delta S(0,0)$ values are indicated by a dot, while $\Delta S(20,20)$ values are represented by a cross	101
Figure 2.49 Difference (mm) between $\Delta S(0,0)$ and $\Delta S(20,20)$ arrays in relation to point index	101
Figure 2.50 Resolution values in relation to row position in the acquired frame. On the top is presented the first row, then the middle row and finally the last row. Scans are performed with a Tele lens, at 600 mm of distance and tilt angles of (40°, 40°).....	104
Figure 2.51 Resolution values in relation to row position in the acquired frame. On the top is presented the first row, then the middle row and finally the last row. Scans are performed with a Tele lens, at 600 mm of distance and tilt angles of (60°, 60°).....	105
Figure 2.52 Only the central portion of each frame can be used to perform the methodology, so that all acquired scans with similar operative conditions can have the same rectangular structure	107
Figure 2.53 Composition of two different scans: the first one performed at a less scanning focusing and the second one at an high distance. The black portion represents no acquired areas. The third image is the composition f the first two.....	109
Figure 3.1 Spherical System coordinates	115
Figure 3.2 Definition of plane and solid angle	116
Figure 3.3 Definition of radiance.....	116
Figure 3.4 The electromagnetic spectrum.....	117
Figure 3.5 Bourguer's Law	121
Figure 3.6 Radiation emitted by a surface: spatial and directional distributions (Maldague, 2001).....	121
Figure 3.7 Models of black bodies	122
Figure 3.8 Plank's Law: the spectral radiance of a blackbody (Maldague, 2001).....	124

Figure 3.9 Fraction of the blackbody emission in the wavelength band (0 to λ) (Maldague, 2001).....	126
Figure 3.10 The incident flux is divided into reflected flux, absorbed flux and transmitted flux.....	127
Figure 3.11 Focal Plane Array Detectors configuration.....	138
Figure 3.12 Scanning System Configuration.....	140
Figure 3.13 Schematic depiction of an Infrared measure of related to an object (2) through an infrared camera (4). 3 is the atmosphere and 1 in is the surrounding environment.....	142
Figure 3.14 Thermal analysis of fiber orientation in composite materials and elliptical thermal obtained pattern (Maldague 1993).....	147
Figure 3.15 A corroded bent pipe is inspected through a thermal-camera in order to detect the presence of defects: experimental set up (Maldague, 2001)	149
Figure 3.16 Experimental apparatus for thermographic inspection on turbine blades using internal stimulation: experimental set up (Maldague, 2001)	150
Figure 3.17 Sample geometries inspection through PPT and LT: stair veneered coating of variable thickness (Maldague, 2001).....	151
Figure 3.18 Some examples of passive infrared thermography applied to buildings insulation defaults (Candoré, 2008)	152
Figure 3.19 Analysis of mineral based coating for buildings: experimental set up and thermal images acquired for different samples (Kolokotsa, 2012).....	153
Figure 3.20 Some examples of thermography inspection on buildings surface: on the top the heat flux of the same building is presented (Hoyano, 1999) in summer (on the left) and in winter time (on the right). In the bottom part, a continuous surface monitoring is performed and the visible and infrared images are proposed (Sham, 2012).....	154
Figure 3.21 Bridge deck delamination map created by thermal IR images (Endsley, 2012)	155

Figure 3.22 Infrared and visible images on power transmission equipments: a transformer on the left and an electric cable on the right (Chou, 2009)	155
Figure 3.23 Thermal image of an inspected photovoltaic panel module: the central cell presents an unexpected behavior (Botsaris, 2010)	156
Figure 3.24 Thermal images of a subject talking on a hand-held mobile phone after 1 minute (on the left) and after 15 minutes (on the right) of talking (Lahiri, 2012)	158
Figure 3.25 Thermal image of left lower limb of a 28 years old male diabetic patient suffering from vascular disorder (a). (b) Temperature profile along the red line indicated shown in (a). An arrow indicate shows the lowest temperature (Lahiri, 2012)	159
Figure 3.26 Murals paintings of the abbey of “Saint Savin sur Gartempe” and the thermographic inspection performed. The third image represents the IR image of the analyzed area: on the back wheel represented, some detachments are recognized (Bodnar, 2012)	161
Figure 3.27 Mosaic inspection by thermography: a) building facade; b) IR image of the squared area in a); c) enlargement of the squared area (Meola, 2005)	162
Figure 3.28 The main facade of the Cathedral of Matera and the location of the thermographic data collection (Danese, 2010)	163
Figure 4.1 Djin Block No.9, in Petra (Jordan), a picture of the heritage monument (on the left), the acquired surface with a photographic texture (in the middle), and the surface with a thermographic texture (on the right) (Cabrelles, 2009)	171
Figure 4.2 Thermographic inspection and 3D reconstruction: a case study. On the left, an image fusion between IR a visible images is performed and an orto-thermogram is then obtained (in the middle). On the right, the final thermographic 3D representation is shown (Langüela, 2012)	172
Figure 4.3 The thermographic equipment including the specimen in the navigation cage. On the right, the thermogram used as a texture for the 3D acquired shape (Satzger, 2006)	173
Figure 4.4 Diagrams of thermography visualization: a conventional approach (on the left) and a video projection based approach (on the right) (Iwai and Sato, 2010)	174

Figure 4.5 Experimental result for a cluttered scene: on the left there are paint tubes under environmental light; in the middle the thermal image is shown; on the right the projection is applied (Iwai and Sato, 2010).....	174
Figure 4.6 Volume visualization at four different cutting levels. The MR information is clearly visible together with the surface temperature (Bichinho et al., 2009)	176
Figure 4.7 3D thermography example. Images from the top-left: the real object, the IR image, the surface acquired, the surface with the visible texture and the thermogram on the surface acquired (Barone et. al, 2006)	177
Figure 4.8 Methodology for data fusion: workflow	178
Figure 4.9 Example of Pts format files exporting.....	182
Figure 4.10 Points' position in CCD Sensor and Array, in case of the whole frame acquiring	185
Figure 4.11 Acquisition set up.....	186
Figure 4.12 The two thermographic devices used: the Flir ThermoCAM™ SC640 (on the left) and the Testo 882 (on the right).....	188
Figure 4.13 Registration workflow.....	191
Figure 4.14 Temperature array displayed in <i>Matlab</i> environment.....	192
Figure 4.15 Laser Scanner Reference System. On the right in detail the CCD sensor: the acquiring object is considered as posed in front of it.....	194
Figure 4.16 Thermo Camera Reference System.....	195
Figure 4.17 Translations between the two reference systems: on the top the red point is laser scanner reference system origin; on the bottom thermal-camera dimensions. The total distance between the two reference systems origins is defined as sum of the two contributes	196
Figure 4.18 Constant movements (Translations) between the two reference systems	197
Figure 4.19 Camera and world coordinates systems	198

Figure 4.20 Rotation of world coordinates X' and camera coordinate X , using the three Eulerian angles (ϕ , ϑ , ψ) with successive rotations about the X_3' , X_1'' and X_3''' axes	201
Figure 4.21 The central perspective projection (Yilmaz et al, 2008)	202
Figure 4.22 Complex shapes inspection: distance and angle effects (Ibarra-Castanedo et al., 2003)	205
Figure 4.23 Angle and distances influence in thermography inspections: on the left an experimental set up, on the right some temperature maps at angles of 20° , 50° and 80° (Tkáčová et al, 2010)	205
Figure 4.24 Blackbody distances and angle dependence in temperature reading (Tkáčová et al, 2010)	206
Figure 4.25 The problem of shape curvature in TNDT: an original and a rectified thermogram example (Ju et al, 2004)	207
Figure 4.26 Heating analysis of a flat surface specimen (Maldague, 2001)	211
Figure 4.27 Heating analysis of a curved specimen (Maldague, 2001)	212
Figure 4.28 Beam geometry (Gaussorgues, 1994)	214
Figure 4.29 Correction workflow	215
Figure 4.30 Geometrical quantities used for the definition of a correction factor	216
Figure 4.31 Graphical structure representing at the basis of the visualization environment	220
Figure 4.32 Color maps used in the visualization environment	222
Figure 4.33 Experimental acquisitions: at the top, the visible and IR images acquired with the thermal-camera; at the bottom, the 3D acquired shape	223
Figure 4.34 Thermographic image in pixel coordinates, as viewed in <i>Matab</i>	224
Figure 4.35 3D thermogram as represented in Matlab environment: after the registration procedure, a temperature value is coupled with each acquired point	225
Figure 4.36 Thermographic 3D representation into a 3D software	226

Figure 4.37 The prototyped visualization tool: more color maps are created	227
Figure 4.38 The prototyped visualization tool: each triangle of the mesh of study includes point's temperature information.....	228
Figure 0.1 Dimension Diagram (unit mm)	233
Figure 0.1 Standard deviation trend in function of the number of averaged arrays: Tele lens and scanning distance of 600mm (on the top) and 900 mm (on the bottom)	243
Figure 0.2 Standard deviation trend in function of the number of averaged arrays: Middle lens and scanning distance of 600mm (on the top) and 900 mm (on the bottom)	244
Figure 0.3 Standard deviation trend in function of the number of averaged arrays: Wide lens and scanning distance of 600mm (on the top) and 900 mm (on the bottom)	245

Introduction

Over recent years, Time Compression Technologies (TCT) are playing an ever increasing role and importance in the design processes and in project developments. Reverse Engineering (RE), Rapid Prototyping (RP), and Virtual Reality (VR) systems are currently widely used in industrial engineering fields as key tools to reduce product time to market and to improve product quality and performances, cutting down design costs and time. This is the reason why they play an important role in sustaining product innovation and industrial competitiveness.

Particularly, the old and well known design process has drastically changed thanks to the Reverse Engineering systems: in the previous processes, a new idea was developed and implemented within CAD (Computer Aided Design) environment and then converted into the final product; after the RE introduction, a 3D digital object description has been obtained starting from a real object. Design processes can be thus transformed, by changing design workflows, making processes easier, increasing efficiency and decreasing time product development.

These qualities imply that RE could be applied not only in industrial contexts, but also in many other different fields, making remarkable improvements. Biomedical,

cultural heritage, architecture and civil engineering are several of the most common RE application areas.

Laser scanners are some of the most used Reverse Engineering systems, since they can offer a dense point cloud describing almost any object shape complexity in a rather easy and fast acquisition process. Object acquisition process is based on the optical scanning of the object surface from different views, so that more range maps are acquired to describe the whole surface. A post processing phase, which is generally rather elaborate, arranges, organizes and then combines different scans. During this phase, some sub-phases are performed, to reduce data noise, to register acquired frames combining them together. At the end, a refining and filling holes phase follows to show a unique 3D model.

In this technical overview, this work shows two research focuses, which main purpose is to improve performances and application range of the scanning devices.

The first research topic is related to the analysis of error in point coordinates definition, calculated by a laser scanner system. All measuring systems show uncertainty level in provided data and, in particular for these tools, some errors can be observed by a surface noise on acquired surface. Even if in calibration procedures some instruments parameters can be set in order that the acquired surface has high accuracy levels, uncertainties of measurement are present anyway. Within this context, no unified

standards on error definition and well defined procedures for data correction are clearly identified. Supported by these considerations, the aim of the first part of this work is to identify data error related to images acquired by an optical laser scanner, and to propose a method for identifying the systematic portion of the error and for specifying errors correction arrays to compensate for systematic measurements errors.

The aim of this research activity involves the possibility to reduce errors in acquired data through a control and defined method. This feature seems to be promising and useful in many applications in which high accuracy level is strictly required, and when little details on object surface can be smooth in semiautomatic post processing procedures, together with errors. Cultural heritage and biomedical are some application fields in which the present methodology would lead to improve the acquisition process, along with the design and quality control phases of small components.

Moreover, the second research topic, related to scanning devices and their application procedures has been investigated. Currently, one of the most interesting research topics related to acquiring tools consists of integration process of data coming from different sources and including different information. In particular, within this context, a method for data fusion has been proposed in order to integrate 3D geometrical data, with temperature information, obtained by a thermographic investigation process.

Non Destructive Testing (NDT) are widely used in quality control processes in order to detect product defects and imperfections since early stages, in order to avoid and prevent any damages, that, sometimes, can lead to dangerous events or onerous and costly effects. Within this context, Infrared Thermography offers the possibility of detecting subsurface imperfections and changes in material composition, identified as a temperature difference, represented by a color map. Thanks to its efficiency in detect changes, non visible to the naked eye in an extremely fast way, this approach is currently widely used not only in industrial control quality processes, but also in architectural field and civil engineering inspections: in cultural heritage it is used as important support device for restoration processes, and in biomedical field as a fast diagnosis tool.

A method for data fusion has been developed, and shown in the present work, in order to integrate 3D geometrical data with surface temperature information. A temperature value is assigned to each acquired point, in order to provide geometry with more information and to read the infrared radiometric data according to the referenced geometry. In particular, in many cases, it can happened that the temperature information, that is generally provided by a color map image, are not easy to understand and to display their location in the visible image. This is the reason why a possible subsurface defect is not easy to detect. The integration between that kind of information

and a 3D shape information, acquired by a laser scanner tool, makes infrared thermography easier to understand.

A further considered aspect implies that radiation transmission is affected by dispersions due to the camera views and distances. The association of the 3D object geometry information is used to correct the thermographic datum and make thermography outcome independent from the acquisition setting up. On one hand, temperature values are associated with the referenced 3D point, so that defect detection is easier; on the other hand the 3D surface is used to make infrared inspections quantitative and not only qualitative.

The proposed data fusion process is expected to improve thermographic testing in many application cases , since a 3D thermography is analyzed in a multidimensional environment. Potential applications are identified both in civil engineering and in TNDT (Thermography Non Destructive Testing) processes. Moreover it should provide improvements in cultural heritage and biomedical inspections.

In the first part of this thesis, a brief introduction on Reverse Engineering systems and methods is presented. In Chapter 2, the developed methodology for error analysis and correction is described in detail.

The following parts concerns a first thermographic introduction on inspection techniques and methods and Chapter 4 indicates the data-fusion procedure and workflow.

1. Reverse Engineering: systems and processes

Reverse Engineering techniques are currently widely used, since they are able to define a 3D digitalized description, starting from a real physical object. The obtained 3D shape can be used in many different contexts and application: in particular, in new industrial product design process, these techniques, invert the traditional design process and workflows. In product design the CAD – CAM – RP loop often represents the starting point for a new product development or for a redesign and reinvent process. Moreover in many cases, such as car design, clay modeling is one of the most used techniques for new shapes definition and reverse engineering process is the only possibility to transform modeler idea into a 3D digitalized representation. Quality control process is another industrial field in which such technology is currently widely used, in order to compare the final product geometrical features with designed ones (Sansoni et al 2009).

Reverse engineering systems are also commonly used to design customized product, with a user-oriented design method: sport helmets are an example. In biomedical field RE tools helps to design patient prosthesis or anatomical parts (Gibson 2005; Fantini et al. 2012; Fantini et al. 2013).

Finally, in cultural heritage, Reverse engineering is a fast and efficient tool to analyze artworks, and it is widely used in restoration processes or to make copies, or to develop data information or to design the transportation process of an artwork (De Crescenzo et al 2008a; De Crescenzo et al 2008b; Persiani et al 2007; Curuni Santopuoli 2007).

During an acquisition process, 3D point's coordinates are organized in point clouds that take into account point connections and neighborhood information (Beraldin, 2009). All these acquired data can be represented in many different ways and the simplest one consists in a uniform (u,v) parameterization of a depth map. It is arranged as a matrix whose row and column indexes are function of the two orthogonal scan parameters (X, Y). The matrix cells can contain some more information on continuity between points, point's depth measurement (Z), calibration quantities and any other attribute, such as color data.

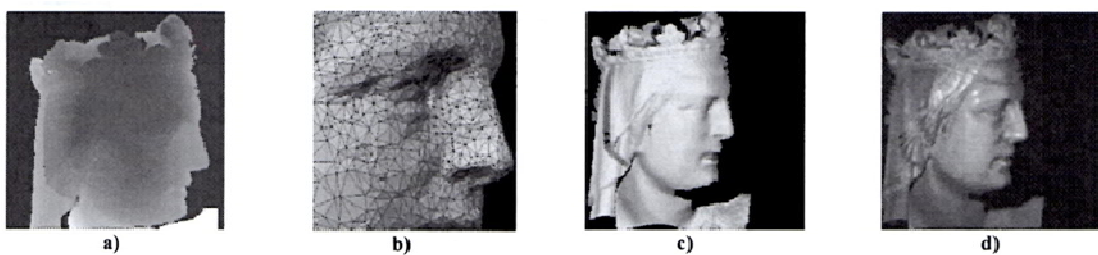


Figure 1.1 Some representation of a 3D point cloud: a) gray scale image range map; b) 3D point connected as a wire-mesh; c) a mesh artificially shaded; d) representation with returned laser intensity (Beraldin, 2009)

The simplest 3D representation depth information can be represented in a grayscale image; moreover a triangulation mesh can be used to display a range image, or using topology dependent slope angles to represent the local surface normal on a given triangle. Surface normal directions are generally used to artificially shade the acquired mesh, in order to highlight and reveal surface details (Figure 1.1).

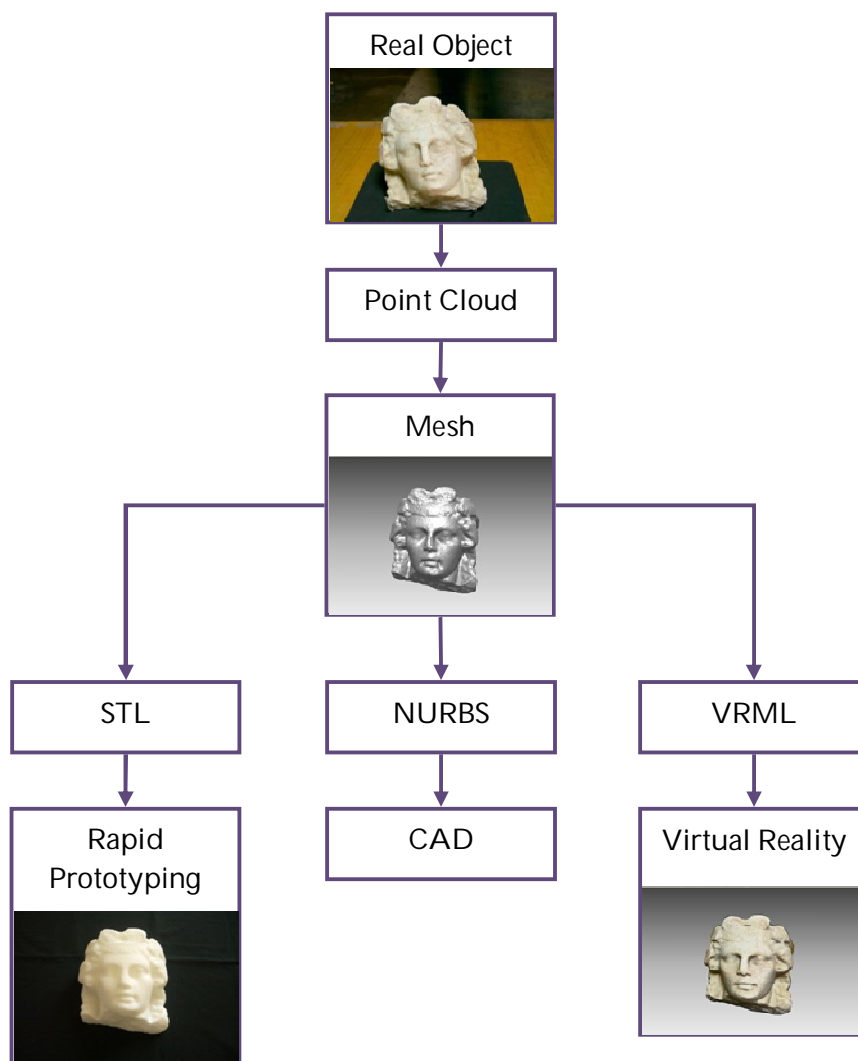


Figure 1.2 Reverse Engineering process and output

Object geometrical description is achieved by many different steps, starting from the acquisition of range maps that described the specimen surface as a discrete point cloud. Data acquired are elaborated and post processed in order to create a 3D surface composed by triangular elements (called mesh) that approach the real surface shape. Such polygonal triangular mesh can be stored in a *stl* (Solid To Layer) file format, which allows exchanges with CAM (Computed Aided Manufacturing) and RP (Rapid Prototyping) tools. Moreover 3D models can be used in Virtual Reality applications using VRML (Virtual Reality Modelling Language) as exchanging file format. A further development can be the realization of a NURBS surface that allows CAD modeling. The whole acquiring and elaboration process is presented in Figure 1.2.

1.1 Reverse Engineering tools

	Triangulation	Time delay	Monocular Images	Passive	Active	Direct	Indirect	Range	Surface Orientation
Laser triangulators	X				X	X		X	
Structured light	X				X	X		X	
Stereo vision	X			X		X		X	
Photogrammetry	X			X		X		X	
Time of Flight		X			X	X		X	
Interferometry		X			X	X		X	
Moiré fringe range contours			X		X		X	X	
Shape from focusing			X	X	X		X	X	
Shape from shadows			X		X		X	X	
Texture gradients			X	X			X		X
Shape from shading			X		X		X		X
Shape from photometry			X		X		X		X

Figure 1.3 Classification of 3D imaging techniques (Sansoni et al, 2009)

Many methodologies and systems for a semi automatic 3D data acquisition are currently used (Figure 1.3): according to the specific case study a technique will be more promising than another one. The choice on what scanning technique to use is dependent on object surface features: its dimensions, its surface complexity, the presence of holes or undersurfaces, reflective or transparency properties, its transportability and accessibility and the potential necessity to acquire other information, such as surface color, required accuracy and performances, time and costs.

In general Reverse Engineering techniques can be classified into two main groups in relation to the request or not of a contact between the acquisition device and the object. In **contact techniques**, point coordinates are evaluated thanks to a contact between the specimen and a probe; used sensors are generally investigating probes that go through object's surface into the 3D environment with a high precision level and with known trajectories. Coordinate Measuring Machines (CMM), articulated arms, and piezo sensors are some examples: they are characterized by high data precision and repeatability, even if they take a long time to scan a complex shape. Moreover, since a contact between object and probe is required and in many case studies it is not possible, they cannot be used in cultural heritage applications or for soft component scanning.

Another group of scanning systems measure points coordinates without a direct instrument – object contact, but an energy flux is radiated on specimen itself and the transmitted or reflected energy is the measured.

Computer Tomography is one of the most used **transmission method**: X-rays pass through analyzed object and their transmitted portion is measured. Different cross section planes are stored as DICOM images: data accuracy level depends on the slicing process. The different gray color level indicates object internal composition. A final object volumetric representation is obtained (Figure 1.4). This technique is not effected by specimen superficial and reflective properties, moreover it is able to detect object

internal holes and structures; on the other hand instruments used are particularly expensive and X-ray emission is required.

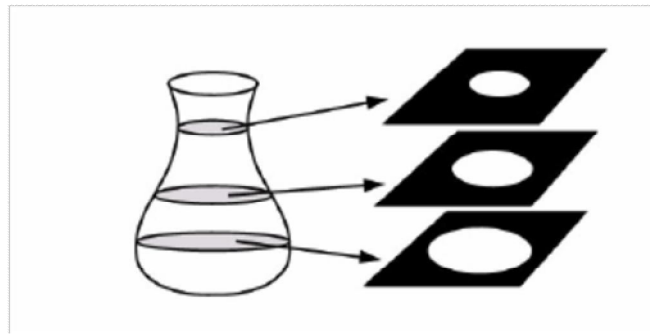


Figure 1.4 Volumetric data: an example

Reflective scanning devices can be optical or non optical, like sonar or microwave radar that measure object distance evaluating the time that an emitted wave (or impulse) takes to come back after its reflection on object surface.

Optical reflective systems are distinguished between active and passive tools: while the first ones are the most used acquiring devices, since they are able to detect in a fast and precise way a large data quantity, **passive scanning systems** used instead light naturally present in a scene. Photogrammetry, as example, is based on the acquisition of many photo images, with a calibrated camera, and taken from different points of view that are processed in order to define points coordinates. The elaboration pipeline consists basically in camera calibration and orientation, image point measurement, 3D point cloud generation, surface generation and texture mapping (Sansoni et al, 2009).

Optical active scanning systems send an energy flow on object surface and its geometry is measured on the basis of the definition of an optical quantity of reflective energy portion (Scopigno, 2005; Scopigno, 2003). A laser or a board spectrum source is used to artificially illuminate a surface, in order to acquire a dense point cloud using triangulation, time-of-flight or interferometric methods.

In **time-of-flight laser scanner**, points coordinates are measured on the basis of the time that emitter laser beam put to come back to the sensor after its reflection on object surface (Figure 1.5) according to Eq 1.1.

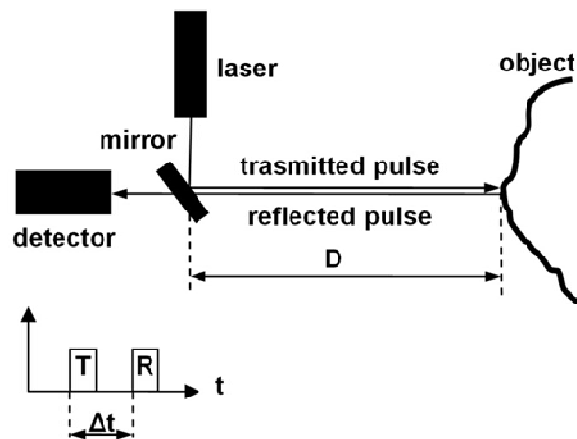


Figure 1.5 Time of flight laser scanner: the measuring principal

$$D = c \frac{\Delta t}{2} ; c \approx 3 \cdot 10^8 \text{ m/s} \quad \text{Eq 1.1}$$

Acquired data accuracy is related to time measurement precision and distances that these instruments are able to detect goes from some meters to some hundreds of meters, with a decreasing accuracy level.

On the other hand, in **optical triangulation laser scanner systems**, object points are defined by a trigonometrical process, between the relative positions of the CCD sensor and laser source and measuring from time to time the reflection angle (Figure 1.6), as indicated in Eq 1.2. Both single-point triangulators and laser stripes belong to this category.

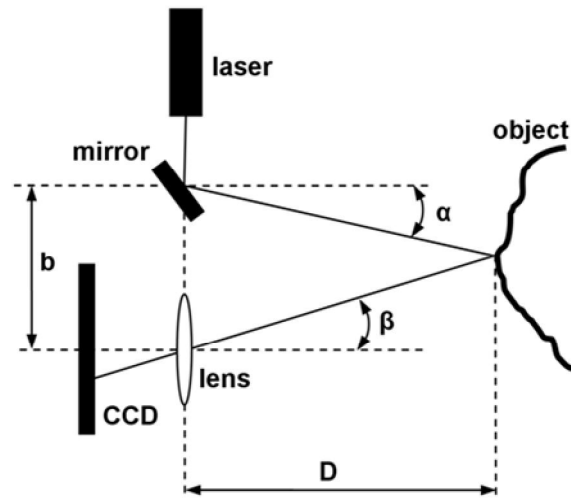


Figure 1.6 Triangulation laser scanner: the measuring principal

$$D = \frac{b}{\tan(\alpha + \beta)} \quad \text{Eq 1.2}$$

Laser triangulators accuracy and their relative insensitivity to illumination conditions are some of the main advantages related to this scanning principle. Single-point laser scanner are widely used in industrial applications for distances, diameters or thickness measurements. On the other hand laser stripes are mostly used for quality control and reverse modeling of heritage.

The triangulation approach is also used by **structured light** based 3D sensors. They project a bi-dimensional patterns of non-coherent light, which move in horizontal direction and scan the whole object surface (Figure 1.7). The surface shape distorts projected fringes that are acquired by a digital camera and elaborated in a range map (Guidi et al., 2010).

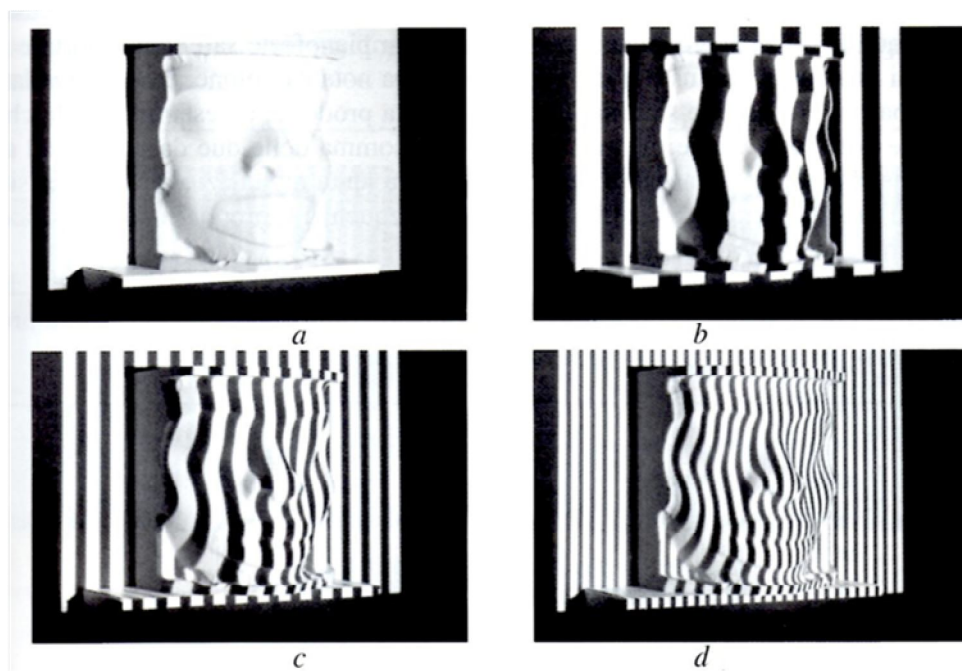


Figure 1.7 Example of a structured light scanning technique on an object surface: increasing fringe density is shown from image a) to image d) (Guidi et al, 2010)

Interferometric methods project a spatially or temporally varying pattern into a surface, followed by mixing the reflected light with a reference pattern. Since their resolution is a fraction of laser wavelength, acquired surface quality is very accurate and they are widely used in surface control, microprofilometry or in CMM calibration procedure.

TECHNOLOGY	STRENGTH	WEAKNESS
Laser triangulators	Relative simplicity Performance generally independent of ambient light High data acquisition rate	Safety constraint associated with the use of laser source Limited range and measurement volume Missing data in correspondence with occlusions and shadows Cost
Structured Light	High data acquisition rate Intermediate measurement volume Performance generally dependent of ambient light	Safety constraints, if laser based Computationally middle-complex Missing data in correspondence with occlusions and shadows Cost
Stereo Vision	Simple and inexpensive High accuracy on well-defined targets	Computation demanding Sparse data covering Limited to well defined scenes Low data acquisition rate
Photogrammetry	Simple and inexpensive High accuracy on well-defined targets	Computation demanding Sparse data covering Limited to well defined scenes Low data acquisition rate
Time-of-Flight	Medium to large measurement range Good data acquisition rate Performance generally independent of ambient light	Cost Accuracy is inferior to triangulation at close ranges
Interferometry	Sub-micron accuracy in micro-ranges	Measurement capability limited to quasi-flat surfaces Cost Limited applicability in industrial environment
Moiré fringe range contours	Simple and low cost Short ranges	Limited to the measurement of smooth surfaces
Shape from focusing	Simple and inexpensive Available sensors for surface inspection and microprofilometry	Limited fields of view Non-uniform spatial resolution Performance affected by ambient light (if passive)
Shape from shadows	Low cost Limited demand for computing power	Low accuracy
Texture gradients	Simple and low cost	Low accuracy
Shape from shading	Simple and low cost	Low accuracy

Figure 1.8 Comparison between optical range imaging technique (Sansoni et al, 2009)

A final scheme of optical scanning devices is shown in Figure 1.8: their strength and weakness are always take into exam when a method should be chosen in a defined application.

In this technical panorama, many research activities are focused on the integration of data coming from different sources, in order to provide more information in the same 3D model. Some examples regard the integration between volumetric and superficial data (Fantini et al., 2005), or data coming from instruments with different resolution level (De Crescenzo et al, 2010). Other works are related on instrument performances and error detection (Some detailed example will be presented in Section 2.2)

1.2 *The acquisition pipeline*

The process from a real object to a 3D shapes is composed by different steps that can change in relation to the instrument and technology used in the reverse engineering process. Considering acquiring object surface with an optical laser scanner, the output of each scan is a range map, that is to say a 3D array of acquired points, which can be post processed as a point cloud or as a triangulated surface (mesh).

The acquisition pipeline is composed by some consecutive following steps that are listed below.

1.2.1 Scans planning and acquisition process

Each scan output is a range map describing the object surface portion in the acquisition frame. A complete 3D description of the whole specimen is obtained from

many different range maps acquired from different points of view. In this context the first phase consists in a detained planning of how many scans are necessary to acquire the surface of interest and where such scans should be taken. This procedure should tend to reduce the number to necessary scans in order to reduce time and costs, and, at the same time, the final model would be without holes or not acquired parts.

Since acquired range maps will be then register together in order to obtain an unique model, it is important to have about 30% of overlapping points between two subsequent point clouds. Moreover, in order to increase final mesh quality, it is important to perform the scanning process with the laser beam as perpendicular as possible to the object surface.

1.2.2 The registration process

The acquisition phase output consists in many different range maps, describing the correspondence portion of the object surface, and each of them has its own reference system. The following phase aims to register all acquired point clouds, saving them in a unique and common coordinate reference system.

A first registration process is performed during the acquisition phase and consists in the identification of at list 3 homologous point belonging to two different scans (Figure 1.9): the software is then able to perform a point registration minimizing the gap between the two considered point clouds.

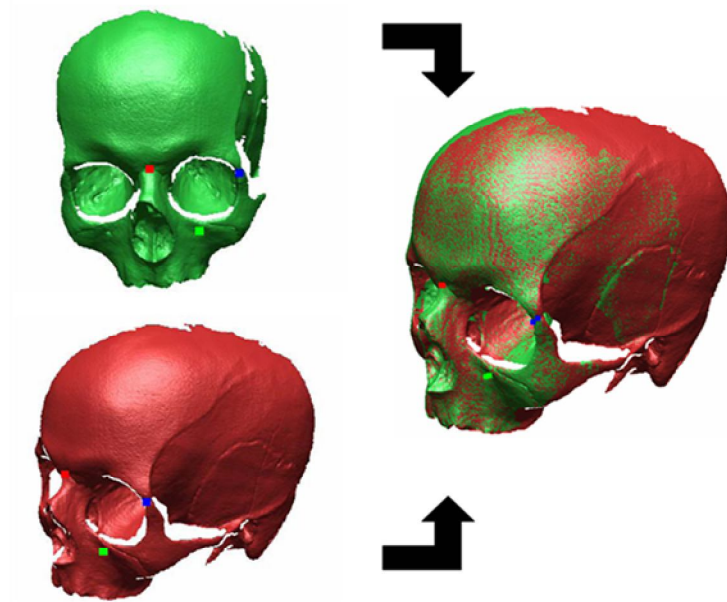


Figure 1.9 Two different range maps are first register by the identification of 3 pairs of homologous points

Once this first phase has been performed, all acquired scans are involved in a refinement registration process, whose aim is to improve the alignment between all range maps at the same time.

1.2.3 Range map merge and refining phases

After the registration process, all acquired frames are each other registered, but they are stored as different shells. A merge phase is then performed in order to obtain a unique mesh, in which the acquired range maps are mixed together. Redundant surface

portions are removed and for each of them the elaboration software considers only the range map portion that best fit that surface patch.

Before this phase some cleaning procedures are performed, in order to remove from each shell some triangles describing no object parts, but the surrounding environment. Moreover boundary points, containing more surface distortions or errors are similarly removed. Non manifold triangles, small clusters, redundant surfaces, long spikes are some of the most common error typologies.

Some holes are then closed and a smooth procedure is performed, in order to remove noise (Figure 1.10).

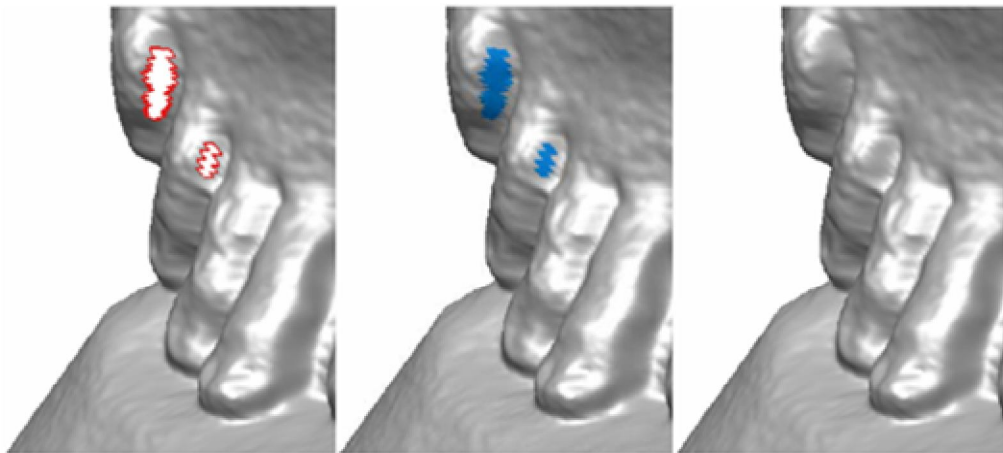


Figure 1.10 Filling holes on an acquired mesh

During the acquisition process many points are obtained to describe a surface portion. In many case studying they are too much and even if a point reduction is performed no surface details are lost and, on the other hand, file size can be much

thinner. Point are remove on the basis of surface curvature, so that at the end of this process, their density is not uniform and more points are used to describe more complex and non uniform surface portions.

The final 3D model is an exact copy of the real object as concerns its geometry, shape and dimensions. In many applications a photo is also acquired and then registered on the final mesh as a texture, so that is color appearance is represented as well.

2. Experimental Error Compensation Procedure

Laser Scanner instruments are widely used in a widespread range of applications and cases, thanks to the possibility of acquiring a large number of points in very few seconds and are capable to describe surfaces of almost every kind of complexity and shape. This feature allows underlining a lot of case studies which use gives the possibility to reduce time in product design and improve quality processes and testing. In spite of these considerations, the employment of scanning instrument is connected to some preliminary considerations leading to a more aware use of those tools.

First of all, some hundreds of thousands of points on object's surface are acquired at the same time. However, it may occur that some useful points are not directly acquired (such as corners or borders), and it is possible to reconstruct them in post processing phase, identifying the other points in range map. A real surface, which is a continuous surface, is numerically changed into a discrete surface and not all surface points are thus acquired (only some of them) and the others are deducted by a software procedure. This has effects on the definition of surface edges. Conversely, it may happen that the same part is acquired many times in different scans, from a different view: so it is described by different point's clouds and in each of them it is impossible to have

exactly the same point's coordinates. During post processing procedure, and in particular during the merge one, only one patch of one range map is selected to describe such surface portion.

Another interesting source of uncertainties in the acquiring procedure arise from the fact that laser scanners, like all measuring instruments, introduce some errors in determining points coordinates, so that if we acquire twice the same surface, under the same conditions, data obtained will never be exactly the same. This is caused by many factors, internal or external to the instrument itself, from the reflective properties of object's surface and operative conditions, to laser scanner calibration and manufacturing features.

All these uncertainty reasons can be grouped into two different classes: a random component and a systematic component. Whereas the random part of error, in each scan, changes in module and sign, so that it is not possible to pre-determine it, the systematic component of error, in principle, can be identified, due to its property to maintain a homogeneous trend. In operational cases, these errors are clearly visible in the acquired mesh as a superficial noise.

Tools for noise reduction and smoothing procedure are present, in common commercial elaboration software, and they apply mathematical transformations which do not take into account errors nature and causes. For these reasons, it may happen that

some little details, present on object surface, are smoothed like a noise disturb, so that they are missing in the 3D representation.

By these considerations, and to overcome the issue above mentioned, an experimental and repeatable methodology is proposed to identify and correct the systematic part of the error in data acquired by an optical triangulation laser scanner, in a well-controlled manner.

Exploiting a reference surface, under well-defined operative conditions, systematic errors are determined in order to reduce their impact on further scans under similar conditions, improving scanning performances in terms of accuracy. A repeatable correction procedure is thus defined, in order to reduce shell noise, caused by the systematic portion of error and without any lost in detail due to an uncontrolled smoothing process. Finally, a parametric library of arrays for error reduction is created according to scanning operative conditions and surface orientation (Eq 2.1): a different array (ΔS) is defined according to acquisition distance d , laser scanner lens f used in the particular application and surface normal orientation (defined by angles α and β). Each point (i,j) of the acquired frame is corrected with its homologous value in the reference array.

$$\Delta S = f (i, j, d, f, \alpha, \beta) \quad \text{Eq 2.1}$$

In spite of an ever increasing use of RE technologies, unified standards and certifications for the evaluation of laser scanner's performances and for determining

measurement's repeatability, accuracy or precision are not yet defined. Moreover, no standards and unified procedures are certified in order to reduce instruments measuring errors.

Nevertheless, instrument's periodical calibration plays a fundamental role in verifying and setting many internal scanning parameters and reducing part of the acquiring error.

In this chapter, a method for error correction is presented: first of all, scanning errors and performances are mathematically analyzed and then methodologies for error evaluation and accuracy increasing available in literature are taken into account. A correction procedure is then proposed and analyzed.

2.1 Mathematical analysis of errors

The evaluation of instrument performances and measurements accuracy are associated to theoretical definition of some basic concepts related to error characterization and uncertainties.

The absolute error of a measurement is the difference between a measured value y^* and the real one y (Eq 2.2):

$$\Delta y = y^* - y \quad \textbf{Eq 2.2}$$

Measurement relative error is the ratio of the absolute error to the actual value (Eq 2.3):

$$\delta y = \frac{\Delta y}{y} = \frac{y^* - y}{y} \quad \text{Eq 2.3}$$

In practical cases measurement real value is unknown and the measured value is the true conventional used one. For this reason it is important to evaluate a range which the actual value is located in: this lead to the definition of the limiting error, which is the smallest range around the measured value y^* , containing the real value y (Eq 2.4):

$$y^* - \Delta y_{min} \geq y \geq y^* + \Delta y_{max} \quad \text{Eq 2.4}$$

Considering measurement errors in repeatable experiments, two different types of error are analyzed: a division into random and systematic error is made. The **Systematic error** (also known as **bias**), is the difference between the mean value calculated from an infinite number of measurements of the same quantity, carried out under the same conditions, and its actual value. Investigating results of the same repeated measurement, this error quantity changes its sign or value according to a specific law or function.

The error component is commonly called **random** error and it is defined as the difference between the result of an individual measurement and the mean value calculated from an infinite number of measurements of a quantity, carried out under the same conditions.

Errors types above defined refer to the results of individual measurements. **Indirect measurements** are those measurements in which the model is provided in form of function of input quantities. In such cases, the error is defined according to the law of

error propagation: an output quantity error, inherent to known errors of input quantities, can be measured by the methods of increments or the methods of the total differential. The method of increment, the exact method, consist of determining the increment of a measurement model function for the known increment of input quantities. For complicate measurement models, error evaluation becomes a long process and therefore it's evaluated by approximated methods, such as the total differential method. It is based on the expansion of the studying function as a Taylor series around the point defined by the actual (conventionally true) values in input (Minkina, 2009).

Uncertainties in measuring processes generates doubts in results itself and they express the lack of accurate knowledge of the measured quantity. In detail, the standard uncertainty of a measurement is the uncertainty of measurement values, that specifies the dispersion of the values that could reasonably be attributed to the measured quantity that can be expresses in the form of the standard deviation (ISO ENV 13005).

To estimate measurement quantitative accuracy, some model inputs are considered as random variables that are described by a probability distribution function. For estimating measurement accuracy, the most important statistics of random variables are the expected value and the standard deviation value. The **expected value** $E(X)$ of a discrete random variable X , which values x_i appear with probabilities p_i is (Eq 2.5):

$$E(X) = \sum_i p_i x_i \quad \text{Eq 2.5}$$

The set of measured values x_i is a finite N-element set. The expected value is substituted by its estimator, that is the arithmetic mean from N independent observations (Eq 2.6):

$$\bar{x} = \frac{1}{N} \sum_{i=1}^N x_i \quad \text{Eq 2.6}$$

A random variable **standard deviation** is the positive square root of the variance (Eq 2.7):

$$\sigma(X) = \sqrt{E[X - E(X)]^2} \quad \text{Eq 2.7}$$

In practical problems an estimator of standard deviation, called experimental standard deviation (Eq 2.8) is used (Minkina, 2009, ISO ENV 13005):

$$\sigma(x_i) = \sqrt{\frac{1}{N-1} \sum (x_i - \bar{x})^2} \quad \text{Eq 2.8}$$

2.1.1 Resolution, accuracy and precision

Some more basis quantities are now introduced: resolution, precision and accuracy.

Resolution is the smallest spatial step that the instrument is able to detect; it can be measured in X, Y and Z directions.

In determining point's coordinates through a series of measures, **precision** (or uncertainty) is standard deviation of that measures: a high precision corresponds to a low standard deviation, and it represents random component of error. Instead, **accuracy** is instrument capability to give, at each measure, a data near to the real value (Azzoni, 2006; Taylor, 2004; Webster, 1999).

The degree of inaccuracy (or the total measurement error δ) is the difference between the measured value and the true value. The total error is the sum of the bias error (β), which is systematic, and the precision error (σ) that is the its random component (Coleman, Steele, 1989). A number of measurements, one after the other, of the same variable, whose real value is V , that is absolutely steady, is performed (Figure 2.1). Since the bias (β) is a fixed error, it is the same for each measurement. The precision error is a random error (σ) and will have a different value for each measurement. Since the total error is the sum of the two components, it will be different for each point (Eq 2.9):

$$\delta_i = \beta + \sigma_i \quad \text{Eq 2.9}$$

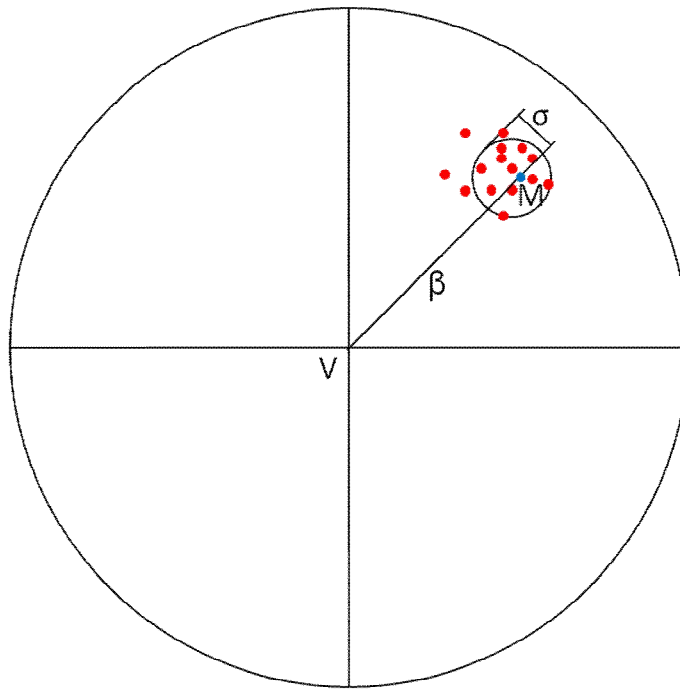
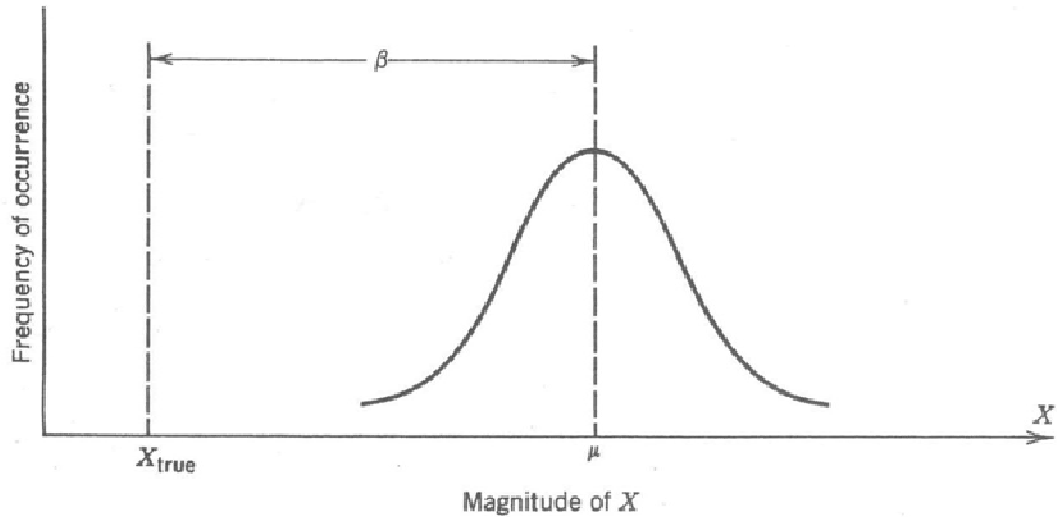


Figure 2.1 The same quantity is measured many times: σ is the precision error and it is random; β is the bias error and it is systematic

Considering to acquire N measurements and N approaches to infinity, data would appear as Figure 2.2. The bias would be given by the difference between the mean value of the N readings (μ) and the true value of X , whereas the precision errors would cause the frequency of occurrence of the readings to be distributed about the mean value.



**Figure 2.2 Error in measurement of a variable in infinite number of readings
(Coleman, Steele, 1989)**

2.2 Error analysis in scanning processes

In spite of an increasing use of scanning devices, and in particular of laser scanner systems, a unified standard or a certified method for performances evaluation does not exist yet. Nevertheless, the necessity of increasing instrument accuracy and measurement repeatability is one of the most pursued research topic. Within this context, instrument calibration plays a fundamental role in defining some instrument internal parameters. Accuracy, repeatability measuring uncertainties can be defined, after a calibration procedure: conceptually, if the geometrical description of the object is defined, the deviation of each point on object's surface can be considered as an accuracy indicator. From this concept, it is possible to find a lot of experimental techniques, with

the aim to define the level of reliability of acquired data, and with the aim to verify and compare different instrument's performances.

Within this context, many experimental techniques are available in literature, in order to define measure confidence level, according to data true value, and to compare performances of different scanning instrument. Boehler et al (2003) perform some tests on different scanning devices (triangulation and time of flight): plane surfaces of different reflectivity are scans from different distances and a best fitting plane is created in order to get indications of the range measurements noise. Moreover, several tests are set up scanning white sphere as targets, with the aim to get information on scanning accuracy. Results show that even if a laser scanner shows better results, this does not means that the instrument is better at all. Instrument reliability has dependences with the specific application and case study. Test performed concerns angular accuracy, which is evaluated scanning two equal spheres, posed at the same distance from the scanning device, but in different positions (Figure 2.3): their horizontal and vertical length is measured and compared.

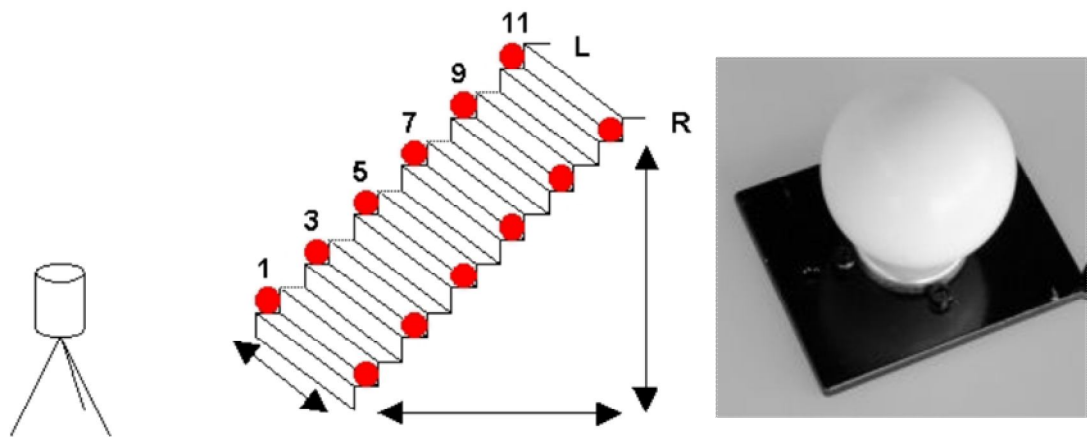


Figure 2.3 Sphere positions on a stairway (Boehler et al, 2003)

As regards resolution analysis, some information is obtained by scanning a target with small slot on its front panel (Figure 2.4): high resolution scanning devices are able to detect the bottom panel too, when the laser beam get through the front panel.



Figure 2.4 The target used for resolution investigation: an example of low (in the middle) and high (on the right) resolution instruments (Boehler et al, 2003)

Some more information are available comparing instrument performances when edge effects and surface reflections occur. Within this context, the presence of corners lead to the identification of wrong points, due to laser beam deviation, in proximity of

discontinuities: the acquisition of a sharp edge gives the possibility to test all the points that are located in a wrong position. Finally, surface reflective properties are due to some errors and uncertainties estimable by comparing plane of different material and color.

Artenese et al 2003, has the aim to define instrument precision value in order to compare three different techniques: optical triangulation laser scanner system, digital photogrammetry and mechanical feeler. A vase has been tested, whose vertexes are determined analytically in a very precise way (Figure 2.5). After the acquisition process the three point clouds have been compared: results shows that points in the middle parts are affected by a less gap than boundary points. Moreover, acquired range maps have different density: photogrammetry and mechanical feeler meshes have lower resolution levels.

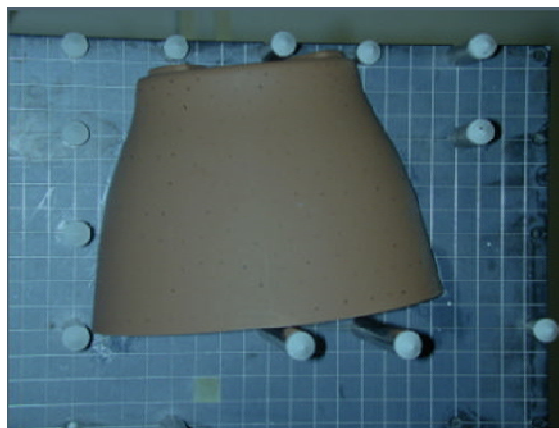


Figure 2.5 The testing vase (Artenese et al, 2003)

In Guidi, Remondino et al, 2007 the evaluation and characterization of 3D scanning devices are performed, by means of a set of comparative tests. Instrument resolution, precision, and accuracy characteristics are calculated for different laser scanner tools: such information is generally provided by instrument's datasheet even if its operative values are unknown quantities. A reference plane has been acquired and determined, elaboration software define instruments precision and resolution. Accuracy is defined after error decomposition in a random and a systematic component. Random noise effects are reduced defining an optimal number of scans, so that the systematic portion is definable. Finally, error random component is removed by a filtering process.

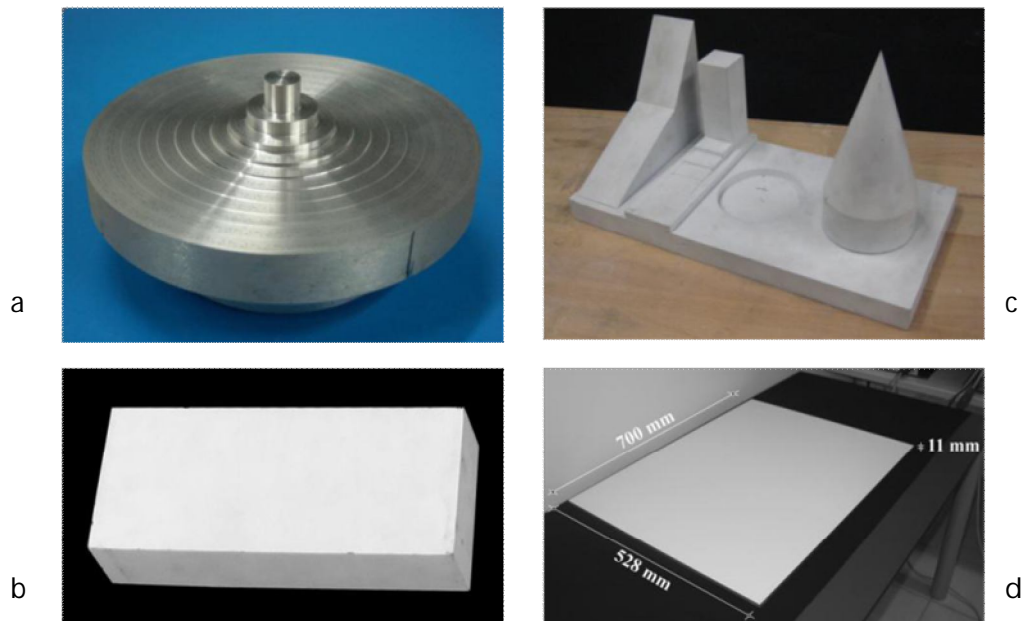


Figure 2.6 Test object used in the experiments to evaluate point resolution in Z (a) direction and in x,y one (b). some solids (c) and planes (d) are evaluated to testing accuracy and uncertainty

Moreover, in Guidi et al, 2010, some experimental processes for evaluating triangulation based range sensors have been performed: in particular resolution, accuracy and uncertainty features are inspected scanning some reference tests objects, geometrically defined, as shown in Figure 2.6.

Many other works are related to the evaluation and characterization of 3D imaging sensors, in order to identify their metrical properties: the importance of this aspect is related to the possibility to compare different scanning instruments and to evaluate data acquired reliability. In particular Beraldin, 2009 reviews the basic principles of 3D imaging systems, related to triangulation and time of flight based laser scanners, in order to evaluate data uncertainties, the parameterization of a 3D surface and systematic errors. More over some uncertainties sources are identified (Figure 2.7).

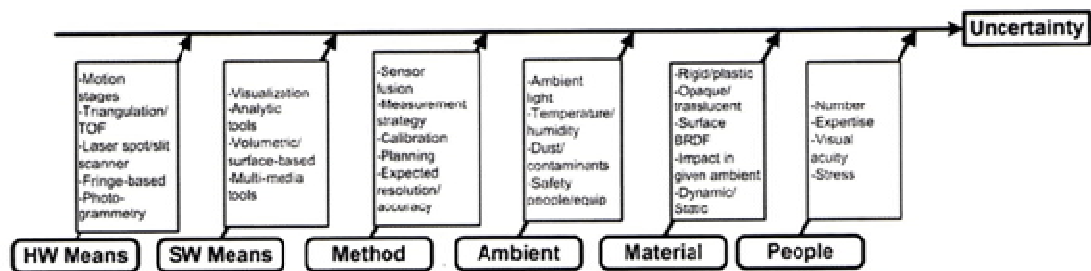


Figure 2.7 Origin of some typical uncertainties in 3D imaging systems (Beraldin, 2009)

In Beraldin et Gaiani, 2005, accuracy, measurement uncertainties and spatial resolution of 3D acquiring devices are taken into exam. They define a dependence of precision values on surface reflectance properties (marble surfaces, as example, induce more errors). Moreover, instrument accuracy is related to objects' shapes:

discontinuities, acute angles and holes can be due to a loss in measurements' accuracy. In optical triangulation scanning system, resolution is limited by laser beam diffraction (Figure 2.8): in fact a light beam, does not keep its beam parallel when it is far from its source and as less is its power, as the laser beam is divergent. This phenomenon can lead to some limitations in X and Y resolution and in Z direction an increase in laser beam power due to interferences (called speckle effect), that restricts resolution and measure accuracy.

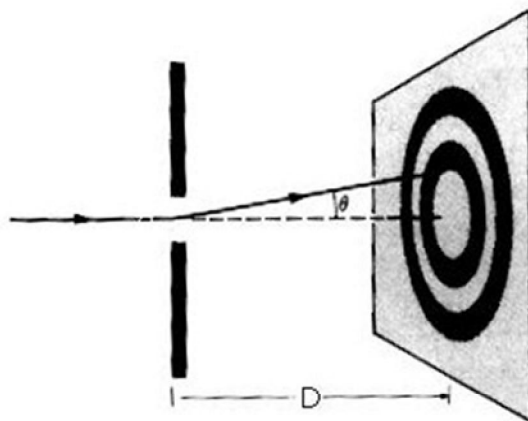


Figure 2.8 Laser beam diffraction

Another aspect is related to error systematic component, which originates oscillations in 3D acquired frames: this effect can be corrected by means of a right sensor design or by a filtering process.

Many others works are more focused on error definition and correction than to systems classification and evaluation. As example, in Xi et al., 2001, an error

characterization has been performed with the final aim to achieve a software compensation. An empirical formula has been identified, relating errors to their influencing factors, like projecting angles and scanning depth. An experimental set up was performed, composed by a reference plane with a reference sphere on it. Many scans are performed changing surface normal directions and scanning distances. The real configuration is also acquired by a CMM tool, so that the two different point clouds have been compared. An error empirical formula is thus defined as function of both the acquiring distance and the angular incidence of the laser beam.

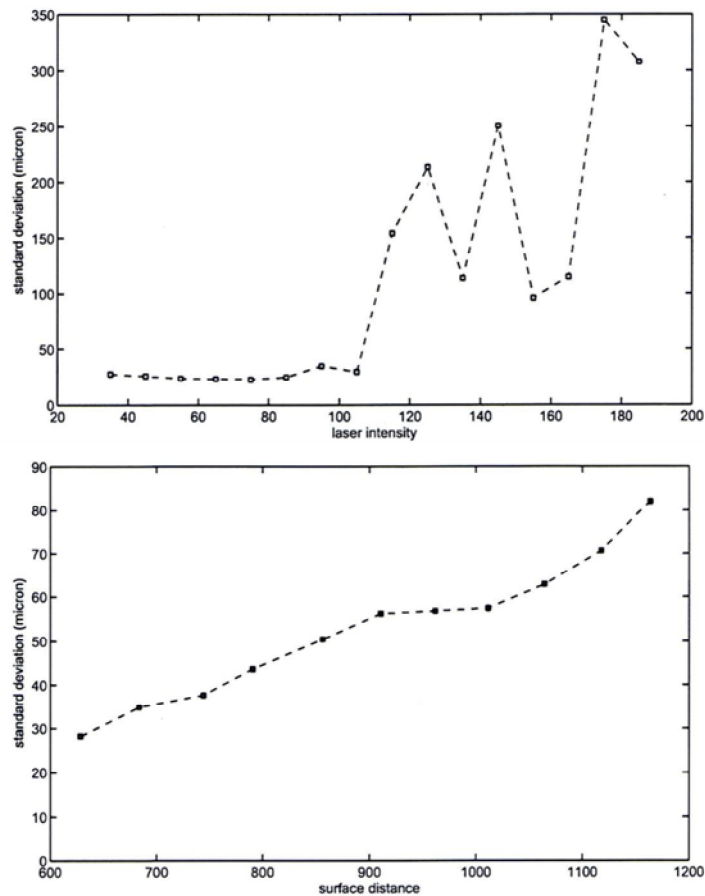


Figure 2.9 Noise standard deviation in relation to the variation of (on the top) scanner laser intensity and (on the bottom) of surface distance (Sun et al, 2009)

A further analysis on noise in 3D scanning procedures has been performed by Sun et al, 2009. They defined as data noise factors the ambient light, the distance of the specimen to the camera, scanner laser intensity and specimen orientation, defined by the angle between the optical axis and the surface normal direction (Figure 2.9).

Many of these analyzed works have inspired the present research activity, in a certain sense that it has been possible to identify scanned performances and errors: a reference specimen has been used and some factors have been considered as particularly influenced in error definition, as focus distance, object surface orientation in respect to laser beam and the optical lens used, during all tests performed. In the following parts, methodology will be presented in detail.

2.3 Methodology guidelines

The proposed methodology has the aim to define laser scanner performances and, in particular, accuracy, precision and resolution are determined for an optical active laser scanner. Moreover, in points' coordinate definition, errors are evaluated, with the final objective to reduce their systematic portion.

Theoretically, the idea inherent to this study considers the acquired data as the sum of three contributions: the real point coordinate value and the local values of the systematic and random errors. If a reference surface is acquired, since we assume that its geometry is known, it is possible to evaluate the error for each acquired point.

The proposed methodology can be divided into three main phases: acquisition phase, elaboration phase, and error correction and compensation procedure. During the acquisition phase, a referenced surface is acquired under different operating conditions, and for each of them, many scans are performed, with the same acquired frame. This dataset is then elaborated, with software for numerical calculus, during the elaboration phase: mesh data acquired under the same operating conditions are conveniently treated to perform a mean process. This process allows to reduce the random portion of error, so that the systematic part of error is the only one that is yet present. During the compensation phase, a comparison between the reference surface geometry and the acquired data is set up, in order to define the error in coordinates of each observed point. A correction array is thus defined, containing, for each acquired point its gap between the real and the measured value, which coincides with the systematic portion of error.

2.3.1 Materials and instruments

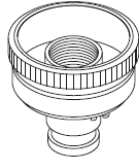
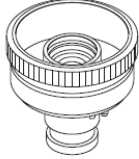
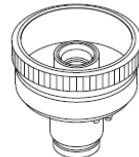
The experimental method has been performed with *Konica Minolta Vivid-9i* laser scanner, which is an optical active triangulation scanning device. The defined error correction arrays are efficient for only this particular instrument (serial number 1501112), since the systematic component of error can be caused by laser scanner

internal parameters. In spite of this fact, the proposed methodology can be applied as presented, or adapted, also to others optical scanning instruments.

	Focal Distance (mm)	Typical Scanning Distance (mm)
TELE	25	600 – 700
MIDDLE	14	700 – 800
WIDE	8	800 – 900

Table 2.1 Konica Minolta Vivid-9i: some instrument information

Konica Minolta Vivid-9i is an optical triangulation laser scanner. It is provided with three lenses (Tele, Middle and Wide), with different focal distances (as described in Table 2.1), which are used in relation to scanning distance and to the expected size of the frame (in Table 2.2 acquired areas are presented). Moreover, some performance parameters are provided, such as accuracy, precision, and resolution at different distances according to the lens used (Table 2.3). More detailed data are shown in Appendix A.

TELE Lens 	Measurement Distance mm		500	600	800	1000	2500
	Object Size mm	Horizontal	93	111	148	185	463
		Vertical	69	83	111	139	347
MIDDLE Lens 	Measurement Distance mm		500	600	800	1000	2500
	Object Size mm	Horizontal	165	198	263	329	823
		Vertical	124	148	198	247	618
WIDE Lens 	Measurement Distance mm		500	600	800	1000	2500
	Object Size mm	Horizontal	299	359	478	598	1495
		Vertical	224	269	359	449	1121

**Table 2.2 Laser scanner optics: area acquirable from each lens. All values are in mm.
Data are taken from Konica Minolta datasheet**

	TELE	MIDDLE	WIDE
<u>Accuracy</u>			
Distance: 600m	±0.05 mm	±0.10 mm	±0.20 mm
Distance: 1000 mm	±0.10 mm	±0.20 mm	±0.40 mm
<u>Precision</u>			
Distance: 600m	0.008 mm	0.016 mm	0.032 mm

Distance: 1000 mm	0.024 mm	0.048 mm	0.096 mm
<u>Resolution</u>			
Distance: 600m	111 x 83 x 40 mm	198 x 148 x 64 mm	359 x 269 x 108 mm
Distance: 1000 mm	185 x 139 x 110 mm	329 x 247 x 176 mm	598 x 449 x 284 mm
Conditions: Using Field Calibration System and Konica Minolta service software; Temperature: 20°C, Relative humidity: 65% or less			

Table 2.3 Performance parameters of Konica Minolta laser scanner. Data are taken from Konica Minolta datasheet

The referenced surface, used in the acquisition process, consists of a painted and opaque glass sheet: the thin varnish film makes the transparent glass opaque (so that points on it can be acquired by an optical system), with low reflective properties and high level of plane finish having a roughness lower than instrument resolution (Figure 2.10). So, the noise in acquired range map is mainly due to instrument and scanning conditions and not to object's surface features.

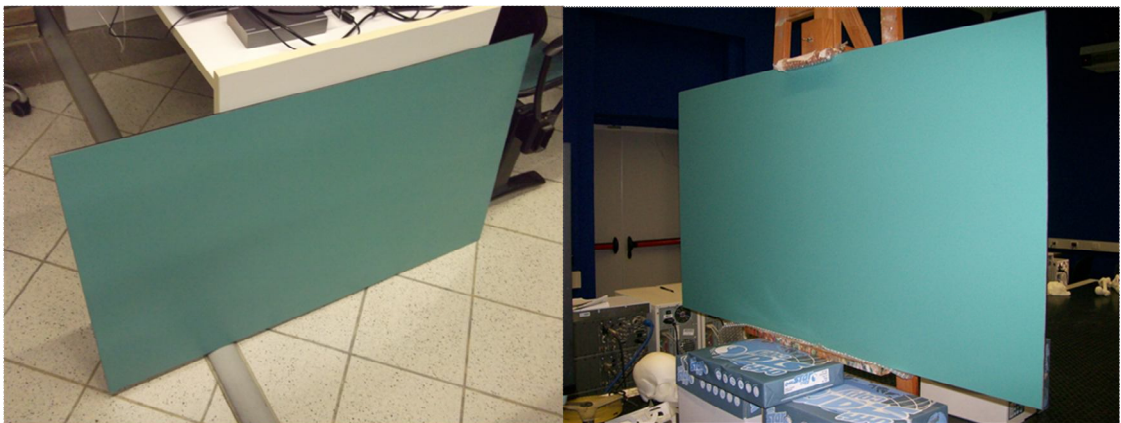


Figure 2.10 The reference surface used for the acquisition process

The glass is produced by *Glaverbel* (www.glaverbel.com) and its dimensions (1200 x 660 mm) are chosen in accordance with the maximum area that the instrument can acquire with the Wide lens at a distance of 1 meter. The glass sheet is 6 mm thick, in order to avoid any flexures and any loss in planarity, which would alter the acquisition procedure.

A referenced surface is necessary to identify error systematic component, for this reason it is necessary to know not only its dimensions and position according to laser scanner location, but also its geometrical features. In particular, planarity attributes are tested by a CMM (Coordinate Measuring Machine) that measure points coordinates by means of a scanning probe. Since the CMM probe can test many points' coordinates on the surface with a precision and repeatability 50% higher than the laser scanner, it is possible to verify that the actual surface flatness has discontinuities under the laser scanner resolution.

2.3.2 Experimental set up

2.3.2.1 Laser scanner calibration

In order to test laser scanner accuracy and precision performances, a preliminary calibration procedure is necessary: simple calibration is performed at the measurement site to determine compensation parameters to balance changes in the instrument's condition, such as changing lenses or modifications in the environment. This enables

standard performance to be maintained even in the user's measuring environment. In particular, the shift from the standard values is determined, and compensation parameters to minimize this changes are calculated.

Theoretically, being performed the same measurement, the measured values should be the same as the standard values which were measured at the time of shipment from the factory, but distortion of the measurement space occurs due to changes in the VIVID 9i/VI-9i condition, such as the tightness of the lens when the lens is changed, changes in the environment temperature, etc., and there is some shift between the output measured values and the standard values. When user calibration is performed, compensation parameters to minimize the amount of shift are calculated, and the 3D parameters set at the time of shipment from the factory are re-optimized. Then, when the actual measurement is performed, 3D generation parameters including the effect of this user calibration are used, so that the standard performance of the instrument is maintained.

A *Field Calibration System* (Figure 2.11) is associated to each scanning device (Vivid manual).

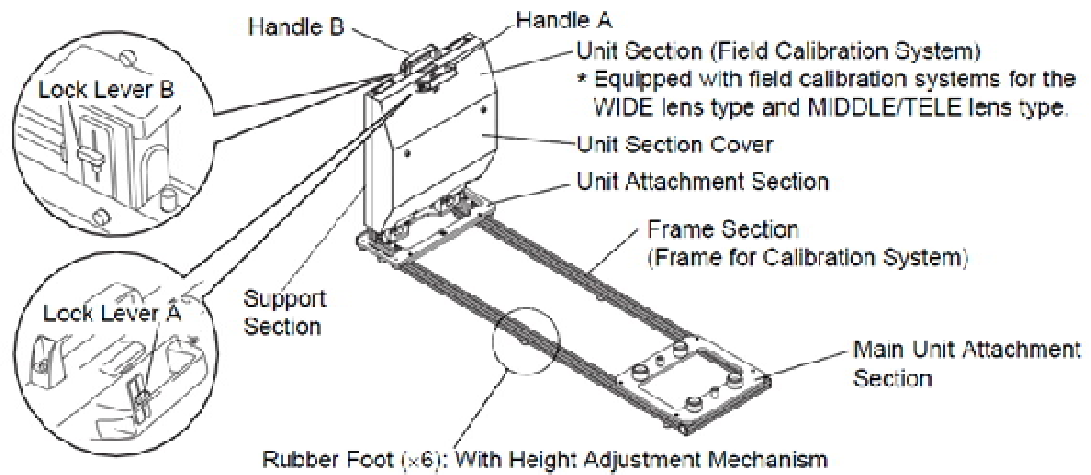


Figure 2.11 The Field Calibration System, parts nomenclature (Vivid manual)

A secure installation location that meets the dimensional requirements is necessary to install the Field Calibration System. Before using the Field Calibration System, a "Calibration Area" for stable and high quality calibration is required, in addition to the place that is necessary to position the Field (Figure 2.12).

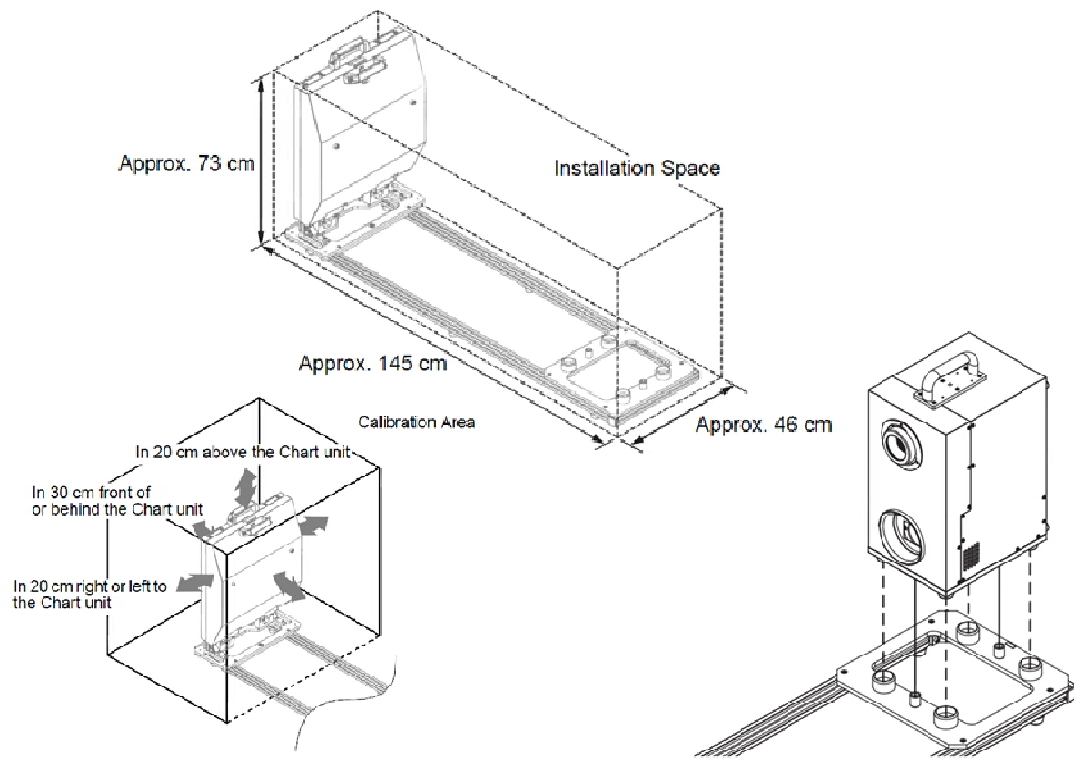


Figure 2.12 The Field Calibration System: the installation space, the calibration area and laser scanner connection (Vivid manual)

Laser scanner is attached into the main unit and the calibration procedure is performed. Two different calibration charts are used, according to the lens used during the acquisition procedure: all lenses are tested. The calibration area has two different covers: the first one is for Wide lens and the second one, with a more little calibration profile, is for Tele and Middle lenses (Figure 2.13).

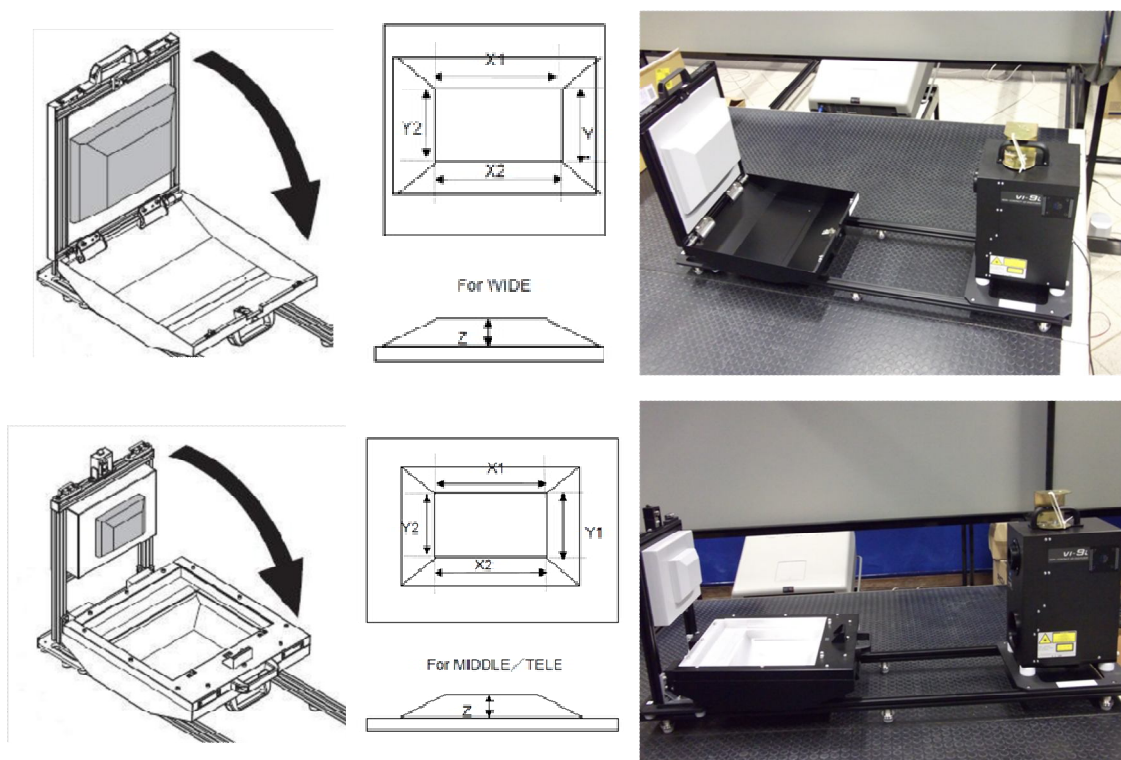


Figure 2.13 The calibration chart: on the top the calibration of the Wide lens and on the bottom Tele and Middle procedures are shown.

Lens used	User calibration chart used	Values stored	Design dimension
TELE	For MIDDLE/TELE	X1,X2	111.0
		Y1,Y2	78.1
MIDDLE	For MIDDLE/TELE	X1,X2	111.0
		Y1,Y2	78.1
		Z	41.5
WIDE	For WIDE	X1,X2	236.7
		Y1,Y2	116.3
		Z	75.0

Table 2.4 Stored Calibration Values and Design Dimensions (Units: mm)

The calibration chart is mounted on the user calibration frame (Measuring distance: 1000mm), and the standard values for each lens (TELE, MIDDLE, and WIDE) are measured. Four standard values (X1, Y1, X2, and Y2) are stored for the TELE lens; for the MIDDLE and WIDE lens, the Z value is also added, so five values are stored (Table 2.4).

The user calibration chart is measured, the current 3D generation parameters are used to perform 3D calculations, and the measurement values are calculated. These measured values and the standard values stored at the time of factory shipment are compared, and the differences are calculated. Compensation parameters to minimize the differences calculated in the above step are computed, and the 3D generation parameters are re-optimized. When the compensation parameters calculated in the above step are used and the user calibration chart is measured again, the remaining error amount or residual difference (the remaining difference when the error could not be completely eliminated) is displayed. The residual differences are shown as the output results after determining whether or not user calibration was performed properly.

2.3.2.2 Reference surface structure

An experimental configuration has been set up to perform all necessary scanning. The main requirements imply the possibility to fix the glass sheet rigidly, so that it would be possible to control its movements in a precise way. Moreover, its

position should remain constant and fixed with respect to laser scanner position, during the whole acquisition phase. While at the very beginning of this experimentation the glass sheet was posed vertically and rigidly fixed, during the fine tuning of the methodology, a structure has been customized to this application, in order to achieve the described purposes.

The structure is designed as a mechanical device, capable to give the glass sheet two degrees of freedom: two independent rotation angles (α , β) of the plane are defined according to the rotation around its symmetrical axis, which are indicated X and Y axis, as shown in Figure 2.14.

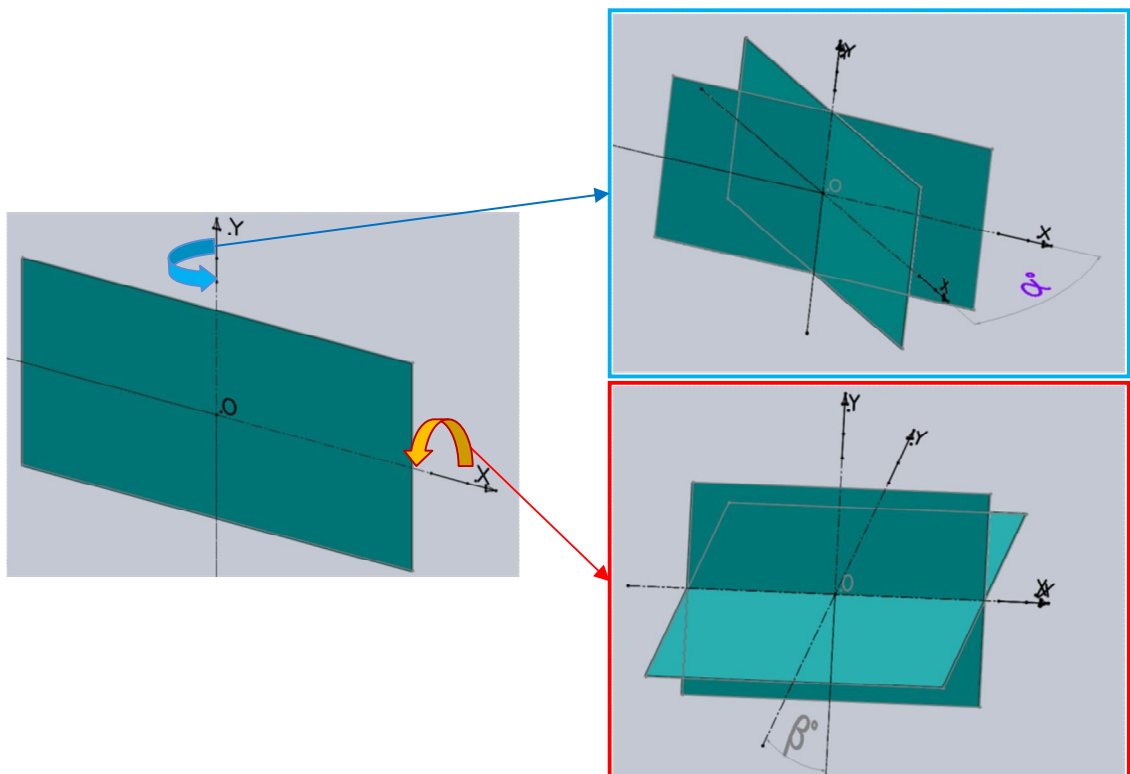


Figure 2.14 Glass sheet degree of freedom

One degree (1°) is the minimum rotation angle expected, in order to have a suitable precision level. Moreover, as shown in Figure 2.14, the sheet focal point O, is expected to remain firm and constant during the whole acquisition, even if the structure is moved.

A mechanical structure is thus been defined and designed. A CAD model was elaborated, in *SolidWorks* (*Dassault Systèmes SolidWorks Corporation*): a parametric software for CAD modeling. The structure consists of aluminum frame, supported by two pillars. Inside this frame, an aluminum structure supports the glass sheet. The two degrees of freedom are obtained as follows: the rotation angle α , around Y axis, is permitted through a couple of bearings, located as joints between the frame and two clamps structures which support top-down the plane. The second angle β , is defined by another couple of bearings located as joints between the frame and the two pillars; such bearings are located one on the left and one on the right of the reference plane. Two gears enable to manage all movements.

In details: the glass sheet has been first of all fixed with two clamps, attached in the middle of its longer side (1.2 m one), one at the top and the other at the bottom. Such clamps are composed by an aluminum L sectioned bar, connected with a front plate (its dimensions are 500 x 40 x 5 mm) by 4 screws (ISO 7380 M5x20), as shown in Figure 2.15.

A pivot is fixed into each L sectioned bar, in order to fix the reference plane into the moving frame. Two bearings are thus used to allow free rotations around the Y fixed axis.

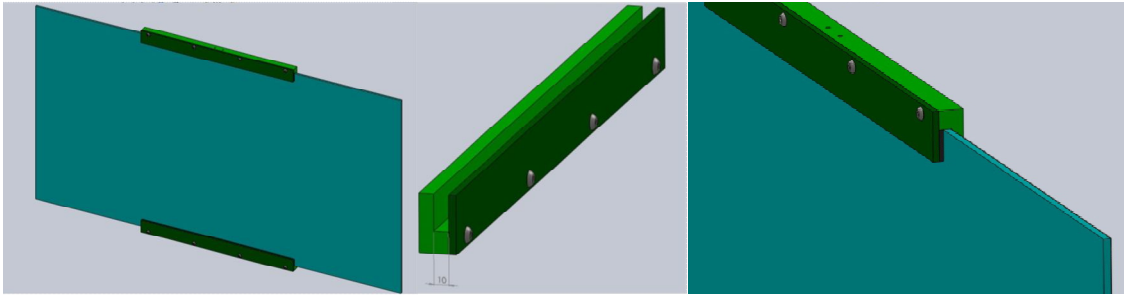


Figure 2.15 Glass sheet fixing: clamps connections

The four shafts are made by a lathe, two for each rotation. The two shafts which refer to Y axis are fixed with two screws to the L section bar and inserted into the two bearings. Whereas the down shaft is the driving one, the upper one is guided. Shaft's connection is shown in Figure 2.16.

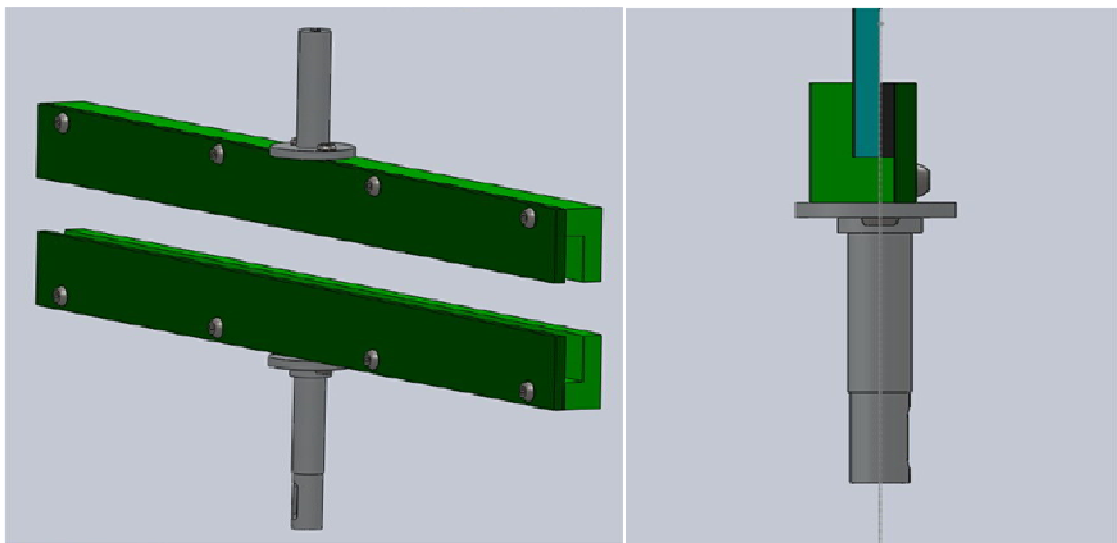


Figure 2.16 Upper and lower shafts

A frame was thus designed to hold the glass sheet. An aluminum tubular system (50 x 50 x 4 mm of section), is chosen in order to keep weight under a high value. Moreover, metal inserts are put into bar extremities, to allow screws strong fixing. Final frame dimensions are 1330 x 813 mm, in order to contain the glass sheet easily.

The sizing of all the other components is thus defined. Endless screw gears are selected, realized by *Tramec S.r.l.*: the selected model is XA 30 100 B3. This choice is justified by dimensional parameters and by the necessity to move objects without the transmission of high powers. Their representation is shown in Figure 2.17.

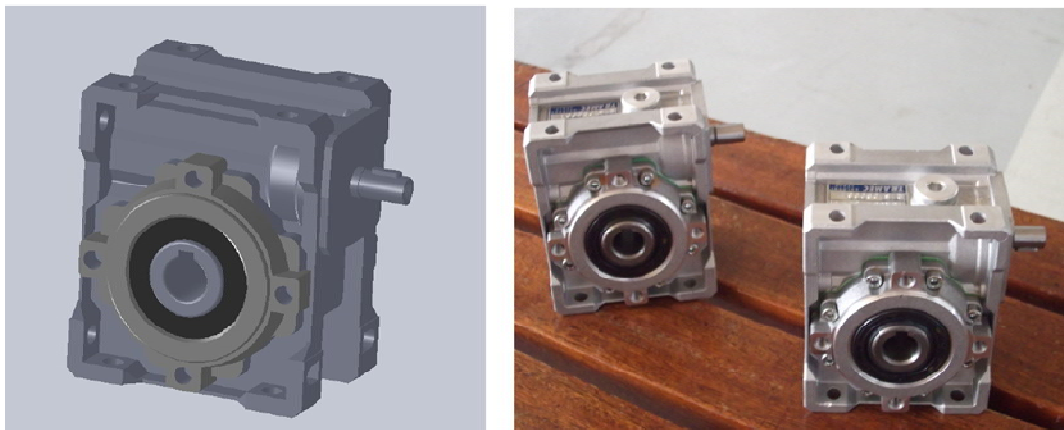


Figure 2.17 Gears: XA 30 100 B3 *Tramec S.r.l.*

According to gears' shaft diameter (14 mm), bearings are thus sized, considering the internal ring 15 mm wide. SKF 6002-2RSH bearings are chosen: two of them to move shafts directed as Y axis and the other two are for moving around X axis. Each bearing is contained into a box: four boxes are realized, with internal diameter of 32 mm, according to bearing external size, and the external diameter is 36 mm. A fixing flange (55 mm

diameter) is realized into boxes to allow their connections with the frame, by means of 4 M4 screws. The assembly of bearings and boxes with the frame in *SolidWorks* is shown in Figure 2.18.

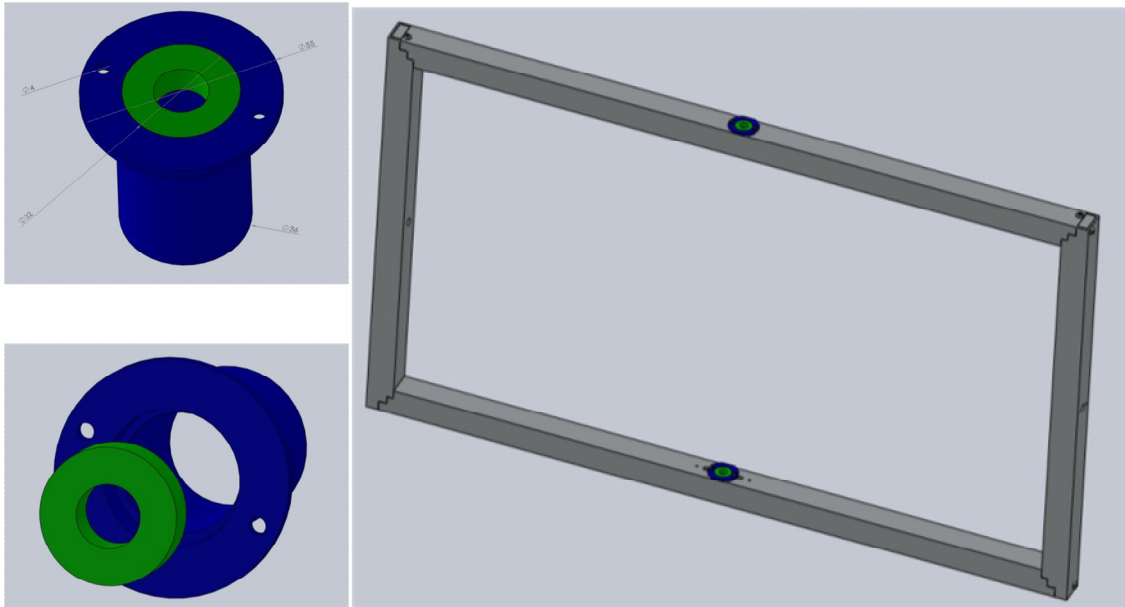


Figure 2.18 Bearings and their boxes insert into the frame: on the left the boxes are designed in blue, in green the bearings are sketched. On the right, their position into the up and bottom part of the frame

The driving shaft is connected, by means of a key UNI 6607, to the gear. The guided one is instead fixed up to the bearing.

Similar considerations are done for the shaft related to X axis: both of them are fixed to the external frame by means of screws, and they are inserted into two lateral pillars. Aluminum commercial pillars are used, size 100 x 50 x 4 mm. The final assembly between the frame and shafts and bearings is shown in Figure 2.19.

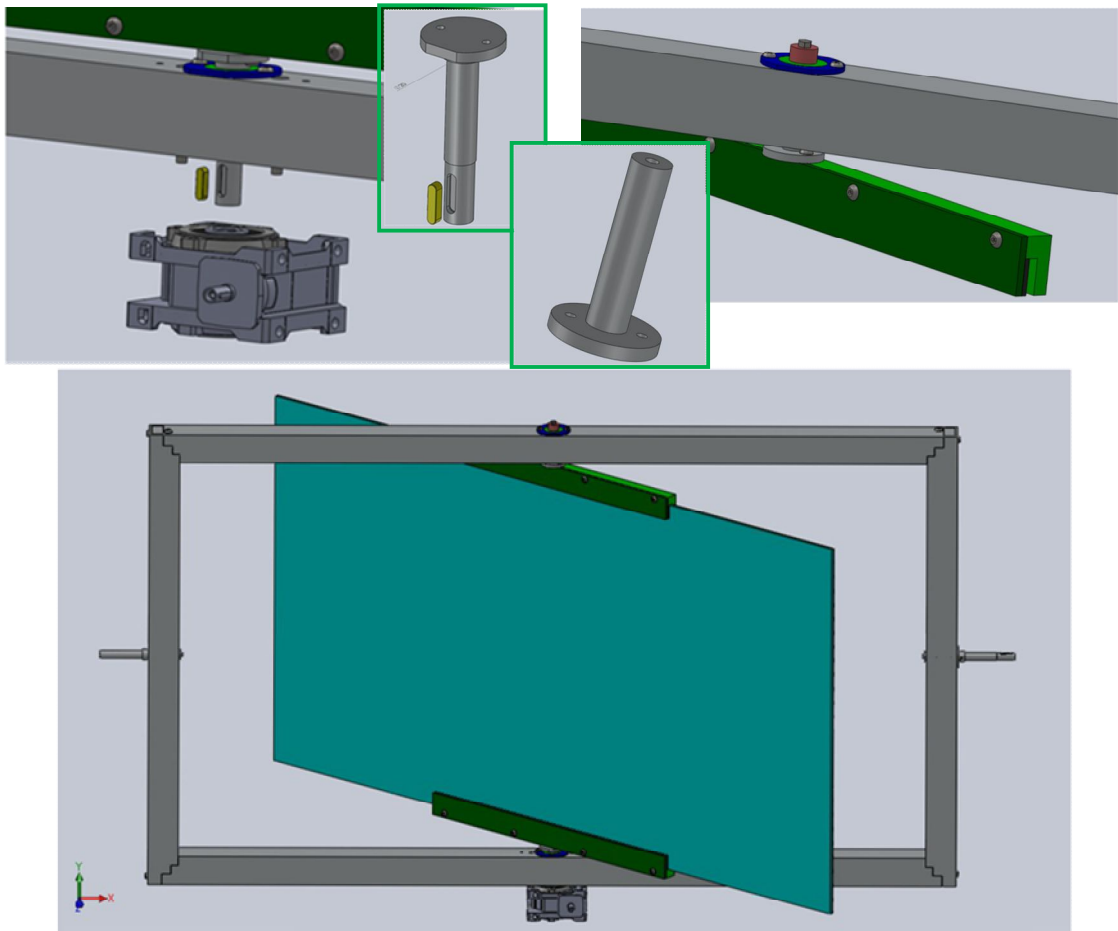


Figure 2.19 Shaft/frame connection

Finally, two goniometers, and two pins, are positioned near the two gears, in order to measure movements of α and β angles (Figure 2.20).

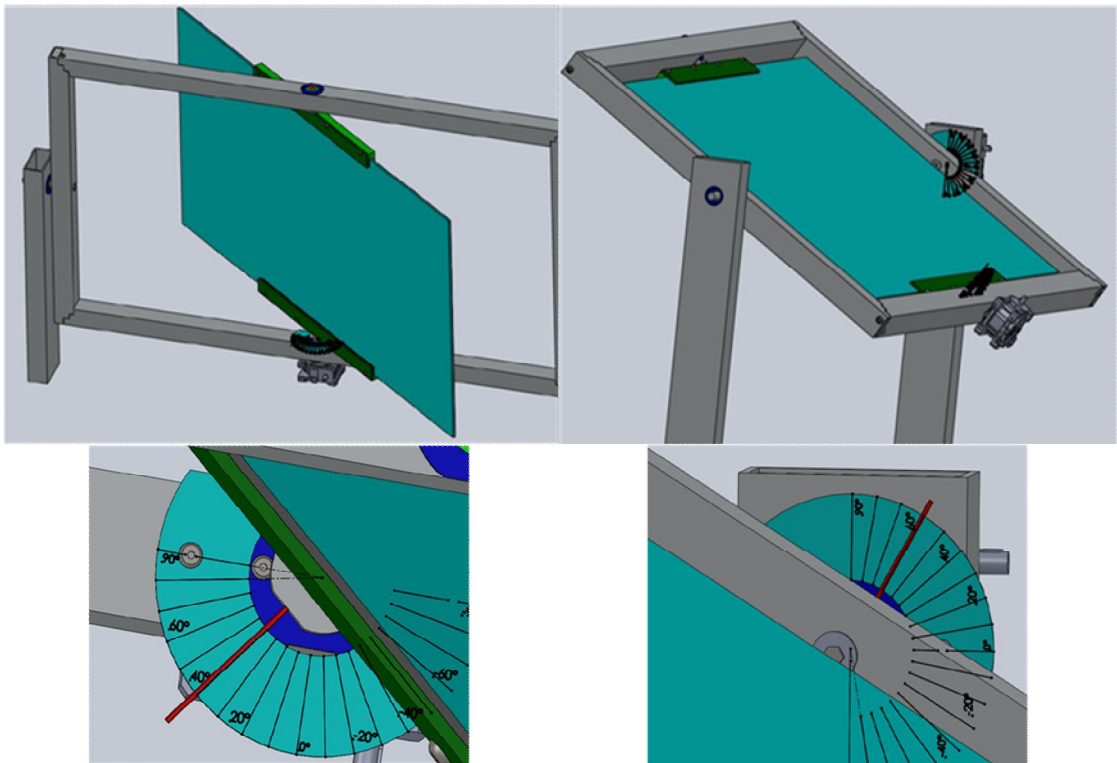


Figure 2.20 Two goniometers are fixed to measure angular movements

The final assembly and realized configuration is showed in Figure 2.21.

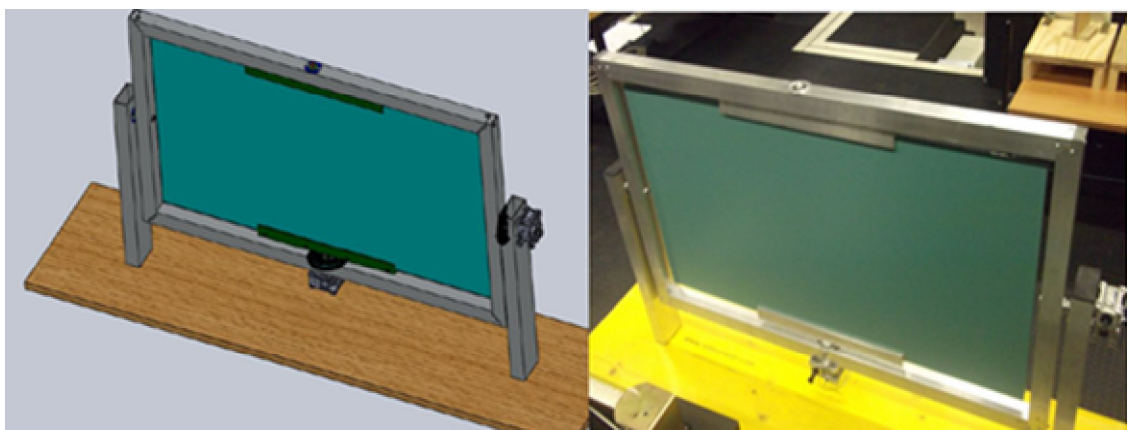


Figure 2.21 The realized structure and its CAD definition

Considering this structure, laser scanner is in front of the reference plane at a distance that changes from a scanning set to another one. During a first experimental phase laser scanner is posed with the laser beam oriented perpendicularly to the reference plane. This first choice is to reduce laser beam spread and considers a simple configuration. During the following phases the reference surface is moved (by means of gears in the realized structure) and different oblique configurations are considered. The influence of angle in the definition of correction array is thus considered.

2.3.3 Acquisition phase

During the acquisition phase, a large number of scans is acquired, maintaining operating conditions as constant as possible (such as scanning options and environmental conditions) and without change the scanning frame.

At first, the reference plane is considered perpendicular to the laser beam. 20 scans are collected for this step of the method. As output for each scan, a range map, containing points on the reference surface, is stored not only as RAW data, but also as structured ASCII array of 3D coordinates. All 20 range maps, and consequently all 20 arrays, are different to each other: this is principally due to errors present in each range map. A large number of scans on the same frame and performed at the same operating condition due to a progressive reduction of the random component of the error. This part will be discussed in the following section.

All scans are realized maintaining, as much as possible, laser beam perpendicular to the scanning plane, in order to reduce its dispersion. With this purpose, laser scanner is posed, parallel to the glass, which is fixed to a bearing structure, as shown in Figure 2.22.

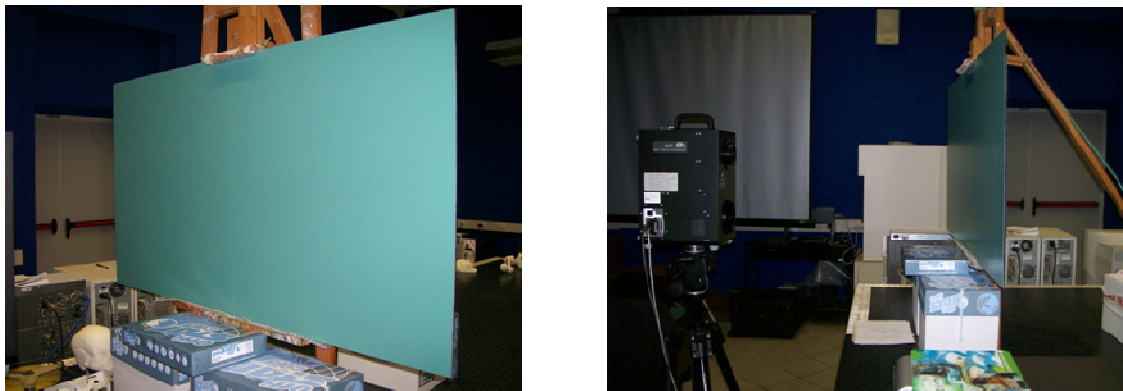


Figure 2.22 The scanning process with laser beam perpendicular with the reference surface, a first set up, before the support structure development

The main requirement for this initial experimental phase is to get the laser beam perpendicular to the acquiring plane, to reduce any laser dispersions.

A set of 20 scans is collected changing every time the lens and the distances from the instrument to the reference plane: all the three lenses are used and chosen distances are 600, 700, 800, 900 and 1000 mm. At the end of the acquisition process, a library of $20 \times 5 \times 3 = 300$ scans is collected for each combination between lenses and distances.

The software used to manage the acquisition process is *Polygon Editing Tool* (PET 2.0 ®, Konica Minolta Holdings Inc., Osaka, Japan), associated with this laser scanner, offering a good control of all acquisition parameters (such as focal distances, filtering

processes or data reduction and store) and it can also be used during post processing. No automatic tools for point's reduction or noise filtering are set up at this experimental level.

All scans are presented as an array containing 3D points coordinates: this laser scanner model can acquire until 307200 points, arranged in 640 columns and 480 rows (Figure 2.23). Such arrays are then stored as another array with 307.200 rows and 3 columns, containing respectively the X, Y and Z coordinates of each point.

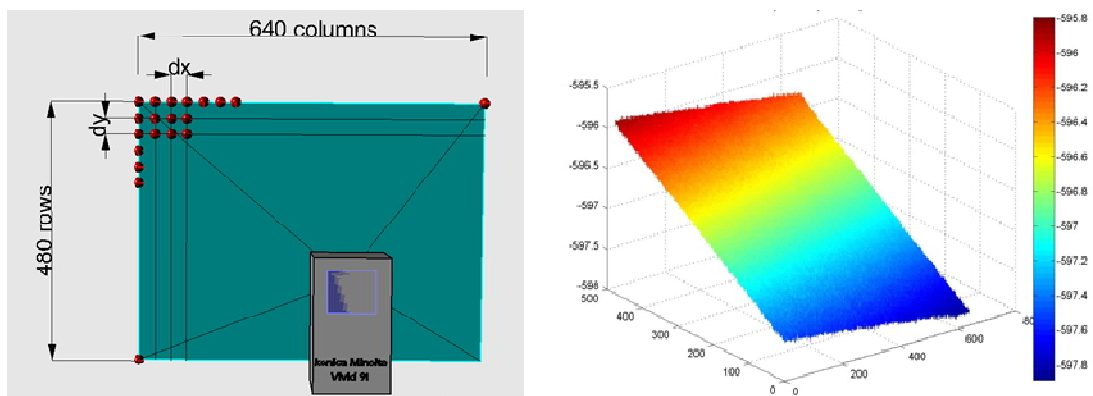


Figure 2.23 On the left: representation of the acquisition process; on the right: example of real scan.

After the perpendicular configuration a different setting is performed and the reference surface is moved of α and β angles. At this condition 20 more scans are performed for each pair of angles, for each lens and at two reference distances (600 and 870 mm). α and β are increased of 10° at each setting change, except for the first angular range, which is of 5° . This angular step was chosen considering that less than this value will not have a reliable influence on the correction array definition. No measurements

have been performed for tilt angle superior than 60° , since in practical cases the acquisition quality decay quickly with surface inclination increasing.

$\alpha \backslash \beta$	0°	5°	10°	20°	40°	60°
0°	<i>Previous setting</i>	$(0^\circ, 5^\circ)$	$(0^\circ, 10^\circ)$	$(0^\circ, 20^\circ)$	$(0^\circ, 40^\circ)$	$(0^\circ, 60^\circ)$
5°	$(5^\circ, 0^\circ)$	$(5^\circ, 5^\circ)$				
10°	$(10^\circ, 0^\circ)$		$(10^\circ, 10^\circ)$	$(10^\circ, 20^\circ)$		
20°	$(20^\circ, 0^\circ)$		$(20^\circ, 10^\circ)$	$(20^\circ, 20^\circ)$	$(20^\circ, 40^\circ)$	$(20^\circ, 60^\circ)$
40°	$(40^\circ, 0^\circ)$			$(40^\circ, 20^\circ)$	$(40^\circ, 40^\circ)$	$(40^\circ, 60^\circ)$
60°	$(60^\circ, 0^\circ)$			$(60^\circ, 20^\circ)$	$(60^\circ, 40^\circ)$	$(60^\circ, 60^\circ)$

Table 2.5 Angular acquired combinations

According to the angular combinations shown in Table 2.5, for each angular pair 20 scans are acquired for both distances and lenses. 20 scans x 23 angular pairs x 2 distances x 3 lenses = 2760 scans are acquired in this phase. All angles are considered as positive. An acquisition setting is shown in Figure 2.24.

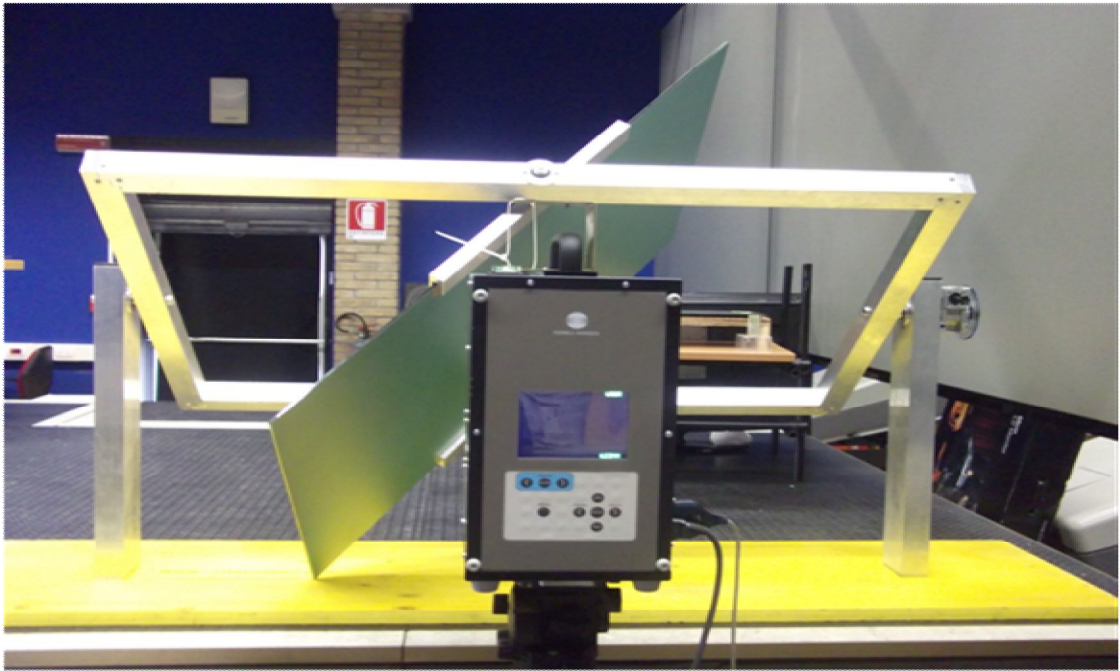


Figure 2.24 An acquisition setting

2.3.4 Elaboration phase

The acquisition phase has as output a library of arrays, containing 3D coordinates of points acquired with all the scans configurations (gives by a combination of lenses, distances and angles). These arrays are firstly used to verify instrument resolution, precision and accuracy and, then, to analyze systematic component of the error, with the final aim to reduce its influence in further scans, optimizing their quality. Each set of scans is composed by 20 different arrays, and the following procedure is

equally performed on all different sets. All this phase is performed through the creation of routines, in Matlab (*Mathworks Inc.*) for arrays elaboration.

Acquired meshes are exported as an ASCII file and then saved in a txt file format, so that they can be easily loaded in *Matlab* environment. As already mentioned, from a 480 x 640 frame, they are now saved as an array containing 307200 rows (one row for each point) and 3 columns (one column for each 3D coordinate X , Y , Z).

The first analysis consists in resolution determination and verification: the mean, minimum and maximum distances between two near points are evaluated in X and Y directions, verifying the least measure detected by the scanner. The laser beam is more scattering in the boundary part of each scan. Frames external parts are thus more affected by errors: for this reason, the further process consists in a point's reduction for each scan, and consequently for each array.

Verifying distances in both principal directions between two near points (dx and dy), their dispersions are visible numerically and graphically, so that it is possible to determine how many points must be removed from original arrays with a rigorous criterion. From a first analysis, looking at dx and dy , it is possible to identify, at a first sight, an approximate number of points to remove in each row and column. In order to verify if the chosen number of points gives a sufficient improve, a further routine is elaborated, computing the percentage decreasing of the standard deviations σ_{dx} (Eq 2.10) and σ_{dy} (Eq 2.11) of the arrays containing the values of the reduced arrays of dx and dy .

$$\sigma_{dx} = \sqrt{\frac{\sum_{i=1}^{n_{\Delta x}} (dx_i - \overline{dx})^2}{n_x (n_y - 1)}} \quad \text{Eq 2.10}$$

$$\sigma_{dy} = \sqrt{\frac{\sum_{i=1}^{n_{\Delta y}} (dy_i - \overline{dy})^2}{n_y (n_x - 1)}} \quad \text{Eq 2.11}$$

Where n_x is the number of rows, n_y is the number of columns and \overline{dx} and \overline{dy} are defined in Eq 2.12 and Eq 2.13:

$$\overline{dx} = \frac{1}{n_x (n_y - 1)} \sum_{i=1}^{n_{\Delta x}} dx_i \quad \text{Eq 2.12}$$

$$\overline{dy} = \frac{1}{n_y (n_x - 1)} \sum_{i=1}^{n_{\Delta y}} dy_i \quad \text{Eq 2.13}$$

The option runs between more precise data, but with a low number of points (and a loss in real object description) or less precise data, but with greater number of points. A reasonable compromise consists in a reduction of both the standard deviations σ_{dx} and σ_{dy} of 10%. All arrays in the same dataset have to be reduced of the same quantity. In following phases these reduced arrays will be elaborated (Figure 2.25).

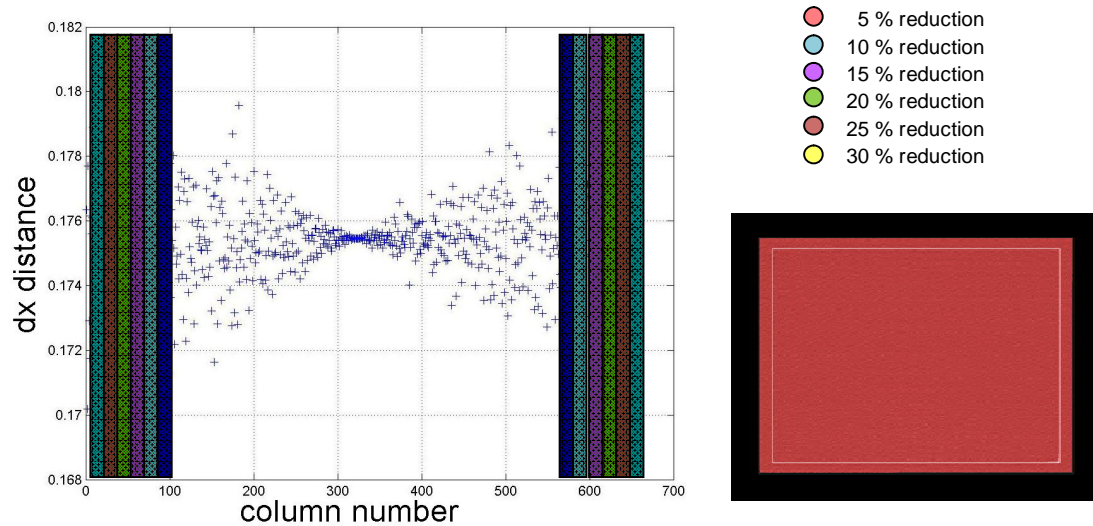


Figure 2.25 An example of reduction process: on the left a visualization of the distances between two near points: it is possible to notice a wide dispersion in boundary parts.

The subsequent step considers error random component reduction. In acquisition phase, the same frame is acquired 20 times with the same operative conditions: in spite of this, the output consists in 20 scans, which are never exactly the same, due to the measurement errors in each of them. The reduction of the random part of errors is possible averaging out the point's coordinates of the 20 reduced scans. Considering that the random part of error changes in every scans in module and sign, it tends progressively to reduce autonomously, with the average of the 3 points' coordinates. In *Matlab* environment, arrays of the same data setting are loaded and a routine is performed to calculate the average value of each point. New arrays are in output, and their values are a media of input data.

Starting from the range map, and the corresponding array, obtained from the average of the single scans after their reduction, best fitting plane is determined identifying a plane that approximates the point's coordinates of the reduced range maps. Indicating con n the number of acquired points that lie in a plane (x, y, z) and (x_i, y_i, z_i) are their 3D coordinates, it is possible to define a function $\phi(x, y, z)$, which best fit acquired points, according to an identified criteria. From a mathematical point of view, the function $\phi(x, y, z)$, depends on some parameters to be defined in order to minimize errors.

A *Matlab* routine is developed: acquired points are loaded and an approximation plane is defined through principal components technique. This method consider an array composed by $n \times p$ quantitative variables (which are points coordinates); an orthogonal transformation creates a number q ($q < p$) of artificial variables called principal components, that are linearly uncorrelated and with maximum of variance. In a geometrical approach, data array is a point cloud in the 3D environment: during the principal component analysis, an orthogonal projection from the initial reference system to principal component one, so that associated eigenvalues are the biggest ones (Figure 2.26).

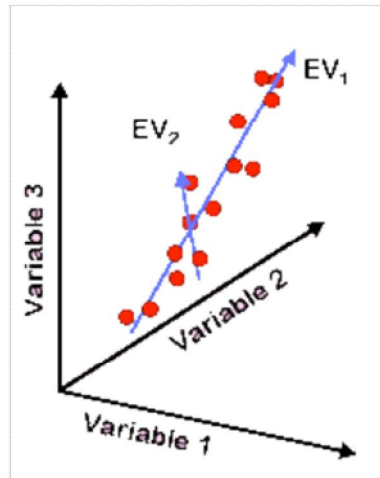


Figure 2.26 Principal components 3D space

Another method to define the best fitting plane is the last squared method. This technique defines a function F , which seems a data interpolation. In particular, such function should minimize the square of the sum of all distances between each observed point (y_i) (Eq 2.14) and its correspondent point (y_i^*) in the interpolated plane (Figure 2.27).

$$F(d) = \sum_i (y_i^* - y_i)^2 \quad \text{Eq 2.14}$$

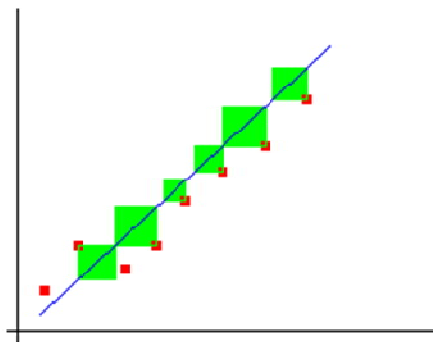


Figure 2.27 Last square method: example of application in the bidirectional space

Since in this study, the measurement errors in the three axes are of the same order, principal component approach is preferred to the least squared method.

From a comparison between acquired data and best fitting plane coordinates it is possible to define an error value for each acquired point. Surface deviation is defined as the maximum distance, considered as absolute value, between each range map and the determined best fitting plane (Eq 2.15). Error's standard deviation is also defined as the deviation between the acquired surface and the reference plane (Eq 2.16).

$$Sd = \max |z_{ij} - z_{ij}^*| \quad \text{Eq 2.15}$$

$$\sigma_z = \sqrt{\frac{\sum_{i=1}^{n_x} \sum_{j=1}^{n_y} (z_{ij} - z_{ij}^*)^2}{n_x n_y}} \quad \text{Eq 2.16}$$

where n_x and n_y are respectively the numbers of rows and columns, and z_{ij}^* is the corresponding value on the best fitting plane of z_{ij} (z value of the point identified by (i,j) in the range map).

Increasing at every step the number of range maps in the mean process, it is possible to visualize error's standard deviation σ_z trend in function to the number of averaged scans: an initial fall is in correspondence to the first scans, due to a reduction of error's random component. Increasing any time the number of scans, the trend goes on decreasing its value with a little variation. After the fourth average, standard deviation decreasing is not so relevant, so that the final choice is to stop mean process at the fourth array. In this way, the final best fitting plane is determined on the basis of the first fourth scans.

Finally, for each scan the error distribution is graphically represented as the absolute difference between z_{ij} of an acquired array (after the reduction phase) and the corresponding z^*_{ij} of the best fitting plane. At the end a complete work flow of this phase is presented in Figure 2.28.

The presented workflow has been applied in both analyzed configuration: with laser beam perpendicular to the reference surface and with angles between them. *Matlab* routines has been adapted for both settings.

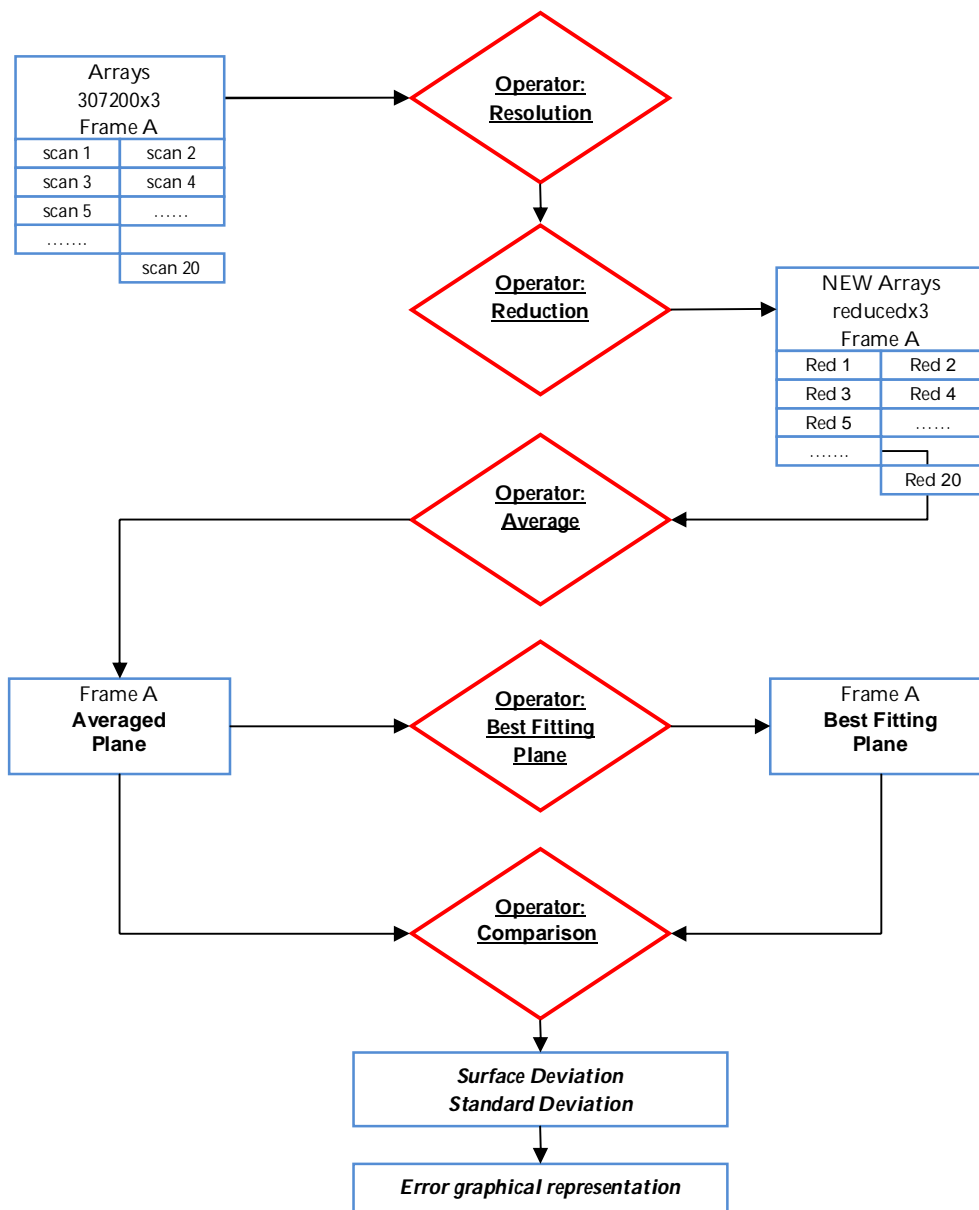


Figure 2.28 Elaboration phase workflow

2.3.5 Compensation phase

The aim of the elaboration phase is to determine some data information on acquired point, in order to isolate error systematic component.

The idea inherent to this correction process assumes that the z coordinates acquired in each scan, here generically identified as q_o , are sum of three components (Eq 2.17): the real value q_i , the random error (Δa) and the systematic one (Δs) (Azzoni, 2006; Taylor, 2004; Webster, 1999).

$$q_o = q_i + \Delta a + \Delta s \quad \text{Eq 2.17}$$

Averaging acquired range maps, data obtained (q_{om}) correspond to the mean value of point's coordinates, and the resulting real value (q_{im}) is identified with the best fitting plane of the averaged range map (Eq 2.18): at this step the random component of error is noticeably reduced. Data is now precise, but not accurate.

$$q_{om} = q_{im} + \Delta s \quad \text{Eq 2.18}$$

In each group of scans, acquired under the same conditions of distances between scanner and object, with the same lens and surface normal direction, is determined a different array (Δs) of data correction (Eq 2.19). Systematic error follows always the same rule and it is now possible to determine its trend:

$$\Delta s = q_{om} - q_{im} \quad \text{Eq 2.19}$$

For the compensation phase (obtaining a data q_o^* without this type of error) it is sufficient to deduct from the acquired value (q_o) the systematic component (Δs), as shown in Eq 2.20.

$$q_o^* = q_o - \Delta s \quad \text{Eq 2.20}$$

At the end of this phase, initial data are affected anymore by the systematic component of error, but only by the random one (Eq 2.21):

$$q_o^* = q_i + \Delta a \quad \text{Eq 2.21}$$

By these considerations, systematic error values are calculated as the difference between scan's points and best fitted points, and can be considered as an indication of accuracy level.

A different correction array for systematic error Δs is defined for each operating condition: it can be used in practical cases, to subtract coordinates of an object acquired at under similar conditions.

2.4 Results: Laser beam perpendicular to the reference surface

The whole methodology (acquisition phase, elaboration phase and compensation phase) has been firstly applied with the laser beam perpendicular to the reference surface, in order to minimize laser beam dispersion effects.

Set of scans are performed changing operating conditions: 5 scanner/surface distances (600, 700, 800, 900 and 1000 mm) and three lenses are used (Figure 2.29, Figure 2.30). An array library is thus created: all point clouds are stored firstly in an ASCII file format, and then in a txt file, in order to treat them as a tabulated array.

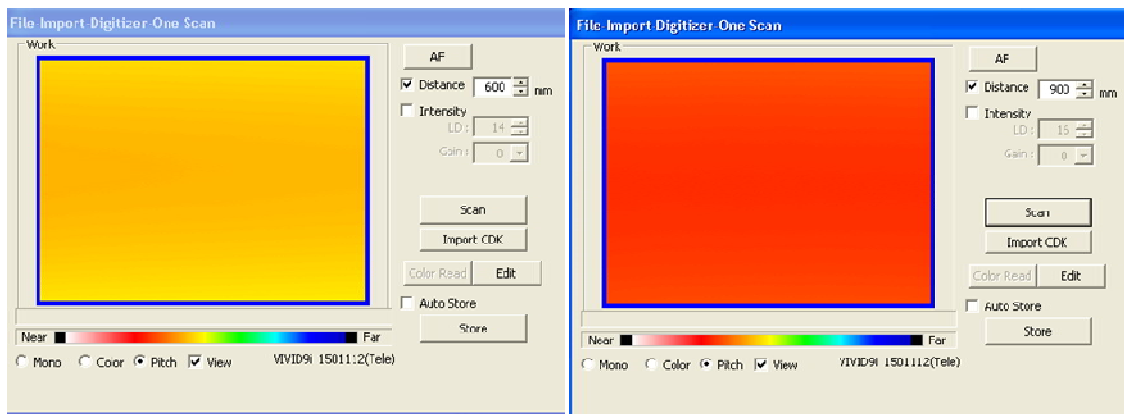


Figure 2.29 The acquisition process: two acquired frame as seen in PET. Scans are acquired with a Tele lens at a distance of 600 mm (on the left) and 900 (on the right)

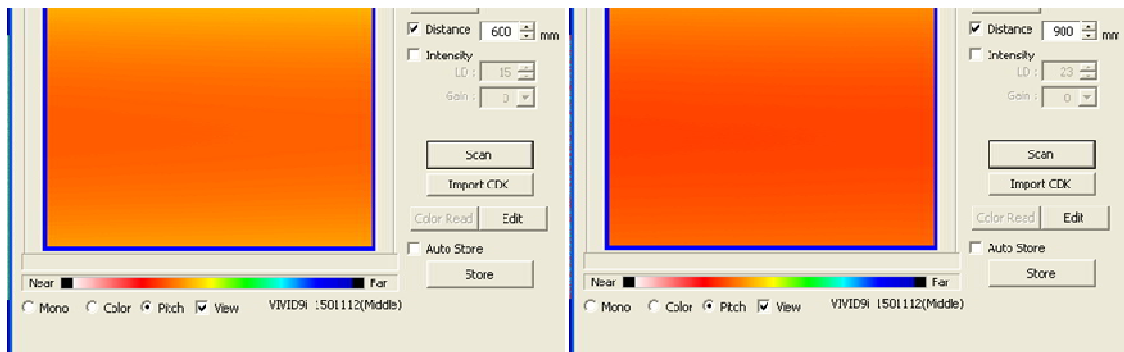


Figure 2.30 The acquisition process: two acquired frame as seen in PET. Scans are acquired with a Middle lens at a distance of 600 mm (on the left) and 900 (on the right)

Each array is related to a surface portion, which area depends on lens focal distance, scanning distance and a numerical constant (Eq 2.22):

$$w = d/f * 4.8 \quad \text{Eq 2.22}$$

Where w is area width, d is the scanning distance, f is the focal distance and 4.8 is a numerical constant related to the CCD sensor that is 1/3" (Figure 2.31). Similarly, it is possible to define area high as (Eq 2.23):

$$h = d/f * 3.6 \quad \text{Eq 2.23}$$

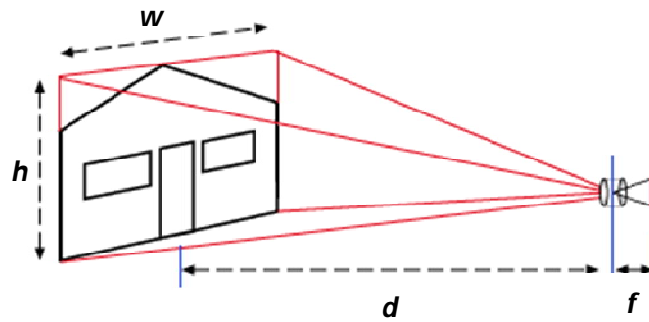


Figure 2.31 Area of the acquired frame in relation to scanning and focal distances

For each acquired set of scan, it is possible to test area acquired in order to compare real values with computed ones (with formulas above described). Real acquired areas are determined evaluating point's distances in *Matlab* environment; frame acquired have area values close to computed ones: some values are shown in Table 2.6.

LENS	DISTANCES	THEORETICAL/ REAL AREA	AREA VALUES
TELE	600 mm	Theoretical Area	115.20 × 86.40 mm
		Real Area	112.06 × 84.01 mm
	900 mm	Theoretical Area	172.80 × 129.60 mm
		Real Area	162.76 × 122.05 mm
MIDDLE	600 mm	Theoretical Area	205.71 × 154.29 mm
		Real Area	199.79 × 149.77 mm
	900 mm	Theoretical Area	308.57 × 231.43 mm
		Real Area	289.39 × 216.98 mm
WIDE	600 mm	Theoretical Area	360 × 270 mm
		Real Area	350.80 × 263.12 mm
	900 mm	Theoretical Area	540 × 405 mm
		Real Area	515.60 × 386.66 mm

Table 2.6 Theoretical and real values of acquired area for the lenses and at 600 and 900 mm of distance

The presented analysis proceeds with the visualization of the acquired surface in *Matlab*, by means of a 3D representation of coordinates of acquired points: Z values are map as a grid in a 640 x 480 array, and presented in a color map (Figure 2.32). The described procedure is equally performed on all different sets, even if here is presented only for a single group (Tele lens and 600 mm of acquiring distance); the other results are shown as tables and figures in Appendix B.

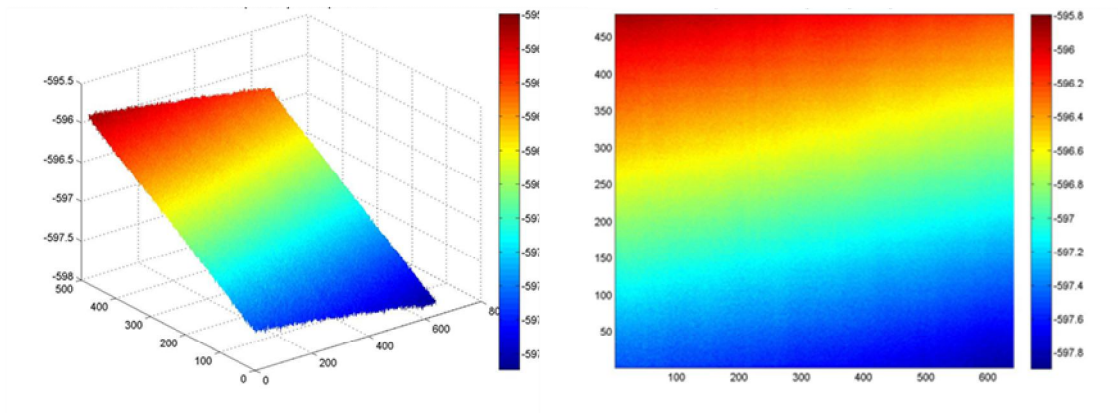


Figure 2.32 3D graph of an acquired surface portion. Point's Z coordinates are view as a color map; coordinate values are in mm

The elaboration phase starts with a point reduction: in order to decrease errors and data dispersions, some boundary points are removed. To perform this task, points resolution is evaluated, computing point's distances in x and y directions: dx and dy , vectors are defined for each scan Figure 2.33. Some graphs (Figure 2.34) and tables (Table 2.7) on resolution evaluation are created, in function of the number of arrays involved in the mean process.

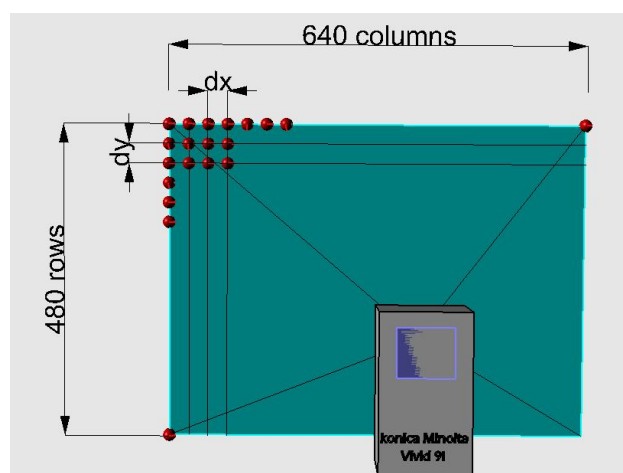


Figure 2.33 dx and dy distanced between two near points are evaluated, in order to define local points resolution

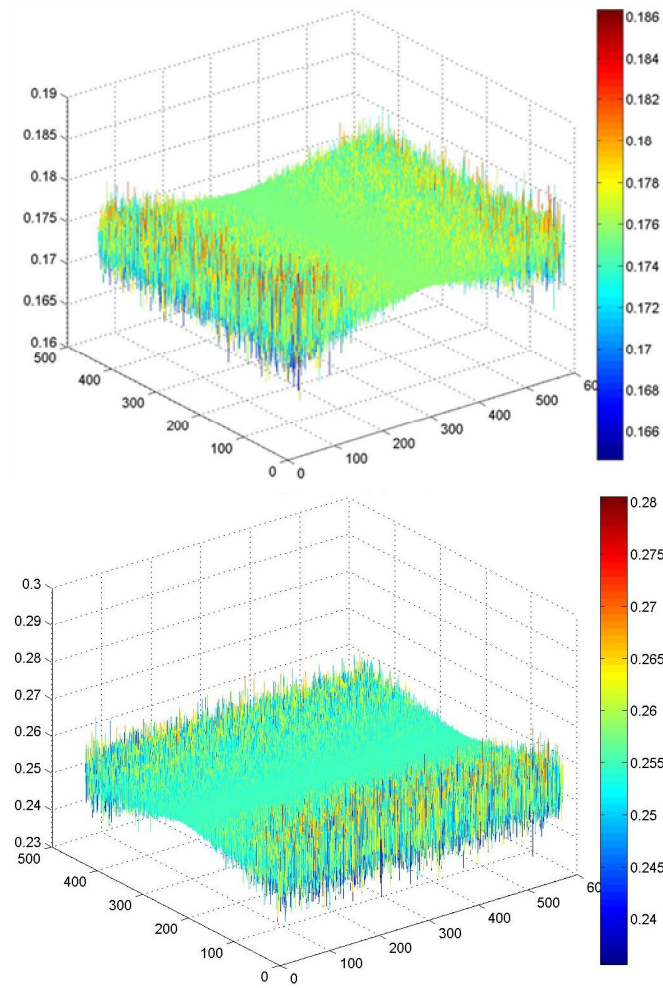


Figure 2.34 3D graph on points distances in x (on the top) and y (on the bottom) directions (all values are in mm)

Moreover, in order to visualize how many points should be necessary to remove, dx and dy arrays, that represent points distances, are represented according to their location into the acquired frame: dx vector is thus graph for the first, the 240th and the last row, whereas dy vector is graph for the first, the 320th and the last column (Figure 2.35, Figure 2.36).

N° of mean arrays	MEAN RESX	MEAN RESY	MIN RESX	MIN RESY	MAX RESX	MAX RESY
1	0.1754	0.1754	0.1647	0.1668	0.1863	0.1840
2	0.1754	0.1754	0.1653	0.1673	0.1864	0.1839
3	0.1754	0.1754	0.1651	0.1675	0.1858	0.1839
4	0.1754	0.1754	0.1654	0.1666	0.1861	0.1843
5	0.1754	0.1754	0.1647	0.1667	0.1866	0.1838
6	0.1754	0.1754	0.1647	0.1665	0.1865	0.1835
7	0.1754	0.1754	0.1661	0.1664	0.1861	0.1848
8	0.1754	0.1754	0.1655	0.1669	0.1855	0.1848
9	0.1754	0.1754	0.1664	0.1666	0.1863	0.1840
10	0.1754	0.1754	0.1655	0.1669	0.1860	0.1844
11	0.1754	0.1754	0.1642	0.1667	0.1862	0.1840
12	0.1754	0.1754	0.1664	0.1665	0.1866	0.1836
13	0.1754	0.1754	0.1664	0.1665	0.1859	0.1837
14	0.1754	0.1754	0.1660	0.1669	0.1859	0.1838
15	0.1754	0.1754	0.1660	0.1675	0.1854	0.1836
16	0.1754	0.1754	0.1656	0.1664	0.1860	0.1838
17	0.1754	0.1754	0.1658	0.1668	0.1857	0.1839
18	0.1754	0.1754	0.1664	0.1668	0.1854	0.1834
19	0.1754	0.1754	0.1667	0.1666	0.1856	0.1835
20	0.1754	0.1754	0.1658	0.1666	0.1853	0.1836

Table 2.7 Mean, Min and max resolution values in X and Y directions, in function of the number of arrays involved in the mean process. Tele lens, 600 mm distance.

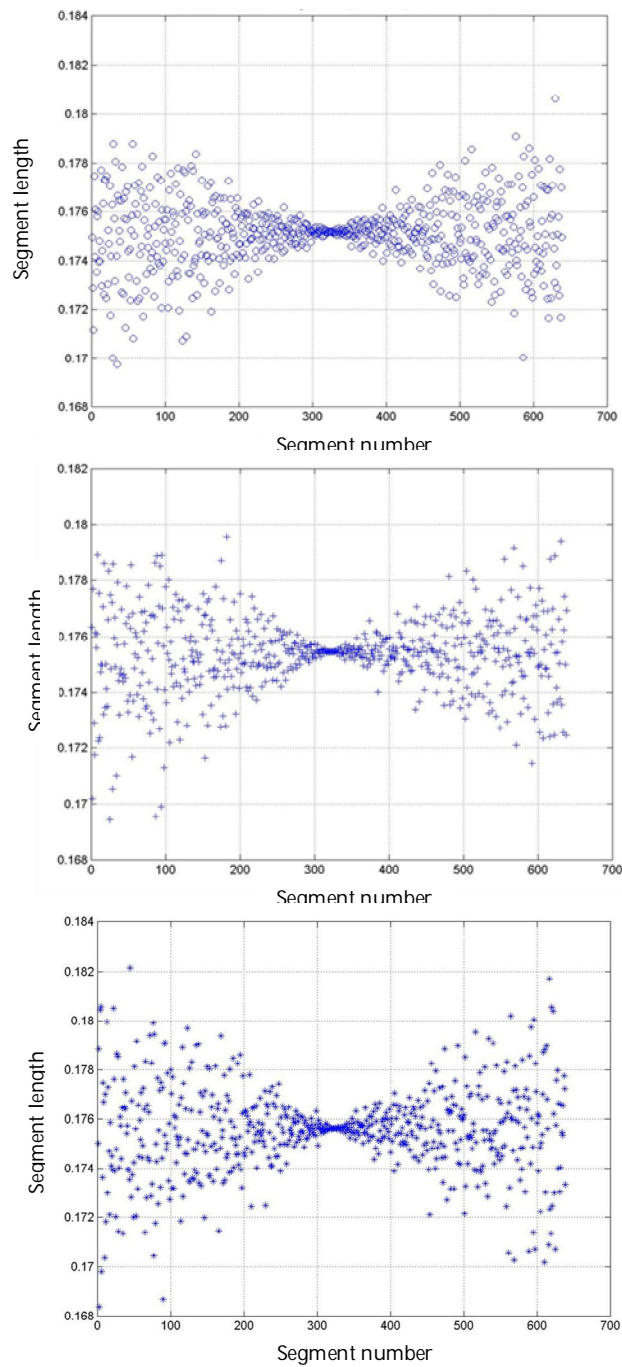


Figure 2.35 Segment lengths in dependence on its position in the frame (column: segment position which runs from 1 to 640): the first image corresponds to the first row, the second one to the middle row (240) and the last one to the last row (480)

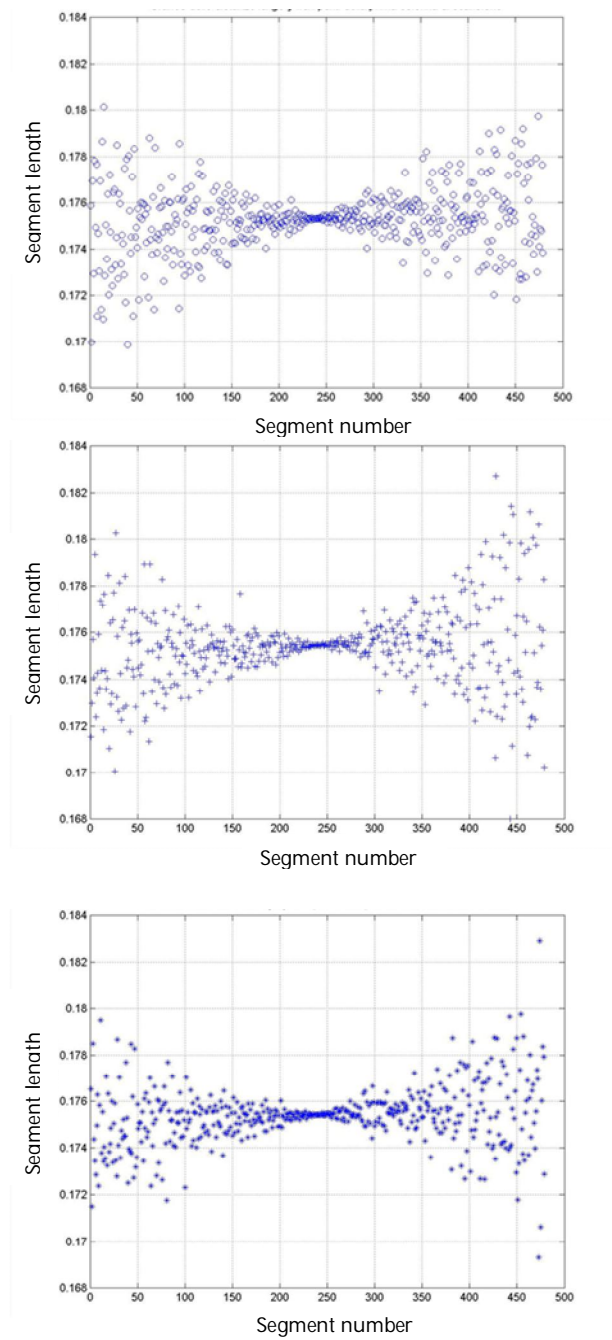


Figure 2.36 Segment lengths in dependence on its position in the frame (row: segment position which runs from 1 to 480): the first image corresponds to the first column, the second one to the middle column (320) and the last one to the last column (640).

Looking at segments length, it is thus possible to identify a number of points to remove in each column and row; the procedure continues with a *Matlab* routine, in which the resolution standard deviation is computed in order to verify how many points are necessary to remove in order to have a less dispersive datum. In Table 2.8 are shown how many points it is necessary to remove for each row and column symmetrically in order to reduce standard deviation of the distances vector of the indicated percentage.

LENS	DISTANCE	ROW/ COLUMN	Resolution Standard deviation reduction					
			5%	10%	15%	20%	25%	30%
TELE	600 mm	row	12	24	35	46	58	69
		column	15	30	45	61	76	92
	900 mm	row	12	25	37	49	61	73
		column	17	34	50	66	82	98
MIDDLE	600 mm	row	11	22	34	45	56	68
		column	14	28	42	56	70	85
	900 mm	row	12	24	36	48	59	72
		column	15	28	43	58	73	89
WIDE	600 mm	row	11	22	34	46	58	69
		column	12	25	39	53	68	83
	900 mm	row	10	22	32	44	57	68
		column	11	23	35	49	63	78

Table 2.8 Point to remove symmetrically for each row and column in order to have a reduction of point's distances standard deviation

The selection is a compromise between an always more precise data, but with low points to describe the object, and with a consequent lost in information, and a less precise datum, but with a high number of points to describe the object surface. The final choice is to reduce points distances standard deviation of 10%.

All arrays are reduced of the adequate number of points according to the lens used and to the acquiring distance. All arrays belonging to the same data set must have the same size.

Then the media process is performed, in order to reduce error random component. Finally, for each data set, the best fitting plane is defined and thus the error array and points standard and surface deviation. For each acquired range map it is possible to graph error array, as the difference between the acquired array and the best fitting plane, with represent the real surface. In Figure 2.37 a pseudo color representation of point's error is shown as an array of 480x640 points: it is possible to notice which areas are more affected by a larger difference between points and the best fitting plane. This aspect is not to be intended that clearer points are affected by a bigger error value: in fact the shift of many points from their real position, can cause a consequent change in the best fitting plane position, which is created are function of points coordinates.

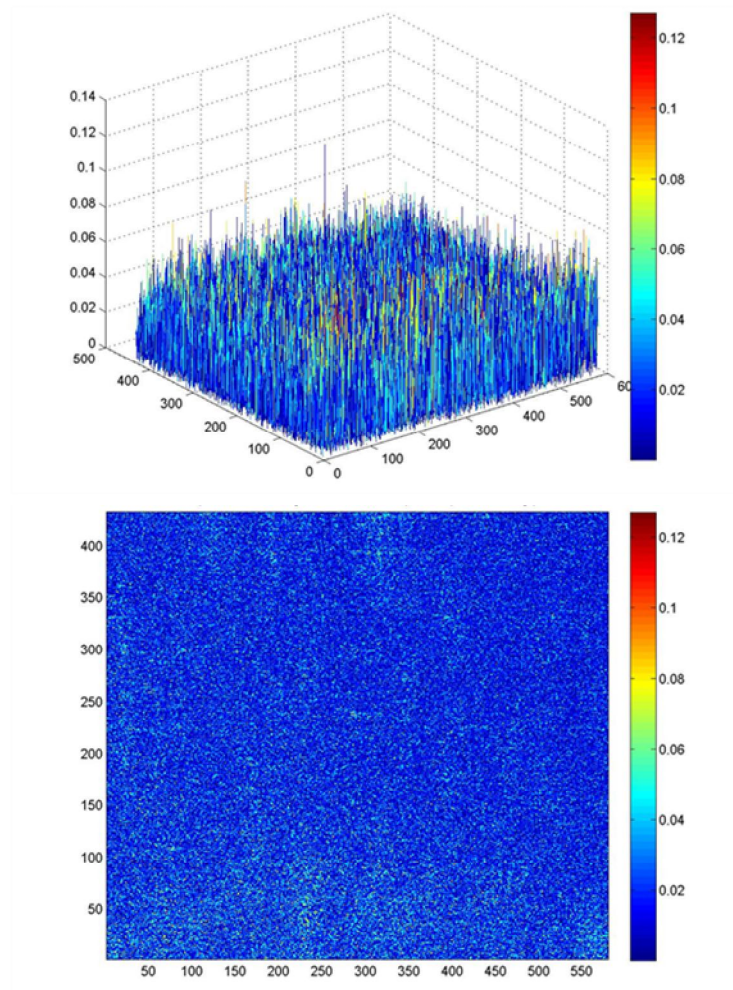
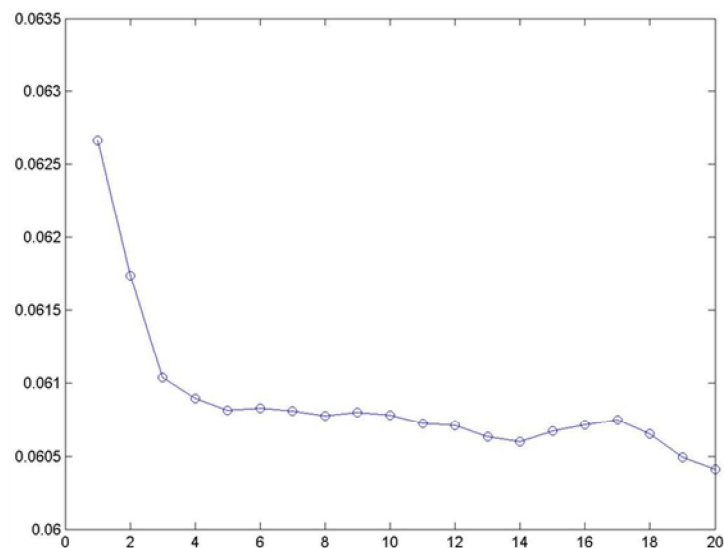


Figure 2.37 3D graph of the shifting between acquired points and the best fitting plane. All values are in mm

A further interesting data analysis concerns point's standard deviation: during the mean process, it is possible to evaluate its value in function of the number of arrays involved, so that it is possible to graph its trend. Averaging acquired and reduced arrays, computed points standard deviation has a sudden decrease in correspondence of error random component reduction. Increasing the number of averaged arrays, point's

standard deviation continues to decrease and turns nearby a range. A reasonable minimum point is located in proximity of the fourth averaged array: in fact till this value, point's standard deviation decrease and then its curves is affected by some oscillations near a mean value. Following graphs (Figure 2.38) represents point's standard deviation in relation of averaged scans, lens used and scanning distance.

Finally, tables on standard and surface deviation is relation to averaged arrays are shown; different lenses and distances are evaluated (Table 2.9).



**Figure 2.38 Standard deviation trend in function of the number of averaged arrays:
Tele lens and scanning distance of 600mm**

AVERAGED ARRAYS	SRF.DEV.	STD.DEV.
1	0.3194	0.0627
2	0.3164	0.0614
3	0.3152	0.0611
4	0.3176	0.0611
5	0.3178	0.0610
6	0.3096	0.0611
7	0.3110	0.0610
8	0.3296	0.0610
9	0.3406	0.0610
10	0.3334	0.0610
11	0.3243	0.0609
12	0.3299	0.0609
13	0.3294	0.0608
14	0.3309	0.0608
15	0.3257	0.0609
16	0.3316	0.0609
17	0.3378	0.0610
18	0.3225	0.0608
19	0.3157	0.0607
20	0.3219	0.0606

Table 2.9 Surface and standard deviation in relation to the number of averaged arrays. Tele lens and 600 mm distance. All values are in mm

With the definition of an error punctual value, for each scanning set, it is possible to perform the correction phase as above described. Systematic error values are calculated as the difference between scan's points and best fitted points, and can be considered as an indication of accuracy level. Acquired and corrected plane are compared and evaluated in a TELE lens and with 600 mm of acquiring distance (Figure 2.39).

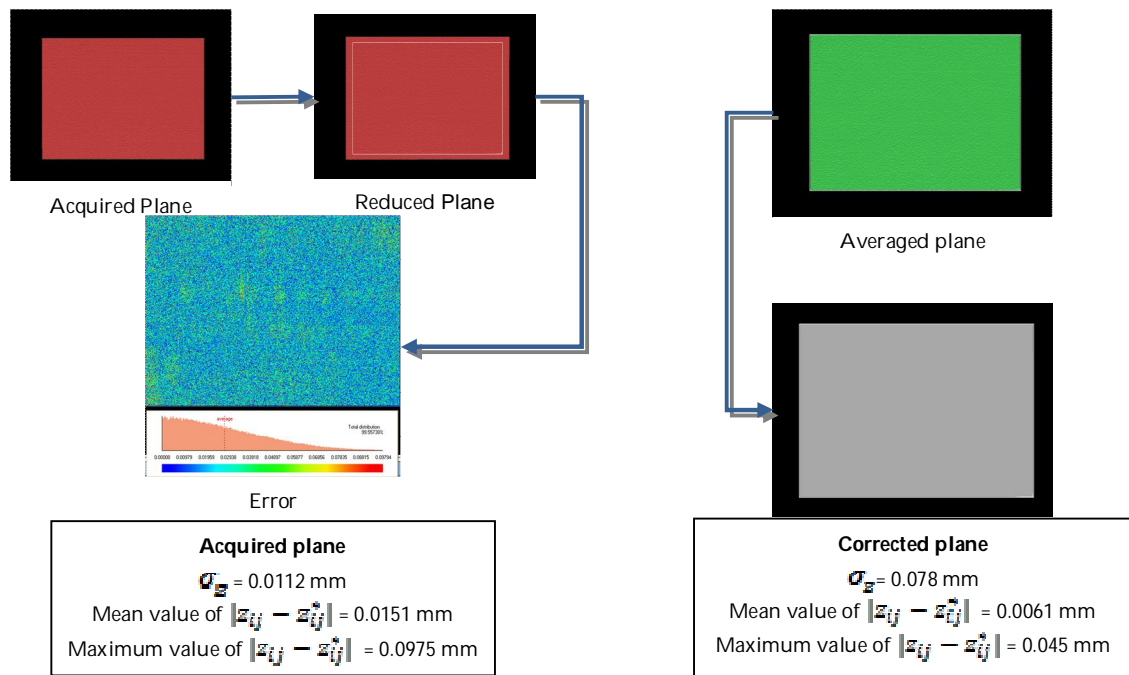


Figure 2.39 Acquired and reduced plane: from the difference between the reduced plane and the best fitting plane errors in coordinates' determination are evaluated. Averaged and corrected plane: from the difference between the corrected plane and the best fitting plane errors in coordinates' determination are evaluated

This procedure final output consists in a library of compensation arrays to be used for systematic error correction. From 3D scan's representation without systematic error component, it is clearly possible to notice a significant noise reduction, also definable by the determination of the mean and maximum error. In Table 2.10 a comparison between Minolta data sheet, the directly acquired data and the processed ones is shown. It is important to notice that data processed have accuracy values significantly reduced compared to acquired ones (low values correspond to a high accuracy level), and they are close to Minolta data sheet, obtained in laboratory conditions, with a defined and meticulous procedure.

TELE 600 mm	Minolta Data sheet	Experimental Data		
		Acquired Data	Processed Data	
Accuracy	0.05 mm	0.0975 mm	0.045 mm	Maximum value of $ z_{ij} - z_{ij}^* $
		0.0151 mm	0.0061 mm	Mean Value of $ z_{ij} - z_{ij}^* $
Precision	0.008 mm	0.0112 mm	0.0078 mm	σ_z

Table 2.10 Comparison between Minolta Data Sheet and experimental data for a specific case with the Tele lens and at a scanning distance of 600mm

A final note is related to define precision value and to test correction array reliability.

40 scans are acquired at the same operative and environmental conditions, with a Tele lens and at distance of 600 mm. These scans are grouped in 10 clusters of four scans each. The number four is due to the fact that during the average process in proximity of the fourth scan the random component of error results compensate at most (this aspect has been discussed above). Each scan has been reduced at 250560 points, since 24 rows and 30 columns have been symmetrically removed. Then, 10 ΔS arrays for systematic error correction are been computed and compared. The correction mean value (Eq 2.24) and correction standard deviation (Eq 2.25) has been computed for corresponding points in different arrays. Such analysis has been firstly performed for some key points and then for the whole array (Table 2.11).

TELE 600 mm 10 ΔS arrays	First Point	Middle Point (n° 124990)	Last Point (n° 250560)
Correction mean value (mm)	0.0207	0.0044	0.0172
Correction Standard Deviation (mm)	0.0037	0.0045	0.0061

Table 2.11 Correction arrays comparison: evaluation of the mean value and standard deviation of the correction related to some key points

$$\Delta S(i,j)_{mean} = \frac{1}{10} \sum_{n=1}^{10} \Delta S(i,j)_n \quad \text{Eq 2.24}$$

$$\sigma_{\Delta S(i,j)} = \sqrt{\frac{1}{9} \sum_{n=1}^{10} (\Delta S(i,j)_n - \Delta S(i,j)_{mean})^2} \quad \text{Eq 2.25}$$

Considering all correction values, the mean standard deviation ($mean \sigma_{\Delta S(i,j)}$) is 0.0046. Since for each point, correction standard deviation is at least an order of magnitude littler then the correction value itself, it is possible to underline the reliability of the defined correction arrays and thus of the whole methodology.

Finally, considering all the 40 scans is determined the precision value of the acquired data, as reported in Table 2.10. Similarly to what just described, for some key points are respectively evaluated the mean acquired value (Eq 2.26) and data standard deviation (Eq 2.27): results are repot in Table 2.12. The same analysis is the performed on the whole acquired (and reduced) range map.

TELE 600 mm 40 Acquired arrays	First Point	Middle Point (n° 124990)	Last Point (n° 250560)
Mean value (mm)	-623.3559	-624.4978	-625.6147
Correction Standard Deviation (mm)	0.0129	0.0104	0.0132

Table 2.12 Arrays comparison: evaluation of the mean value and standard deviation of the correction related to some key points

$$Z(i, j)_{mean} = \frac{1}{40} \sum_{n=1}^{40} Z(i, j)_n \quad \text{Eq 2.26}$$

$$\sigma_{Z(i, j)} = \sqrt{\frac{1}{39} \sum_{n=1}^{40} (Z(i, j)_n - Z(i, j)_{mean})^2} \quad \text{Eq 2.27}$$

Considering all acquired data, the mean standard deviation ($mean \sigma_{Z(i, j)}$) is 0.012. This value is defined as the precision of the acquired measure.

2.5 Results: oblique angle between the laser beam and the reference surface

The presented analysis has been equally performed in case the laser beam is not perpendicular with the reference surface. In the following part results are presented.

The first step is the acquisition phase: changing the glass sheet tilt angles (α, β), 20 scans are acquired for each configuration. In Figure 2.40 are shown such frame as

acquired by PET software. The rainbow color bar assigns a red color to near points and a blue one to farer ones.

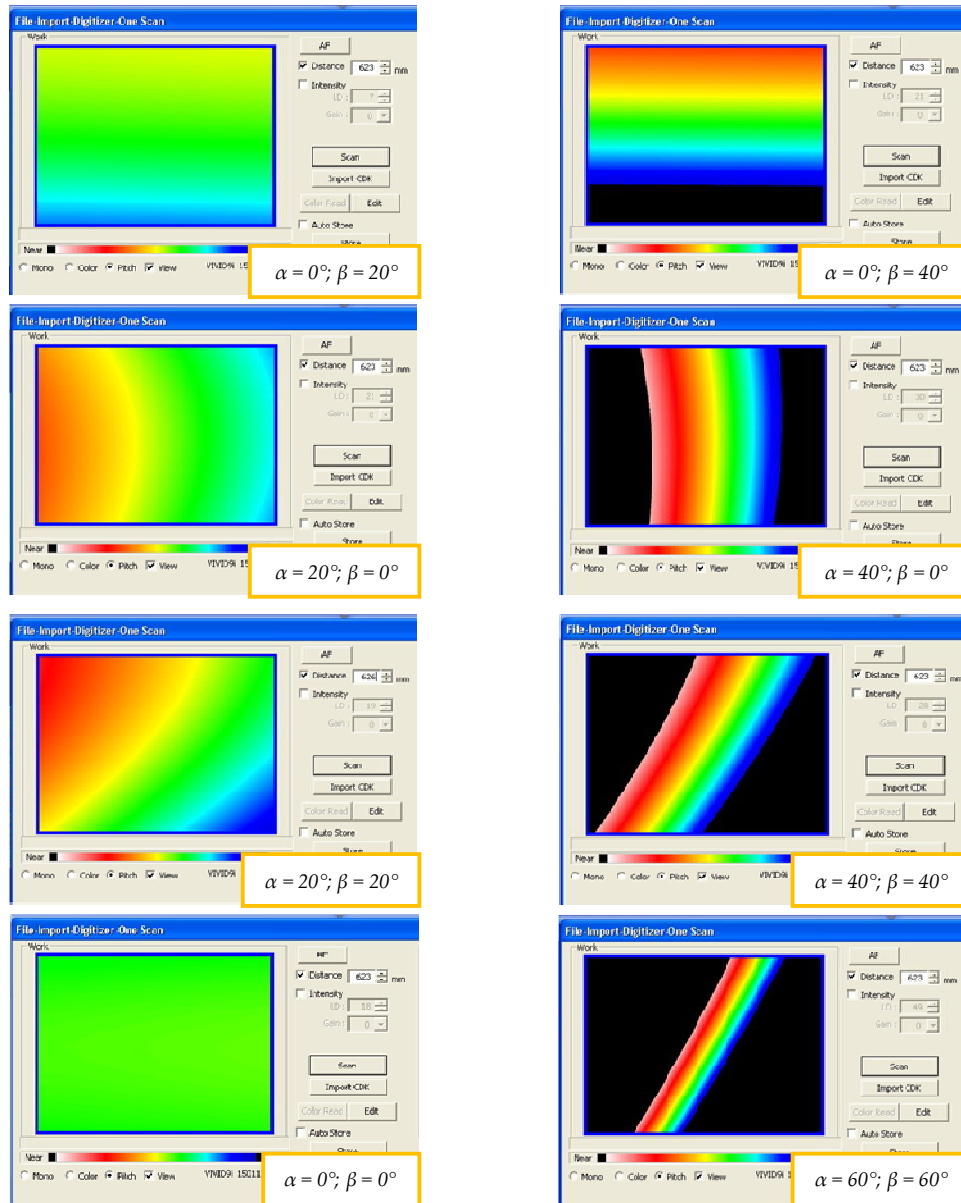


Figure 2.40 some acquisition frame: Tele lens, 600 mm of scanning distance and changing tilt angles.

All acquired range map are saved in a *txt* file format and then elaborated in *Matlab*. A first important consideration is that when the tilt angles pairs (α, β) are both less than 20° , the acquired range map are rectangular and composed by 307200 points (see tilt angle combinations green highlighted in Table 2.13).

$\alpha \backslash \beta$	0°	5°	10°	20°	40°	60°
0°	<i>Previous setting</i>	$(0^\circ, 5^\circ)$	$(0^\circ, 10^\circ)$	$(0^\circ, 20^\circ)$	$(0^\circ, 40^\circ)$	$(0^\circ, 60^\circ)$
5°	$(5^\circ, 0^\circ)$	$(5^\circ, 5^\circ)$	$(5^\circ, 10^\circ)$	$(5^\circ, 20^\circ)$	$(5^\circ, 40^\circ)$	$(5^\circ, 60^\circ)$
10°	$(10^\circ, 0^\circ)$	$(10^\circ, 5^\circ)$	$(10^\circ, 10^\circ)$	$(10^\circ, 20^\circ)$	$(10^\circ, 40^\circ)$	$(10^\circ, 60^\circ)$
20°	$(20^\circ, 0^\circ)$	$(20^\circ, 5^\circ)$	$(20^\circ, 10^\circ)$	$(20^\circ, 20^\circ)$	$(20^\circ, 40^\circ)$	$(20^\circ, 60^\circ)$
40°	$(40^\circ, 0^\circ)$	$(40^\circ, 5^\circ)$	$(40^\circ, 10^\circ)$	$(40^\circ, 20^\circ)$	$(40^\circ, 40^\circ)$	$(40^\circ, 60^\circ)$
60°	$(60^\circ, 0^\circ)$	$(60^\circ, 5^\circ)$	$(60^\circ, 10^\circ)$	$(60^\circ, 20^\circ)$	$(60^\circ, 40^\circ)$	$(60^\circ, 60^\circ)$

Table 2.13 Acquired range maps with different tilt angles combinations: in green are highlighted rectangular arrays, that is to say, arrays in which all points are acquired; instead in yellow are highlighted arrays where not all points are acquired

As concerns all the others angular combinations (yellow highlighted in Table 2.13), laser scanner is not able to acquire the whole frame, and this fact is mainly due to focus matters and lens properties. As it is possible to notice in Figure 2.41, in frame portions no points are acquired. These range maps have different points number that changes from a scan and the following one. It is no possible to know previously how many points the acquired frame will have.

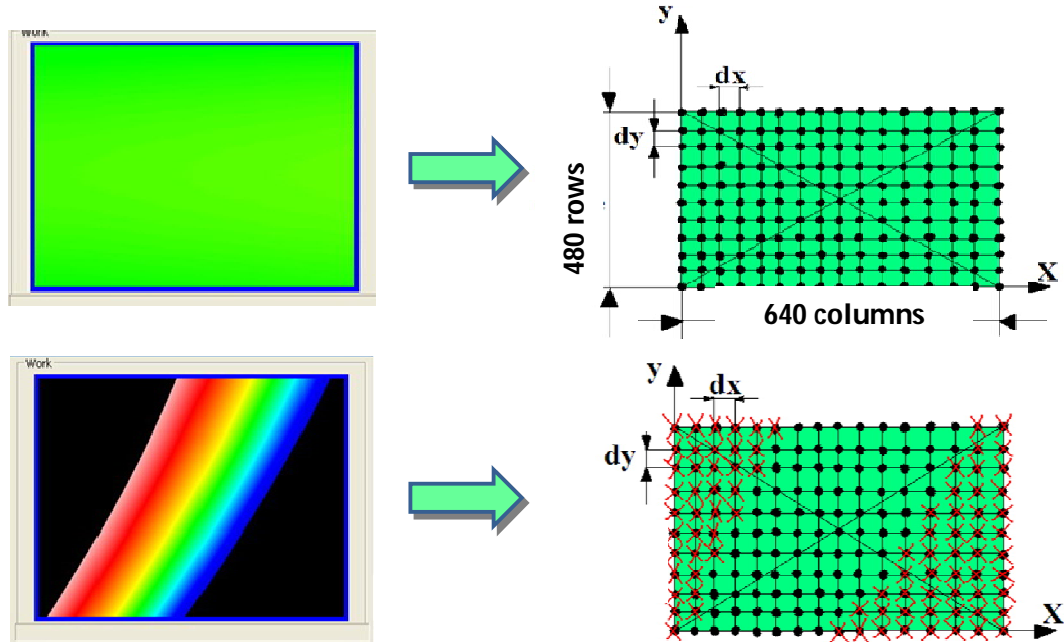


Figure 2.41 Only with some angular combination, the whole frame is completely acquired; in all the other conditions only some central points are stored, and in many parts no points are present

The described methodology and analysis is thus performed only on rectangular arrays, since it is no possible to apply the same considerations as done before, on the other frames. This is due to the fact that in such points clouds it is no possible to identify the same number of points, so that acquired meshes cannot be elaborated in *Matlab* as the other ones. Moreover it is no possible to know points location easily and thus both point reduction and mean processes have no sense in this configuration. Potential solutions will be presented in the following section.

In rectangular cases the area of the acquired frame is computed, since it was possible to define a rectangular shapes of area $w \times h$, as done in the previous section (Table 2.14).

LENS	ANGLES	THEORETICAL/ REAL AREA	AREA VALUES
TELE 600 mm distance	(0°, 0°)	Theoretical Area	115.20 × 86.40 mm
		Real Area	112.06 × 84.01 mm
	(0°, 20°)	Real Area	118.26 × 90.76 mm
	(20°, 0°)	Real Area	125.62 × 88.04 mm
	(20°, 20°)	Real Area	126.27 × 99.34 mm

Table 2.14 Area acquired at 600 mm distance with a Tele lens, in dependence on different geometrical parameters

All arrays are loaded in *Matlab* in order to perform the reduction, the mean and the best fitting processes. First of all 3D points are illustrated: Z coordinates are graph in function of i, j pixel coordinates in the CCD sensor (Figure 2.42).

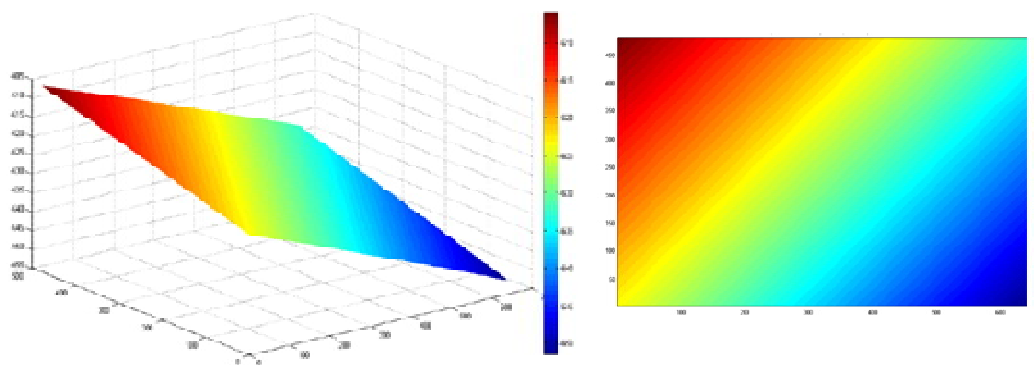


Figure 2.42 3D representation of points coordinates in *Matlab* environment. Tele lens 600 mm of distance, $\alpha = 20^\circ$, $\beta = 20^\circ$

In order to remove some boundary points, where the laser beam is more scattered, points resolution is analyzed and graph: in Figure 2.43 point resolution is visualized both in x and y directions. Moreover, two vectors containing points distances in x and y directions are created and are then graph for the first; in Figure 2.44 and Figure 2.45 the middle and the last rows and columns, considering the two tilt angle of 20° each are shown.

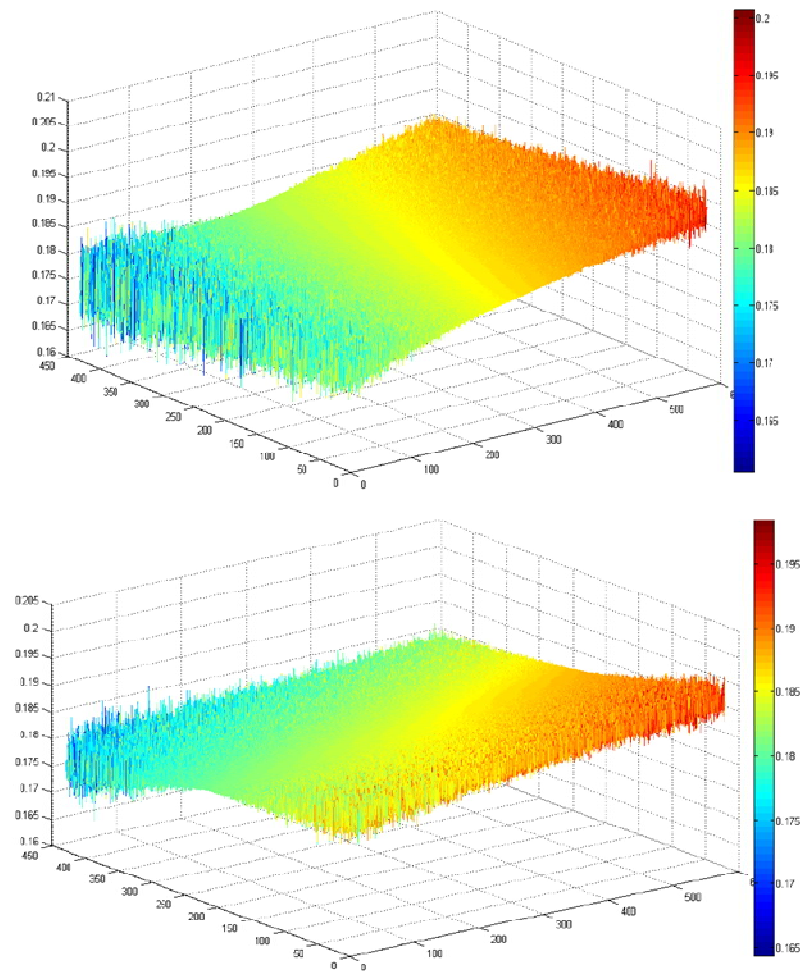


Figure 2.43 Points resolution in X and Y directions, in function of their location in the frame. Tele lens, 600 mm of acquiring distance and $(20^\circ, 20^\circ)$ of tilt angles

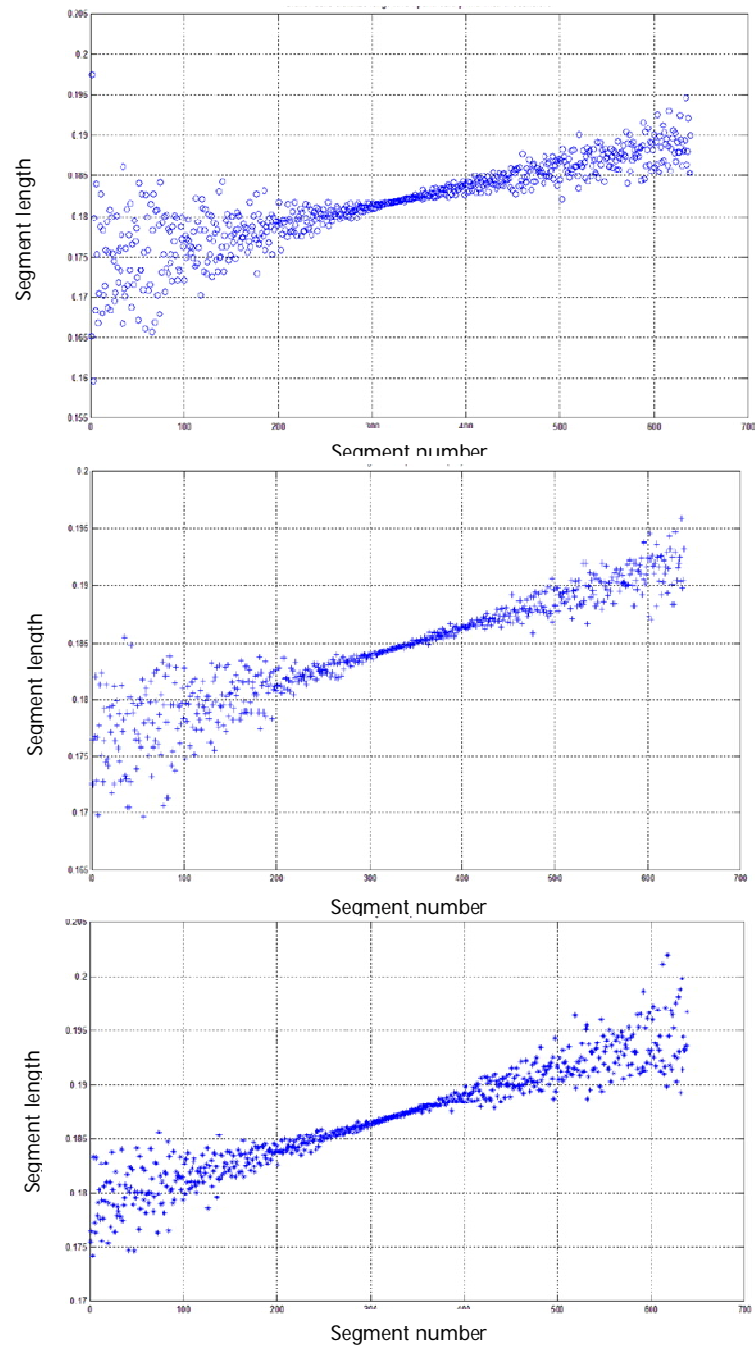


Figure 2.44 Segment lengths in dependence on its position in the frame (column: segment position which runs from 1 to 640): the first image corresponds to the first row, the second one to the middle row (240) and the last one to the last row (480). Tele lens, 600 mm of scanning distance and tilt angles of 20° each

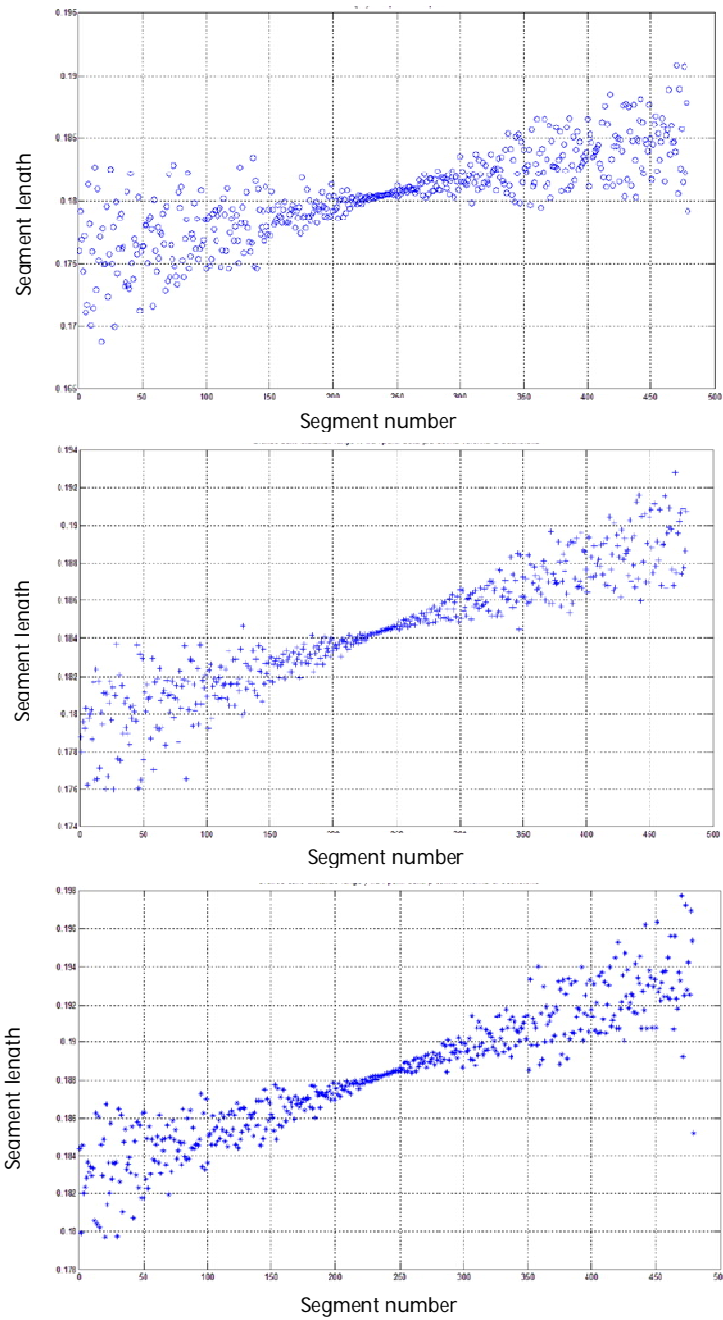


Figure 2.45 Segment lengths in dependence on its position in the frame (row: segment position which runs from 1 to 480): the first image corresponds to the first column, the second one to the middle column (320) and the last one to the last column (640). Tele lens, 600 mm of scanning distance and tilt angles of 20° each

Point reduction is performed on the basis of a percentage reduction of resolution standard deviation, evaluated as standard deviation of the vector containing distances between two near points (Table 2.15). a reasonable choice is to reduce resolution standard deviation of 10%. All acquired range maps are thus reduced of 29 rows and 32 columns symmetrically.

Lens	Distance (mm)	$(\alpha; \beta)$		5%	10%	15%	20%	25%	30%
TELE	623 mm	$(0^\circ; 0^\circ)$	row	12	24	35	46	58	69
			column	15	30	45	61	76	92
		$(20^\circ; 20^\circ)$	row	17	29	39	51	61	73
			column	19	32	50	62	82	92

Table 2.15 Points to remove symmetrically in each row and column in order to have a decrease of standard deviation of vectors of distances between two near points

In the following steps, reduced arrays are averaged and then a best fitting plane is defined. By the difference between acquired points and best fitting plane it is possible to define a punctual error value on 3D points coordinates (Figure 2.46).

Error standard deviation in function of the number of arrays involved in the meaning process is evaluated (Figure 2.47), in order to identify the optimal number of arrays to obtain a reduction of error random component, and thus the number to range maps to average in order to find the right best fitting plane. As defined in the perpendicular configuration, also in this case the fourth mean process is considered enough for random error compensation.

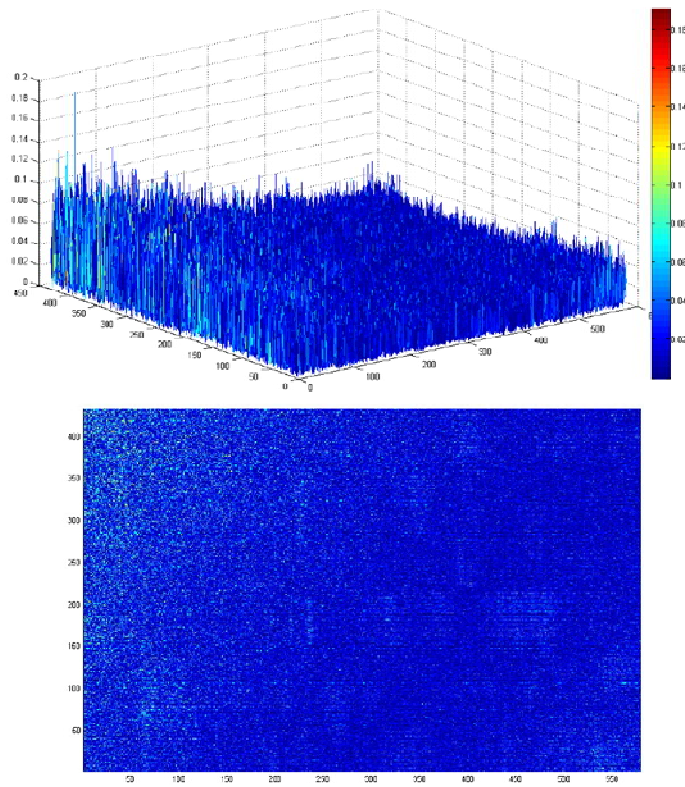


Figure 2.46 Error representation in pseudo color, in function of points position in the acquired frame. Case study with geometric parameters α and β of 20° each.

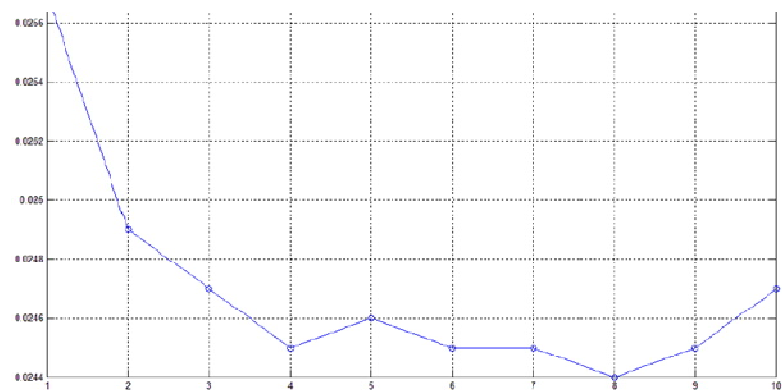


Figure 2.47 Error standard deviation in relation to the number of arrays involved in the mean process. Tele lens, 600 mm of acquiring distance and $(20^\circ, 20^\circ)$ of inclination

In surface and error standard deviation are presented, together with point's resolution (mean, maximum and minimum values in both directions) in dependence to the number of averaged arrays (Table 2.16).

MEAN ARRAYS	SRF. DEV.	STD. DEV.	MEAN RESX	MEAN RESY	MIN RESX	MIN RESY	MAX RESX	MAX RESY
1	0.1923	0.0257	0.1843	0.1844	0.1555	0.1627	0.2044	0.2012
2	0.1889	0.0249	0.1843	0.1844	0.1582	0.1617	0.2041	0.2009
3	0.1835	0.0247	0.1843	0.1844	0.1588	0.1610	0.2041	0.2005
4	0.1828	0.0245	0.1843	0.1844	0.1572	0.1604	0.2045	0.2010
5	0.1889	0.0246	0.1843	0.1844	0.1566	0.1601	0.2042	0.2002
6	0.1915	0.0245	0.1843	0.1844	0.1576	0.1605	0.2039	0.2005
7	0.1935	0.0245	0.1843	0.1844	0.1568	0.1604	0.2040	0.2003
8	0.2000	0.0244	0.1843	0.1844	0.1576	0.1604	0.2040	0.2009
9	0.1937	0.0245	0.1843	0.1844	0.1586	0.1606	0.2037	0.2010
10	0.1885	0.0247	0.1843	0.1844	0.1575	0.1607	0.2043	0.2009

Table 2.16 Surface and standard deviation and points resolution in relation to the number of averaged arrays. Tele lens, 600 mm distance and (20°, 20°) of angles.

Arrays for error compensation are thus defined for different tilt angles (as presented in Table 2.13) and for different lenses and distances and the correction procedure is applied. Such arrays are used to correct errors in an acquired frame and accuracy and precision values are compared in Table 2.17. Processed data have accuracy

value nearer to Minolta data sheet ones and they are more précised then data directly acquired.

TELE 600 mm $\alpha = 20^\circ, \beta = 20^\circ$	Minolta Data sheet	Experimental Data		
		Acquired Data	Processed Data	
Accuracy	0.05 mm	0.1936 mm	0.0766 mm	Maximum value of $ z_{ij} - z_{ij}^* $
		0.0187 mm	0.0066 mm	Mean Value of $ z_{ij} - z_{ij}^* $
Precision	0.008 mm	0.0144 mm	0.0086 mm	σ_z

Table 2.17 Comparison between Minolta Data Sheet and experimental data for a specific case with the Tele lens and at a scanning distance of 600mm, tilt angles of 20°

A final comparison between correction arrays related to the laser beam perpendicular to the scanning surface and with different angles is finally performed. $\Delta S(0^\circ, 0^\circ)$ and $\Delta S(20^\circ, 20^\circ)$ were analyzed in order to see differences and to tests the necessity to have a different correction arrays in relation to different surface normal directions. The first considered feature is that both arrays and their difference are of the same order of magnitude: this means that there is a wide variation on data obtained with the first and the second case and this should justify the employment of a different correction array for each different set up. In order to picture what above discussed, first 30 homologous points of $\Delta S(0^\circ, 0^\circ)$ and $\Delta S(20^\circ, 20^\circ)$ correction arrays are graph (Figure

2.48), moreover their differences (Figure 2.49) are presented. As it is possible to see, both values are of the same order of magnitude.

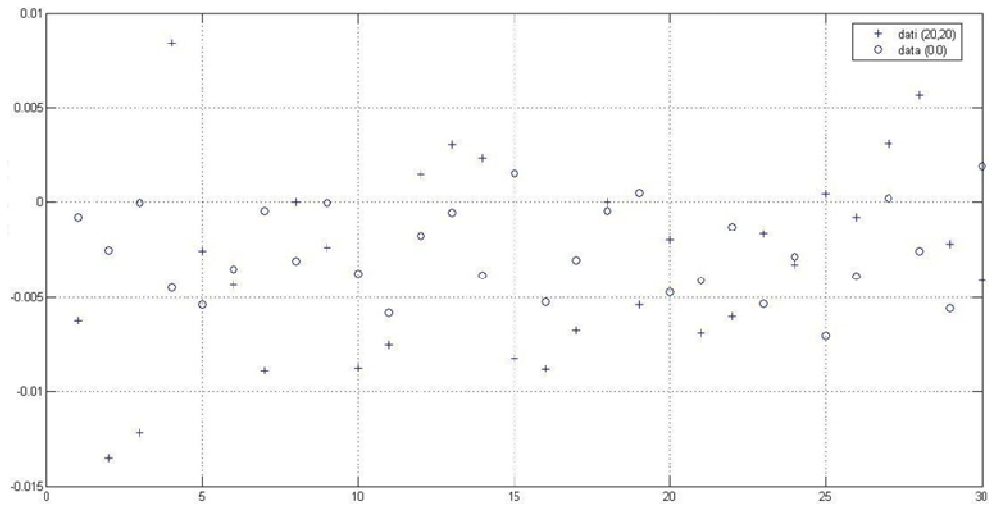


Figure 2.48 Correction value (mm) in relation to point index. $\Delta S(0,0)$ values are indicated by a dot, while $\Delta S(20,20)$ values are represented by a cross

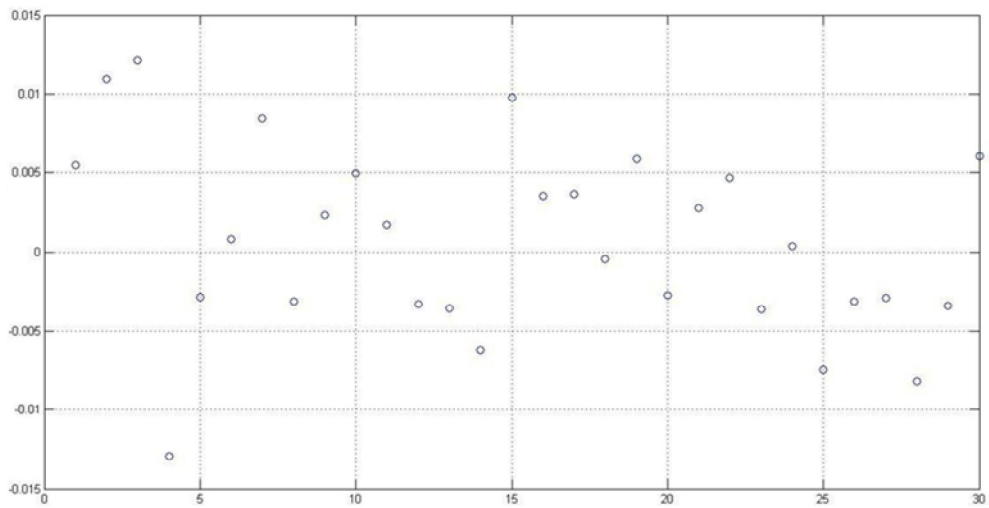


Figure 2.49 Difference (mm) between $\Delta S(0,0)$ and $\Delta S(20,20)$ arrays in relation to point index

2.5.1 Non rectangular frames

If at least one tilt angle is more than 20° , the acquired range map does not fill up the whole CCD sensor and some pixels do not register any point coordinates, so that acquired point clouds are not rectangular. This due to the fact that two consecutive acquired scans have different point number, and since 3D coordinates are not exactly the same it is no possible to identify the same point in both scans: there are not correspondences between two consecutive scans.

Under these conditions the mean process is no more possible, so that the methodology cannot be applied as presented to such acquired arrays.

In this context analysis on point resolution are performed: a *Matlab* routine was written to compute distances between two near points. In case the distance is more than 5 mm, it automatically considers the point as in the following row. This script also offers the possibility to identify how many rows are acquired and how many points in each row. By these analysis some data are conceived (Table 2.18), regarding point resolution and point distances standard deviation.

Array	Std. Dev.	Mean Res	Min Res	Max Res	Number of rows	Max number of point in each row	Min number of point in each row
(0°,40°)	0.0140	0.1848	0.1655	2.8646	379	640	19
(0°,60°)	0.0220	0.1832	0.1545	2.8703	265	640	15
(20°,40°)	0.0072	0.1830	0.1505	0.3916	480	640	220
(20°,60°)	0.0080	0.1828	0.1520	0.3952	436	565	29
(40°,0°)	0.0092	0.1848	0.1600	0.2110	480	374	337
(40°,20°)	0.0093	0.1843	0.1557	0.2130	480	367	330
(40°,40°)	0.0101	0.1837	0.1475	0.3247	480	320	287
(40°,60°)	0.0113	0.1827	0.1401	0.2262	480	297	149
(60°,0°)	0.0092	0.1866	0.1663	0.2097	480	231	208
(60°,20°)	0.0093	0.1861	0.1650	0.2121	480	226	203
(60°,40°)	0.0101	0.1858	0.1555	0.2182	480	196	176
(60°,60°)	0.0127	0.1860	0.1443	0.2286	480	149	133

Table 2.18 Points distances standard deviation, mean, minimum and maximum resolution values for the first scan of all non rectangular frames.

Such resolution data are visualized in relation of their location into the acquired frame. Graphs are presented for the first, the middle and the last acquired rows for different tilt angles pairs (Figure 2.50, Figure 2.51). By these representations it is also possible to analyze that in the first rows, the laser beam acquires more points than in the lower frame portion.

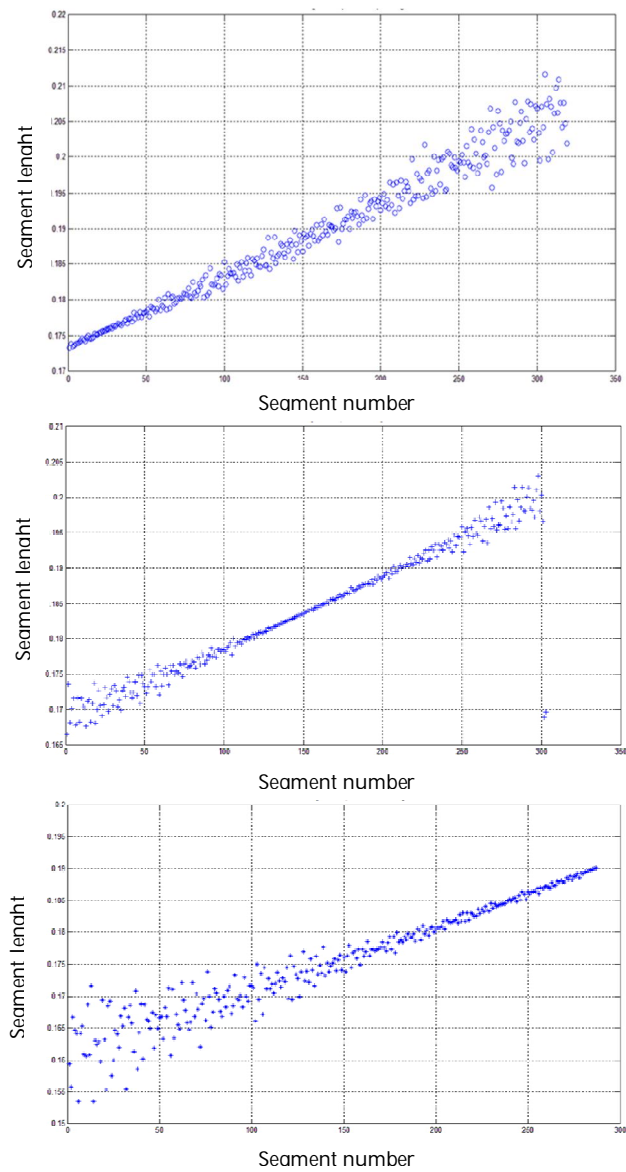


Figure 2.50 Resolution values in relation to row position in the acquired frame. On the top is presented the first row, then the middle row and finally the last row. Scans are performed with a Tele lens, at 600 mm of distance and tilt angles of (40°,40°)

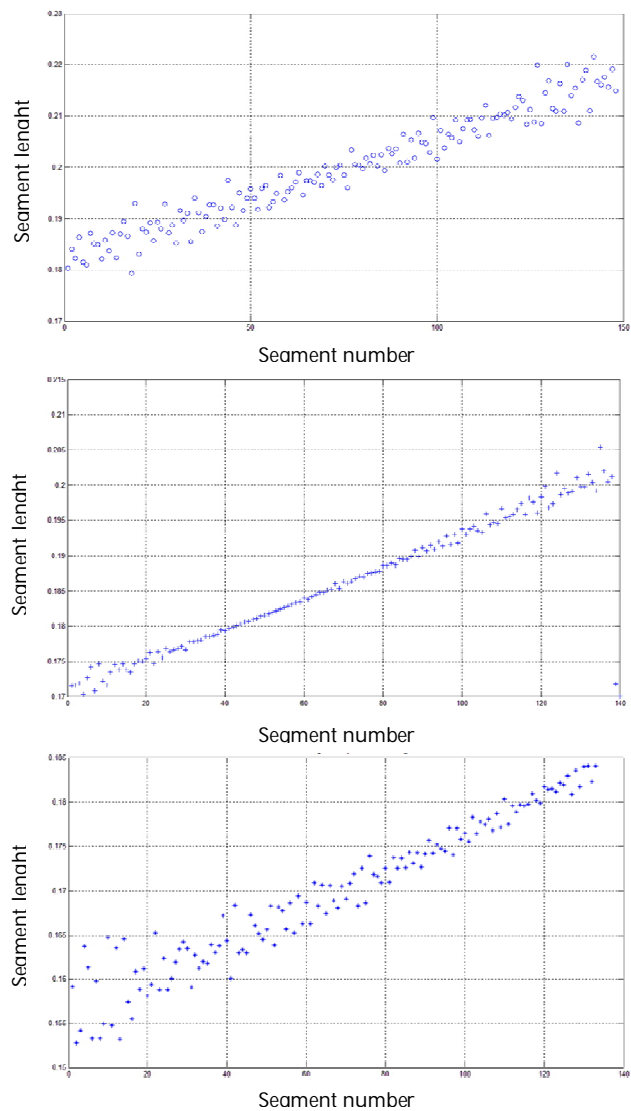


Figure 2.51 Resolution values in relation to row position in the acquired frame. On the top is presented the first row, then the middle row and finally the last row. Scans are performed with a Tele lens, at 600 mm of distance and tilt angles of (60°,60°)

2.5.1.1 Systematic error compensation arrays for non rectangular frames

In case object surface normal has directions which forms with the laser beam an angle superior than 20°, no compensation arrays to reduce systematic error component

have been defined with the proposed methodology. Some guidelines are now defined in order to overcome this trouble.

The first consideration concerns the acquiring system. Laser scanner is an optical instrument with a focus depth of about 15 cm: during the scanning process the wider and central frame portion is in focus and everything is into this depth of field is in focus at the same time, all other frame portions are not acquired. For this reason laser scanner is not able to gain the whole reference surface, when it is in a too inclined configuration. This means that this is not a methodological trouble but it is an instrument limitation that doesn't allow performing the methodology in a severe set up. The employment of different lenses or of an instrument with a wider depth of field is expected to improve the acquisition process and thus to acquire rectangular range maps even if the reference surface is more inclined than 20° .

Moreover, in practical cases, a mesh acquired from a perpendicular point of view is always more precise and more detailed than a mesh acquired diagonally. For this reason in case it would be necessary to use a correction array to compensate errors and noises and the normal direction is too inclined so that the correspondence correction array is not defined, the scanning process should be planned in order to move laser scanner and object respecting positions so that the laser beam is perpendicular to the surface to be acquired.

However, it would be possible to define an error compensation array, with some expedients. The first considers the employment of more reduced arrays: the reduction process is one of the first steps in the elaboration procedure. In this context the acquired mesh can be reduced of many points so that only a small rectangular area is defined in the middle of each frame (Figure 2.52). All scans acquired under the same operative conditions are reduced to the same number of points, arranged in the same way. This technique leads the methodology to the same workflow as before, so that the following phases can be performed in the same way.

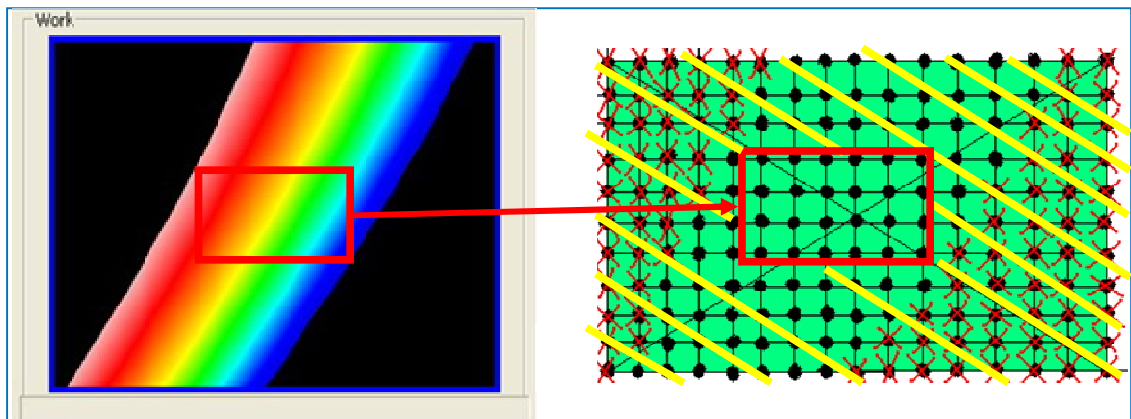


Figure 2.52 Only the central portion of each frame can be used to perform the methodology, so that all acquired scans with similar operative conditions can have the same rectangular structure

This method has the main advantage to lead the process back to the described methodology, without any changes in developed *Matlab* routines and a compensation array is defined. On the other hand, defined correction arrays are user to compensate systematic errors during real applications and case studies. For this reason the use of

correction arrays only on a little central frame portion leads to delete all points which don't belong to this area, so that much more scans are necessary to describe the whole object surface. In practical cases this solution is considered not convenient from an operative point of view.

A second approach, has been deeply developed, considering the possibility to define unknown correction arrays (related non rectangular frames, since not all points have been acquired) starting from known arrays. For the same focusing distance, some linear dependences has been investigated between known arrays, in order to verify the existence of a low able to link together configurations acquired with different tilt angles. After many different relation exploited, any linear association has not been identified till now and other experimental techniques has been exploited, since the mathematical one provided non useful results.

A third final approach considers that since the described limitations are related to focusing troubles, the same frame can be acquired twice, but with different focusing distances: the acquisition process is thus split into two parts. Considering, as example, to acquire the range map at 600 mm of scanning distance, the same frame its acquired twice: the first time with 580 mm of focusing, and the second one with 620 mm. The first range map contains all points of half frame, while the second one will acquire the other portion (Figure 2.53).

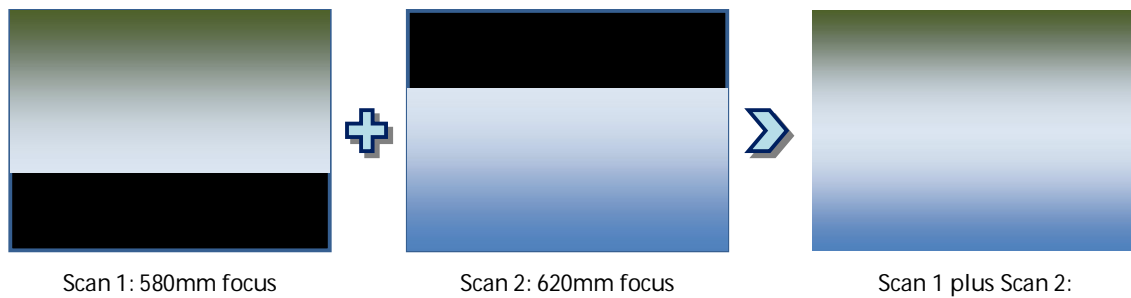


Figure 2.53 Composition of two different scans: the first one performed at a less scanning focusing and the second one at an high distance. The black portion represents no acquired areas. The third image is the composition f the first two

This technique suggests splitting the acquisition, elaboration and correction processes into two parts, so that, finally two ΔS arrays are relate to the same configuration, but refers to different points. These two arrays are then composed together so that it would be possible to compensate systematic component of errors in operative conditions, when surface normal direction is more than 20° .

This approach has the main advantage to give an error compensation array in a rather simple way, and the described methodology can be implement under some little changes connected to points reduction. On the other hand such correction array are define acquiring distances that are no constant anymore. This feature can introduce some more uncertainties, which will be taken under examination.

3. Infrared Thermography

Infrared (IR) Thermographic Systems evaluate object's surface temperatures by measuring the magnitude of emitted infrared radiation and provide images that represent surface temperature called *thermograms*.

All objects at a temperature above absolute zero (-273.15°C) emit electromagnetic radiation in the form of rays: in particular, when the object is at ambient temperature, the emission falls into the infrared portion of the electromagnetic spectrum so that it cannot be seen by the unaided eye. A radiometer converts the radiated energy into an electronic signal and then into a visible image, in which each energy level may be represented by a color level. Considering that the energy emitted by a body is mainly function of its surface temperature value, knowing the material properties of the surface, it is possible to measure object temperature through thermography.

Inspection for predictive maintenance, non-destructive evaluation of thermal and mechanical properties, building sciences, military reconnaissance and weapons guidance, medical imaging, and cultural heritage conservation are some fields in which IR thermography is commonly employed in order to reveal malfunction, leaks, material loss, delamination, etc. (Griffith B. et al., 2000).

There is a distinction between radiometric imaging for the determination of absolute temperature and thermal imaging for the achievement of relative temperature information, or *thermal signature*. Hence, infrared thermography can be used as qualitative or quantitative inspection: radiometry devices are used for precise temperature measurement whereas viewing devices are designed for qualitative comparisons. Anyway, also during a quantitative thermographic inspection, images are usually first evaluated for qualitative thermal signature to discern the presence and proximity of a feature of interest or defect.

In the next paragraphs, thermographic applications with radiometric images are presented with the aim to understand the thermographic principal aspects. Moreover, the fundamentals at the basis of temperature measurements are analyzed.

3.1 *Fundamental Physical principles and theory of operation*

Technical instruments for thermographic inspection mainly include a camera equipped with an optical lens and an interface necessary to analyze the acquired data. An infrared detector is the core of the camera: it absorbs the IR energy emitted by the object, whose surface temperature is to be measured, and converts this electrical energy to electrical energy.

A cornerstone of the IR measurement is the electromagnetic field that transfers energy, which carried amount is dependent on its wavelength and on all carrying photons. In general, an electromagnetic radiation transfers a *radiant energy* Q_e .

The *flux* is the instantaneous measure of the quantity of radiation: it describes a source propagating in the form of a beam, or received by a detector, and it is the radiant energy per unit time.

$$\Phi_e = \frac{dQ_e}{dt} \quad W \quad \text{Eq 3.1}$$

All materials produce a thermal flux: material temperature causes particles oscillations which creates an energy flux. This energy flux of particles resulting by oscillations creates thermal emission. There are two different ways to understand thermal emission transport: the first one is to consider *photon emission*, the second one is to consider *electromagnetic waves*. Photons are energy particles with zero mass at rest, and with a discrete quantity of energy, called *quantum*. Electromagnetic have specific frequency and energy. The two concepts are linked together: in fact, for a given wavelength λ , the liberated photonic energy W , due to particles oscillations is:

$$W = \frac{hc}{\lambda} \quad \text{Eq 3.2}$$

where $h = 6.63 \times 10^{-34} \text{ Js}$ is the Planck constant and $c = 3.0 \times 10^8 \text{ ms}^{-1}$ is the speed of the light (Maldague, 2001). The wavelength of emitted radiation varies inversely with the

transition energy: this means that in the infrared region, the wavelength is long, whereas the radiation energy is low; this implies that it is not easy to detect infrared radiation.

The definition of a radiant flux is inherent to the description of some more physical quantities, useful for the characterization of such radiant energy in time and space: they are also referred to as *radiometric quantities*.

3.1.1 Emitted and incident radiations

The radiant flux emitted by an extended source for surface units is called *radiant exitance* M_e :

$$M_e = \frac{d\Phi_e}{dA} \quad \text{Wm}^{-2} \quad \text{Eq 3.3}$$

Similarly, the radiant flux, which is incident on a surface per unit area, is called *radiant irradiance* E_e :

$$E_e = \frac{d\Phi_e}{dA} \quad \text{Wm}^{-2} \quad \text{Eq 3.4}$$

Now, it is important to introduce some basic concepts and notations that will be used in the following paragraphs.

A *spherical system of coordinates* (Figure 3.1) requires three variables to locate a point on a sphere surface, which coordinates are

- the radius r , which is the distance from the sphere center, located at (0,0,0);

- the azimuthal angle ϑ ;
- the zenith angle φ .

Point P is thus located in (r, ϑ, φ) .

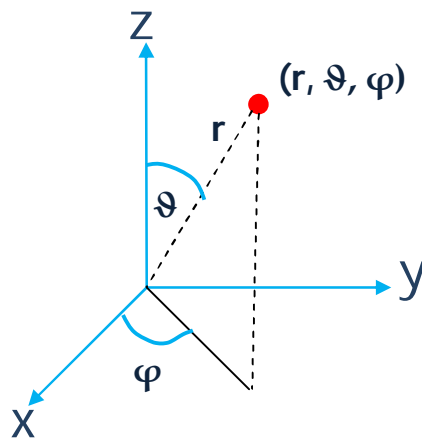


Figure 3.1 Spherical System coordinates

Suppose we have two lines which point of interception is O: the angle $d\alpha$ corresponds to the fraction of the infinite plane defined by these two lines. $d\alpha$ is thus given by the ratio between the arc length given by the intersection of a circle radius r , centered at O and the two lines to this radius: $d\alpha = l/r$. By this preliminary consideration, a *solid angle* is the fraction of the space contained within an infinite cone, centered at O (Figure 3.2). Consider the intersection of a sphere, centered at O with radius r , and a cone of infinite extent, and observe that the ratio of the intercepted surface dA_r on the sphere to the square of radius r is measured as the solid angle

$d\omega = dA_n/r^2$ (the subscript n indicates that the differential surface element is normal to the cone axis). The units for a solid angle are *steradians* (sr).

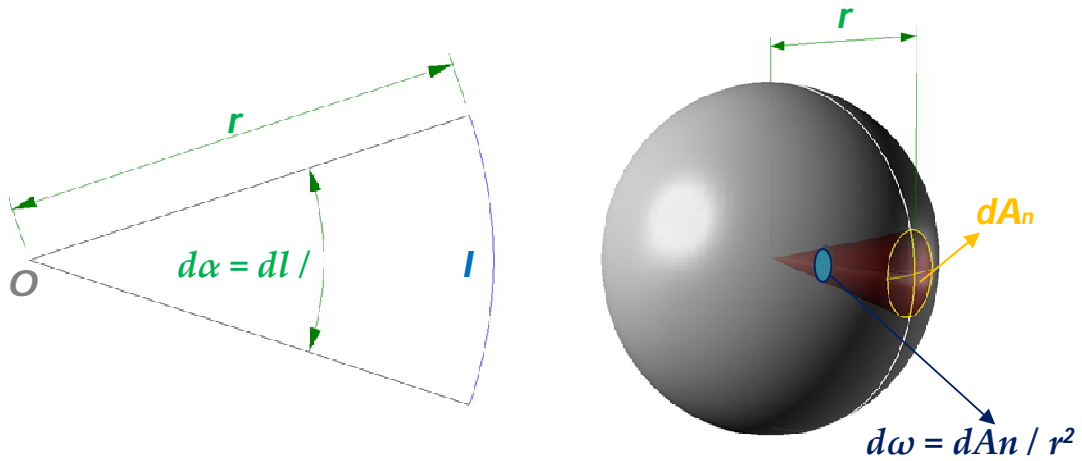


Figure 3.2 Definition of plane and solid angle

Referring to the solid angle concept, the radiant intensity of a source in a given direction is the ratio of the flux ϕ emitted by a source, in the direction defined by the parameters (ϑ, φ) and the solid angle $d\omega$ within which the intensity is evaluated:

$$I_e = \frac{d\Phi_e}{d\omega} \quad \text{Eq 3.5}$$

Figure 3.3 Definition of radiance

Radiance is one more basic concept: it is the radiant flux emitted by an extended source for solid angle units and from the surface, an area projected onto a plane, normal to the specific direction of propagation (Figure 3.3).

$$L_e = \frac{d^2 \phi_e}{dA_p d\omega} = \frac{d^2 \phi_e}{dA \cos \theta d\omega} \quad \text{Eq 3.6}$$

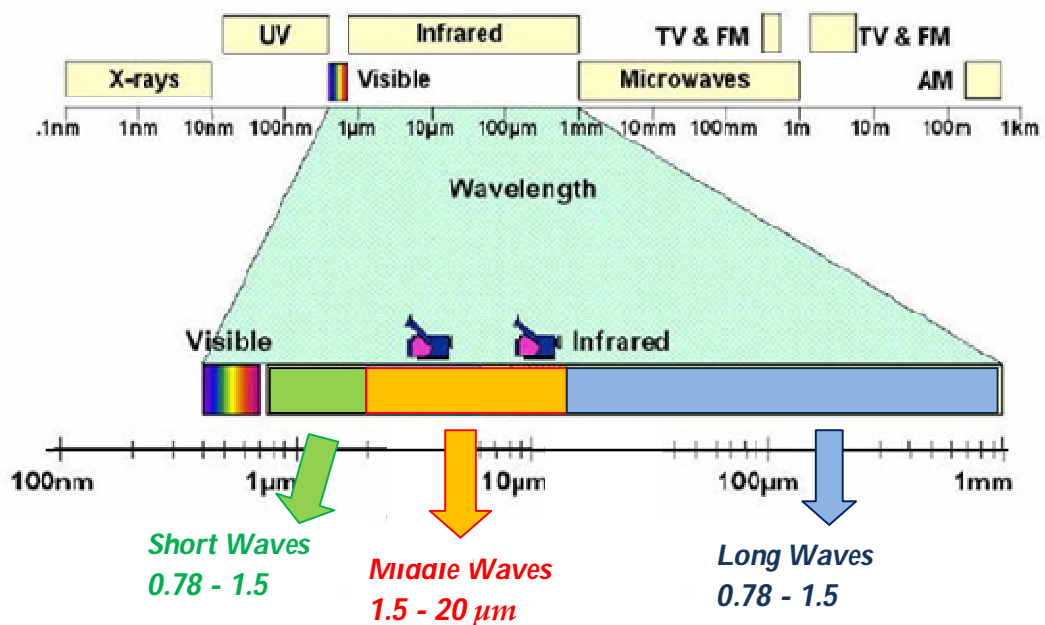


Figure 3.4 The electromagnetic spectrum

With increasing wavelength, and according to their source of emission and employment, the spectrum of radiation is divided into specific bands (**Errore. L'origine riferimento non è stata trovata.**): γ -rays, χ -rays, ultraviolet (UV) rays, visible rays, infrared (IR), radio waves and microwaves. Moreover, the IR spectrum can be split into

near IR (0.78 ÷ 1.5 µm wavelength), middle IR (1.5 ÷ 20 µm wavelength), and far IR (20 ÷ 1000 µm wavelength). The wavelength bands are related to the detector capabilities: near infrared is detected by special photographic emulsions, by photo emissive cells, and by photoconductive and photovoltaic detectors; middle infrared is detected by thermal, photoconductive, and photovoltaic detectors; radiation in the far infrared can be measured by thermal detectors (Gaussorgues, 1994).

Many phenomena are strictly related to spectral bands: this is the reason why radiometric quantities have to be related to wavelength. In this context, the *spectral radiant flux* Φ_λ refers to an infinitesimal wavelength interval.

$$\Phi_\lambda = \int_{\lambda_0}^{\lambda_1} \phi_e d\lambda \quad \text{Eq 3.7}$$

Similarly, the other radiometric quantities can be referred to wavelength.

The *spectral radiance* $L'(\lambda, \vartheta', \varphi')$ is the rate at which energy (or an emitted flux ϕ') is emitted, at a given wavelength λ , from a surface patch dA , in the specific direction (ϑ', φ') , passing through dA_n (Maldague, 2001).

$$L'(\lambda, \vartheta', \varphi') = \frac{d^3 \phi'}{dA \cos \vartheta' d\omega' d\lambda} \quad \text{Wm}^{-2} \text{sr}^{-1} \mu\text{m}^{-1} \quad \text{Eq 3.8}$$

This equation describes the spectral radiance as the ratio of the emitted flux ϕ' to the surface element subtended by the solid angle $d\omega'$ and immediately surrounding the flux direction (ϑ', φ') per unit of wavelength interval $d\lambda$. This projected surface element is, in fact, the surface element perpendicular to the emitted radiation ($dA \cos \vartheta'$).

The *radiant power* per unit area, for an emitting surface, can be computed by integrating $L'(\lambda, \vartheta, \varphi)$ over any finite angle and finite wavelength range, if the spectral and directional distribution of the spectral radiance is known. This quantity is known as the *spectral exitance* $M(\lambda)$. For a Lambertian emitter (which is an isotropically diffuse emitter):

$$M'(\lambda) = \pi L'(\lambda) \quad \text{W m}^{-2} \mu\text{m}^{-1} \quad \text{Eq 3.9}$$

The *total exitance* is the radiant power per unit area emitted over all wavelength and all directions:

$$M' = \pi L' \quad \text{W m}^{-2} \quad \text{Eq 3.10}$$

Either from reflection or emission at other surface, the radiation incident on a surface has also spectral and directional distributions: the concepts discussed above can be adapted, and the incident *spectral radiance* $L(\lambda, \vartheta, \varphi)$ can be introduced:

$$L(\lambda, \vartheta, \varphi) = \frac{d^3 \phi}{dA \cos \vartheta d\omega d\lambda} \quad \text{W m}^{-2} \text{sr}^{-1} \mu\text{m}^{-1} \quad \text{Eq 3.11}$$

This equation represents the incident spectral radiance as the ratio of the incident flux ϕ for the wavelength interval $d\lambda$ from the direction (ϑ, φ) to the projected surface element $(dA \cos \vartheta)$, subtended to the solid angle $d\omega$ and surrounding the flux.

Finally, the *spectral irradiance* $E(\lambda)$ is defined as the spectral radiant power at the wavelength λ incident per unit area upon a surface from all directions in the hemispheric space above the specified surface:

$$E(\lambda) = \frac{d\phi(\lambda)}{dA} \quad \text{Eq 3.12}$$

The total irradiance is defined as the radiant power at all wavelengths incident per unit area upon a surface and from all directions:

$$E = \int_0^\infty E(\lambda) d\lambda \quad \text{Eq 3.13}$$

If the incident radiation is isotropic, that is, independent of the direction (ϑ, φ) , then $E(\lambda) = \pi L$. It is important to note that, as for the irradiance, the specified surface is the actual surface dA , whereas, as for the radiance, the specified surface is the projected surface $dA \cos \vartheta'$.

The *exposure* is the time integral of radiance, that is to say, the energy received per unit surface area:

$$\mathcal{L} = \int_{t_1}^{t_2} L(t) dt \quad \text{Eq 3.14}$$

The *Bouguer's Law* is the relation between the irradiance E of a receiving surface, due to a source S , and the intensity I of that source in the direction of the receiver lying at a distance d (Figure 3.5):

$$E = \frac{I \cos \vartheta_R}{d^2} \quad \text{Eq 3.15}$$

This inverse square dependence on the distance from the source is valid if the linear dimensions of the source are small compared with the distance d (Gaussourgues, 1994).

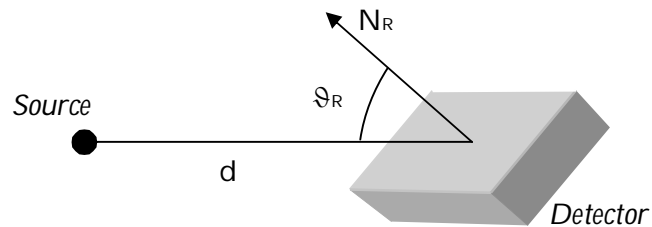


Figure 3.5 Bourguer's Law

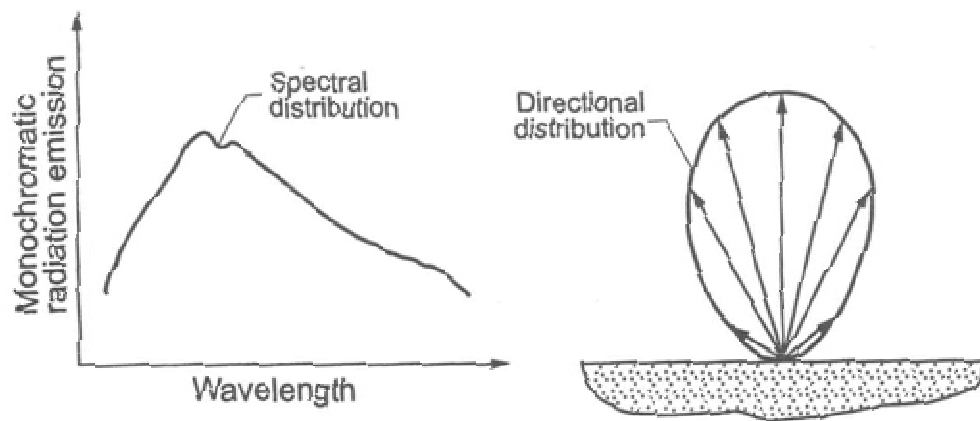


Figure 3.6 Radiation emitted by a surface: spatial and directional distributions (Maldaque, 2001)

Energy emitted from a surface has various features: many wavelengths are emitted in a non-uniform distribution of energy in all directions (Figure 3.6).

3.1.2 Blackbody

An instrument absorbing all radiated energy from any direction and at each wavelength is called *blackbody*. It is a *perfect radiator*, since it has the property of emitting

the received radiated energy until thermodynamic equilibrium with its surrounding environment has been reached. For a given temperature and wavelength, no other surfaces are able to emit more energy than a black body. Moreover, the emitted radiation is function of the blackbody temperature and it is independent from the emitting direction: for this reason, blackbody is also called *isotropically diffuse emitter*, or *Lambertian emitter* (Maldague, 2001).

A cavity with a small aperture or a flat surface with a perfectly absorbing coating can be considered blackbodies, even if they are not perfect blackbodies: in such cases, the isotropic emission is not received by the whole surface (Figure 3.7).

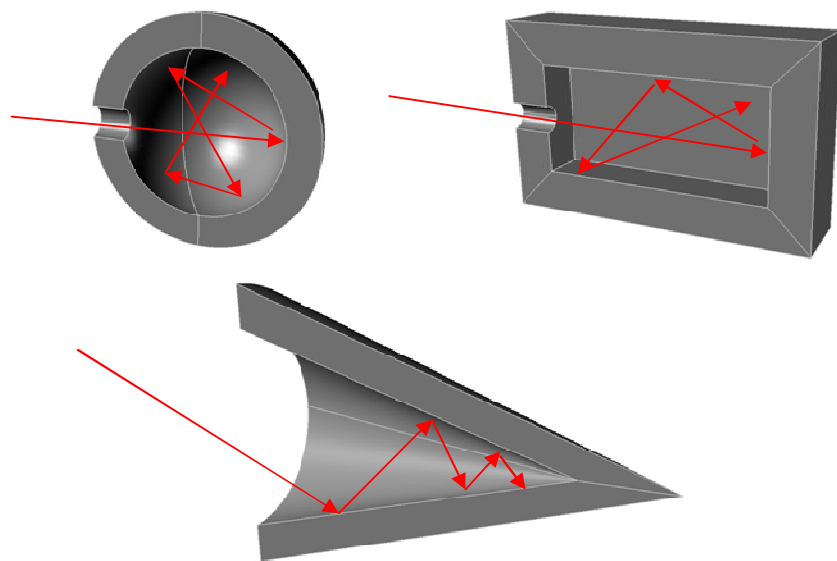


Figure 3.7 Models of black bodies

3.1.3 Planck's Law

The Planck's Law describes the distribution of emitted energy as a function of wavelength based on a given temperature. The spectral radiance, the power radiated by a blackbody b per unit surface and per unit of solid angle:

$$L_{\lambda, b}(\lambda, T) = \frac{2hc^2}{\lambda^5 [\exp(hc/\lambda KT) - 1]} \quad \text{W m}^2 \mu\text{m}^{-1} \text{sr}^{-1} \quad \text{Eq 3.16}$$

where $h = 6.6256 \times 10^{-34}$ Js is the Planck's constant, $k = 1.38054 \times 10^{-23}$ JK⁻¹ is Boltzmann's constant, $c = 2.998 \times 10^8$ ms⁻¹ is the speed of the light and T is the absolute temperature of the blackbody in degrees Kelvin.

The Planck's Law is commonly represented by a curve family (Figure 3.8) showing that, for a given temperature, magnitude of the emitted radiation varies with wavelength.

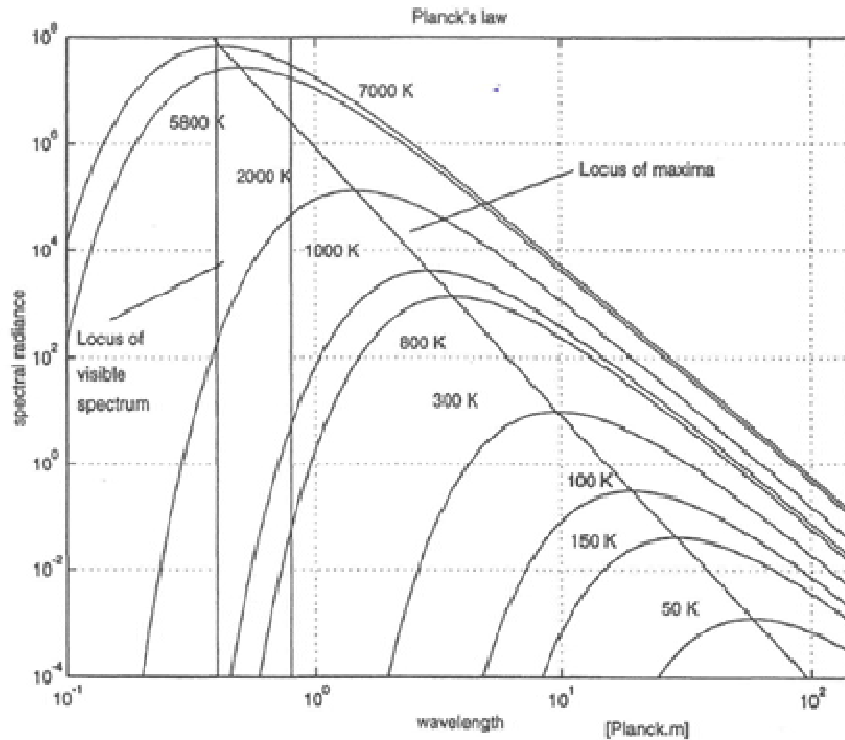


Figure 3.8 Planck's Law: the spectral radiance of a blackbody (Maldague, 2001)

3.1.4 Wien displacement Law

Looking at Planck's curves (Figure 3.8), the spectral radiance curve at a constant temperature passes through a maximum. The locus of the maximum spectral range for a given temperature corresponds to a line which is obtained by derivation of Planck's law and it is known as the Wien's Law:

$$\lambda_{\max} = \frac{2897.7}{T} \quad \text{Eq 3.17}$$

3.1.5 Stephan-Boltzmann Law

Stephan-Boltzmann Law is obtained by integrating Planck's Law over all wavelengths ($0 \leq \lambda \leq \infty$). It provides the total exitance M_b for a blackbody at temperature T :

$$M_b = \sigma T^4 \quad \text{Eq 3.18}$$

where σ is known as the Stephan-Boltzmann constant and $\sigma = \pi^5 k^4 / 15 c^2 h^3 = 5.67 \times 10^{-8} \text{ W m}^{-2} \text{ K}^{-4}$.

3.1.6 Radiation emitted in a spectral band

The fraction $F(\lambda_1, \lambda_2)$ of the total emission in a spectral band (λ_1 to λ_2) is obtained by integration of Planck's Law (Figure 3.9):

$$F(\lambda_1, \lambda_2) = \frac{\int_{\lambda_1}^{\lambda_2} L_{\lambda,b}(\lambda) d\lambda}{\int_0^{\infty} L_{\lambda,b}(\lambda) d\lambda} = \frac{L_{\lambda,b}(\lambda) d\lambda}{\sigma T^4} = F(0, \lambda_2) - F(0, \lambda_1) . \quad \text{Eq 3.19}$$

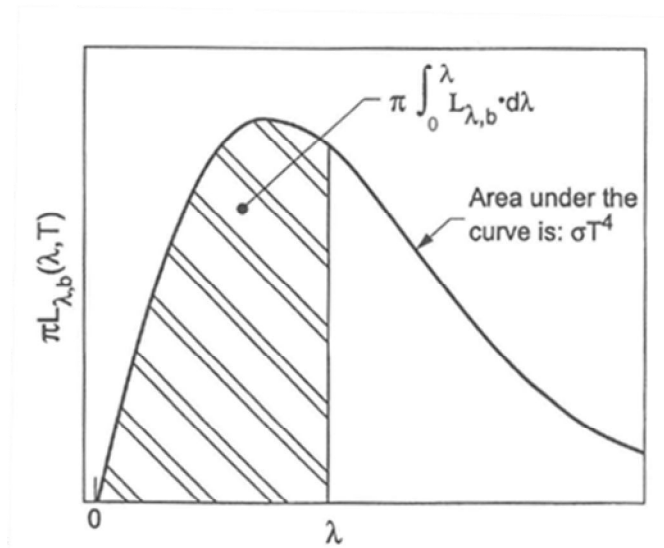


Figure 3.9 Fraction of the blackbody emission in the wavelength band (0 to λ) (Maldague, 2001)

3.1.7 Reflection, Absorption and Transmission

In real world, perfect blackbody does not exist and the above laws are not applied to normal objects, unless certain corrections are made.

Non-blackbodies absorb only a fraction ϕ_A of incident radiation ϕ_i , reflect a fraction ϕ_R , and transmit a fraction ϕ_T (Figure 3.10). In general cases, these absorbed, reflected, transmitted fractions of the incident flux depend on wavelength, orientation, and temperature, and also on the surface quality. Whereas the reflected flux does not affect the object, the absorbed flux increases the internal thermal energy, the medium temperature: according to the energy conservation law, every energy exchange is mutually compensated. When this kind of system is in a state of thermodynamic

equilibrium, the energy released into the ambient medium, as radiation plus reflected and transmitted energy, must be equal to the energy introduced into the system by absorption.

It is, thus, necessary to introduce the spectral emissivity $\varepsilon(\lambda)$, which is to balance absorptance $\phi_A(\lambda)$, where

$$\phi_A(\lambda) = \varepsilon(\lambda) \quad \text{Eq 3.20}$$

and

$$\varepsilon(\lambda) + \phi_R(\lambda) + \phi_T(\lambda) = 1 \quad \text{Eq 3.21}$$

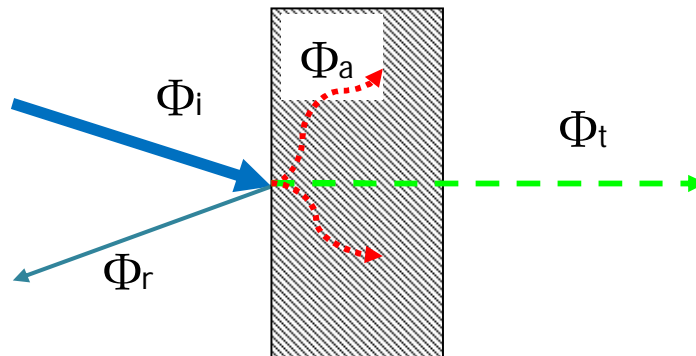


Figure 3.10 The incident flux is divided into reflected flux, absorbed flux and transmitted flux

For an opaque medium, $\phi_T(\lambda) = 0$, and reflection and absorption are surface phenomena; for perfect mirrors, $\varepsilon(\lambda)$ and $\phi_T(\lambda)$ are equal to zero; for a blackbody, every incident flux is absorbed and $\varepsilon(\lambda) = 1$ and $\phi_R(\lambda) = 0$, $\phi_T(\lambda) = 0$.

In some situations, such as for isotropically diffuse emitter surfaces (i.e. Lambertian reflectors), the *reflected radiance* is uniform within the hemispherical space above the surface, being independent of the reflected direction.

The following coefficients are introduced: absorbance coefficient α , reflectance coefficient ρ , and the transmission coefficient τ . They are defined as ratios:

$$\alpha = \frac{d\Phi_a}{d\Phi_i} \quad \text{Eq 3.22}$$

$$\rho = \frac{d\Phi_r}{d\Phi_i} \quad \text{Eq 3.23}$$

$$\tau = \frac{d\Phi_t}{d\Phi_i} \quad \text{Eq 3.24}$$

Absorbance, reflectance, and transmittance are linked together, considering the flux exchange on a semitransparent object:

$$\rho + \alpha + \tau = 1 \quad \text{Eq 3.25}$$

For an opaque object, transmission does not occur:

$$\rho + \alpha = 1 \quad \text{Eq 3.26}$$

3.1.8 Emissivity

In the case of real surfaces, the blackbody emission is corrected by a value of emissivity, namely ε . Emissivity is the ability of a surface to emit energy: for this reason, it is expressed as the ratio of the radiation emitted by a surface to the radiation emitted by the blackbody and it is a unit-less quantity ranging between 0 and 1.

Emissivity is not a constant and depends on the wavelength, on the direction of observation relative to the radiating surface, and on the temperature of the surface. Moreover, the emissivity of a surface in the visible range often bears no relation to its infrared emissivity¹.

The spectral-directional emissivity of a surface at a temperature T emitting at a wavelength λ in the direction (ϑ', ϕ') is defined as:

$$\varepsilon(\lambda, T, \vartheta', \phi') = \frac{L'_{\lambda}(\lambda, T, \vartheta', \phi')}{L_{\lambda,b}(\lambda, T)} \quad \text{Eq 3.27}$$

There are many methods to determine emissivity right value. A first experimental approach consists of sticking on the object's surface a piece of material of accurately known emissivity and good thermal conductivity (or paint part of it using a special coating having the same features). Then, it is necessary to heat up the object to a

¹ For example, snow has a very low emissivity in the visible portion of the spectrum, whereas it has blackbodies like proprieties in the infrared. This characteristic allows a fairly snow return to the liquid state, even under exposure to sunlight. In fact, most of the visible solar radiation is diffused and reflected; the higher infrared emissivity allows the re-emission of absorbed infrared energy (Gaussorgues, 1994).

temperature of at least 50°C higher than the ambient temperature and then set up the camera spot point on the part of the object with the sticker (or previously painted). Since the emissivity in this part is well known, it is possible to set up its value on the camera together with the values of atmospheric temperature, ambient temperature, camera-to-object distance, and atmospheric humidity. After that, it is possible to read the spot point temperature of the area where emissivity is known and move the spot point outside that area. Finally, since the two read temperatures (emissivity known temperature and emissivity unknown temperature) should be the same, it is possible to change emissivity value in the camera setting until the read temperature is the same as for the “clean” area of unknown emissivity (Minkina and Dudzik, 2009).

Material	Temperature	Emissivity
Rubber	24 °C	0.86
Wood	20 °C	0.90
Paper	20 °C	0.93
Gold	100 °C	0.02
Shiny Aluminum	20 °C	0.04
Common Paint	20 °C	0.90

Table 3.1 Emissivity values for different materials

A variant of this method consists of determining the object temperature through a contact probe. Then, the emissivity parameter in the camera should be tuned until the same reading of temperature is obtained (Minkina and Dudzik, 2009).

In practical cases, it is not always necessary to define all dependencies and some common situation can occur. In IR thermography temperature measures require knowledge of emissivity values: tabulated values are commonly provided for normal incidence and for a given temperature range. Table 3.1 lists emissivity values for various surfaces and temperatures.

The *Kirchhoff's Law* provides a link between the absorption and emission processes and, thus, between emissivity and absorbance, since:

$$\varepsilon(\lambda, \vartheta', \varphi') = \alpha(\lambda, \vartheta, \varphi) \quad \text{Eq 3.28}$$

This is demonstrated by considering a blackbody composed by a closed and opaque cavity and a small object within it. At thermal equilibrium, all involved fluxes are compensated since temperatures are equal, and, in particular, the absorbed flux is equal to the emitted one.

A dissipative body is a body whose emissivity is independent of angle of observation ϑ : it is called *Lambertian surface*, since it satisfied the condition of Lambertian Law.

3.2 Thermographic inspection

Infrared thermography is a widely used tools for NDT (nondestructive testing), thanks to its properties: it is a noncontact technique with a wide area detection of subsurface defects, and can be used to complement the other common inspection technologies.

On one hand, there are key points in Infrared thermography assessment such as the fast inspection rate, the non-contact needed with the studying object, the provided results relatively easy to interpret, and the wide application range. On the other hand, some difficulties may occur during an IR examination: the first occurring thing is due to the fact that it is difficult to obtain quick thermal stimulation which is uniform on a wide area, apart from the fact that a thermal stimulation induces to other thermal effects (convective and radiative thermal losses) that can lead to misunderstandings. Other criticalities are related to the limited thickness that the instrument is able to inspect, and the emissivity troubles (Maldague, 2002).

3.2.1 Thermography techniques

3.2.1.1 Active and Passive Thermography

There are two main approaches in a thermographic inspection. These approaches are *passive* and *active*: in the first approach, structures and materials are tested at their

natural temperature differences, and in the second approach, relevant thermal contrasts are induced by an external stimulus.

Within the active approach domain, many different techniques have been developed, like Pulse Thermography (PT), Step Heating (SH), Lock-in Thermography (LT) and Vibro-Thermography (VT).

3.2.1.1.1 Pulsed Thermography PT

Pulsed thermography is a technique which consists of briefly heating, with a pulse source, the specimen and then recording its temperature decay curve. The heating energy propagates by diffusion under the surface and the presence of a subsurface defect appears as an area of higher temperature with respect to the surrounding areas. Such phenomenon occurs in different ways, depending on defect deepness: deeper defects are observed later and with a reduced thermal contrast. In particular, the observation delay time t is a function of the square of the subsurface defect depth z :

$$t \sim z^2/\alpha \quad \text{Eq 3.29}$$

α is the material thermal diffusivity. This equation also indicates that the radius of the smallest detectable defect should be, at least, one to two times larger than its depth under the surface (Maldague, 2002).

PT is one of the most used thermal stimulation methods, thanks to its inspection quickness (from a few ms, for high thermal conductivity specimens, to a few seconds for low thermal conductivity materials). The shortness of the heating phase has also the advantage of preventing damages to the component, with respect to longer heating time.

Different configurations are possible: point inspection (in which the heating source is a laser or a focused light beam), line inspection (in which the heating source is a line lamp or a scanning laser), and surface inspection (in which the heating source is a lamp or a flash lamp and there is a complete analysis of the phenomenon, even in case of non-uniformity of the heating source).

Moreover, two different approaches are used: reflection and transmission. In reflected cases, the thermal source and the detector are located on the same side of the inspected component, whereas, in transmitted cases, they are located one on each side of the component. Generally, the reflection approach is used for detection of defects located close to the heated surface, and the transmission approach is used for detection of defects close to the rear surface.

3.2.1.1.2 Lock-in Thermography

In Lock-in thermography, a periodic thermal stimulation is submitted to the case study, and the generated thermal waves are detected and recorded. Lock-in terminology refers to the necessity to monitor the exact time dependence between the reference input

signal and the output signal. The resulting oscillating temperature field (which follows the oscillating thermal stimulus), in the stationary regime, is remotely recoded through its thermal IR emission, with the aim to observe its amplitude and phase.

Resulting IR images are different from thermographic ones: both phase and amplitude images are available. The first ones are related to the propagation time, whereas amplitude images are related to the thermal diffusivity. The depth range of amplitude images is roughly given by thermal diffusion length μ :

$$\mu = \sqrt{2k/\omega\rho c} \quad \text{Eq 3.30}$$

where k is the thermal conductivity, ρ is the mass density, c is the specific heat and ω is the modulation frequency. Eq 3.30 means that a low modulation frequency will probe deeper (Maldague, 2002).

3.2.1.1.3 Pulsed Phase Thermography PPT

In some way, this process combines advantages of both pulse thermography and LT. In fact, a specimen is pulse-heated, as in PT, and the mix of frequencies of the thermal waves are unscrambled by performing the Fourier transform of the temperature decay, on a pixel by pixel basis, thus enabling computation phase images, as in LT.

These are the steps that follow: for each pixel (i, j) , the temporary decay $f(x)$ is extracted from the image sequence, and then the discrete Fourier transform $F(u)$ is

computed (where u is the frequency variable). Finally, the phase is computed from the real $R(u)$ and imaginary $I(u)$ components of $F(u)$. The main difference is that in PPT the analysis is performed during the transient and not during the stationary mode, as it happens in LT.

3.2.1.1.4 Step Heating SH

In this process, the increase of surface temperature is monitored during the application of a long heating pulse at low power. Temperature-time relations are connected to specimen feature and defects. Different information is possible to be analyzed, such as: the temperature line scan at a specific time after heating, the collection of temperature line scans as function of time, and the reconstructed image at a specific time.

This technique is often applied to evaluate composite structures or to evaluate coating thickness.

3.2.1.1.5 Vibrothermography VT

In vibrothermography, a conversion from mechanical to thermal energy occurs: under the effect of mechanical vibrations, induced externally to the structure at a few fixed frequencies, heat is released by friction precisely at defect location. If there is a

change in the mechanical excitation frequency, the local thermal gradients may change accordingly.

VT allows the detection of flaws hardly visible by other IR thermography techniques and the inspection of large structural areas. On the other hand, the required mechanical loading may be difficult to achieve (Maldague, 2002).

3.2.2 Thermography instruments

Many IR imagers are *radiometers* that, in such cases, are able to measure temperature values; on the contrary, a *non-radiometric* tool is used when a quantitative measurement of temperature is not required, but a qualitative image is necessary to be displayed. Non-radiometric imagers are used, for example, for night vision and surveillance applications.

Infrared thermographic systems are composed, at a minimum, by a detector and an image formation component. More complete instruments also integrate an image processing tool and a display system.

Many factors are involved in the choice of the IR detection system (like the temperature of the specimen and the amount of available money): one important aspect consists of the selection of the operating wavelength band (Maldague, 2002). Commonly, the useful portion of the IR spectrum ranges from 0.8 to 20 μm and some criteria in band selection are: operating distances, indoor-outdoor operations, and body's temperature

and emissivity. As Planck's law highlights, high temperature bodies emit most of their radiation in the short wavelengths, therefore, objects at ambient temperature (300 K) peaks in the long wavelengths range. Low wavelengths are preferred for outdoor operations.

The two basic IR devices are focal plane arrays (FPA) and scanners.

The most common infrared camera has a *Focal Plane Array (FPA)*: in this technological tool, each pixel which makes up an IR image is measured with an individual detector. Detectors are arranged in a flat, two-dimensional array, which is placed in the focal plane of the optical system of the imager (Figure 3.11).

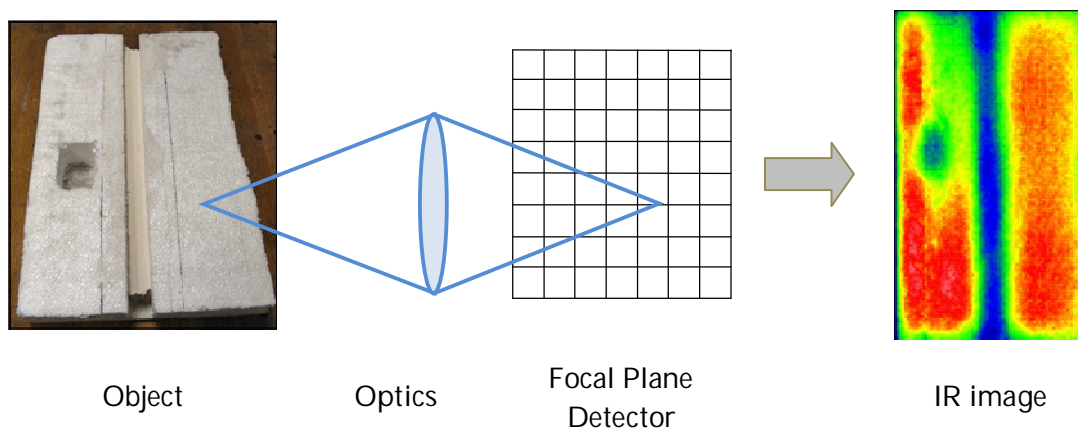


Figure 3.11 Focal Plane Array Detectors configuration

FPA are based on two different detector types: *Photon Absorbers* and *Photon Detectors*. Micro-bolometer belongs to the first type: the absorber is made of a passive energy absorbing material that is warmed by the IR radiation. The increased temperature is proportional to the surface radiosity. The detector temperature is then

determined by measuring a temperature dependent material property such as electrical resistance. The pixels are typically 30 by 30 μm and are micro-machined in monolithic wafers that also incorporate signal acquisition and processing. On the contrary, photon detectors are active elements: a photon striking the detector triggers a free charge, which is collected and amplified by an electronic circuit. Detectors and read-out circuits are constructed on different substrates and are electrically connected into a hybrid assembly by Indium bump bonding. A variety of detector materials are used today, each with a specific spectral range and specialized application. Common detectors are summarized in Table 3.2.

Detector Material	Wavelength [μm]	FPA Size	Sensing	Operability	Cooling
InGaAs	0.9-1.6	320 x 240	Detection	> 99%	Uncooled
InSb	3.0 – 5.0	1024 x 1024	Detection	> 99%	Cooled 70K
QWIP (GaAs/AlGaAs)	8.0 – 9.0	512 x 512	Detection	> 99%	Cooled <70K
Microbolometer	7.5-13.5	(limited by optics)	320 x 240	Absorption	Typical of
Si process	Uncooled	HgCdTe	1.0 – 20.0	(Limited by optics)	1024x1024

Table 3.2 Focal Plane Arrays Devices

In a *scanning imaging system*, one or more detectors are combined with a single or multiple-axis mirror system: images are thus acquired combining individual measurements (Figure 3.12). Single point measurement is combined into a line; many lines then compose the final image. These systems have the main advantage of being

able to acquire image arrays of any size, but the main limitation is that the frame rates are relatively low, if compared to FPAs.

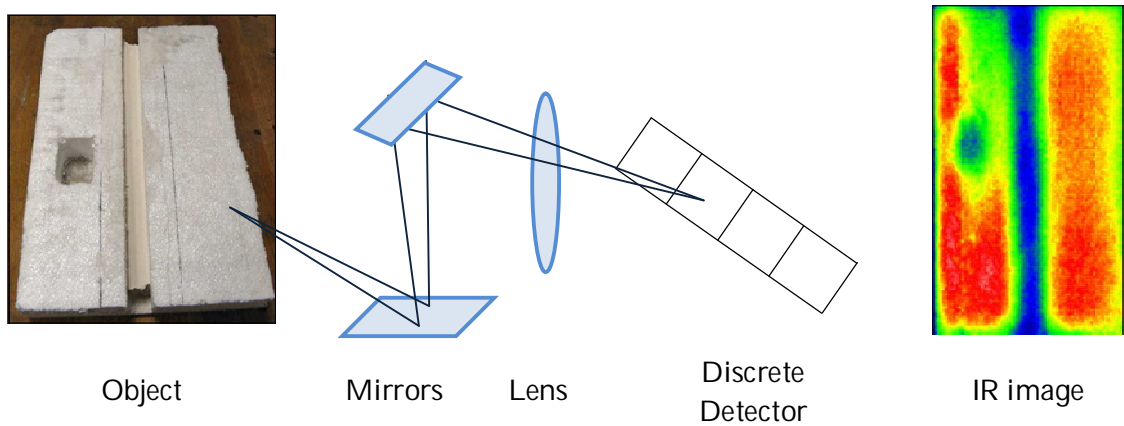


Figure 3.12 Scanning System Configuration

3.3 Thermography measurements

Bodies' thermal radiation is a theory strictly related to temperature measurements by infrared camera. Many different heat fluxes are to be taken into account:

- the flux emitted by the investigating object φ_{ob}
- the flux emitted by the environment and reflected by the investigating object φ_{refl}
- the flux emitted by the atmosphere φ_{atm}

- the flux emitted by camera optical components and filters (in many mathematical models, its influence is considered negligible on the measure)

These fluxes are expressed as follows (Minkina, 2009):

$$\varphi_{ob} = \varepsilon_{ob}(T_{ob}) TT_{atm}(T_{atm}) M_{ob}(T_{ob}) \quad \text{Eq 3.31}$$

where ε_{ob} is object surface emissivity; M_{ob} is object's radiant exitance (Wm^{-2}); TT_{atm} is the band transmittance of the atmosphere; T_{atm} and T_{ob} are atmosphere's and object's temperature, respectively (K).

$$\varphi_{refl} = [1 - \varepsilon_{ob}(T_a)] \varepsilon_a(T_a) TT_{atm}(T_{atm}) M_a(T_a) \quad \text{Eq 3.32}$$

where ε_a is ambient surface emissivity; M_a is ambient radiant exitance (Wm^{-2}); T_a is ambient temperature (K).

$$\varphi_{atm} = [1 - P_{atm}(T_{atm})] M_{atm}(T_{atm}) \quad \text{Eq 3.33}$$

where M_{atm} is atmosphere radiant exitance (Wm^{-2}); T_{amb} is ambient temperature (K). Figure 3.13 shows a diagram illustrating environment – object interactions in temperature measurements.

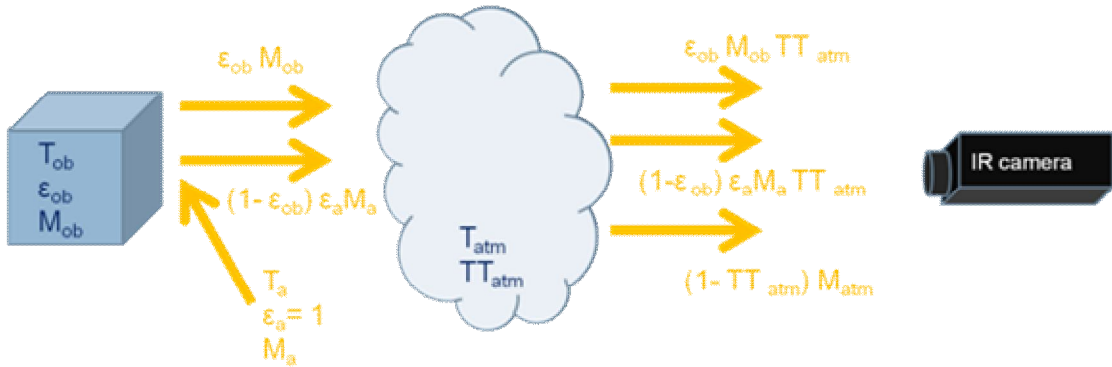


Figure 3.13 Schematic depiction of an Infrared measure of related to an object (2) through an infrared camera (4). 3 is the atmosphere and 1 in is the surrounding environment

The camera output signal s can be described as (Minkina, 2009):

$$s \approx C (\varphi_{ob} + \varphi_{refl} + \varphi_{atm}) \quad \text{Eq 3.34}$$

where C is a parameter depending on atmospheric damping, camera's optical components, and detector's proprieties (Minkina, 2009).

3.3.1 Measuring uncertainties

Uncertainties are key notes in every measuring system and inherent to the assessment of measure accuracy. For this reason, it is important to evaluate error's causes in order to reduce misunderstandings and data evaluations. In general, the absolute error of measurement is the difference between the real and the measured temperature values: depending on their nature, errors can be thus divided between

systematic errors and random ones. In particular, systematic errors can be grouped in errors of methods, calibration mistakes, and electronic path deficiencies.

In practical operative conditions, methodology errors occur in case of incorrect and roughly evaluation of information provided as input to thermo camera, such as object emissivity, environment relative humidity, and environment temperature.

Other inaccuracy on measuring values are related to the influence of the ambient radiation (direct or reflected from the object) arriving at the camera detector, detector noise, object's shape influence (in particular, shape effects will be deeper analyzed in the following chapter), and incorrect evaluation of atmospheric transmission and radiance (Minkina, 2009).

The atmosphere between the source of radiation and the detector is usually caused by measurement perturbations. This effect is due to many causes: first of all, the emitted infrared energy is attenuated by the atmosphere, whereas temperature gradient and turbulence create inhomogeneities in the air refractive index, all of which tend to degrade image quality. Finally, the atmosphere is itself a source of radiation; in particular, this effect is mainly due by two phenomena: the self-absorption by the atmospheric gases, and the absorption due to scattering by particles in the air, by molecules and by aerosols (Gaussorgues, 1994). As regards the first effect, the problem of the energy attenuation introduces a systematic error that depends on the working wavelength, the spectral band used, the distance and weather conditions.

3.4 Applications

Infrared Thermography origins come from the early 1800s, when the English physicist William Herschel found out a thermal radiation outside the deep red in the visible spectrum: this invisible light was later called *infrared*. During next years, thanks to many other scientists' studies, infrared thermography has become a useful technique to mapping object's surface temperatures (Meola C., Carlomagno G. M., 2004).

The *military* field was the first to develop infrared imaging systems and to use them since the Second World War. New applications have been developed during the ages, with technology advances, and thermography is currently used in many different fields, from medicine for diagnosis and treatment planning to agricultural applications, for example to detect ice propagation into cultures, with the aim to develop new frost protection technologies. Other applications involve environment (IR thermography can be used to monitor pollution propagation), building surveys, and cultural heritage. Most IR applications concerns industrial purposes, related to maintenance, non-destructive evaluations, technological fields and thermo-fluid dynamics (Meola C., Carlomagno G. M., 2004), which use of such technologies can help to improve products design and fabrication.

In practice, observations of surface effects due to the propagation of heat in the material can be used to obtain information about the internal structure of the medium. Generally observations must be made during the transient regime, because they rely on

the relative heat transfer rates within the material. Radiation contrasts become undetectable as soon as the temperature equilibrium is reached (Gaussorgues, 1994). This method reveals very useful in non-destructive testing, as it is possible to detect inhomogeneities in thermal pulse propagation due to discontinuities in the structure of the component under examination.

3.4.1 Thermography in industrial processes

Since infrared thermography provides a real-time temperature mapping, it is an essential tool for observation, testing and control of industrial processes. Many applications can be counted in many different fields: product quality is often very dependent on the precision of thermal parameter control in the manufacturing process; the detection of air bubbles in float glass manufacturing process is an example. Moreover, infrared thermography is the only thermal test to detect rapidly moving objects: for example, in the nuclear industry, the temperature of encapsulation of radioactive waste is monitored by infrared imaging of the flow of molten bitumen.

The testing of a process by infrared thermography can be performed either by a passive or an active method.

3.4.1.1 Active Pulsed thermography

In pulsed thermography, the work piece being inspected is submitted to a thermal pulse and the subsequent temporal temperature response refers to the subsurface flaws, and the optimal time of observation is proportional to the square of the depth for the defect considered.

Pulsed thermography with **external stimulation** is used for material properties studies, by means of lamps, thermal radiators, lasers or air/water jets. Some examples refer to graphite-epoxy composites and aluminum bonded laminates: this choice is due to that fact that these two materials have opposite thermal behaviors and properties (Maldague, 2001).

TNDT techniques applied to *composite material* allow to evaluate impact damages: in aerospace industry, the service life of a graphite-epoxy component can be reduced drastically as a result of impact damage, such as bird strike, introducing fiber breakages or delaminations. In such cases, TNDT is well suited for damage detection in composite structures, since it is well suited to detect delaminations and can be deployed directly on-site, requiring only an external access (Maldague, 2001).

Thermal methods are also used to characterize industrial materials: a typical problem consist of evaluating the fiber-resin ratio in a graphite-epoxy piece. Inappropriate temperature, pressure, or assembly conditions can cause epoxy resin evacuation: if this happens composite mechanical properties will be completely different

from the designed ones. **Errore. L'origine riferimento non è stata trovata.** shows a common configuration: since the material has an oriented structure with anisotropic properties, an elliptical pattern can be observed. The ratio between the two ellipse axes is related to the fiber orientation (Maldague 1993).

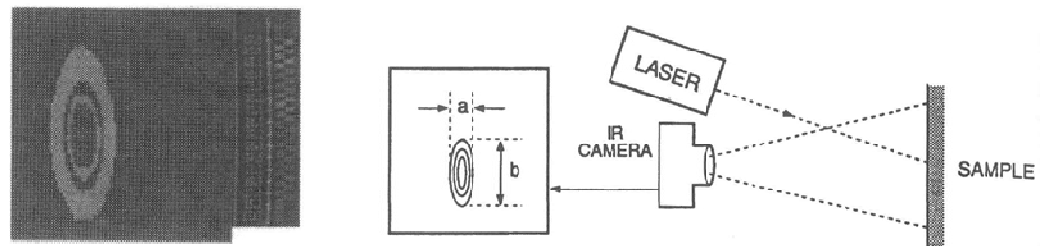


Figure 3.14 Thermal analysis of fiber orientation in composite materials and elliptical thermal obtained pattern (Maldague 1993)

Thermography in *aluminum industry* is considered as an important alternative to NDE technique. Bonded laminates, for example, are particularly investigated: aluminum-aluminum and aluminum-foam are increasingly used in many industrial fields (such as transports). Since unpainted aluminum has a low emissivity ($\epsilon \sim 0.05$), thermal inspection is possible only if high-emissivity is applied to the object surface: static and mobile configurations are then studied, in order to detect defects (Maldague, 2001).

In Ghosh 2011, pulsed thermography is applied for quantitative non-destructive evaluation in Fiber Reinforced Polymer strengthened bridges. The use of externally-bonded Fiber Reinforced Polymer composites is an efficient method for the strengthening of deficient concrete components in civil infrastructures. By this

consideration, monitoring and inspection are essential subjects to ensure public safety. A test program was performed with a cycling load applied on an examination specimen.

Pulsed thermography is used in many quality control applications, in order to evaluate product conformity to the standards. In this context, an interesting application refers on the use of pulsed thermography for space launch vehicles inspection (Burleigh, 1994). Components of *space vehicles and aircraft* are generally inspected completely, in all their parts, for safety reasons. Ultrasonic x-ray and “coin tapping” (a defect altering the noise frequency) are common NDT techniques used on these applications, along with the use of thermography that is now increasing. In Atlas space launch vehicles, for examples, the thrust structure at the aft end is a composite sandwich comprised of aluminum honeycomb core, with fiberglass sheets. TNDT were used to test on these parts during manufacture, assembly and on the launch pad at Cape Canaveral, providing improvements in inspection time and costs (Burleigh, 1994).

In all these applications, the thermal contrasts obtained over defective areas are generally small (few degrees), whereas the thermal stimulation of the inspected surface causes an increase in temperature of up to 10°C: this aspect is related to the difficulty to obtain a wide surface including high energy deposit with uniform distribution.

In some other applications, the structure itself can provide thermal stimulation originated from its interior: in such cases, the thermal perturbation consists of changing the temperature of a circulating fluid. Some examples include the evaluation of a

corrosion damages in pipes, due to the flow corrosive liquids, or the analysis of internal structure of jet turbine blades. In the case of pipes corrosion evaluation, the aim is to detect cavitation damages in pipes before catastrophic failure occurs without any defected components replacement (Figure 3.15).

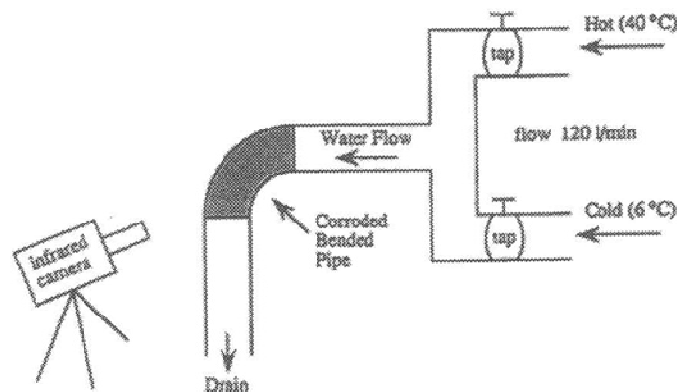


Figure 3.15 A corroded bent pipe is inspected through a thermal-camera in order to detect the presence of defects: experimental set up (Maldague, 2001)

The assessment of jet turbines blades is another possible application for the inspection of inner surface with internal perturbations, through a gas or liquid rig as thermal stimulation (Figure 3.16). The failure of one blade can lead to dramatic consequences, considering blade's high rotation speed during operations. To prevent these types of incidents occurring, blade temperature can be continuously monitored in order to detect earlier sudden abnormal blade temperature rise, before any potential failure. According to the basic principles for blades inspection through thermography, it can be considered that the flow circulation of a fluid, at various temperatures in transient thermal regime, allow to detect blocked passages through delayed arrival of

the thermal front. Supported by these considerations, if thickness of a blade's portion is unexpectedly increased, any thermal disturbance will reach the outer surface of this portion after a time period longer than that required (Maldague 1993).

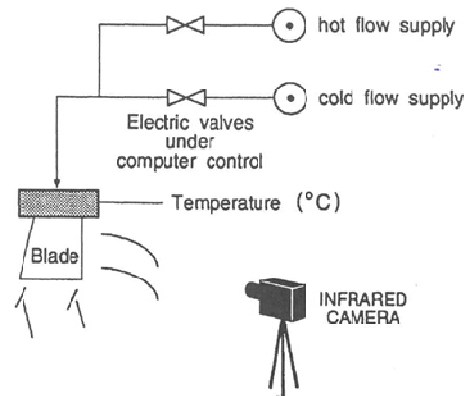


Figure 3.16 Experimental apparatus for thermographic inspection on turbine blades using internal stimulation: experimental set up (Maldague, 2001)

3.4.1.2 Lock-in and pulsed phase thermography

Lock-in thermography responds selectively to induced temperature oscillations and to their local delay time. Supported by these considerations, this method is well suited to investigate situations in which dynamic heat transport may be affected by inhomogeneities in material structure and subsurface.

In many applications, wood is employed as an external layer with cheaper material insight. In these cases, it is important to assert proper bonding between the core and the wood skin, for both esthetical and structural reasons. Lock-in thermography thus offers interesting results, whereas ultrasonic and x-ray do not. Many tests

demonstrated the capability to detect subsurface structure up to 2 mm in depth and as small as 4 mm in diameter.

In case of pulse phase thermography, a long thermal pulse of 20 to 30 s is used with low-frequency content, suitable to detect deeper artifacts. In Figure 3.17, it is possible to see an example of wood inspection using both lock-in and pulsed phase thermography.

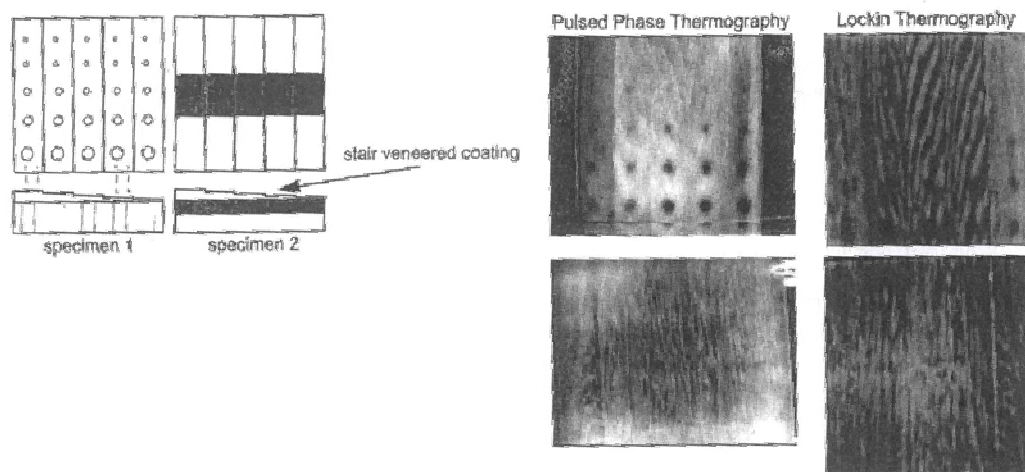


Figure 3.17 Sample geometries inspection through PPT and LT: stair veneered coating of variable thickness (Maldague, 2001)

Lock-in thermography can also be employed to determine defect detections and fatigue cracks (Izumi, 2010). For example, in Wu 1998, phase sensitive modulation thermography is combined with modulated ultrasound: in ultrasonic testing the defect detection is performed “selectively” without considering the intact structures around the defects, whereas in lock-in thermography, through optical excitation, the defect detection is performed considering all the other structural features.

3.4.1.3 Passive thermography

An important field of inspection by TNDT is of considerable importance in the **construction industry** application. Many research studies are focused on the detection of thermal losses and building's thermal insulation improvement, in order to save energy. The detection of trapped moisture in walls and roofs, the localization of buildings insulation defaults, the estimation of heat losses, and the historical building refurbishment are some of the problems commonly encountered in thermography practice.

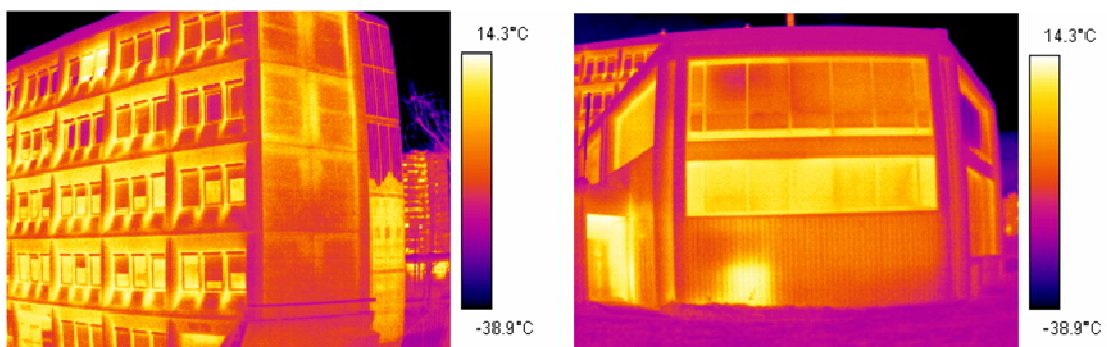


Figure 3.18 Some examples of passive infrared thermography applied to buildings insulation defaults (Candoré, 2008)

Buildings' thermal diagnosis is evaluated also through active thermography: in Candoré 2008 is presented a study on the definition of a method for insulation defects detection by stimulated IR thermography (Figure 3.18).

Green buildings and sustainable constructions have a wide interest in actual research: Kolokotsa et al. 2012 presents an analysis of mineral based coatings as a passive solar technique that contributes to buildings' energy efficiency. The thermal

performances of a series of mineral based samples are tested by infrared thermography (Figure 3.19): different samplers are exposed to the external environmental conditions and, through IR images analysis, a quantitative result on the energy efficiency is provided.

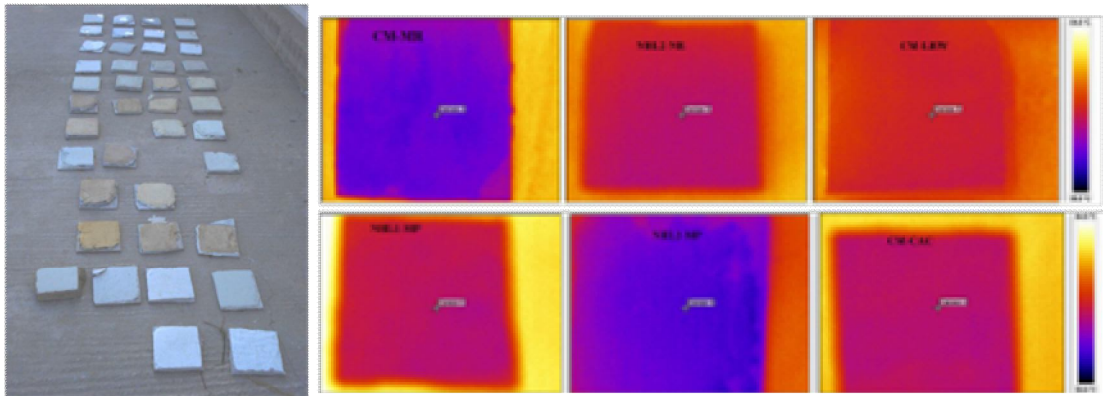


Figure 3.19 Analysis of mineral based coating for buildings: experimental set up and thermal images acquired for different samples (Kolokotsa, 2012)

The temperature distribution on surface buildings by thermography is one of the most useful applications: in Hoyano 1999, measurements on two different external surface buildings are presented with the aim of defining their heat characteristics by time-sequential thermography. Other interesting examples are in Sham 2012: a technique for continuous surface temperature monitoring is applied to investigate the nocturnal sensible heat release characteristics by buildings (Figure 3.20).

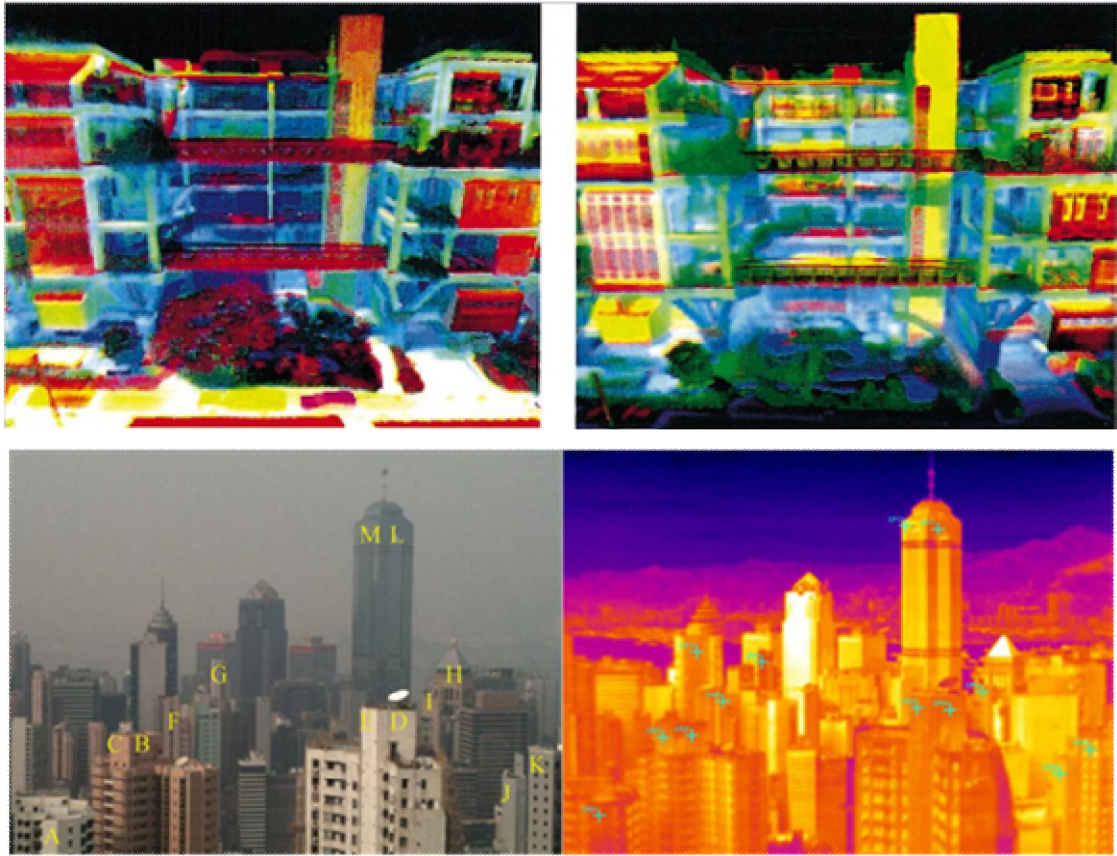
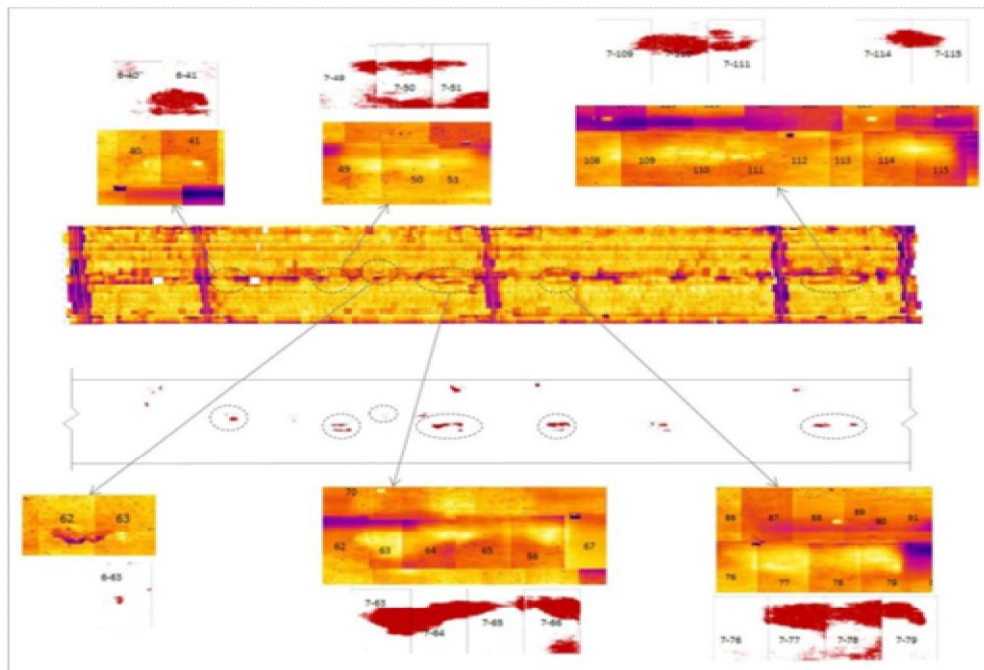


Figure 3.20 Some examples of thermography inspection on buildings surface: on the top the heat flux of the same building is presented (Hoyano, 1999) in summer (on the left) and in winter time (on the right). In the bottom part, a continuous surface monitoring is performed and the visible and infrared images are proposed (Sham, 2012)

Other applications for TNDT are related to roads and bridges: in these cases, detection of delaminations and breakdown of cement matrix are possible, due to differences in thermal conductivities (Figure 3.21). In this context, a case study regards the structural health monitoring of bridge infrastructures by the development of a bridge condition decision support system to compare up-to-date bridge condition metrics from multi data inputs (Endsley, 2012).



Predictive maintenance for electrical utilities is one of the most known application fields for passive thermography. In this context, an automated diagnosis system is developed in Chou 2009: experiments are performed on capacitors, transformers, and other power transmission equipment (Figure 3.22).

An interesting case study (Botsaris, 2010) applies thermography as an estimator of photovoltaic module performances, in which a fast and accurate *in situ* temperature monitoring is really important. A comparison between the thermographically measured operating temperatures with the expected ones has been performed (Figure 3.23).

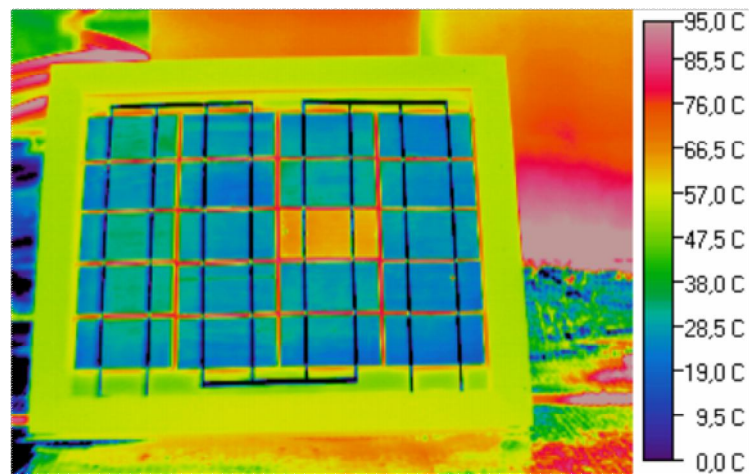


Figure 3.23 Thermal image of an inspected photovoltaic panel module: the central cell presents an unexpected behavior (Botsaris, 2010)

3.4.2 Medical Imaging

High body temperature has always been considered as proof of illness. Body temperature range between 36.6 and 37.5°C could be considered as normal, but if it range beyond that values, it could be considered as indicator of possible illness. As human body and skin produce infrared radiation naturally, since the 1960s infrared thermography has been considered as a diagnostic method in medical sciences (Lahiri, 2012). Supported by these considerations, IRT has been extensively used in many

different medical fields, like diabetic neuropathy, vascular disorder, breast cancer detection, thermoregulation study, fever screening, muscular or rheumatologic pain, and so on. An early diagnosis is possible from infrared images, since thermal patterns are easily recognizable and thermographic findings are generally easy to interpret in comparison with other clinical findings for potential associations.

In human infrared thermography, some procedural notes should be pointed out: the temperature and humidity of the experiment-room is kept within comfortable limits, and the patient is kept in a comfortable environment, so that the mild thermal stress produces results in vasoconstriction aided cooling of skin. Moreover, the patient should be protected from exposure to direct sunlight until a “thermal acclimation time” is needed to achieve thermal equilibrium (Lahiri, 2012).

Thermoregulation is a monitoring process in which heat is transferred from the core to the skin by blood passing through peripheral blood vessels, losing body heat faster. Thermography is a useful monitoring tool for thermoregulation process. As an example, in the majority of healthy people, temperature of hands, feet, and face increases after immobilization. This aspect is due to blood redistribution, which causes skin temperature to rise after immobilization and relaxation. An example of thermoregulation is presented in Lahiri, 2012, in which the local heating in ear-skull region has been monitored through IRT while talking with hand-held mobile phones: they observed temperature increasing with higher specific absorption rate mobile

phone. Figure 3.24 shows a facial thermal image after 1 minute and 15 minutes talking: temperature increases up to 4.59°C (Figure 3.24).

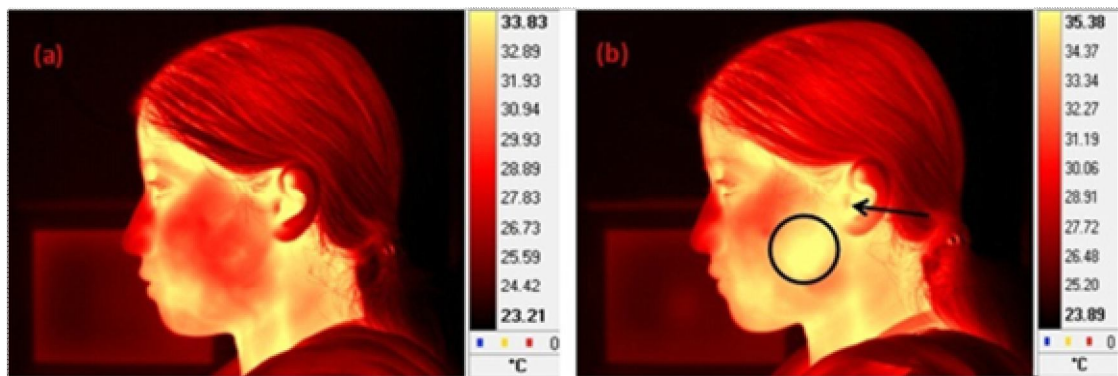


Figure 3.24 Thermal images of a subject talking on a hand-held mobile phone after 1 minute (on the left) and after 15 minutes (on the right) of talking (Lahiri, 2012)

Breast cancer is one of the most common cancers for women and early detection is a key factor for successful treatment and survival chances. In this context, infrared thermography is considered as an adjunctive diagnostic tool, since it provides additional and functional information under thermal and vascular tissues condition: tumors, generally, have an increased metabolic rate and blood supply leading to localized high temperature spots over such areas (Lahiri, 2012).

IRT is also a support tool in **diabetic neuropathy** and **vascular disorder** diagnosis. The major part of diabetic patients is affected by foot complications, due to blood supply (vascular disorder) and loss of sensation (neuropathy): they both cause changes in skin surface temperature which are detectable by thermography. Many studies found relationship between diabetic patients and abnormal temperatures

patterns of feet and hands: in particular, diabetes at-risk patients have significantly higher mean foot temperature (mean value of 30.2°C) compared to the normal patients (mean value of 26.8°C). A diabetic patient is also affected by vascular disorder (Figure 3.25): feet distal portions are at a lower temperature due to slow blood circulation and varicosity induced inadequate venous drainage (Lahiri, 2012).

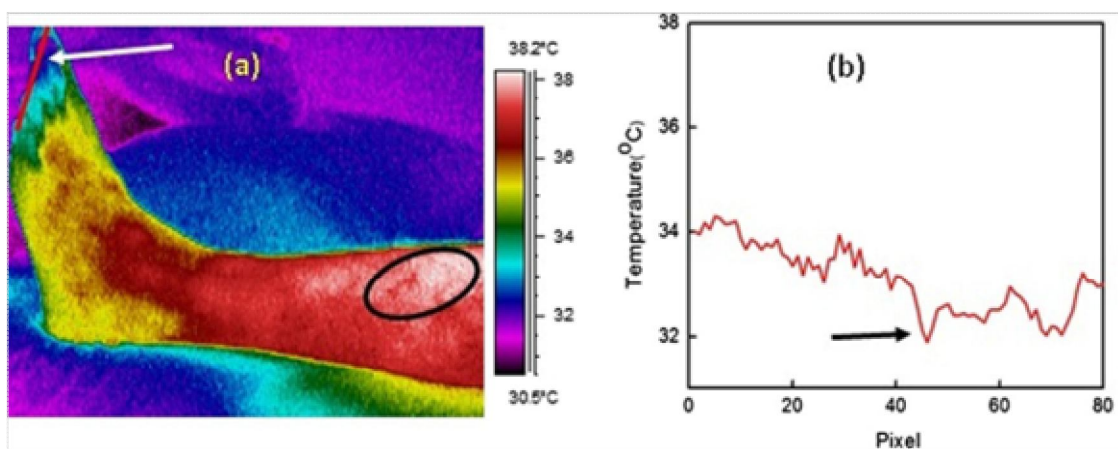


Figure 3.25 Thermal image of left lower limb of a 28 years old male diabetic patient suffering from vascular disorder (a). (b) Temperature profile along the red line indicated shown in (a). An arrow indicate shows the lowest temperature (Lahiri, 2012)

Many studies on infrared thermography medical applications evaluate its effectiveness for **mass screening of fever**, recording IR images of neck and facial region. In fact, it was recently used successfully for mass screening of fever in patients contracted SARS, a highly infectious disease caused by corona virus. In this context, mass screening was the main program to be conducted for the detection of potential SARS infected persons to prevent the spread of this disease (Lahiri, 2012). The SARS case

is an example of how IRT can be a powerful tool for initial mass screening of people during public health crisis.

Many other useful IRT applications in medical field can be signed: dental diagnosis, dermatological applications, blood pressure monitoring, rheumatic disease diagnosis and eye syndrome and ocular diseases (Tan, 2009).

3.4.3 Architectural and cultural heritage

Cultural heritage conservation processes require continuous monitoring, in order to detect defects' conditions at an incipient stage, so that any restoration treatments can be easily and efficiently planned. In such cases, thermography plays an important role in order to identify degradation causes and to define cause-effect relations.

The exposure to adverse environmental conditions, thermal and mechanical stress, temperature and humidity excursions (which can cause material expansions and contractions with no control) are some of the artworks main degradation causes. In particular, some materials, such as wood or parchment, are significantly affected by thermo-hygrometric variations; others can be easily affected by corrosion, crack propagation or consistency loss. Frescos, mosaics, and paintings have some common degradation causes, such as pollution and vapor absorption.

Some interesting case studies are presented in Bodnar 2012, in which stimulated infrared thermography is used as a support tool for mural paintings' restoring. At the

abbey church of “Saint Savin sur Gartempe”, which is a UNESCO world heritage site, the nave’s continuous barrel vault is completely covered with mural paintings, which have been recently restored. During restoration works, the zone surrounding the back wheel of the painted wagon was studied through stimulated infrared thermography analysis (Figure 3.26) and some gradual detachments were observed. Moreover, in the same work, salt damages were detected by IRT. These studies show the importance that photo thermal methods have in helping mural paintings restoration, and it seems to be precise, fast, and objective.

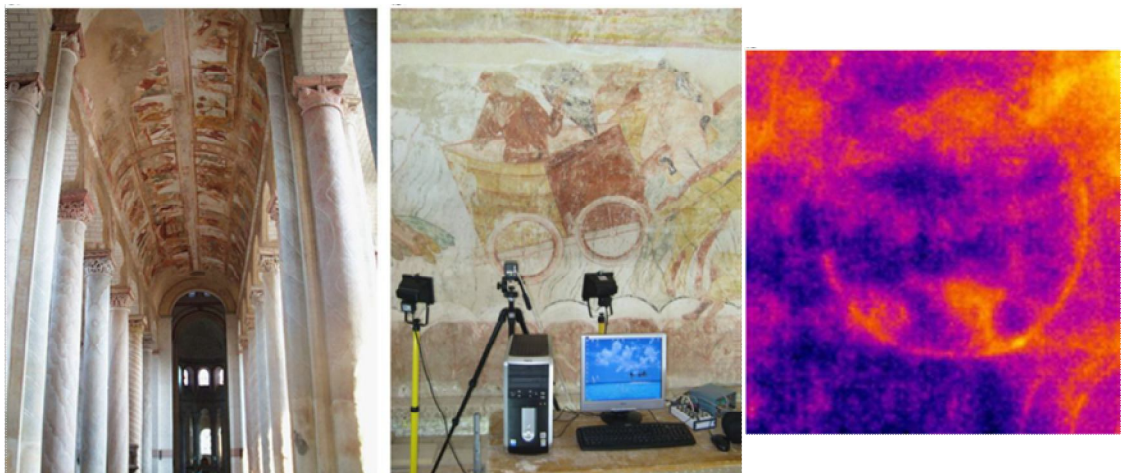


Figure 3.26 Murals paintings of the abbey of “Saint Savin sur Gartempe” and the thermographic inspection performed. The third image represents the IR image of the analyzed area: on the back wheel represented, some detachments are recognized (Bodnar, 2012)

Thermography can be usefully employed as a diagnostic tool. In fact, it may help temperature variations monitoring in protected areas, and it represents also a valuable tool for non-destructive evaluation of artworks and buildings of historical or civil

interest, for being able to show the presence of humidity, separations, and, in some cases, stone compositions. For example, in Ludwig 2012, a methodology to assess the state of conservation of the facades, especially ceramic finishing, is developed and applied on historical buildings.

Periodic inspection of architectural structures should be planned to evaluate existing conditions and discover buildings deficiencies at an incipient stage. In this context, in many cases, thermography is applied as a multi-methodological approach to non-destructive evaluation of architectural structures. In Meola 2005, a multi-disciplinary and multi-methodological approach to NDE applied to architectural structures is proposed and IR thermography is meant to be used in addition to other techniques, such as ultrasonic and electric-type and micro-geophysical methods. Passive infrared thermography was applied to control the condition of mosaics covering some external walls of the case study building. Images were acquired by the transient cooling process, after several hours to sun exposure. It resulted that some parts of the mosaic were damaged and assessed to be in urgent need of repair and restoration, because of detached wall tiles and air bubbles (both are shown in Figure 3.27).

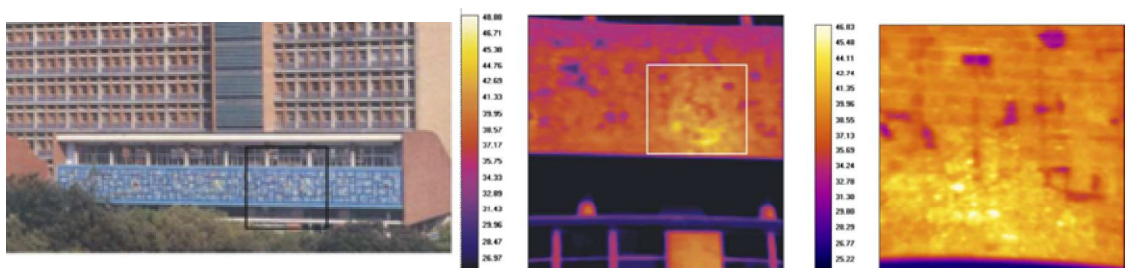


Figure 3.27 Mosaic inspection by thermography: a) building facade; b) IR image of the squared area in a); c) enlargement of the squared area (Meola, 2005)

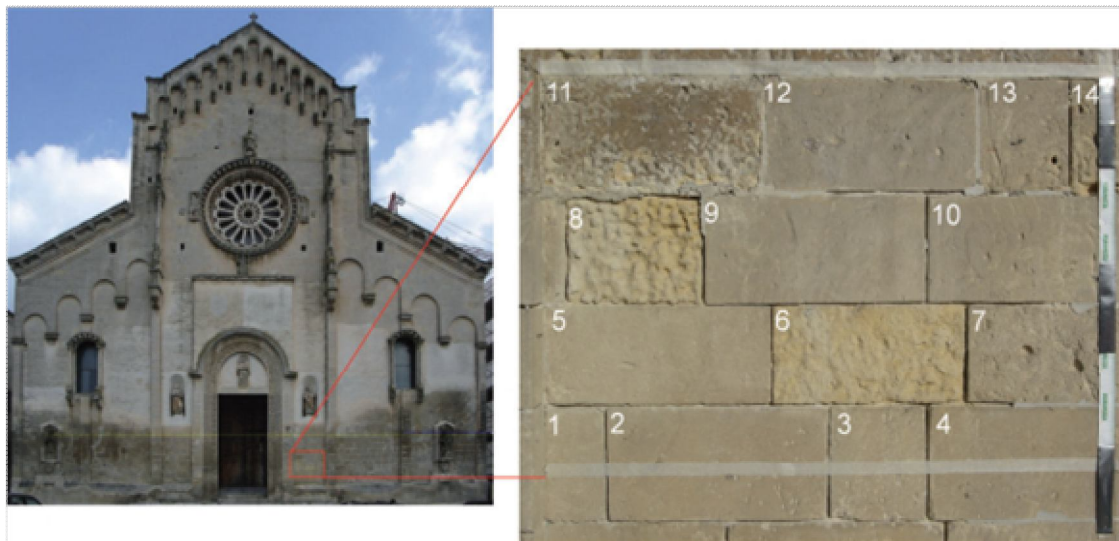


Figure 3.28 The main facade of the Cathedral of Matera and the location of the thermographic data collection (Danese, 2010)

The employment of IR images offers the possibility to create profile of temperature variations that provide information about thermal inertia. In Danese 2010, a visual analytical exploration of multi-temporal IRT images of a historic building has been performed with the aim to identify patterns of similarities and differences in the spatio-temporal variation in a wall temperature and to verify if such patterns could be attributed to material type and decay level. The presented case study involves the facade of the Cathedral in Matera (Italy), that is made up of local calcarenite entirely, and the performed work has the aim to identify degradation pathologies on that material (Figure 3.28). Many IR images of the same referenced surface were acquired at 30 minutes distances from each other, and were combined together into a multi dimensional dataset. Different patterns are identified: some of them identify different levels of

surface alveolization and erosion, other patterns show material loss, and some others show humidity level and presence of water in calcarenite.

Thermography can be used into a multidisciplinary approach for cultural heritage protection, based on the diagnostics of the environmental surroundings. In Ristić 2011, this protection approach is applied in a specific case study, in which an important accident situation occurred. Kraljevo earthquake occurred in November 2010, causing considerable damage in several buildings of heritage protection which needed to be checked and then restored. In such a case, IRT was used for an early damage detection of some buildings and for determining the impact of climate and moisture conditions.

4. IR thermography and RE: the data fusion process

Reverse Engineering tools are widely used in many fields of science contributing considerably to quality control processes and product design, which technologies aim to reduce product time to market. Moreover, in cultural heritage branch, Reverse Engineering are useful tools for restoration support. In particular, optical tools can offer the surface description of the object of study, outputting a point cloud as a data file.

However, infrared thermography systems are commonly used as non destructive testing tools, and presently wide used in many application fields. Infrared thermography systems are able to detect subsurface defects and material irregularities, according to surface temperature.

The use of IR techniques is related to two basic needs of finding, in an easy and fast way, the physical location of the target object according to the acquired temperature values, and inspecting complex geometries and non planar surfaces. To overcome the trouble of conventional thermography visualization, many IR cameras superimpose the captured IR image on to the real image of the target object: this solution helps an observer to understand IR image's location in the physical space, even if the superimposition corresponds to an image point matching and related points'

temperature values. Moreover, there are some promising applications in which it is particularly difficult to find geometric correspondences between a real object and the displayed information on a screen, such as, for example, a scene, including no geometric or radiometric distinctive features, and a clutter scene (Iwai and Sato, 2012).

The inspection of complex geometries and non planar surfaces is the other aspect related-to an unsophisticated use of IR techniques. As outlined in Section 3.4, infrared inspection is affected by surfaces' geometry and, if this aspect is not considered, some misunderstandings can occur.

Supported by these considerations, the basic idea of the work described below is to overcome the noted difficulties that often make thermography an essential tool for qualitative researches. Advantages and opportunity of both Reverse Engineering and Infrared Thermography tools are integrated: if optical RE offers a superficial data, IR thermography is used to deduce the subsurface structure or the material analysis. In this context, the final aim is to define a common "virtual environment" in which it is possible to analyze temperature and superficial coordinates at the same time. Moreover, through Reverse Engineering, the real object shape is well defined and can be employed to determine geometric irregularities for temperature correction.

During this activity, methodologies have been developed, and many improvements are expected in the future analysis of many case studies: as surface features are produced as a result of internal deformations, this aspect will bring

significant advantages to both industrial fields and quality control processes. Moreover, in civil engineering it is expected to be simpler to relate buildings external appearances or coatings to the buildings internal features.

In this chapter, methodology guidelines are described at first, and then analyzed in detail, through the description of physics and conceptual principals inherent to the integration and to the temperature correction processes. A visualization environment has been prototyped and an example is finally shown.

4.1 Data fusion between surface data and infrared data

This research activity is focused on defining a method to integrate geometric – surface data to temperature data: the main purpose is thus to develop a tool able to display both surface and temperature data within the same environment, in order to better understand temperature configurations with respect to the object's shape and independently from the user's point of view. This tool is expected to be integrated, in the near future, in post processing steps of Reverse Engineering processes, as well as in infrared thermography reports. Moreover, since thermal tomography techniques are widely used (Maldague, 2001), the developed process would like to create an environment in which it will be possible to analyze surface and volumetric data. The technological advantages and improvements in thermography interpretation and data evaluation are expected, and should reduce misunderstandings.

The integrating model should be in accordance with some basic features and requirements: first of all, points' temperature values would have to be used in place of IR images and the integrating model should be independent from the specific instrumentation used. In addition to this, starting from two different data format and information, the method-would integrate and combine data that should be merged into a common file format creating a unique 3D reference system. Other than that, at least another main feature is related to the object's shape: once temperature points are associated to surface coordinates, the corrected temperature profile should be obtained in accordance with the thermal-camera point of view and be subsequently adapted to fit the available object's shape.

4.2 *Data fusion: state of the art*

The integration of several data coming from different sources is an interesting research field, which aims to have a wide view of the case study, within its working context and according to its physical characteristics. In particular, many studies concern the integration between 3D surface data and thermal data, but they differ not only in the application field and in the used RE instrument, but also in the type of integration performed. Data fusion can be performed at different levels: in fact, texture mapping is performed by the image registration that is based on the identification of homologous points, for visible and infrared imagery. Similarly, texture mapping can be done through

specific visible markers, which are reported in terms of temperature and surface. Other integration processes, that can be carried out instead of texture representations, consider temperature values in accordance with geometric shapes., Furthermore, another data fusion procedure considers the projected temperature profiles, represented through a color map, as displayed on the object.

The following section shows some integration examples related to the methods applied to the used process.

4.2.1 Integration processes by texture mapping methods

A *texture* file is an image file, with *.jpg* or *.btm* (bitmap) extension, which is used to add color to a 3D model. At the end of the color adding process, an RGB value is associated to the coordinates of each acquired point. Photographic textures are often used in 3D visualizations: a picture is taken either from the Reverse Engineering instrument or from a metric/non metric camera. In case of picture from the Reverse Engineering instrument, the photo results already registered on the point cloud, so that a color feature is already associated to each point of the final mesh in a semi-automatically manner. This is due because the image acquisition is obtained from the same point of view of the instrument used for the definition of the range map. In case of picture from a metric/non metric camera, the image is not referenced yet. It is thus necessary to define some transformations, like scaling, rotations, and translations, and to

process and stretch it, in order to find out correspondences between the image's pixels and the acquired point.

InfraRed image can be used as texture for the mesh acquired through a RE instrument, and not through metric/non metric camera. Texture mapping application can also include a combination between an infrared image and the RE-instrument acquired shape. In Cabrelles 2009, it is shown a method to record accurately and exhaustively a heritage monument by means of Terrestrial Laser Scanning (TLS), related to close-range photogrammetry and thermal imaging. TLS system provides a 3D point cloud and the integration of photogrammetry provides a model-based photograph enhancement. The integration between TLS data and thermographic data provides further information about the current state of conservation of the historic monuments. The presented case study is a tomb, *Djin Block No.9*, in Petra (Jordan). All acquired images, captured by visible or infrared spectrum, are positioned and oriented in the object space for surface texture acquisition (Figure 4.1). A further example of IR information mapped to 3D geometry is presented in Voltolini 2007, in which quantitative analyses are then performed.

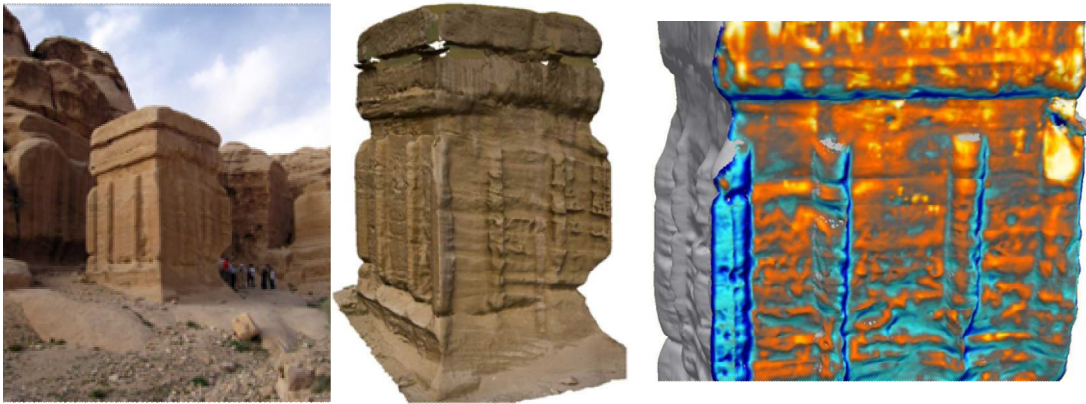


Figure 4.1 Djin Block No.9, in Petra (Jordan), a picture of the heritage monument (on the left), the acquired surface with a photographic texture (in the middle), and the surface with a thermographic texture (on the right) (Cabrelles, 2009)

In case of old buildings, geometry and spatial associations are very important to locate the position with potential thermal defects; moreover, heat losses measurement is not possible if area is not included in the quantification method, and, especially in old buildings, it is not always possible to identify or update geometric representations. In such cases, the acquisition process is inherent to the most accurate thermographic inspection. In Langüela 2012, visible and IR images sequences are acquired from the same point of view and then registered through an image fusion process. An image matching technique is then applied for a 3D surface reconstruction based on a photogrammetry-based method. IR images result automatically registered on the final mesh (Figure 4.2).

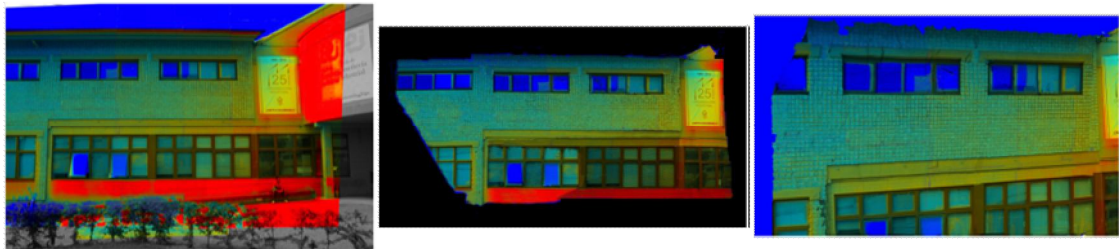


Figure 4.2 Thermographic inspection and 3D reconstruction: a case study. On the left, an image fusion between IR a visible images is performed and an orto-thermogram is then obtained (in the middle). On the right, the final thermographic 3D representation is shown (Langüela, 2012)

4.2.2 Integration processes with marker registration

Within this context, *marker* is a reference point commonly used for image matching or for registration in RE applications. In this type of applications, a marker is a represented object both in thermal images and in visible images that can be used to register infrared images in a more precise way, for range maps acquisition, including limitation that come from potential uncertainties.

As an example, in Satzger 2006, a specimen 3D surface is captured through a fringe projection system: the specimen is rigidly connected to a navigation cage, including some specific optical marks that the infrared camera can record making possible the registration process (Figure 4.3).

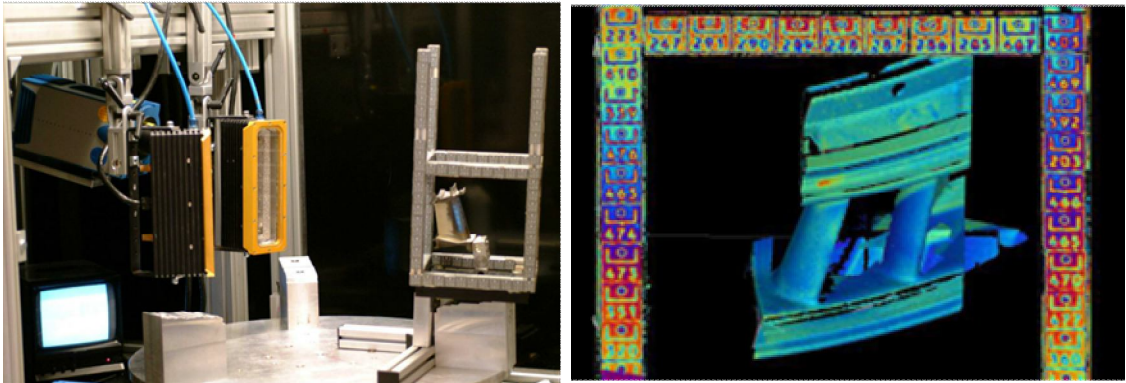


Figure 4.3 The thermographic equipment including the specimen in the navigation cage. On the right, the thermogram used as a texture for the 3D acquired shape (Satzger, 2006)

4.2.3 Video projection as integration process

In all application processes already mentioned, thermography image is mapped on a 2D screen: the real object space differs from the displayed object space. The aim of the Iwai and Sato (2010) contribution is to overcome this trouble. They presented a novel approach in which the captured thermal image is optically and simultaneously superimposed on the target object in the real space through a video projection-based method (Figure 4.4).

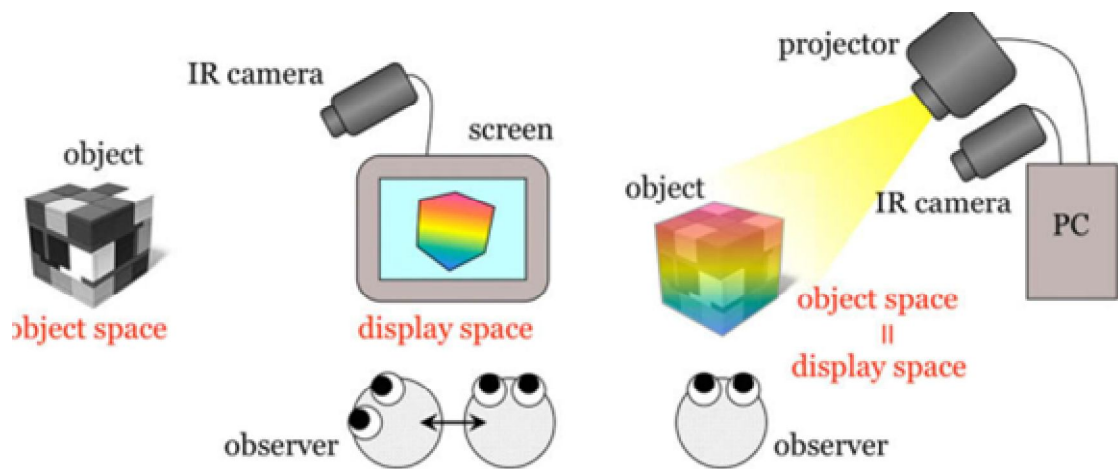


Figure 4.4 Diagrams of thermography visualization: a conventional approach (on the left) and a video projection based approach (on the right) (Iwai and Sato, 2010)

The integration process consists of the geometric registration of the infrared image to the object. The final image is projected through radiometric compensation displaying the desired color to the object's surface. An example is shown in Figure 4.5.

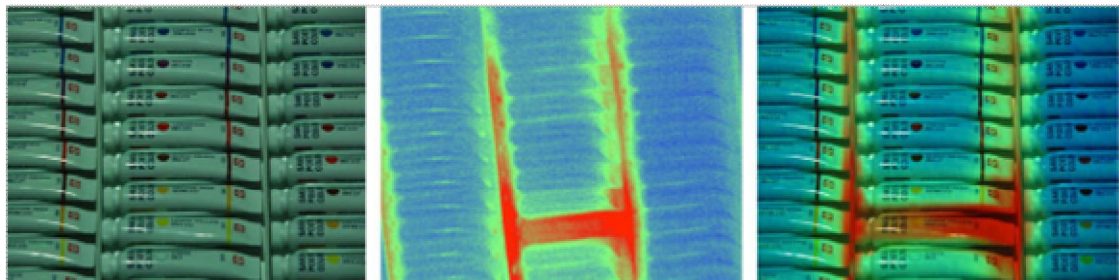


Figure 4.5 Experimental result for a cluttered scene: on the left there are paint tubes under environmental light; in the middle the thermal image is shown; on the right the projection is applied (Iwai and Sato, 2010)

4.2.4 Integration processes with volumetric RE systems

Volumetric Reverse Engineering systems, such as Magnetic Resonance (MR) and Computer Tomography (CT), are widely used, especially in biomedical applications. Such technologies provide many images related to cross sectional features of the patient or of the specimen and through post-processing procedures and elaboration procedures, it is possible to obtain a 3D image.

As discussed in Section 3.4.2, digital infrared thermal imaging is a valuable auxiliary tool for the early detection of many diseases in medicine; the relationship between thermal images and the 3D reconstructed volume can lead to a whole interpretation of medical data, overcoming thermography lacks of information regarding local anatomy. Such data combination enhances the clinical analysis of the patient by merging together the anatomical and physiological information into one-image dataset. In Bichinho et al. 2009, it is proposed a tool, which combines MR images and IR images: a thresholding technique is used to define object's external contour for a MR dataset. A 2D projection is then created: it is a representation of the external anatomical shape related to the real object and it is used for pixel matching with the equivalent IR image. The thermographic image is thus projected onto the related object contour (Figure 4.6). Some similar procedures are also applied in Brioschi et al. 2007.

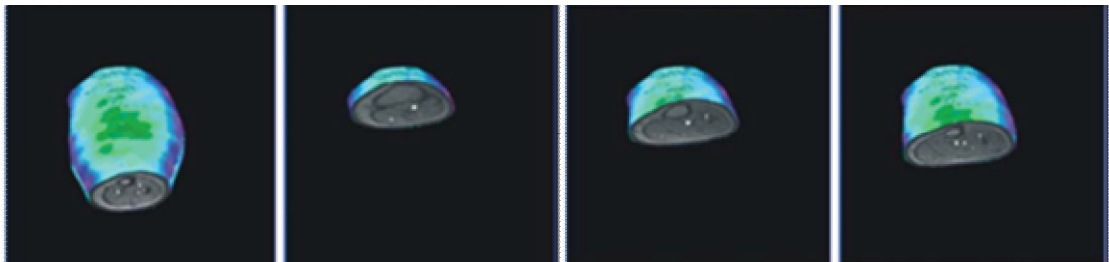


Figure 4.6 Volume visualization at four different cutting levels. The MR information is clearly visible together with the surface temperature (Bichinho et al., 2009)

4.2.4 Integration processes with calibration procedures

The above described integration methods are related to image level: a registration process is performed between a 3D shape and an image (texture) which is projected on the 3D surface. Different and more promising methods carry out integration at a point level, in order to get point temperature values being involved.

In Barone et al, 2006 and 2011, an integration procedure is proposed and biomedical applications are performed. A 3D optical digitizer is based on an active stereo vision approach; the 3D optical digitizer and the thermographic tool are fixed onto the same support. Thermal data are acquired after a calibration procedure. The 3D thermogram is achieved by a composition of the infrared image with the 3D geometry (Figure 4.7): since the two systems are calibrated together, it is possible a direct association of temperature values to point coordinates.

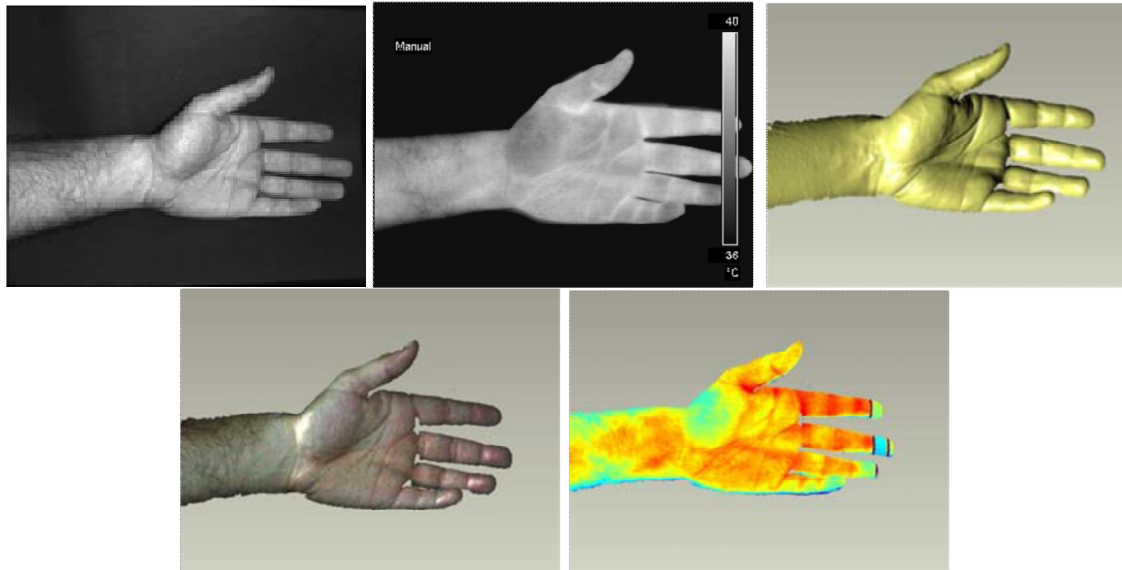


Figure 4.7 3D thermography example. Images from the top-left: the real object, the IR image, the surface acquired, the surface with the visible texture and the thermogram on the surface acquired (Barone et. al, 2006)

4.3 Methodology

This research activity includes a procedure for the definition of a 3-Dimensional thermogram. The whole process can be divided into three main activities steps (Figure 4.8): acquisition phase, data elaboration procedure, and definition of a visualization tool.

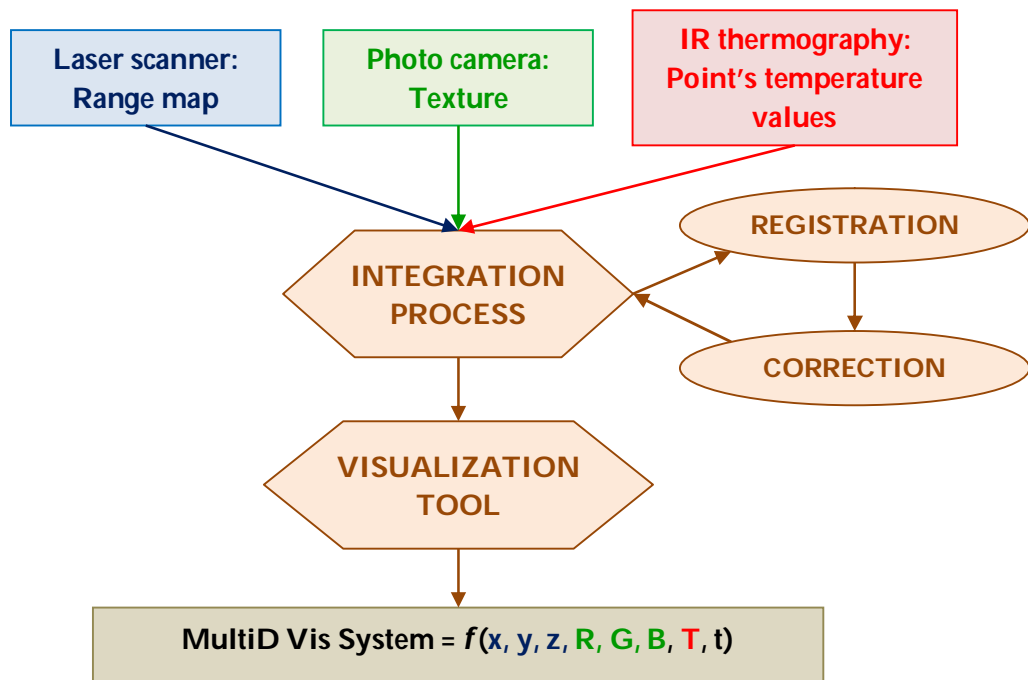


Figure 4.8 Methodology for data fusion: workflow

The acquisition procedure is performed at three different levels: range map, texture, and point's temperature values. The object shape is acquired by an optical laser scanner tool and, simultaneously, by texture of the specimen external appearance and then inspected by infrared system. Different acquiring tools provide data collection at different information levels. Data integration can be found in a wide knowledge of the case study sample, from a physical and geometrical point of view.

Object's 3D shape is obtained by an optical laser scanner: processed data can be created in point or mesh format suitable for visualization work which offers a detailed description of the specimen surface geometry. Moreover, texture can be captured and then applied to the geometrical model, in order to provide its external image features.

The image can be acquired both from the laser scanner and from an external camera, with particular optical lenses and features. In the case of the external camera, the image is obtained from the same point of view than the laser scanner: thus, the texture can be applied to the 3D shape without further image transformations. Otherwise, if the texture is captured with a support system, that is external from the laser scanner, an image processing phase should be needed for the information extraction, in which geometrical transformations are applied to the acquired photo in order to define the same laser scanner view.

The other acquisition phase is the thermographic one: the thermal-camera and the laser scanning are geo-referenced systems that can define their respective positions.

The outcome of the acquisition phase is information collection which has to be connected and linked together in the following phases, for better reading the case study.

The next phase is related to the definition of an integrating process method. During the registration phase, all collected data are transferred to the same reference system, so that it is possible to identify, for each acquired point, a temperature value coming from the infrared thermography. Texture images are registered as well.

As outlined in Section 3.3.1, object's geometry and surface's shapes deeply influence temperature values determined by the infrared thermography inspection. The basic idea of this part of activity consists of the use of geometry related to the image acquired during the scanning process for defining a geometric factor necessary to correct

temperature values. The form factor of points' temperatures is then corrected. The form factor includes, for each point, the direction of its normal vector and the distance from the acquiring system. This procedure aims to define the real temperature values, independently from the camera view and distance.

Finally, not only the 3D coordinates, but also corrected temperature values are associated to each surface point.

The final phase includes the visualization tool requirements needed to get geometrical and temperature information within the same virtual and navigable environment. Moreover, time information can be added to the system, considering acquiring more IR images of the same scene at different time sequences. Time information can help understanding of the non-stationary phenomenon and can be useful in IR tomography applications.

4.3.1 The acquisition process

Different systems and tools are used in the acquisition procedure, with the aim to acquire different data from different sources.

Reverse Engineering technologies are used to acquire 3D shape of the object of study. As highlighted in Chapter 1, many systems can be exploited to achieve surface geometrical information: in this application, as well as in the study presented in Section 2.3.1, *Konica Minolta Vivid-9i* Laser Scanner has been used. It is an optical active system

which calculate points' coordinates through triangulation principles (more detailed information is presented in Appendix A).

Laser scanner offers a range map as outcome of each scanning procedure: a point cloud containing all points coordinates can be displayed as a mesh including information about points' connections and surface's normal vectors. *Polygon Editing Tool* (PET 2.0 ®, *Konica Minolta Holdings Inc., Osaka, Japan*) is the software which manages the whole scanning processes. Each acquired range map is saved as a *.cdk* file format and then processed in the *RapidForm* (*3D Systems Inc, Korea*) software. Elaboration phase can then be performed, if filling holes procedure or smoothing procedure should be necessary. The final mesh is then saved with a specific file extension that can be read in a numerical computing programming language. According to the saved file format, the same mesh is described with different highlighted information: some more detailed notes are shown in Appendix D.

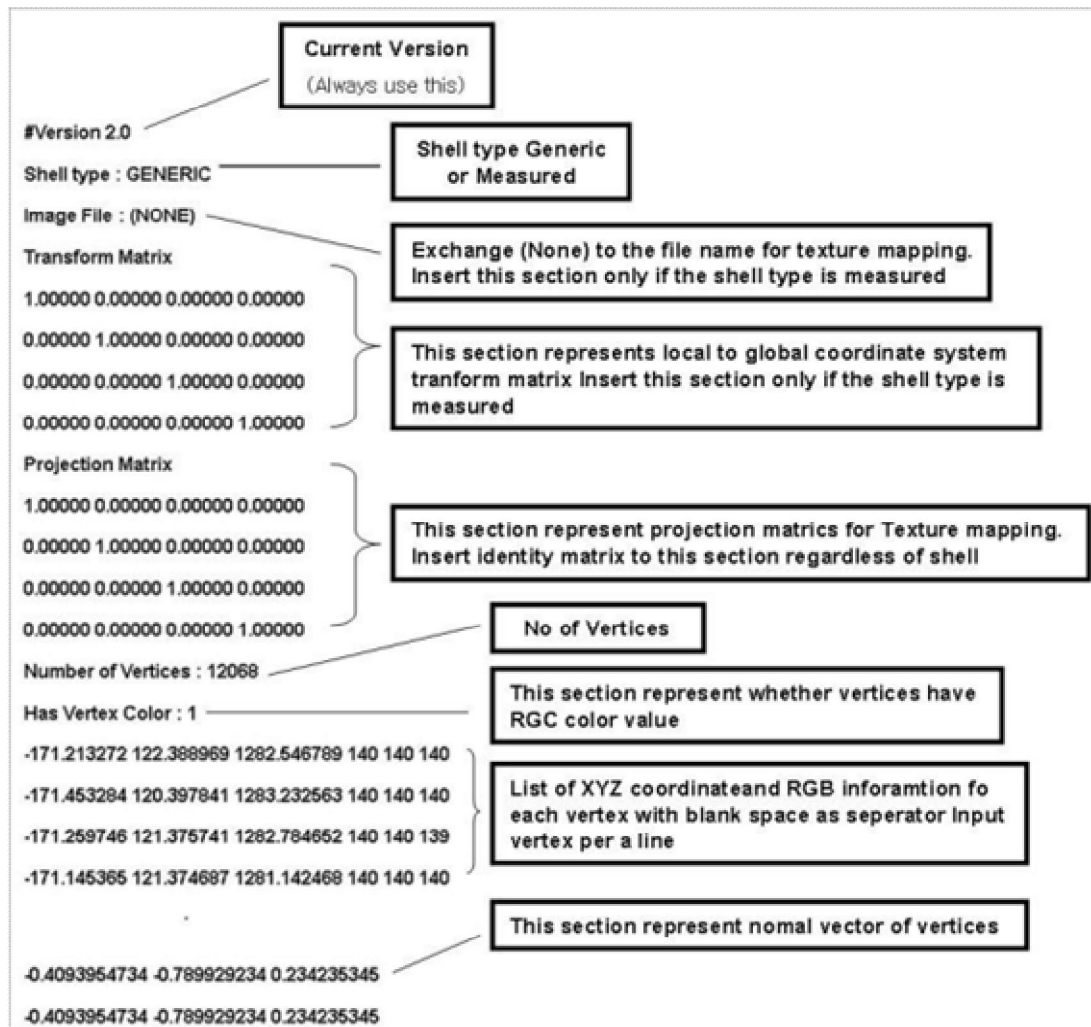


Figure 4.9 Example of Pts format files exporting

Among all different file formats, the selected file is the one with point format (*pts*), which is suitable for arrays numerical computing. *PTS* is an open *ASCII* format used for exchanging point cloud data with other software. It is composed of formal header and coordinates of each vertex (Figure 4.9). The mesh, exported with *pts* extension, can be read as an array in which the number of rows is two times than the

number of acquired points, and the number of columns is three: the first half of the array describes X , Y and Z coordinates for each point (one point for each row), as acquired in laser scanner reference system. In the second half of the array, for each acquired point, the normal vector is described through N_x , N_y and N_z coordinates (Table 4.1 shows an example). The point's normal vector is the average₇ of the normal vector. The normal vector is related to every triangle mesh vertex, weighted according to the areas. Pts files are then changed in .txt files, in order to be imported for the following integration process.

Laser Scanner CCD sensor can store an array of 480 x 640 points: the export process changes the array size in such a way that the array shows 3 columns (X , Y and Z coordinates) and the number of rows depends on the number of acquired points (it is doubled, as discussed above). Matrix store process consists of points' index changing in the file format. The first point in the column array coincides with the point (1,1) in the CCD configuration, whereas the point 2 is the point (1,2) in the CCD sensor. The first row in the CCD is related to the first part of the column array, which is-composed by 640 points. Point indexed (2,1) correspond to the point described at row 641 of the stored array (Figure 4.10).

-189.3400268555	397.5000000000	-705.0200195313
-189.3400268555	400.0000000000	-705.0200195313
-189.3899383545	400.0000000000	-702.5097656250
-189.3899383545	397.5000000000	-702.5097656250
-189.3400268555	395.0000000000	-705.0200195313
-189.3899383545	395.0000000000	-702.5097656250
-189.3400268555	392.5000000000	-705.0200195313
-189.3899383545	392.5000000000	-702.5097656250
-189.3400268555	390.0000000000	-705.0200195313
-189.3899383545	390.0000000000	-702.5097656250
.....
0.9996467486	0.0000000000	0.0265777724
0.9995848932	0.0000000000	0.0288104362
0.9999122121	0.0000000000	0.0132502110
0.9999122121	0.0000000000	0.0132502110
0.9996467486	0.0000000000	0.0265777724
0.9999122121	0.0000000000	0.0132502110
0.9996467486	0.0000000000	0.0265777724
0.9999122121	0.0000000000	0.0132502110
0.9996467486	0.0000000000	0.0265777724
0.9999122121	0.0000000000	0.0132502110
.....

Table 4.1 Example of the first ten point of a mesh saved in a pts file format: the first part of the table correspond to point's coordinates in mm, whereas the second part are the normal vector correspond to the respective acquired point. The three coordinates are shown in the column

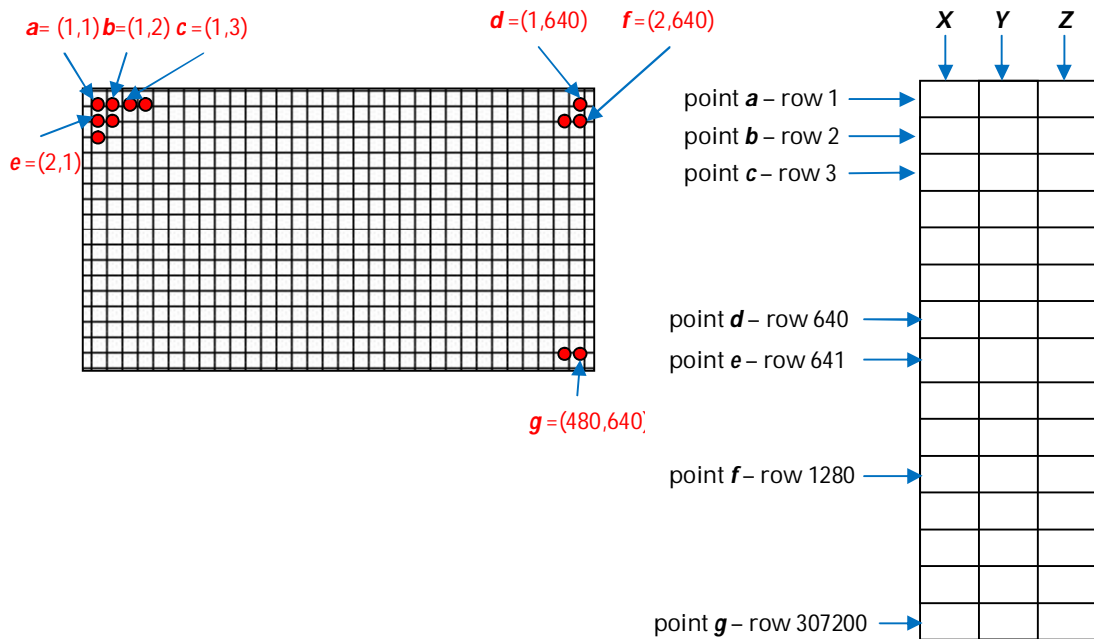


Figure 4.10 Points' position in CCD Sensor and Array, in case of the whole frame acquiring

It is possible to acquire the photographic image from the laser scanner by means of an available option and tool into the scanning instrument. It gives the possibility to register a texture on the acquired mesh in an easy and fast manner. The acquisition process is not possible for the temperature information. In order to link together infrared and geometrical information, it should be possible to define instrument positions and movements. To determine transformations between the thermal-camera reference system and the laser scanner system, it is necessary to use a connection device. The connection device will have the aim to reduce uncertainties in the instruments degree of freedom and to help define instruments respected movements.

Since laser scanner systems requires a tripod tool to acquire any surface image, and thermal-camera devices often use a tripod tool too, the same stand is used for both instruments to easy link their reference systems together. In particular, a C section bar has been customized for this particular application and fixed onto the laser scanner as a connection tool between the two instruments (Figure 4.11). That connection device was realized according to the optical center of both systems and to their cases.

Moreover, the connection device gives the possibility to move both systems with the same tripod, at the same time, so that it is possible to measure in a quite precise way, how necessary thermal-camera movement is to have the same frame acquired with the laser scanning device.



Figure 4.11 Acquisition set up

4.3.2 Infrared system devices

During the whole activity, different infrared tools have been used. In particular, during the first part of this study, it has been used *Flir ThermaCAM™ SC640*, whereas, during the second part the study focused to the use of the *Testo 882* (Figure 4.12).

Both instruments are full real time radiometric thermal-cameras. The choice of using two different instruments is based on the fact that at a final stage of the experimentation an additional camera was purchased, the Testo Camera, to take the advantage of the used-method comparison in order to get empirical results irrespective of the instrument used. Neither instrument resolution, nor the working spectral range influenced the used method.

Flir ThermaCAM™ SC640 detector has a Focal Plane Array (FPA) uncooled microbolometer with a resolution of 640 x 480 pixels. The lens has a focal distance of 8 mm and a Field of View (FOV) of 32°. The working spectral range is from 7.5 to 13 μm .

The main features related to Testo 882 are the available spectral range from 8 to 14 μm with a detector of 320 x 240 pixels. A relevant option of this instrument is the Super Resolution tool: this technology improves the image quality, increasing the usable, geometric resolution of the thermal image by a factor of 1.6 and it provides four times more readings, comparable with a higher detector resolution (www.testo.com). The Super Resolution technology uses the natural hand movement to take multiple slightly offset photos in rapid succession: an algorithm can be used to convert these individual

thermal photos into a high resolution image. Real readings are taken, and no interpolation processes are performed.

More detailed information on instruments features and performances are shown in Appendix E.



Figure 4.12 The two thermographic devices used: the Flir ThermoCAM™ SC640 (on the left) and the Testo 882 (on the right)

Both cameras have their own software for image reading and report making: Flir Quick Report is the software used by Flir, whereas IR Soft is the software used by Testo. Generally, IR images are loaded and it is possible to modify some input parameters, such as environment humidity, atmospheric temperature or surface emissivity. Additionally, temperature analysis are performed, changing color pallet, referring visible to IR images, setting up isothermal areas, or defining temperature profile along arbitrary lines.

In this work, the most interesting thing has been the possibility to be moved from acquired images to point temperature values: for this reason, that kind of softwares have

been used to export an array containing acquired temperature values. Flir ThermaCAM, for example, acquires an array containing 640 x 480 points and 307200 temperature values have been collected at each acquired image. Those values, in Celsius degree, have been exported as a table and then saved in a *txt* file format.

4.4 Data Registration

During the registration phase, data coming from laser scanner and IR thermography had to be transformed in the same coordinates reference system. To easier perform this activity, the two instruments were linked together, during the acquisition process.

Input and output of this phase have been both arrays: coordinates of acquired points have been presented in an array of size $2n \times 3$, where n is the number of acquired points. As above discussed, the first part of this array is formed by point's coordinates, whereas in the second part normal vectors are arranged. The number of acquired points depends on specimen size, scanner-object distances and lens used: the maximum number of acquired point is 307200 (according to the CCD sensor size, which is 640x480 pixels).

Point's temperature values are the second input array: the size of this array depends on IR camera resolution and capability. *Flir ThermaCAM SC640* has been noticed to be able to measure more temperature values points than the laser scanner

camera: since its detector size is 640x480 pixels, at each image it can evaluate temperature in 307200 different points, at the same time. Otherwise, *Testo 882* has lower resolution capabilities and, at each measure, it acquires 76800 temperature values, which correspond to a detector size of 320x480.

At the end of the process, a unique array was provided and the size of the final matrix was $nx4$: at each point, it was associated a temperature value in addition to its coordinates.

The described procedure was entirely performed in *Matlab*: this software, necessary for numerical calculations, has been used to process routines and rules in order to associate its temperature value to each point.

The defined registration method is outlined in Figure 4.13; in the next paragraph, all steps are described in detail.

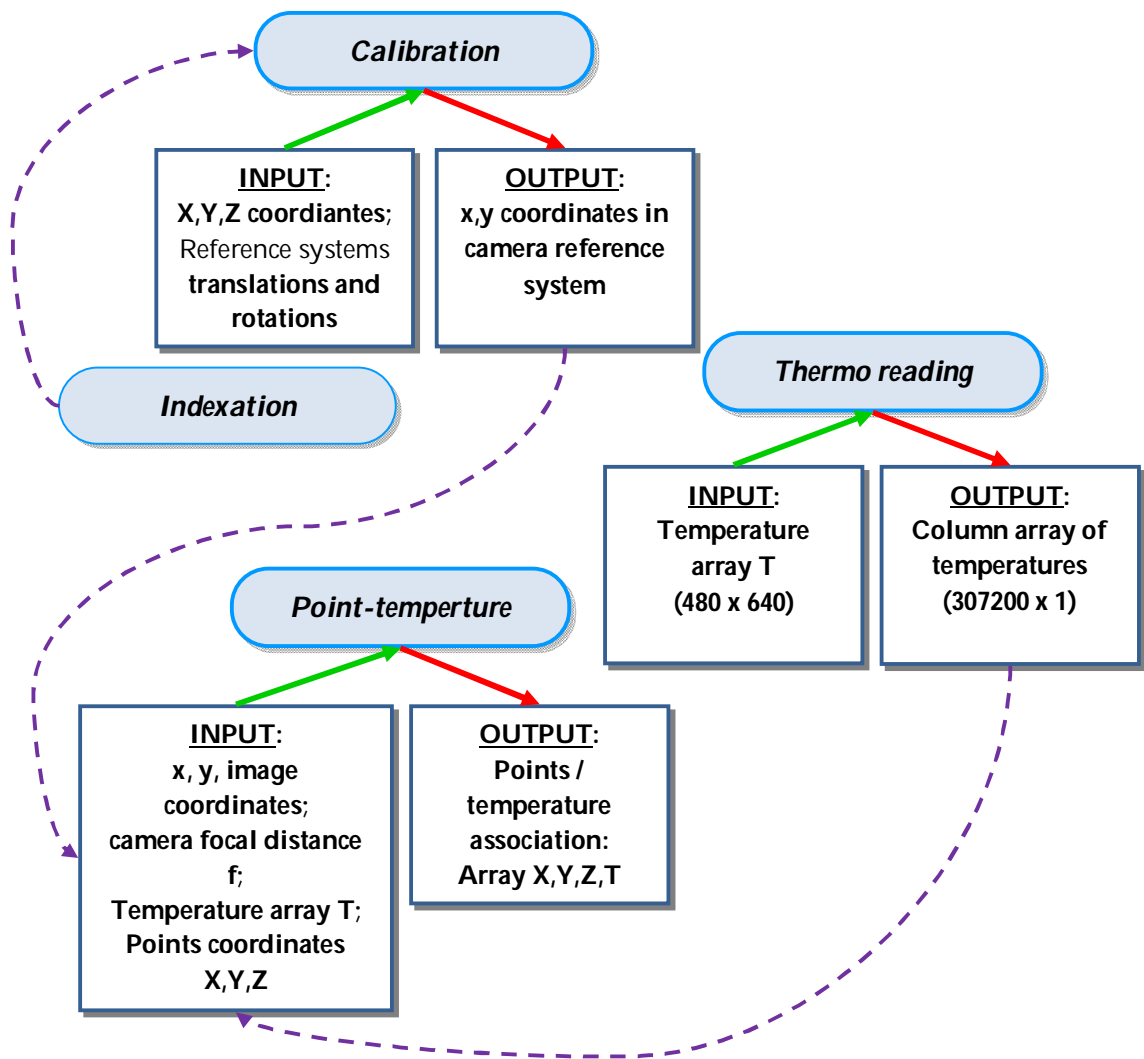


Figure 4.13 Registration workflow

4.4.1 The registration workflow

All input arrays were loaded in *Matlab* environment. Point's coordinates were acquired through a 640 x 480 CCD array; when they were saved in a points file format, they were stored as a list in which the first point coincided with the point in the first row

and in the first column of the CCD sensor (Figure 4.10). Temperature values were saved in the same size of the infrared detector: the final format was thus different from the point coordinates array. The first step consisted of reducing temperature array to the size of the scanning array: the temperature array was thus transformed in a column vector, in which the first value coincided with the point (1,1) of the temperature array, whereas the last value was the pixel (m,n), where $m = 480$ (240 for *Testo* camera) and $n = 640$ (320 for *Testo* camera). In *Matlab* environment, it has been also possible to display temperature values as a *mesh*, in which the X and Y coordinates coincided with the pixel position, and the Z coordinate was the temperature value. A color map was used to display temperature changes (Figure 4.14).

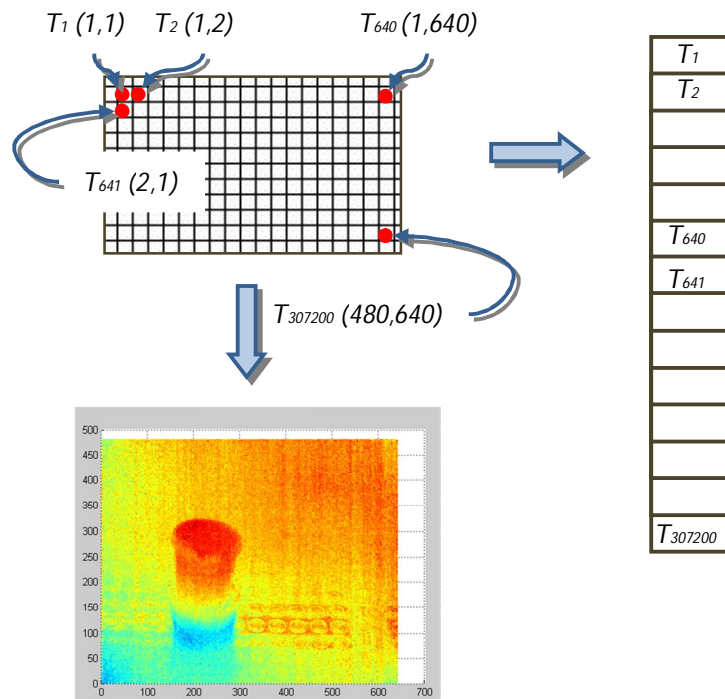


Figure 4.14 Temperature array displayed in *Matlab* environment

Similarly, a visualization routine could be defined for surface's depiction, through point's visualization in *Matlab*. While performing this activity, it was important to notice that *Konica Minolta Laser Scanner* can acquire up to 307200 points, arranged as an array of 480 x 640 points. In practical operational activities, in very few cases, acquired points have been the whole acquirable points, and, in many parts of the frame, no points were present. Since, in those pixels, no points' coordinates have been acquired, when acquired points were stored as an array, no correspondences have been present between acquired points and their position into the frame. Thus, an indexation process was-necessary to identify points positions and then to identify correspondences between points and temperatures.

To perform this activity, it has been created a routine, in which, for each acquired point, pixel coordinates (i,j) depended on lens focal distance, and pixel dimension depended on CCD sensor (for laser scanner *Konica Minolta* it is 0.0132mm). The indexation has been obtained through a linear interpolation of acquired points, in order to define correspondences with points that should be acquired when their X and Y coordinates were positioned in the center of every pixel. At the end of this process, it has been thus possible to display a 3D shape in *Matlab* environment, and, moreover, since point's location is known, to register temperature values on the acquired shape.

A calibration process was then performed, and the image orientation corresponded, at each pixel, to the 3D coordinates. This activity was divided into two

main parts: in the first one, thermal-camera reference system has been oriented as well as the laser scanner system; in the second one, correspondences between points and coordinates have been identified.

The two reference systems were analyzed in detail: laser scanner system was centered into CCD sensor. The origin was posed in sensor center, the X-axis was positive for point on its right, the Y-axis was positive for those points which were greater than the center and the positive part of the Z-axis was turned into the laser scanner (Figure 4.15).

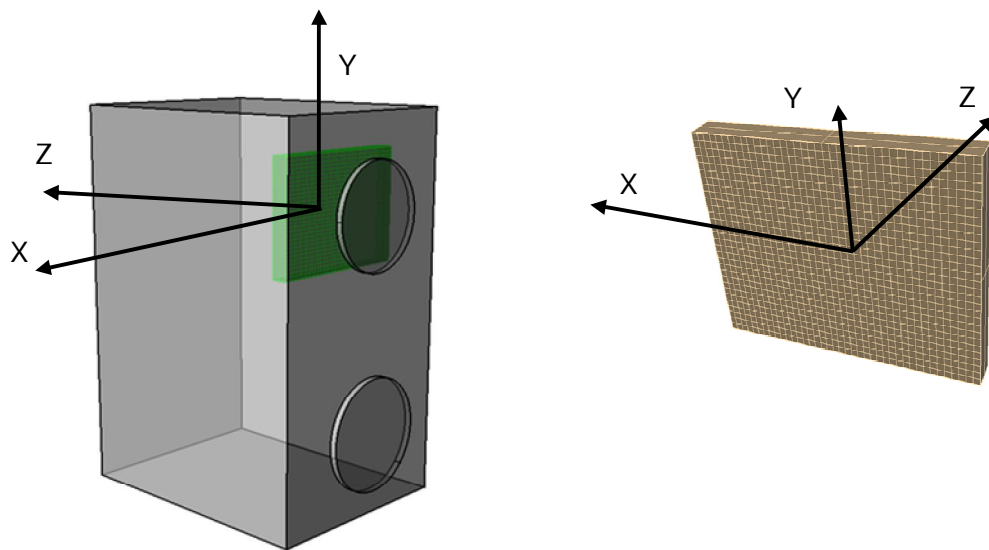


Figure 4.15 Laser Scanner Reference System. On the right in detail the CCD sensor: the acquiring object is considered as posed in front of it

Similarly, thermal-camera reference system was into the detector, but the axis origin was the intersection of the optical axis with the image plane. In a pixel oriented view, the center was the upper-left corner of the image. Then, the y-axis was directed

downwards (Figure 4.16). Since an output image was obtained, no Z-axis has been defined.

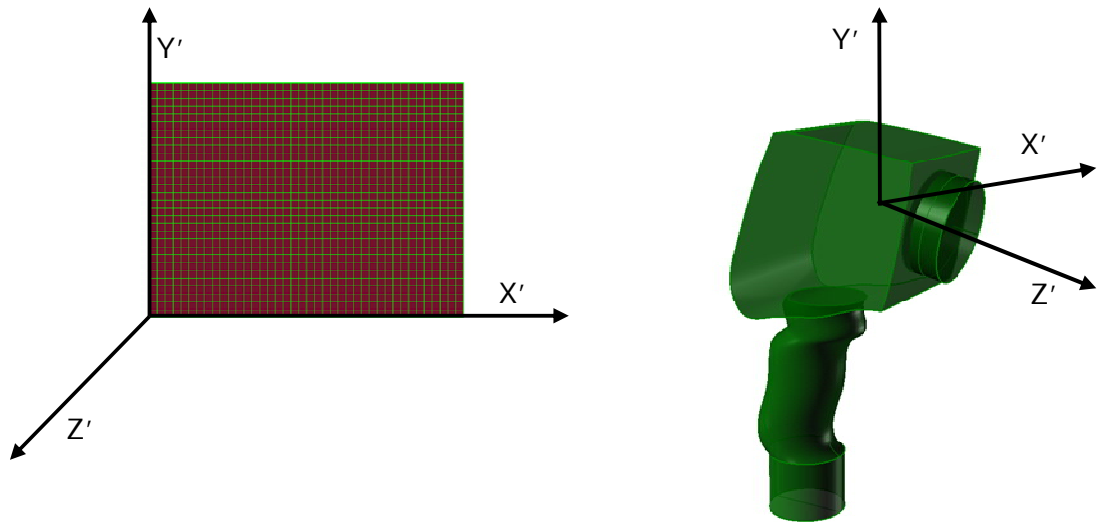


Figure 4.16 Thermo Camera Reference System

This two reference systems had to be linked together: to perform this activity, it was necessary to define which kind of transformations the thermal-camera system had to perform, to overlap laser scanner system. Some movements could be constant for every acquisition: those transformations depended on the laser scanner and the thermal-camera dimensions, and on the tripod and connection tool structures.

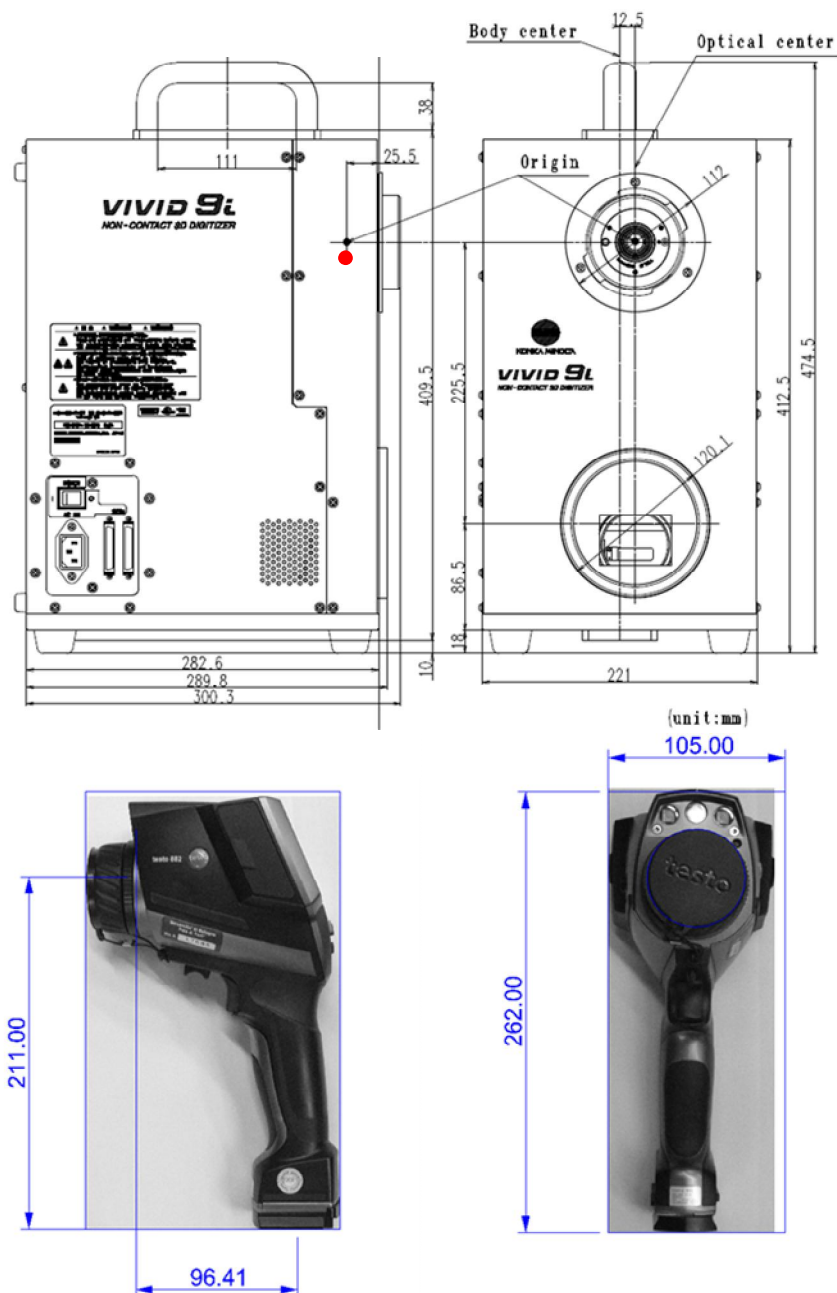


Figure 4.17 Translations between the two reference systems: on the top the red point is laser scanner reference system origin; on the bottom thermal-camera dimensions. The total distance between the two reference systems origins is defined as sum of the two contributes

These transformations have been highlighted as translations and can be summarized in Figure 4.17. In Figure 4.18 the connecting device is shown: its dimensions have to be considered in the total translation movements.

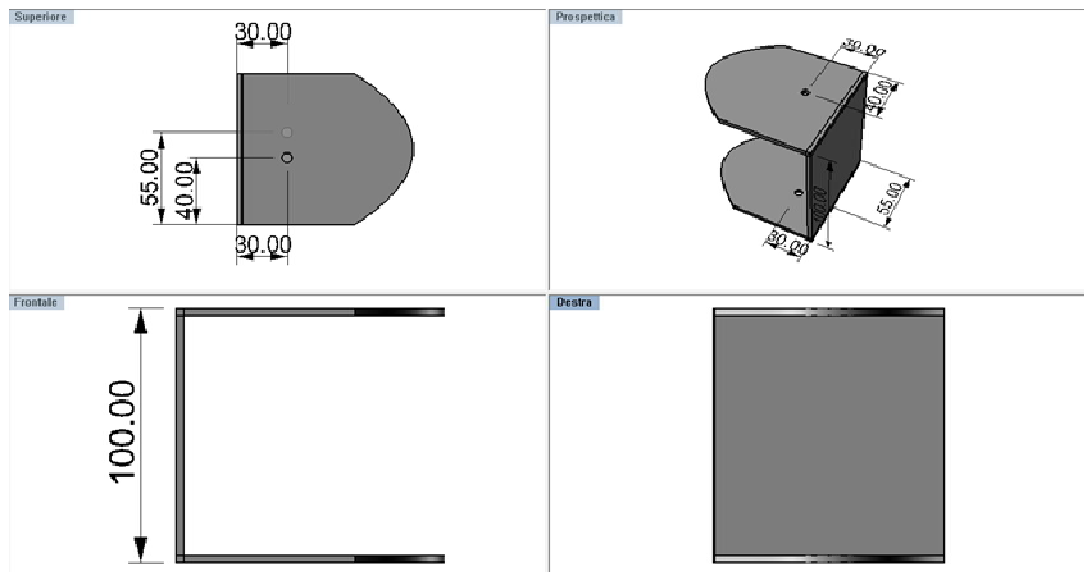


Figure 4.18 Constant movements (Translations) between the two reference systems

Other movements change during the acquisition process can be as follows: since laser scanner and camera lenses have different focal distances and they had been overlapped, they could not acquire the same frame. For this purpose, it would have been necessary to move the tripod in order to acquire the thermographic image, when laser scanner had already acquired object's 3D shape. These movements were performed without moving the tripod, but only its head: this is a very important aspect to define clearly, and in a fast and an enough reliable way, which movements have been carried out. Such movements are translations or rotations.

Both constants and variable movements have been noted and then applied in the simulation environment to define reference systems transformations. Then, co-linearity equations have been used to define for each acquired point its corresponding pixel in the thermographic image, and thus its related temperature value.

4.4.2 World and camera coordinates systems

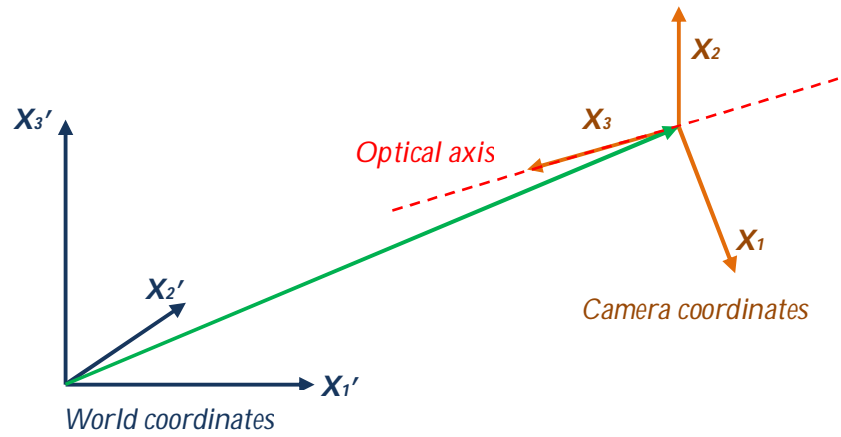


Figure 4.19 Camera and world coordinates systems

Object's position in a 3D space can be described in two different ways (Figure 4.19). The first one is based on the use of a coordinate system, which is related to the observed scene. This are called *world coordinates* and indicated as column vectors (Eq 4.1):

$$\mathbf{X}' = [X_1', X_2', X_3']^T \quad \text{Eq 4.1}$$

A second coordinate system, known as the *camera coordinate*, is fixed to the moving camera observing a static or dynamic scene (the X_3 axis is aligned with the *optical axis* of the camera system) (Eq 4.2):

$$\mathbf{X} = [X_1, X_2, X_3]^T \quad \text{Eq 4.2}$$

In this application, the world coordinate system coincided with the laser scanner system, whereas the thermal-camera reference system coincided with the camera system. Transition from world to camera coordinates required a *translation* and a *rotation*: a translation vector \mathbf{T} has been necessary to shift the origins of the camera system to the origin of the laser scanner system. The orientation of the coordinates system has been then changed by a sequence of rotations around suitable axis, so that the two reference systems coincided to each other.

Mathematically, translations have been described by vector subtractions, whereas rotations by multiplication of the coordinate vector coincided with a matrix (Eq 4.3):

$$\mathbf{X} = \mathbf{R} (\mathbf{X}' - \mathbf{T}) \quad \text{Eq 4.3}$$

A common procedure to define the rotation transformation has been the three Eulerian rotation angles (ϕ, ϑ, ψ) : the rotation from the shifted world coordinate system, into the camera coordinate system that is decomposed into three steps (Figure 4.20):

1. Rotation about \mathbf{X}_3' axis by ϕ (Eq 4.4, Eq 4.5):

$$\mathbf{X}'' = \mathbf{R}_\phi \mathbf{X}' \quad \text{Eq 4.4}$$

$$R_{\phi} = \begin{bmatrix} \cos\phi & \sin\phi & 0 \\ -\sin\phi & \cos\phi & 0 \\ 0 & 0 & 1 \end{bmatrix} \quad \text{Eq 4.5}$$

2. Rotation about X_1'' axis by ϑ (Eq 4.6, Eq 4.7):

$$X''' = R_{\vartheta} X'' \quad \text{Eq 4.6}$$

$$R_{\vartheta} = \begin{bmatrix} 1 & 0 & 0 \\ 0 & \cos\vartheta & \sin\vartheta \\ 0 & -\sin\vartheta & \cos\vartheta \end{bmatrix} \quad \text{Eq 4.7}$$

3. Rotation about X_3'' axis by ψ (Eq 4.8, Eq 4.9):

$$X = R_{\psi} X''' \quad \text{Eq 4.8}$$

$$R_{\psi} = \begin{bmatrix} \cos\psi & \sin\psi & 0 \\ -\sin\psi & \cos\psi & 0 \\ 0 & 0 & 1 \end{bmatrix} \quad \text{Eq 4.9}$$

In this standard mathematical approach, the right-hand coordinates system is used and rotation angle is counted in a positive direction going counter-clockwise.

Cascading the three rotations R_{ϕ} R_{ϑ} R_{ψ} , the matrix is yielded:

$$\begin{bmatrix} \cos\psi \cos\phi - \cos\vartheta \sin\phi \sin\psi & \cos\psi \sin\phi + \cos\vartheta \cos\phi \sin\psi & \sin\vartheta \sin\psi \\ -\sin\psi \cos\phi - \cos\vartheta \sin\phi \cos\psi & -\sin\psi \sin\phi + \cos\vartheta \cos\phi \cos\psi & \sin\vartheta \cos\psi \\ \sin\vartheta \sin\phi & -\sin\vartheta \cos\phi & \cos\vartheta \end{bmatrix} \quad \text{Eq 4.10}$$

The inverse transformation, from camera to world coordinates, which is the transformation used in this process, is given by the transpose of the matrix Eq 4.10.

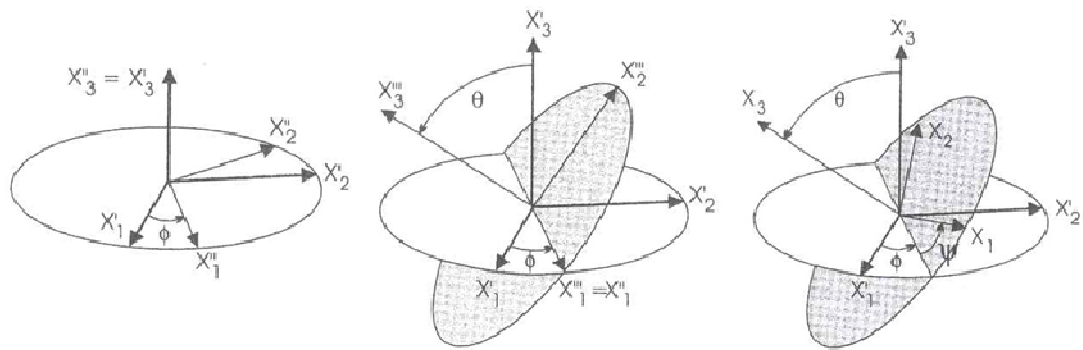


Figure 4.20 Rotation of world coordinates X' and camera coordinate X , using the three Eulerian angles (ϕ, ϑ, ψ) with successive rotations about the X_3', X_1'' and X_1''' axes

Once defined the transformation to change the thermal-camera reference system into the laser scanner system, correspondences between points and pixels have been defined. This process has been inspired by some principles which are strictly related to photogrammetric Reverse Engineering process: *digital close range photogrammetry* measures objects directly from photographs or digital images captured with a camera at close range. The mathematical model inherent to this process is the *central perspective projection*: the world coordinate system is positioned in object's space, whereas the origin of the camera reference system is at the perspective camera center O , its z-axis coincides with the optical axis and it is directed away from the image plane.

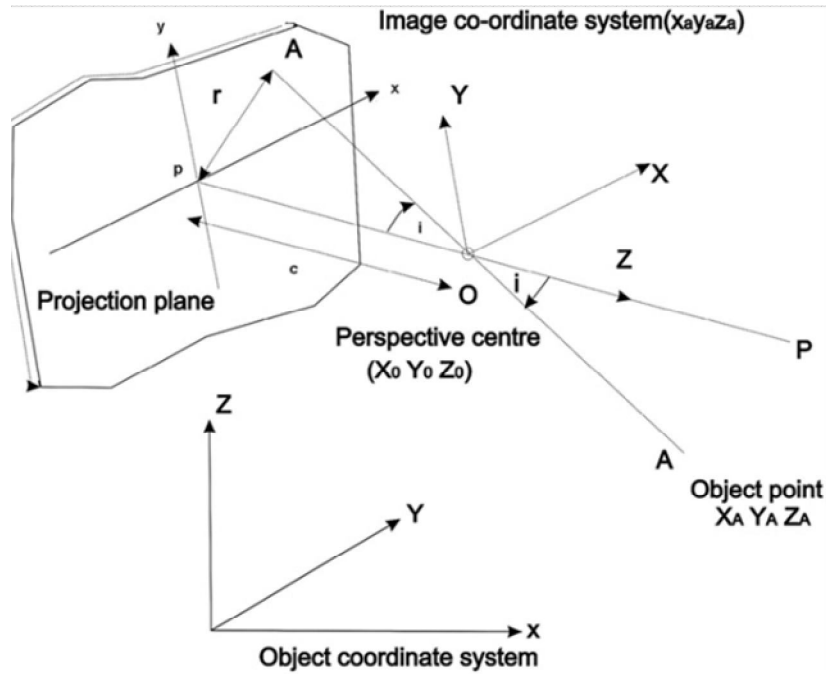


Figure 4.21 The central perspective projection (Yilmaz et al, 2008)

A point **A** in object's space has coordinates (X_A, Y_A, Z_A) ; its projection, through **O**, in the image plane, expressed in the camera coordinate system, gives the coordinate points **a** $(x_a, y_a, -c)$, where **c** is the camera focal length (Figure 4.21) (Eq 4.11). **A** and **a** are called *homologous*.

$$X_A = X_0 + (-\mu)R^T x_a \quad \text{Eq 4.11}$$

where μ is a positive scalar quantity, proportional to the object distance from **A** to **O** (Yilmaz et al, 2008). The reverse transform is given as (Eq 4.12):

$$\begin{bmatrix} x_a \\ y_a \\ -c \end{bmatrix} = \mu^{-1} \begin{bmatrix} \gamma_{11} & \gamma_{12} & \gamma_{13} \\ \gamma_{21} & \gamma_{22} & \gamma_{23} \\ \gamma_{31} & \gamma_{32} & \gamma_{33} \end{bmatrix} \begin{bmatrix} X_A - X_0 \\ Y_A - Y_0 \\ Z_A - Z_0 \end{bmatrix} \quad \text{Eq 4.12}$$

Vectors $(\mathbf{X}_A - \mathbf{X}_O)$ and \mathbf{x}_a are collinear, but of opposite sense. The third equation of the reverse transform above can be written explicitly in term of the scaling factor μ , and substituted in the first two equations, leading to the collinearity equations (Eq 4.13, Eq 4.14):

$$x_a = \frac{-c [\gamma_{11} (X_O - X_A) + \gamma_{12} (Y_O - Y_A) + \gamma_{13} (Z_O - Z_A)]}{[\gamma_{31} (X_O - X_A) + \gamma_{32} (Y_O - Y_A) + \gamma_{33} (Z_O - Z_A)]} \quad \text{Eq 4.13}$$

$$y_a = \frac{-c [\gamma_{21} (X_O - X_A) + \gamma_{22} (Y_O - Y_A) + \gamma_{23} (Z_O - Z_A)]}{[\gamma_{31} (X_O - X_A) + \gamma_{32} (Y_O - Y_A) + \gamma_{33} (Z_O - Z_A)]} \quad \text{Eq 4.14}$$

At the end of this process, for each acquired point, a (x,y) coordinate has been associated. These correspondences are in *mm*: to find the correspondent pixel in the IR image it has been necessary to transform such mm values in pixels values, through an indexation process. To perform this calculus the thermal-camera pixel dimension has been defined as (Eq 4.15):

$$\text{pixeldim} = \frac{f * \tan\left(\frac{\text{fov}}{2} * \frac{\pi}{180}\right)}{320} \quad \text{Eq 4.15}$$

where f is lens focal distance, fov is thermal-camera field of view and it is a data from datasheet². Finally, univocal correspondence between (x,y) coordinates and pixels has been defined along with temperature vector, and it has been associated to laser scanner acquired points. To each point it has been associated different information, such as: the

² A camera field of view (fov) is an optical feature depending on both lens focal distance and image plane dimensions. In particular the field of view is the angle of the shot, when the focal distance is at infinity. Since the image is generally rectangular and its dimensions are $w \times h$, the fov can be horizontal or vertical:

$\text{fov}_H = 2 \arctan\left(\frac{w}{2f}\right)$ and $\text{fov}_V = 2 \arctan\left(\frac{h}{2f}\right)$.

3D coordinates (X, Y, Z) ; the normal vector (N_x, N_y, N_z) , showing directions of the acquired surface, and the temperature value (T) . Moreover, a photographic data (R, G, B) could have been associated.

4.5 Data correction

Temperature values are affected by shapes and geometry properties; the use of the 3D system can be applied to define a correction factor for the thermographic data, in order to obtain point temperature values, independently from camera views.

As anticipated in Section 3.3.1, “heat” measured by an infrared camera depends on the distance and the angle between the camera and the object of study. Therefore, when complex shapes are examined, the surface geometry produces a signal distortion that may lead to faulty defect detection. Heat emission and absorption is at maximum level when the normal to the surface is parallel to the direction of the flow of energy and the signal is weaker when the angle between the normal to the surface and the direction of the flow increases (Ibarra-Castanedo et al., 2003). Without object’s shape information, defects located under the surface just below point B in Figure 4.22 are difficult to detect by TNDT.

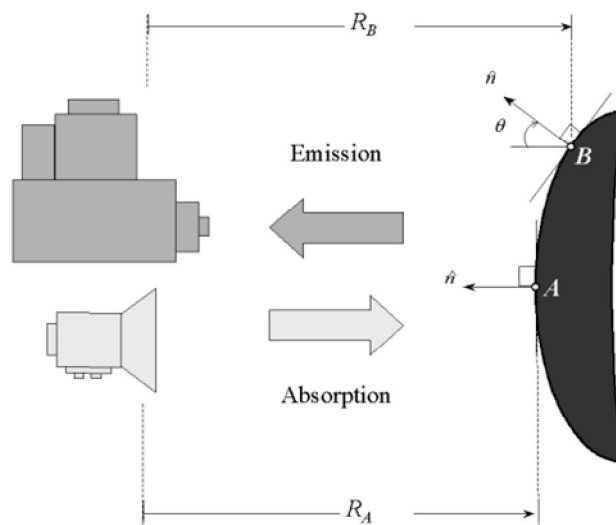


Figure 4.22 Complex shapes inspection: distance and angle effects (Ibarra-Castanedo et al., 2003)

In Tkáčová et al 2010, some experimental data on distance and angle influence in temperature acquisition process by thermography are presented: in particular, biomedical application is analyzed. Various measurements are taken at 5 different subject distances and 8 different camera-subject angles, as shown in Figure 4.23.

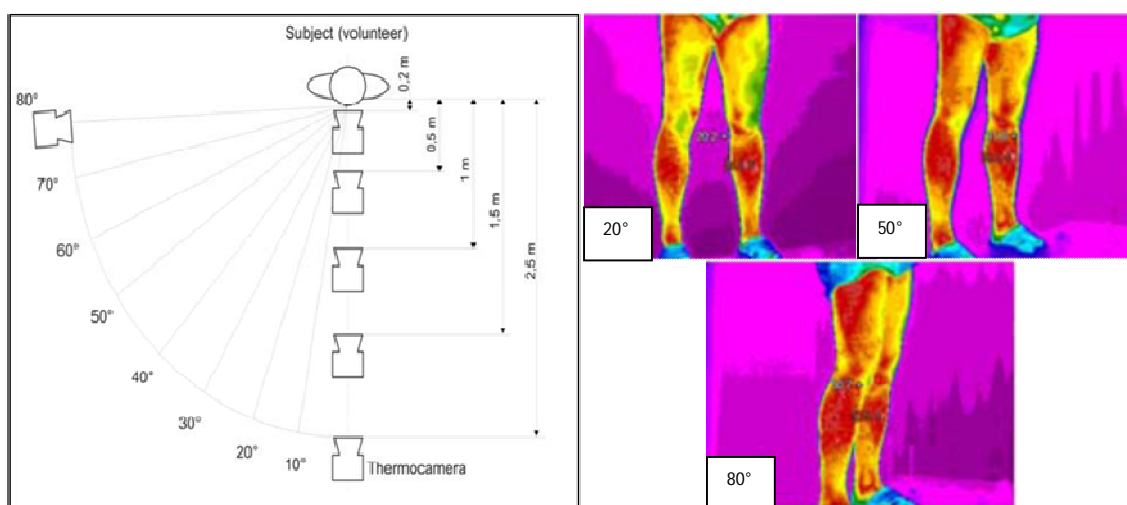


Figure 4.23 Angle and distances influence in thermography inspections: on the left an experimental set up, on the right some temperature maps at angles of 20°, 50° and 80° (Tkáčová et al, 2010)

Moreover, a blackbody plate had been analyzed at different distances and angles, showing an illusory decreasing in temperature profile: the main results are reported in Figure 4.24.

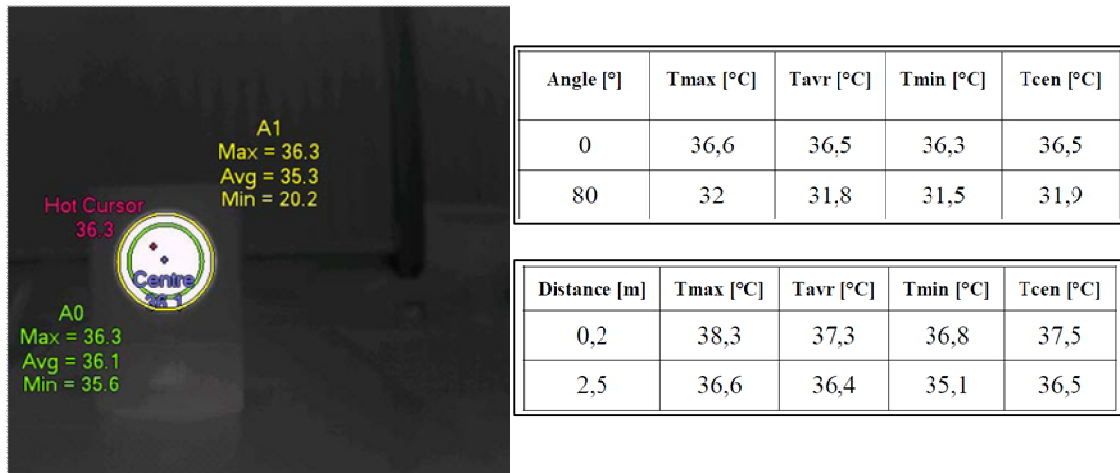


Figure 4.24 Blackbody distances and angle dependence in temperature reading (Tkáčová et al, 2010)

The aim of this part of the work is to generate standardized thermograms, which could be used for quantitative studies. The idea inherent to this study is to define a correction factor for each acquired point which is function of point's normal vector and of its distance from thermal-camera detector. The acquired 3D profile is thus a tool to define a new thermogram which is independent from camera position and object's shape.

4.5.1 Non planar geometry inspection

In general, applications of Thermographic Non Destructive Testing (TNDT) to non planar surfaces produces distortions mainly due to two effects (Maldague, 2001): the first one considered the inspection of the heated surface and the area parallel to the heating device that would receive more energy with respect to the related perpendicular area. The second effect asserted that areas parallel to the IR camera emit more energy in its direction (Figure 4.25).



Figure 4.25 The problem of shape curvature in TNDT: an original and a rectified thermogram example (Ju et al, 2004)

Many methods for shape correction in TNDT have been identified. The idea related to such work is to use thermographic equipment to get information on object's geometry. Once its shape is known, it is possible to correct thermograms for non-planar effects (Maldague, 2001).

4.5.1.1 Point – Source Heating Correction

A high power bulb, on the top of the camera, is used as thermal stimulation devices. A calibration procedure is performed, to obtain the *early recorded thermogram* (ERT) in the 3D inspection volume, located in front of the IR camera. It is acquired just after the thermal stimulation. More ERTs are recorded at a range of distances in front of the IR camera, in order to obtain a complete databank of the expected temperature distribution within the inspection volume. After this calibration phase, the inspection is performed and the correction consists of matching specimen with the ERT of the database on a pixel-by-pixel basis. This matching produces a range image of the scene inspected, which can be used furtherly to correct subsequence thermograms from the specimen.

The main disadvantages are related to the fact that this method is limited to objects of restricted curvature; moreover the correction technique is related to the point-source-like heating device, providing non uniform heating patterns.

4.5.1.2 Video Thermal Stereo Vision

In these techniques, in addition to the standard TNDT apparatus, a video camera and an illumination device are required. The reflectance information of the scene into a visual image makes it possible to determine surface curvature (which is described by ϑ

angle). The hypothesis assumed is that the inspected surface is *Lambertian* and opaque.

Under these conditions, the visible image obey to the following relation (Eq 4.16):

$$L = K_d \cos \vartheta + C_d \quad \text{Eq 4.16}$$

where L is the digitized intensity value, K_d and C_d are the overall calibration constants of the visible imaging system and they are found experimentally. The orientation image ϑ can be computed. The thermogram correction is performed after an image registration procedure, in order to align visible and IR image formats with corresponding pixel-to-pixel format, obtained between the two images,. Curvature correction of the thermogram is done by dividing temperature values by $\cos \vartheta$.

However, the temperature correction procedures can also lead to some disadvantages: in fact, it is necessary to cover the specimen surface with a paint which has both *pseudo-Lambertian* properties in visible spectrum and acceptable emissivity values in the IR one.

4.5.1.3 Direct Thermogram Correction

In this correction procedure, no extra hardware (like video camera and illuminating source) is required. If cases in which the heating device provides little dependence on distance, Eq 4.16 can be adapted and L is the digitized value of the thermogram and K_d and C_d the overall calibration constant of the infrared imaging system and ϑ is the angle between the normal to the surface patch and the direction of

IR camera observation. This equation can thus provide an estimation of local surface orientation ϑ . The correction process is performed using an ERT image after a thermal pulse.

The main disadvantage consists of the assumption that the distance is large enough so that local depth variations on the specimen do not affect the IR emission process.

4.5.1.4 Shape from Heating

As in the other correction methods, this method is based on two-dimensional analysis of the early thermogram in the recorded sequence, which is the first useful thermal image of the sequence, in which defect contrast have not yet developed. Intensity variations are thus exclusively related to the surface geometry and not to the presence of a flaw.

The assumptions of this method consider the heating flux as orthogonal to the specimen (the heating flux is perpendicular to the specimen axis), when the heating has a little dependence on distances and the surface emissivity is high.

Specimen early thermogram is analyzed row by row and each row is divided into segments. If a **segment is linear**, as in the case of flat surfaces, the orientation angle ϑ is computed (Eq 4.17), as it shown in Figure 4.26

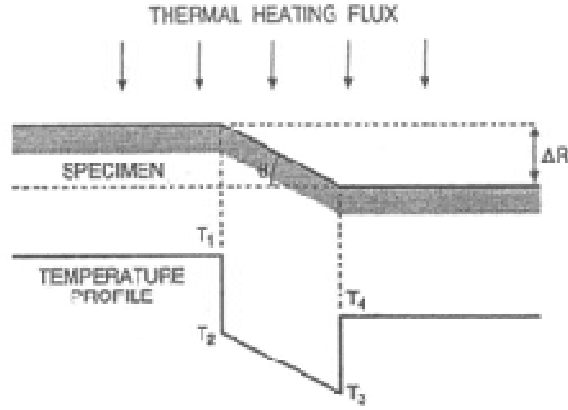


Figure 4.26 Heating analysis of a flat surface specimen (Maldague, 2001)

$$\cos \theta = \frac{T_2 - T_3}{T_1 - T_4} \quad \text{Eq 4.17}$$

In case of the distance R increasing and a the slope S consecutively increasing, some more relations can be taken into account (Eq 4.18):

$$S = \frac{\Delta T}{\Delta R} = \frac{T_1 - T_4}{\Delta R} \quad \text{Eq 4.18}$$

Substituting Eq 4.17 into Eq 4.18, it comes:

$$\Delta R = \frac{T_2 - T_3}{S \cos \theta} = \frac{\Delta T}{S \cos \theta} \quad \text{Eq 4.19}$$

In case of **non linear segments**, variations of distance R are lower than variations due to orientation θ . It is then assumed that, for small segments, temperature variations are proportionally to orientation θ only (Eq 4.20) (Figure 4.27):

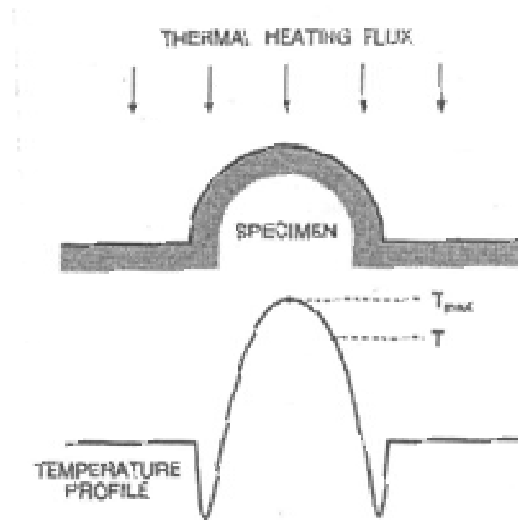


Figure 4.27 Heating analysis of a curved specimen (Maldague, 2001)

$$T - T_i = (T_{\max} - T_i) \cos \theta \quad \text{Eq 4.20}$$

where T_{\max} is the local maximum temperature close to the pixel of study, which is at temperature T . By knowing T_i (the before heating temperature), it is possible to calculate the local surface orientation.

4.5.1.5 Experimental Correction Methods

In many medical fields, thermography is widely used, such as in diagnosis of diabetes. In these applications, body temperature in flat parts (like the palm of the hand) is almost the same, whereas in curving surfaces, like fingers, great differences are shown, even if the temperature value should be almost the same.

In Chen et al. 2005, an experimental methodology was pointed out. Body's parts are assumed as a cylinder, and geometrical considerations are carried out in order to determine projecting angles. A Gaussian curve relationship is supposed to be between the real and the measured temperature, according to the projecting angle and to unknown parameters, mathematically defined. An experimental relation was thus determined in order to shift from measured temperature to real temperature in case the shape is close to the cylinder.

4.5.2 Lambert's Cosine Law

The principle of the proposed thermogram correction methods consists of an analysis of Lambert's Cosine Law. This law, also known as the cosine law, determines the relationship between the intensity of radiation emitted by a surface element of a black body and the distribution angle α (Eq 4.21).

$$I_{b\alpha} = I_{b\perp} \cos \alpha \quad \text{W sr}^{-1} \quad \text{Eq 4.21}$$

where $I_{b\perp}$ is the radiant intensity emitted in a direction normal to the surface and $I_{b\alpha}$ is the radiant intensity emitted at angle α to the normal to the surface. This equation states that the radiant emissivity from a *Lambertian* surface is directly proportional to the cosine of angle α between the observer's line of sight and the normal to the surface (Minkina et al, 2009).

Some more geometrical considerations are added to Lambert cosine law, in order to define a temperature correction factor.

It is now considered a source S and a detector R at a distance d from S ; dS and dR are surface elements of the source and the detector respectively. $d\omega_S$ and $d\omega_R$ are the solid angles subtended by dR at dS and by dS at dR respectively (Eq 4.22, Eq 4.23):

$$d\omega_S = \frac{dR \cos \vartheta_R}{d^2} \quad \text{Eq 4.22}$$

$$d\omega_R = \frac{dS \cos \vartheta_S}{d^2} \quad \text{Eq 4.23}$$

where ϑ_R and ϑ_S are the angles between the line joining dS and dR and the normal vectors N_S and N_R to dS and dR respectively (Figure 4.28).

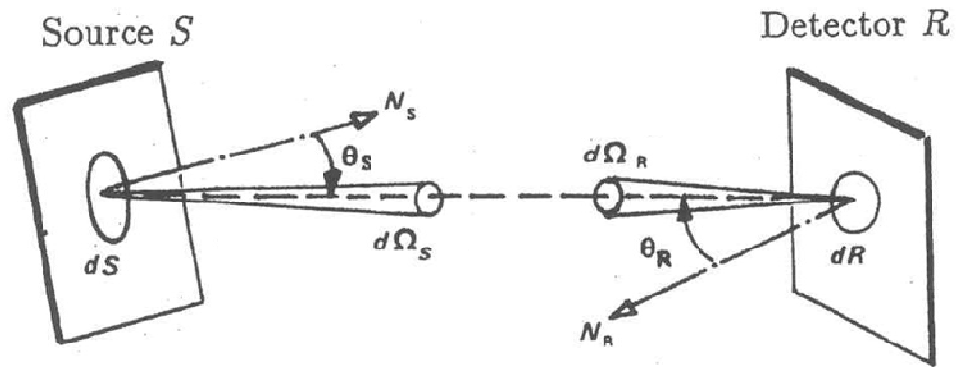


Figure 4.28 Beam geometry (Gaussorgues, 1994)

The geometrical spread of a thin beam subtended by dS and dR is defined by (Gaussorgues, 1994) (Eq 4.24):

$$d^2G = dS d\omega_S \cos \vartheta_S = dR d\omega_R \cos \vartheta_R = \frac{dS dR \cos \vartheta_S \cos \vartheta_R}{d^2} \quad \text{Eq 4.24}$$

This equation is related to the temperature correction procedure described below.

4.5.3 Temperature correction procedure

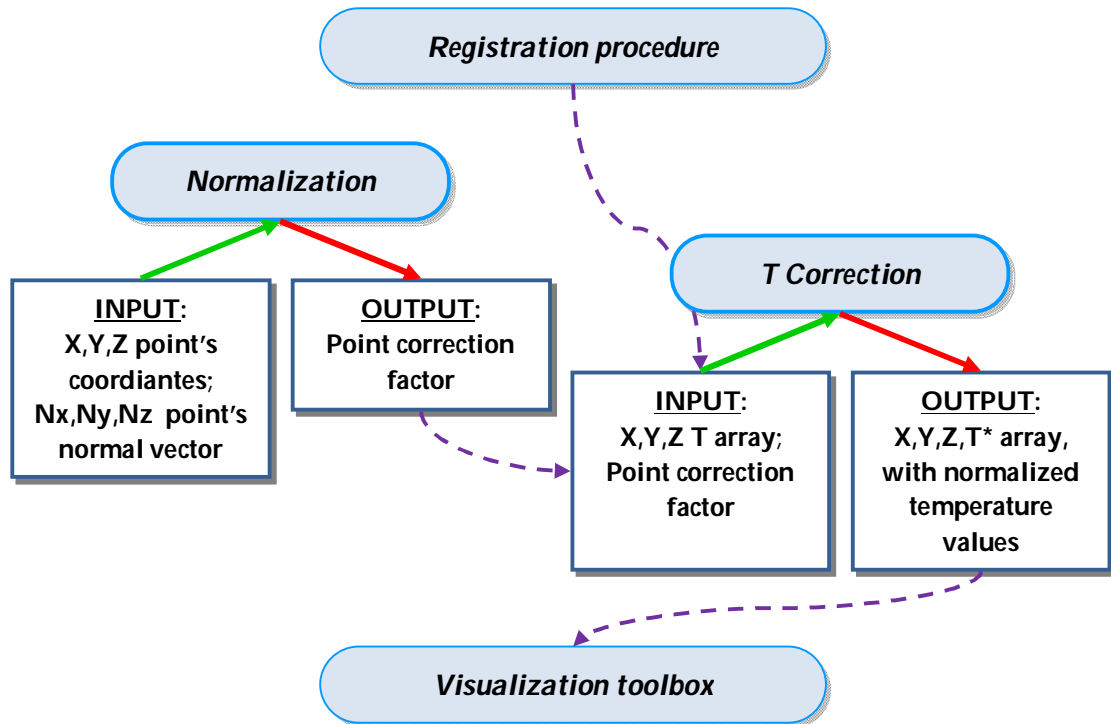


Figure 4.29 Correction workflow

This task has been performed in *Matlab* environment (a representation of the whole workflow is shown in Figure 4.29): point's coordinates and point's normal vector are input values, used to define geometrical correction values (Figure 4.30).

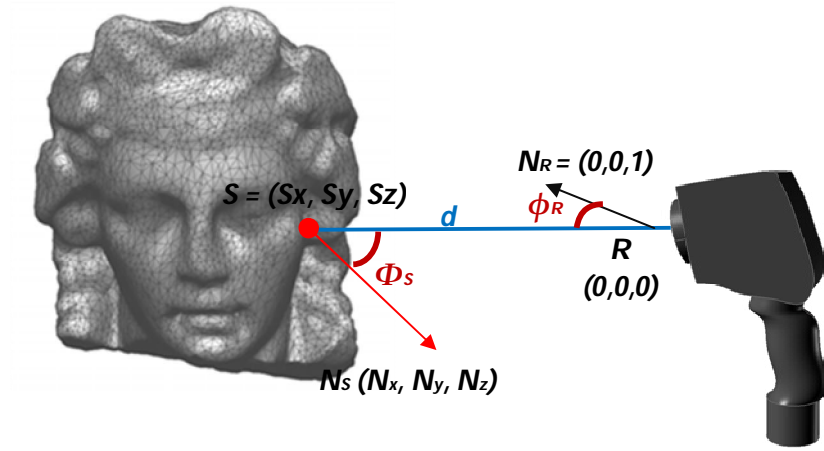


Figure 4.30 Geometrical quantities used for the definition of a correction factor

Point's 3D coordinates are used to calculate the distances between the coordinates and the thermographic tool. A distance value is obtained, in meters, for each point and the related expression is described in Eq 4.25: S is an acquired point and S_x , S_y and S_z are the related 3D coordinates. R is the camera center, and since the camera reference system is moved into the laser scanner system, during the registration phase, R 3D coordinates are $(R_x, R_y, R_z) = (0, 0, 0)$.

$$d = \sqrt{(S_x - R_x)^2 + (S_y - R_y)^2 + (S_z - R_z)^2} \quad \text{Eq 4.25}$$

The other defined parameters are the angle between the association of the camera to each acquired point and the normal direction of the acquired point (ϕ_s), and the normal direction of the instrument (ϕ_R). These values are determined considering the dot product between normal vectors and vector \overline{RS} . N_R coincides with $(0, 0, 1)$ the vector,

whereas \overline{RS} coincides with the point coordinates and N_s is the normal vector at each point and it is exported from the acquiring process.

$$N_R * \overline{RS} = 0 * S_x + 0 * S_y + 1 * S_z = \|N_R\| * \|\overline{RS}\| \cos \phi_R \quad \text{Eq 4.26}$$

$$S_z = 1 * d * \cos \phi_R \quad \text{Eq 4.27}$$

$$\phi_R = \arccos \frac{S_z}{d} \quad \text{Eq 4.28}$$

Similarly:

$$N_S * \overline{RS} = \|N_S\| * \|\overline{RS}\| \cos (\pi - \phi_S) \quad \text{Eq 4.29}$$

$$\phi_S = \arccos \left(- \frac{N_S * \overline{RS}}{d} \right) \quad \text{Eq 4.30}$$

For each acquired point these three quantities are thus defined.

From geometrical and physical quantities enounced in Section 4.5.2, the correction factor for the total exitance M is described as a function of those parameters and it is defined as follows:

$$K' = \frac{d^2}{\cos \phi_R * \cos \phi_S} \quad \text{Eq 4.31}$$

This value is thus the applied radiation measured by the thermal-camera, M , as a multiplicative factor, in order to define a correct value of the emitted radiation M' .

$$M' = K' * M \quad \text{Eq 4.32}$$

Since, the correction is performed on temperature values, the Stephan-Boltzmann law is applied to define the relation between the total exitance and the temperature value (for no black bodies ε is surface emissivity):

$$M = \varepsilon \sigma T^4 \quad \text{Eq 4.33}$$

$$T = \sqrt[4]{\frac{M}{\varepsilon \sigma}} \quad \text{Eq 4.34}$$

A correction factor K is thus defined for acquired temperature T , in order to define the correct value T' .

$$T' = K * T \quad \text{Eq 4.35}$$

$$T' = \sqrt[4]{\frac{M'}{\varepsilon \sigma}} = \sqrt[4]{\frac{K'M}{\varepsilon \sigma}} \quad \text{Eq 4.36}$$

$$K = \sqrt[4]{K'} \quad \text{Eq 4.37}$$

A different factor is defined for each points of the objects surface. Those values are collected in a final array, which is used as multiplicative factor for the acquired temperature. To each point is thus associated a temperature value which is independent from the camera views and from the object shape.

4.6 Visualization environment

For the purposes of this work, visualization environment has been a prototype used to display at the same time, both shapes and temperature data. Some main requirements are thus noted: first of all, the first request concerns the information to be shown in the environment. The 3D mesh, with the acquired photographic texture, and the temperature map have to be shown at the same time, with the possibility to investigate which information each data can provide. Since the texture is a color

information, and the mesh is a geometrical information, those data have to be represented as loaded, without changing the included information during the visualization analysis. Otherwise, thermal data have to be read and analyzed in order to understand defects location. For this reason it is always necessary to change the visualization color map, or to insert isothermal information. All these features are possible in common tools for thermography report.

Moreover, this environment is thought to be navigable both in terms of space and in time. Rotations, translations, and zoom option should be possible to be activated (by keyboard or mouse) and applied to the 3D surface for ensuring space navigability. As regards time, those phenomena, in which a thermal transient is expected, can change their temperature profile very quickly. For this reason, it is important to be able to notice temperature changes as time passes. A time label should thus be added, along with the possibility to switch from a time instant to another one, and under each condition the related temperature map is analyzed.

Finally, the defined environment should be interactive: points' information should be provided, if requested. Both points' coordinate and temperature values are indicated and shown for each acquired point.

Starting from this requirement list, a visualization environment prototype is performed. An Open GL (*Open Graphics Library, Silicon Graphics Inc.*) programming language is used: Open GL is an open source library and platform for 2D rendering and

3D computer graphics and it is widely used in the design of CAD or virtual reality applications, scientific visualization, information visualization, flight simulation and video games.

Thus, a first level prototype is designed. The mesh is saved in a stl-ASCII file format: this format makes a list of all faces of the triangular mesh. Each face is related to its three points and their coordinates to the 3D coordinate system. The visualizing tool has a graphical structure, in which the *.stl* file manages the environment on the top. All faces are associated and listed to this file. For each face, three vertexes are noted. Physical adjectives are connected as attributes: to each vertex, its 3D coordinates (X , Y , Z) are related, together with its normal vector (N_x , N_y , N_z) and its temperature value T_c (Figure 4.31). Different thermograms are associated to different time instants t .

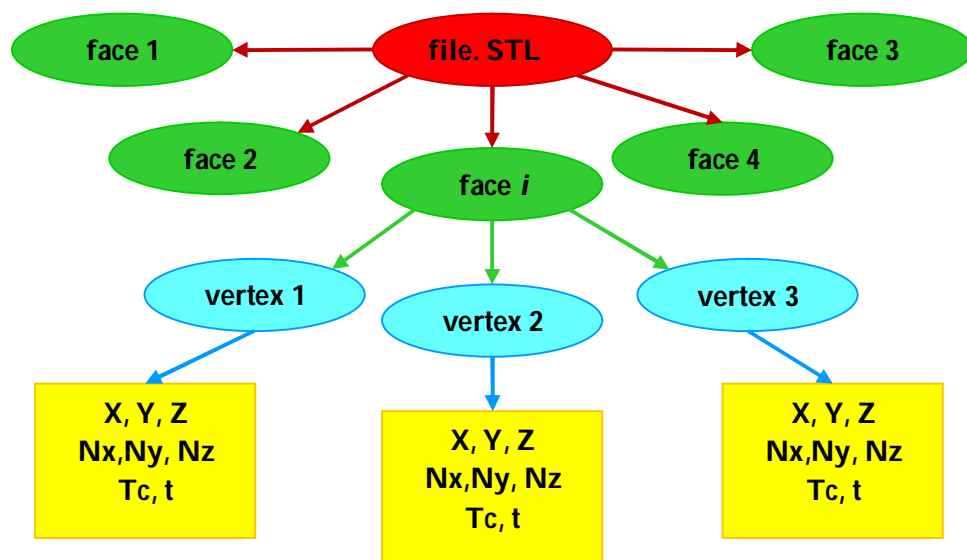


Figure 4.31 Graphical structure representing at the basis of the visualization environment

Data to be displayed have to be loaded into this environment, as follows: the *.stl* file format is loaded, together with a txt file containing correct temperature values as a vector file and stored in the right order to be associated with points. The temperature file is named like the *.stl* file, but with different extension. A progressive name will be assigned for time sequences.

The defined visual environment allows all space movements; moreover, temperature pallet changes are possible. Four interchangeable color maps are so far defined: three of them take inspiration from *Matlab* color maps and they are Grey, Iron (*Matlab* one is called Hot) and Rainbow. In Gray pallet RGB values are always the same to each other: this produces a color map allocating the black color (0, 0, 0) to the high temperature value and the white color (255,255,255) to the low temperature value. Iron color map goes from dark red, to white, and rainbow color map goes from blue to red. Another color map is created with linear increasing of red value in the RGB scale and a linear decreasing of the blue value. Green trend increases up to a medium temperature value and then it decreases up to the maximum temperature value in the analyzed range. In Figure 4.32, the used color maps are shown: on the left, the linear color scale is sketched and, on the right, *Matlab* color scale is shown.

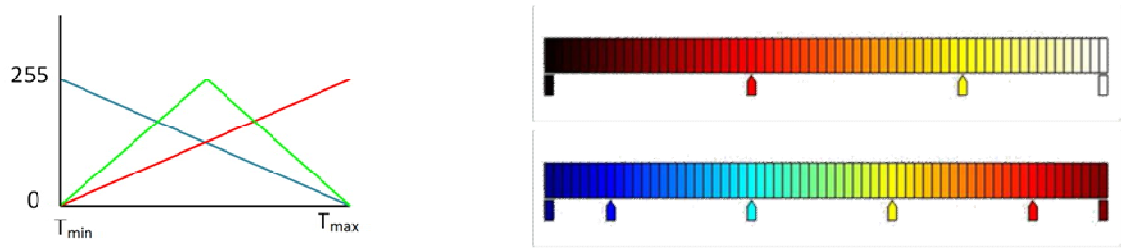


Figure 4.32 Color maps used in the visualization environment

4.7 Experimental case study

Some experimental studies have been performed, in order to refine the proposed methodology and to test it.

Two little cans were used: whereas the first can was kept at ambient temperature, the second can was cooled with a heating source, so that temperature differences were clearly visible through a thermographic inspection. Then, these two cans had been put one on the top of the other one. The same scene had been acquired both with the *Konica Minolta Vivid-9i* laser scanner and then with the thermal-camera (Figure 4.33).

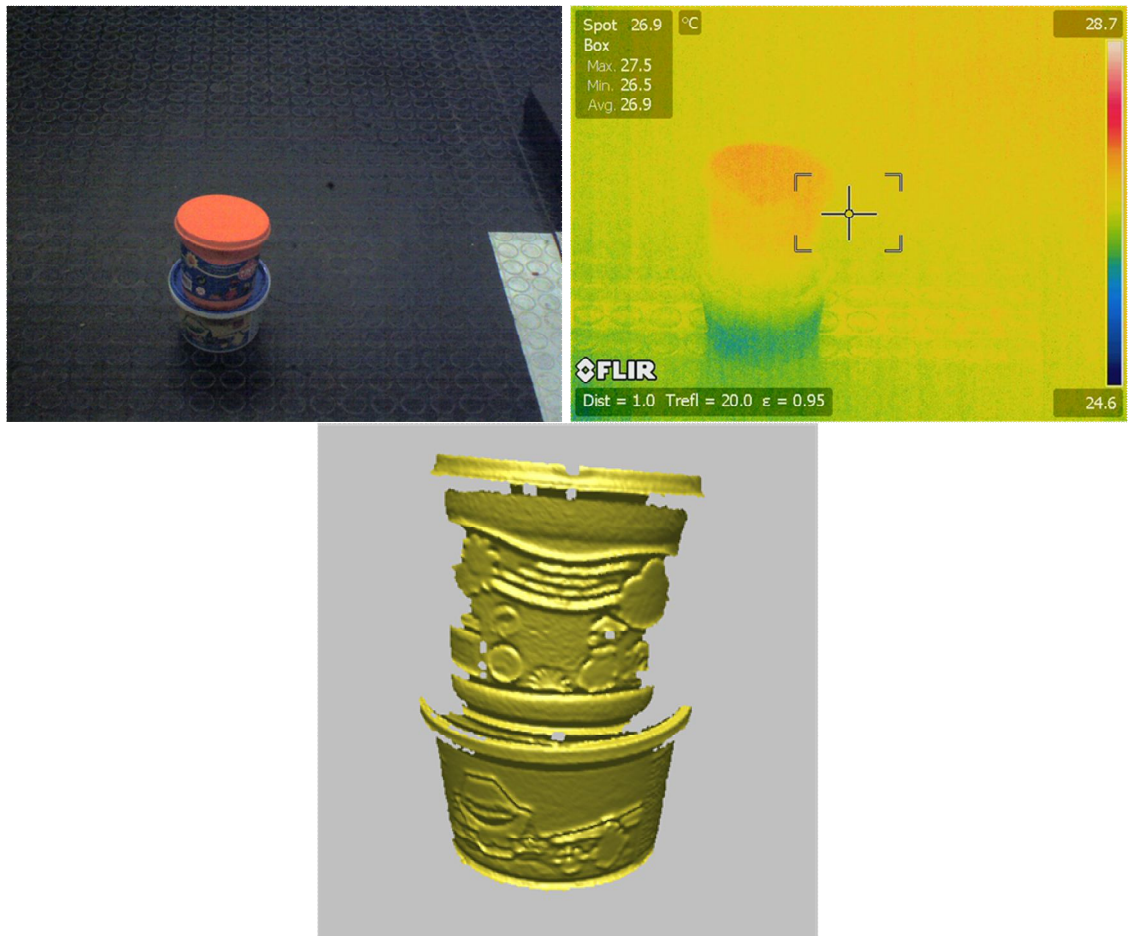


Figure 4.33 Experimental acquisitions: at the top, the visible and IR images acquired with the thermal-camera; at the bottom, the 3D acquired shape

During the acquisition phase, the thermal-camera was connected to the laser scanner through the connecting devices above mentioned. Thus, some translation parameters referred to instrument's dimensions and device structure. A rotational movement was then necessary to focus the same frame: the tripod head was rotated, around its axis of 15° ($\pi/12$ rad). The used laser scanner lens were of middle type, with a

focal distance of 14 mm; 35426 points were acquired and the final mesh was formed by 69358 triangles.

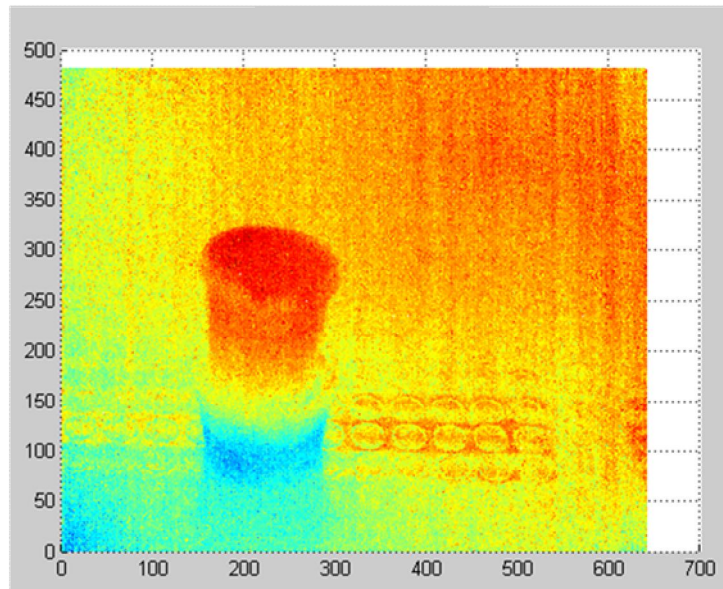


Figure 4.34 Thermographic image in pixel coordinates, as viewed in *Matlab*

The acquired thermogram and the 3D shape were first uploaded in *Matlab* environment (Figure 4.34) and then the registration procedure was performed using input translation and rotation parameters and instruments' optical features. For each of 35426 acquired points a temperature value is associated (Figure 4.35).

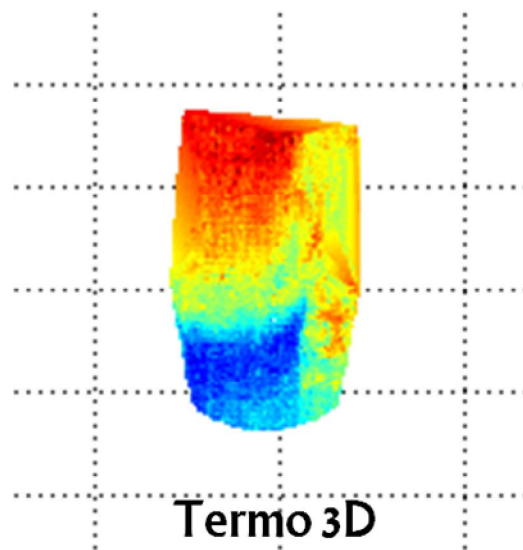


Figure 4.35 3D thermogram as represented in Matlab environment: after the registration procedure, a temperature value is coupled with each acquired point

The correction procedure was then performed: taking into account point's coordinates and their normal vectors, a correction factor was determined for each point and then used as multiplicative factor to correct each temperature value. In Table 4.2, some values related the minimum value, the maximum value, and the mean value of the correction factor are noted. After the temperature correction procedure, the mean difference between temperature before and after the correction procedure was of 0.7650°C.

Minimum Correction Factor	1.0275
Maximum Correction Factor	1.0292
Mean Correction Factor	1.0286
Mean Temperature Difference dt	0.7650

Table 4.2 Thermography correction: some notable values

Data collected were thus represented in a suitable environment. A preliminary visualization was set up into the 3D software. A RGB value was assigned to each point, in correspondence to its temperature value: a linear dependence was considered and a gray color map was created, in which the high temperature value was related to a clearer color, and a higher temperature value was connected to a darker color in the color map scale. Figure 4.36 shows a screenshot in which the 3D surface is displayed with its corrected associated thermogram value. Even if the 3D shape quality offers a clear representation, this visualization environment does not offer the possibility to investigate interactively point's temperature values. Points and temperature are thus displayed in a dedicated stand-alone application.



Figure 4.36 Thermographic 3D representation into a 3D software

The final mesh, in a *stl* file format, and the associated temperature values were loaded into the prototyped visualization tool. It offered the possibility to change color pallets (Figure 4.37) and to consult each triangle of the loaded mesh, in order to know temperature values of each point (Figure 4.38).

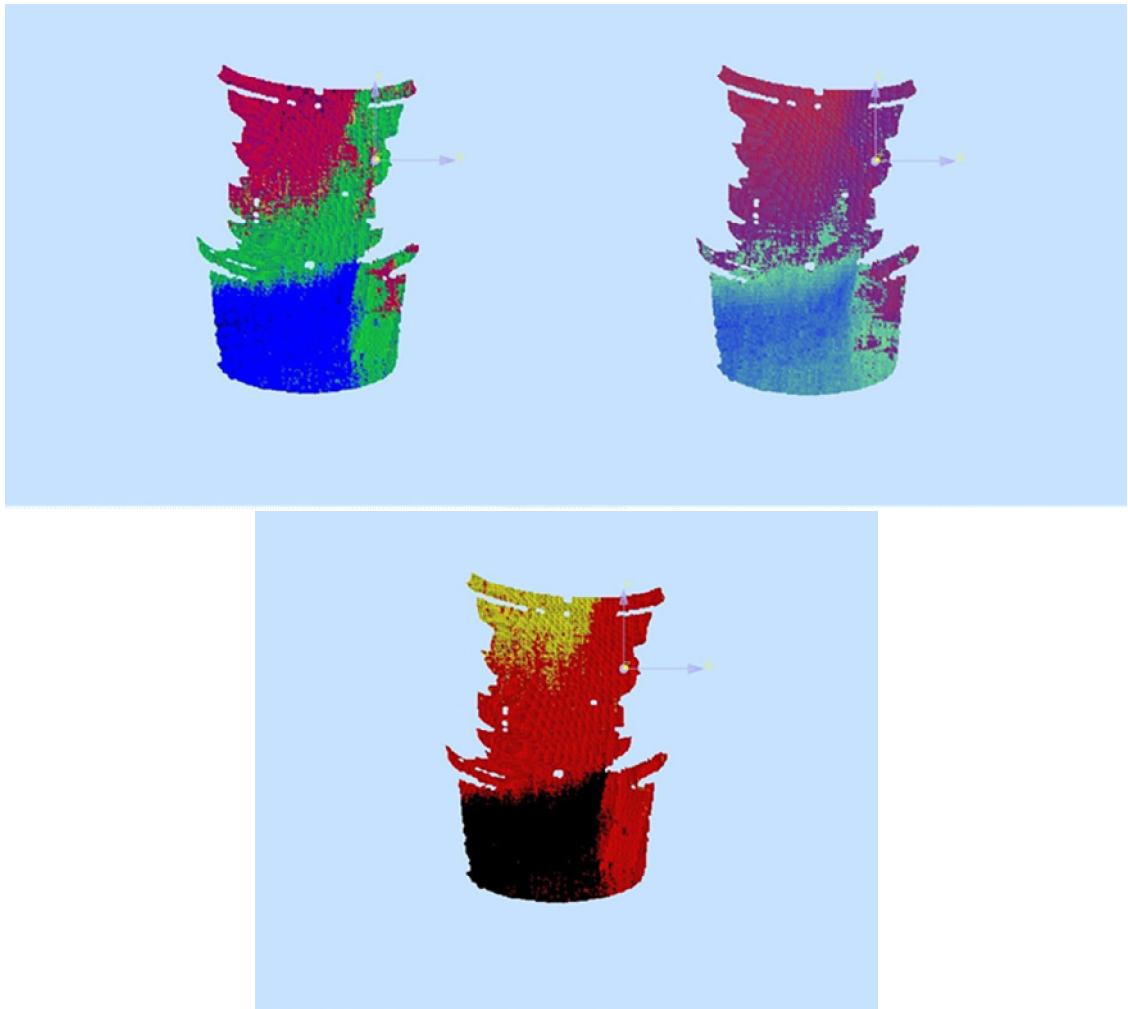


Figure 4.37 The prototyped visualization tool: more color maps are created

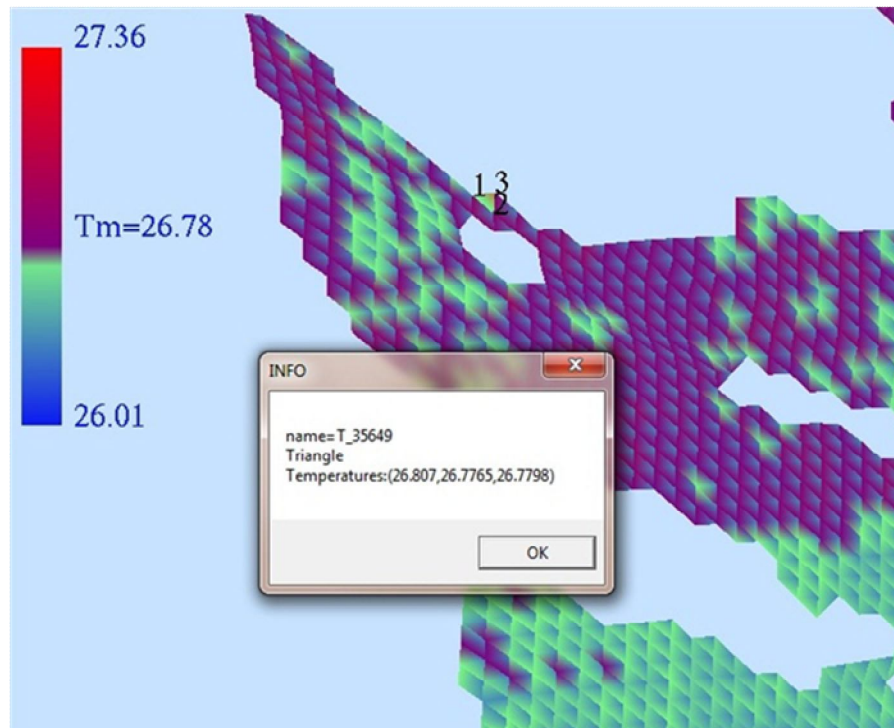


Figure 4.38 The prototyped visualization tool: each triangle of the mesh of study includes point's temperature information

Conclusions

During this research activity, two different advanced methods and techniques have been developed in order to increase measurement accuracy for laser scanner data , and to integrate thermographic data with geometrical information.

The key point of proposed methodologies is the independency of both workflows to specific instrument used: both error correction process and data fusion procedure can be applied in the same way to different laser scanner and thermographic devices. They are independent from instruments features, like resolution, CCD sensor or detector sizes or lenses and their focus distances.

Finally, both presented techniques can be applied to a lot of different scientific areas, in which both Reverse Engineering and thermography are currently widely used, such as, for example, non destructive testing, civil engineering, industrial processes, cultural heritage and biomedical context.

As regards **error analysis**, the presented activity is focused on the identification of systematic error portion, with the aim to define different compensation arrays identified on the ground of some specific operative conditions: for example, a different

array is found in relation to scanning focus distance, used lens and specimen normal directions, in order to improve measurement accuracy. Finally, an array library has been defined.

The proposed methodology will improve scanning quality, particularly useful in those case studies in which high data accuracy is strongly required: quality control and design processes of small components or of precision tools and systems are some potential “*stakeholders*” in industrial engineering. In cultural heritage, Reverse Engineering systems are widely used as restoring support tools for monitoring systems: within this context, little changes in an artwork surface, due to sediments or to usury, is extremely important to be visible and clearly identified. For this reason, little errors in points coordinates definition are an obstacle to shapes exploration and analysis.

Even if the usability of defined correction arrays is strictly limited to the instrument used (they are related to laser scanner serial number, since error systematic portion is connected to instrument features), the whole process can be applied to other different laser scanner instruments, since a rigorous and repeatable methodology has been defined. Within this context, an interesting development is related to time-of-flight laser scanners: even if their physical process for point definition is quite different, the correction workflow could be adapted to such instruments.

Moreover, even if a quite large error compensation library has been already defined, some more activities can be developed to improve the correction process. The

first aspect is related to the integration of the exploration of non rectangular arrays: the methodology to integrate two different arrays acquired with different focusing distances seems promising, but some uncertainties are induced and they have to be defined. In addition, in order to make methodology more appealing and faster, it should be useful to implement an automatic toolbox for 3D modeling software, which in this work is presented as a prototype.

Data fusion process aims to realize a **3D thermogram**, in which temperature values are related to the associated 3D points. Such procedure intends to represent both data, temperature values and 3D points, in the same environment, so that it will be possible to investigate physical properties together with geometrical features for each surface point. Moreover, this temperature – point association allows to make thermography inspection more quantitative reliable, since it is independent from the inspection point of view.

These data fusion and correction processes give the possibility to improve the inspection practice, since data obtained are clearer and more easily interpretable; in addition, it must underlined that the methodology is independent from specific instruments used. These features make the proposed methodology appealing for all potential inspections and testing in which thermography employment is required. In particular, defect detection and location will be easier, even if particular morphological

elements are not present: this aspect is significant in civil engineering assessment, in which many case studies are connected to wide surfaces inspection and in situations in which the repeatability of the same element or geometrical feature will be creating cluttering effects. Moreover, temperature correction value is expected to offers many improvements in particular in active thermography inspection, in which a thermal transient is deeply examined.

Moreover, systems improvements can be achieved: a GPS like system could be used in order to obtain a more precise detection of set up configuration with thermal-camera and laser scanner . Furthermore, such system could allow to move both instruments into a large working area, without lose their reference systems connection. Moreover, an automatic application could be defined, implementing all phases of the presented workflow, in order to make the whole process more fast and user friendly.

Finally, the use of time-of-flight systems in place of triangulation laser scanners can be an interesting upgrade of the presented system. This aspect could extend the applicability of the 3D thermography method to many architectural case studying, where such scanning devices are currently widely used.

Appendix A

Laser Scanner Konica Minolta Vivid-9i technical notes

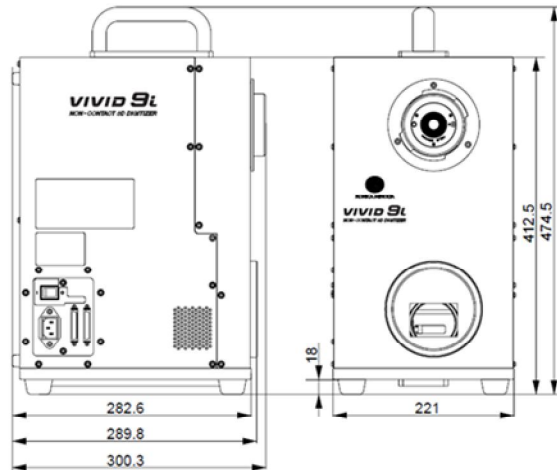


Figure 0.1 Dimension Diagram (unit mm)

Specifications

Model Name	Non-contact 3D digitizer VIVID 9i/VI-9i
Measurement Method	Triangulation, light block method
AF	Image surface AF (contrast method), Active AF
Light-Receiving lens (Interchangeable)	TELE: Focal distance $f=25$ mm MIDDLE: Focal distance $f=14$ mm WIDE: Focal distance $f=8$ mm
Object Distance Range	0.6 to 2.5 m
Scan Range	0.6 to 1.0 m (In Standard mode), 0.5 to 2.5 m (In Extended mode)
Laser Scan Method	Galvano mirror
Laser Class	Class 2 (IEC60825-1), Class 1 (FDA), Max. 30 mW, 690 nm
X Direction Input Range (In Extended mode)	93 to 463 mm (TELE), 165 to 823 mm (MIDDLE), 299 to 1495 mm (WIDE)
Y Direction Input Range (In Extended mode)	69 to 347 mm (TELE), 124 to 618 mm (MIDDLE),

	224 to 1121 mm (WIDE)
Z Direction Input Range (In Extended mode)	26 to 680 mm (TELE), 42 to 1100 mm (MIDDLE), 66 to 1750 mm (WIDE mode)
Accuracy	TELE XYZ ± 0.05 mm/ ± 0.10 mm MIDDLE XYZ ± 0.10 mm/ ± 0.20 mm WIDE XYZ ± 0.20 mm/ ± 0.40 mm (Conditions: Distance 0.6 m/ 1.0 m, KONICA MINOLTA SENSING's standard 3D chart, KONICA MINOLTA SENSING's processing software, temperature 20°C, relative humidity 65% or less)
Precision (Z, σ)	TELE 0.008 mm/ ± 0.024 mm MIDDLE 0.016 mm/ ± 0.048 mm WIDE 0.032 mm/ ± 0.096 mm (Conditions: Distance 0.6 m/ 1.0 m, KONICA MINOLTA SENSING's standard 2D chart, KONICA MINOLTA SENSING's processing software, temperature 20°C, relative humidity 65% or less)
Input Time (per scan)	2.5 sec.
Transfer Time to Host Computer	Approx. 1.5 sec.
Ambient Lighting Condition	Office environment, 500 lx or less
Imaging Element	3D data: 1/3-inch frame transfer CCD (340,000 pixels) Color data: Common with 3D data (color separation by rotary filter)
Number of Output Pixels	3D data: 640 × 480 (640 × 460 in the HIGH QUALITY mode) Color data: 640 × 480
Output Format	3D data: Konica Minolta format, & (STL, DXF, OBJ, ASCII points, VRML) (Converted to 3D data by the Polygon Editing Tool Software / standard accessory) Color data: RGB 24-bit raster scan data
Data File Size	Total 3D and color data capacity: 3.6 MB per data
Viewfinder	5.7-inch LCD (320 × 240 picture elements) * There may be rare cases in which the point that is normally lit or unlit may break up (dot break up); however, this will not have any influence on the scanning data.
Output Interface	SCSI II (DMA synchronous transfer)

Power	Commercial AC power, 100-240 V (50-60Hz), rated current 0.6 A (at 100 VAC)
Dimensions	221 (W) × 412 (H) × 282 (D) mm
Mass Approx.	15 kg (with lens attached)
Temperature / Humidity	Operating environment: 10 to 40°C (50°F to 104°F); 65% RH or less/no condensation; Installation category: II; Pollution degree 2; Maximum altitude 2000 m
Storage Temperature Range	0 to 40°C, 85% or less (at 35°C)/no condensation

Appendix B

Results: Laser beam perpendicular to the reference surface

In this section some more details are presented as support to the definition of the correction arrays for systematic component of error. Tables and figures are added in order to provide more information on data acquired and perform corrections.

N° of mean arrays	MEAN RESX	MEAN RESY	MIN RESX	MIN RESY	MAX RESX	MAX RESY
1	0.2548	0.2548	0.2272	0.2356	0.2817	0.2805
2	0.2548	0.2548	0.2267	0.2350	0.2811	0.2775
3	0.2548	0.2548	0.2266	0.2348	0.2824	0.2770
4	0.2548	0.2548	0.2266	0.2350	0.2806	0.2770
5	0.2548	0.2548	0.2250	0.2351	0.2799	0.2761
6	0.2548	0.2548	0.2270	0.2353	0.2793	0.2766
7	0.2548	0.2548	0.2257	0.2352	0.2789	0.2757
8	0.2548	0.2548	0.2264	0.2347	0.2785	0.2766
9	0.2548	0.2548	0.2268	0.2359	0.2781	0.2761
10	0.2548	0.2548	0.2264	0.2350	0.2790	0.2762
11	0.2548	0.2548	0.2259	0.2362	0.2793	0.2762
12	0.2548	0.2548	0.2271	0.2362	0.2783	0.2760
13	0.2548	0.2548	0.2256	0.2359	0.2793	0.2764
14	0.2548	0.2548	0.2256	0.2359	0.2799	0.2778
15	0.2548	0.2548	0.2257	0.2358	0.2795	0.2774
16	0.2548	0.2548	0.2242	0.2358	0.2786	0.2775

17	0.2548	0.2548	0.2240	0.2361	0.2781	0.2776
18	0.2548	0.2548	0.2260	0.2356	0.2786	0.2775
19	0.2548	0.2548	0.2261	0.2363	0.2785	0.2777
20	0.2548	0.2548	0.2263	0.2358	0.2798	0.2776

Table 0.1 Mean, Min and max resolution values in X and Y directions, in function of the number of arrays involved in the mean process. Tele lens, 900 mm distance.

N° of mean arrays	MEAN RESX	MEAN RESY	MIN RESX	MIN RESY	MAX RESX	MAX RESY
1	0.3127	0.3127	0.2890	0.2888	0.3408	0.3349
2	0.3127	0.3127	0.2897	0.2908	0.3366	0.3348
3	0.3127	0.3127	0.2926	0.2920	0.3352	0.3330
4	0.3127	0.3127	0.2921	0.2923	0.3352	0.3325
5	0.3127	0.3127	0.2909	0.2898	0.3342	0.3338
6	0.3127	0.3127	0.2921	0.2920	0.3293	0.3330
7	0.3127	0.3127	0.2891	0.2929	0.3328	0.3334
8	0.3127	0.3127	0.2908	0.2938	0.3330	0.3332
9	0.3127	0.3127	0.2909	0.2935	0.3323	0.3332
10	0.3127	0.3127	0.2893	0.2936	0.3336	0.3337
11	0.3127	0.3127	0.2904	0.2928	0.3333	0.3328
12	0.3127	0.3127	0.2898	0.2932	0.3328	0.3324
13	0.3127	0.3127	0.2909	0.2939	0.3340	0.3339
14	0.3127	0.3127	0.2866	0.2942	0.3325	0.3349
15	0.3127	0.3127	0.2859	0.2938	0.3324	0.3344

16	0.3127	0.3127	0.2920	0.2929	0.3329	0.3339
17	0.3127	0.3127	0.2892	0.2926	0.3354	0.3350
18	0.3127	0.3127	0.2868	0.2935	0.3357	0.3338
19	0.3127	0.3127	0.2869	0.2942	0.3330	0.3334
20	0.3127	0.3127	0.2882	0.2930	0.3347	0.3349

Table 0.2 Mean, Min and max resolution values in X and Y directions, in function of the number of arrays involved in the mean process. Middle lens, 600 mm distance.

N° of mean arrays	MEAN RESX	MEAN RESY	MIN RESX	MIN RESY	MAX RESX	MAX RESY
1	0.4529	0.4530	0.3956	0.4035	0.5077	0.5007
2	0.4529	0.4530	0.4014	0.4071	0.5027	0.5012
3	0.4529	0.4530	0.4061	0.4096	0.5043	0.4992
4	0.4529	0.4530	0.4020	0.4081	0.5031	0.5032
5	0.4529	0.4530	0.4008	0.4079	0.5038	0.5028
6	0.4529	0.4530	0.3978	0.4092	0.5078	0.4990
7	0.4529	0.4530	0.3988	0.4105	0.5043	0.5007
8	0.4529	0.4530	0.4025	0.4091	0.5058	0.5025
9	0.4529	0.4530	0.4000	0.4084	0.5057	0.5025
10	0.4529	0.4530	0.4021	0.4075	0.5082	0.5049
11	0.4529	0.4530	0.4033	0.4057	0.5086	0.4999
12	0.4529	0.4530	0.4025	0.4087	0.5085	0.5008
13	0.4529	0.4530	0.4022	0.4070	0.5076	0.5024
14	0.4529	0.4530	0.3983	0.4045	0.5024	0.5038

15	0.4529	0.4530	0.3937	0.4018	0.5040	0.5033
16	0.4529	0.4530	0.3970	0.4018	0.5055	0.5033
17	0.4529	0.4530	0.4011	0.4052	0.5034	0.5018
18	0.4529	0.4530	0.4023	0.4051	0.5061	0.5004
19	0.4529	0.4530	0.3946	0.4071	0.5060	0.5051
20	0.4529	0.4530	0.3991	0.4072	0.5036	0.5014

Table 0.3 Mean, Min and max resolution values in X and Y directions, in function of the number of arrays involved in the mean process. Middle lens, 900 mm distance.

N° of mean arrays	MEAN RESX	MEAN RESY	MIN RESX	MIN RESY	MAX RESX	MAX RESY
1	0.5491	0.5494	0.4482	0.4732	0.6417	0.6289
2	0.5491	0.5494	0.4383	0.4728	0.6414	0.6254
3	0.5491	0.5494	0.4474	0.4778	0.6384	0.6239
4	0.5491	0.5494	0.4471	0.4754	0.6400	0.6227
5	0.5491	0.5494	0.4491	0.4773	0.6398	0.6221
6	0.5491	0.5494	0.4483	0.4765	0.6451	0.6236
7	0.5491	0.5494	0.4522	0.4729	0.6350	0.6254
8	0.5491	0.5494	0.4493	0.4748	0.6416	0.6218
9	0.5491	0.5494	0.4577	0.4728	0.6344	0.6245
10	0.5491	0.5494	0.4506	0.4761	0.6425	0.6242
11	0.5849	0.5494	0.4455	0.4810	0.6387	0.6226
12	0.5491	0.5494	0.4573	0.4740	0.6319	0.6241
13	0.5491	0.5494	0.4535	0.4727	0.6395	0.6238

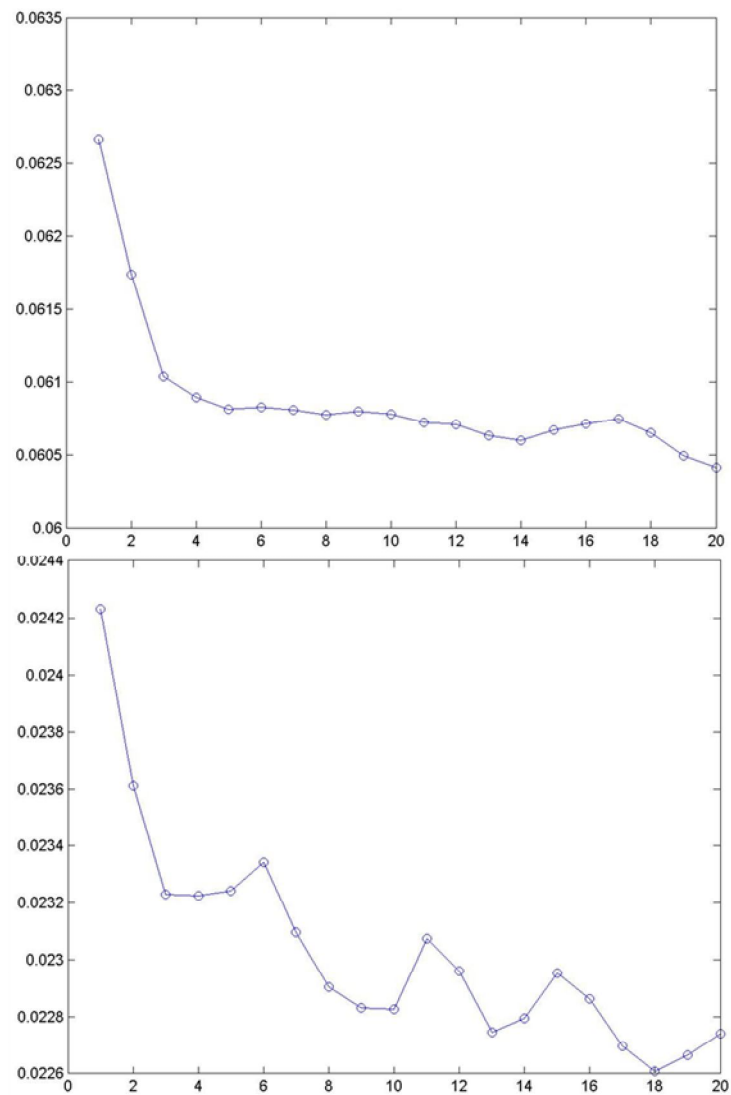
14	0.5491	0.5494	0.4520	0.4729	0.6334	0.6230
15	0.5491	0.5494	0.4601	0.4779	0.6376	0.6237
16	0.5491	0.5494	0.4622	0.4702	0.6340	0.6240
17	0.5491	0.5494	0.4560	0.4770	0.6415	0.6210
18	0.5491	0.5494	0.4553	0.4772	0.6276	0.6222
19	0.5491	0.5494	0.4566	0.4766	0.6386	0.6253
20	0.5491	0.5494	0.4523	0.4780	0.6324	0.6252

Table 0.4 Mean, Min and max resolution values in X and Y directions, in function of the number of arrays involved in the mean process. Wide lens, 600 mm distance.

N° of mean arrays	MEAN RESX	MEAN RESY	MIN RESX	MIN RESY	MAX RESX	MAX RESY
1	0.8070	0.8073	0.5066	0.5883	1.0707	0.9926
2	0.8070	0.8073	0.5495	0.6020	1.0579	1.0049
3	0.8070	0.8073	0.5324	0.6112	1.0500	0.9996
4	0.8070	0.8073	0.5307	0.6331	1.0437	1.0070
5	0.8070	0.8073	0.5702	0.6250	1.0666	0.9891
6	0.8070	0.8073	0.5690	0.6285	1.0402	0.9976
7	0.8070	0.8073	0.5583	0.6384	1.0667	1.0000
8	0.8070	0.8073	0.5799	0.6280	1.0597	0.9979
9	0.8070	0.8073	0.5833	0.6070	1.0486	0.9921
10	0.8070	0.8073	0.5637	0.6400	1.0567	0.9918
11	0.8070	0.8073	0.5722	0.6308	1.0410	0.9906
12	0.8070	0.8073	0.5872	0.6306	1.0533	0.9757

13	0.8070	0.8073	0.5706	0.6373	1.0438	0.9855
14	0.8070	0.8073	0.5777	0.6391	1.0483	0.9711
15	0.8070	0.8073	0.5709	0.6335	1.0598	0.9753
16	0.8070	0.8073	0.5988	0.6171	1.0635	0.9767
17	0.8070	0.8073	0.5854	0.6369	1.0636	0.9747
18	0.8070	0.8073	0.5782	0.6335	1.0642	0.9976
19	0.8070	0.8073	0.5829	0.6369	1.0655	1.0012
20	0.8070	0.8073	0.5652	0.6285	1.0528	0.9774

Table 0.5 Mean, Min and max resolution values in X and Y directions, in function of the number of arrays involved in the mean process. Wide lens, 900 mm distance.



**Figure 0.1 Standard deviation trend in function of the number of averaged arrays:
Tele lens and scanning distance of 600mm (on the top) and 900 mm (on the bottom)**

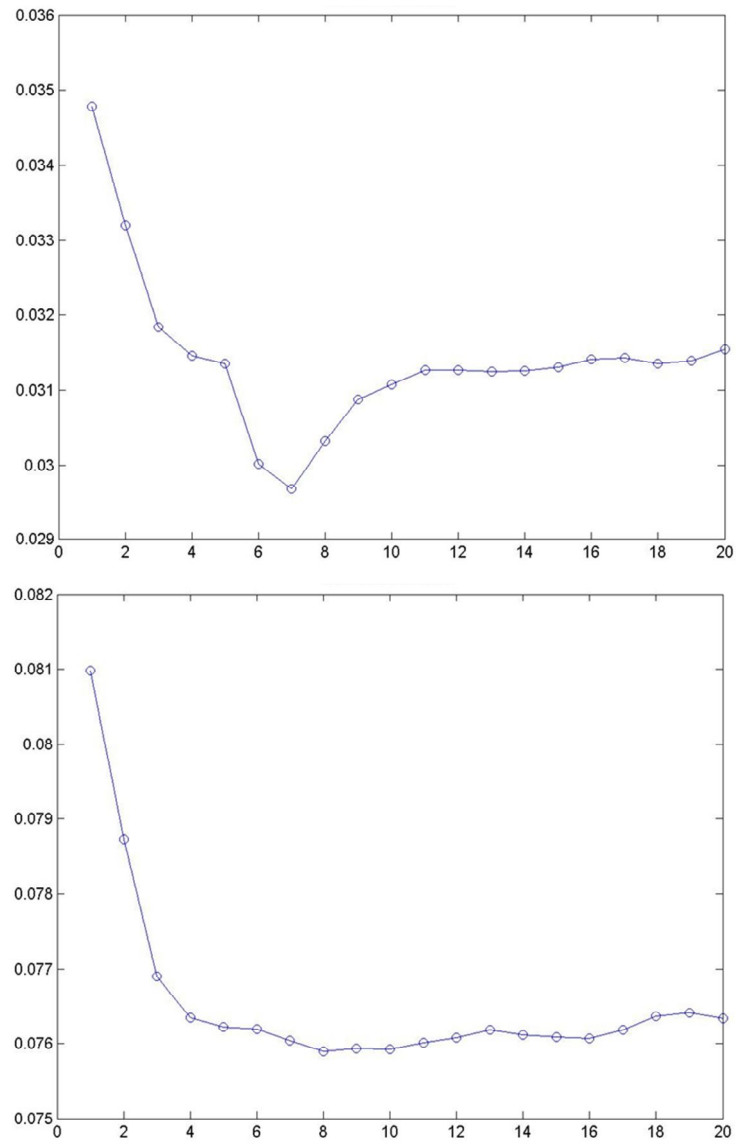


**Figure 0.2 Standard deviation trend in function of the number of averaged arrays:
Middle lens and scanning distance of 600mm (on the top) and 900 mm (on the bottom)**

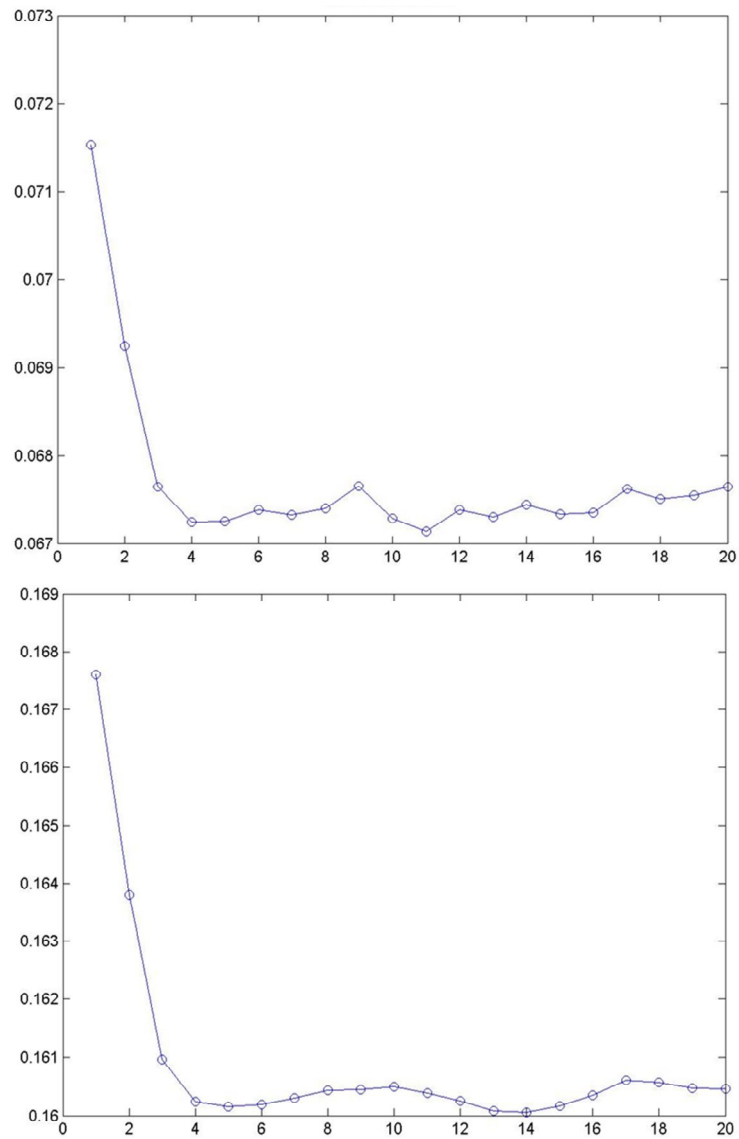


**Figure 0.3 Standard deviation trend in function of the number of averaged arrays:
Wide lens and scanning distance of 600mm (on the top) and 900 mm (on the bottom)**

AVERAGED ARRAYS	SRF.DEV.	STD.DEV.
1	0.1318	0.0242
2	0.1249	0.0234
3	0.1273	0.0233
4	0.1268	0.0234

5	0.127	0.0234
6	0.1397	0.0236
7	0.1366	0.023
8	0.1296	0.0231
9	0.138	0.0229
10	0.1297	0.0231
11	0.1268	0.0233
12	0.1283	0.0229
13	0.1242	0.0228
14	0.1285	0.023
15	0.1242	0.0231
16	0.1223	0.0229
17	0.1213	0.0228
18	0.1239	0.0227
19	0.1228	0.0229
20	0.1229	0.0230

**Table 0.6 Surface and standard deviation in relation to the number of averaged arrays.
Tele lens and 900 mm distance. All values are in mm**

AVERAGED ARRAYS	SRF.DEV.	STD.DEV.
1	0.1643	0.0348
2	0.1539	0.0326
3	0.1470	0.0319
4	0.1546	0.0318
5	0.1521	0.0317
6	0.1405	0.0300
7	0.1432	0.0303
8	0.1490	0.0311
9	0.1504	0.0314
10	0.1558	0.0315
11	0.1534	0.0317
12	0.1634	0.0315
13	0.1630	0.0317

14	0.1476	0.0316
15	0.1512	0.0317
16	0.1570	0.0319
17	0.1494	0.0318
18	0.1549	0.0317
19	0.1578	0.0319
20	0.1491	0.0319

**Table 0.7 Surface and standard deviation in relation to the number of averaged arrays.
Middle lens and 600 mm distance. All values are in mm**

AVERAGED ARRAYS	SRF.DEV.	STD.DEV.
1	0.5253	0.0810
2	0.5125	0.0779
3	0.4935	0.0771
4	0.4928	0.0767
5	0.5100	0.0769
6	0.5243	0.0767
7	0.5235	0.0765
8	0.5209	0.0765
9	0.5133	0.0765
10	0.5152	0.0765
11	0.4978	0.0766
12	0.5208	0.0767
13	0.5267	0.0768
14	0.5005	0.0766
15	0.4993	0.0767
16	0.4971	0.0767
17	0.4843	0.0769
18	0.4845	0.0770
19	0.5182	0.0769
20	0.5111	0.0769

**Table 0.8 Surface and standard deviation in relation to the number of averaged arrays.
Middle lens and 900 mm distance. All values are in mm**

AVERAGED ARRAYS	SRF.DEV.	STD.DEV.
1	0.3210	0.0715
2	0.3257	0.0685
3	0.3326	0.0678
4	0.3438	0.0677
5	0.3389	0.0677
6	0.3368	0.0679
7	0.3545	0.0678
8	0.3473	0.0680
9	0.3320	0.0682
10	0.3335	0.0675
11	0.3407	0.0677
12	0.3456	0.0679
13	0.3522	0.0677
14	0.3324	0.0680
15	0.3386	0.0677
16	0.3381	0.0680
17	0.3259	0.0682
18	0.3451	0.0679
19	0.3372	0.0681
20	0.3413	0.0681

**Table 0.9 Surface and standard deviation in relation to the number of averaged arrays.
Wide lens and 600 mm distance. All values are in mm**

AVERAGED ARRAYS	SRF.DEV.	STD.DEV.
1	0.8458	0.1676
2	0.8020	0.1625
3	0.7945	0.1614
4	0.8235	0.1610
5	0.7664	0.1611
6	0.7514	0.1611
7	0.7635	0.1613
8	0.7838	0.1614

9	0.7676	0.1614
10	0.7561	0.1614
11	0.7910	0.1613
12	0.8190	0.1612
13	0.8361	0.1609
14	0.7683	0.1610
15	0.7747	0.1613
16	0.7653	0.1614
17	0.7696	0.1616
18	0.8249	0.1614
19	0.7610	0.1614
20	0.7951	0.1614

Table 0.10 Surface and standard deviation in relation to the number of averaged arrays. Wide lens and 900 mm distance. All values are in mm

Appendix C

Different materials emissivity values

This section provides a compilation of emissivity data from the infrared literature. These tables comes from Flir Manuals (www.flir.com)

Abbreviations used in table below:

- T: Total spectrum;
- SW: 2 – 5 μm ;
- LW: 8 – 14 μm ;
- LLW: 6.5 – 20 μm ;

<u>Material</u>	<u>Specification</u>	<u>Temperature °C</u>	<u>Spectrum</u>	<u>Emissivity</u>
3M type 35	vinyl electrical tape (several colors)	<80	LW	Ca. 0.96
3M type 88	black vinyl electrical tape	< 105	LW	Ca. 0.96
3M type 88	black vinyl electrical tape	< 105	MW	< 0.96
3M type Super 33+	black vinyl electrical tape	< 80	LW	Ca. 0.96
Aluminum	anodized, black, dull	70	LW	0.95
Aluminum	anodized, black, dull	70	SW	0.67
Aluminum	anodized, light gray, dull	70	LW	0.97
Aluminum	anodized, light gray, dull	70	SW	0.61
Aluminum	anodized sheet	100	T	0.55

Aluminum	as received, plate	100	T	0.09
Aluminum	as received, sheet	100	T	0.09
Aluminum	cast, blast cleaned	70	LW	0.46
Aluminum	cast, blast cleaned	70	SW	0.47
Aluminum	dipped in HNO ₃ plate	100	T	0.05
Aluminum	foil	27	3μm	0.09
Aluminum	foil	27	10μm	0.04
Aluminum	oxidized, strongly	50-500	T	0.2-0.3
Aluminum	polished	50-100	T	0.04-0.06
Aluminum	polished, sheet	100	T	0.05
Aluminum	polished, plate	100	T	0.06
Aluminum	roughened	27	3μm	0.28
Aluminum	roughened	28	10μm	0.18
Aluminum	rough surface	20-50	T	0.06-0.07
Aluminum	sheet, 4 samples differently scratched	70	LW	0.03-0.06
Aluminum	sheet, 4 samples differently scratched	70	SW	0.05-0.08
Aluminum	vacuum deposited	20	T	0.04
Aluminum	weathered, heavily	17	SW	0.83-0.94
Aluminum bronze		20	T	0.60
Aluminum hydroxide	powder		T	0.28
Aluminum oxide	activated, powder		T	0.46
Aluminum oxide	pure, powder (alumina)		T	0.16
Asbestos	board	20	T	0.96
Asbestos	fabric		T	0.78

Asbestos	floor tile	35	SW	0.94
Asbestos	paper	40-400	T	0.93-0.95
Asbestos	powder		T	0.40-0.60
Asbestos	slate	20	T	0.96
Asphalt paving		4	LLW	0.967
Brass	dull, tarnished	20-350	T	0.22
Brass	oxidized	70	SW	0.04-0.09
Brass	oxidized	70	LW	0.03-0.07
Brass	oxidized	100	T	0.61
Brass	oxidized at 600°C	200-600	T	0.59-0.61
Brass	polished	200	T	0.03
Brass	polished, highly	100	T	0.03
Brass	rubber with 80 grit emery	20	T	0.20
Brass	sheet, rolled	20	T	0.06
Brass	sheet, worked with emery	20	T	0.2
Brick	alumina	17	SW	0.68
Brick	common	17	SW	0.86-0.81
Brick	Dinas silica glazed, rough	1100	T	0.85
Brick	Dinas silica, refractory	1000	T	0.66
Brick	Dinas silica unglazed, rough	1000	T	0.80
Brick	firebrick	17	SW	0.68
Brick	fireclay	20	T	0.85
Brick	fireclay	1000	T	0.75
Brick	fireclay	1200	T	0.59
Brick	masonry	35	SW	0.94
Brick	masonry, plastered	20	T	0.94
Brick	red common	20	T	0.93
Brick	red, rough	20	T	0.88-0.93
Brick	refractory, corundum	1000	T	0.46
Brick	refractory, magnet site	1000-1300	T	0.38

Brick	refractory, strongly radiating	500-1000	T	0.8-0.9
Brick	refractory, weakly radiating	500-1000	T	0.65-0.75
Brick	silica, 95% SiO ₂	1230	T	0.66
Brick	Sillimanite, 33% SiO ₂ , 64 Al ₂ O ₃	1500	T	0.29
Brick	waterproof	17	SW	0.87
Bronze	phosphor bronze	70	LW	0.06
Bronze	phosphor bronze	70	SW	0.08
Bronze	polished	50	T	0.1
Bronze	porous, rough	50-150	T	0.55
Bronze	powder		T	0.76-0.80
Carbon	candle soot	20	T	0.95
Carbon	charcoal powder		T	0.96
Carbon	graphite, filed surface	20	T	0.98
Carbon	graphite powder		T	0.97
Carbon	lampblack	20-400	T	0.95-0.97
Chipboard	untreated	20	SW	0.9
Chromium	polished	50	T	0.1
Chromium	polished	500-1000	T	0.28-0.38
Clay	fired	70	T	0.91
Cloth	Black	20	T	0.98
Concrete		20	T	0.92
Concrete	dry	36	SW	0.95
Concrete	rough	17	SW	0.97
Concrete	walkway	5	LLW	0.974
Copper	commercial, burnished	20	T	0.07
Copper	electrolytic, carefully polished	80	T	0.018
Copper	electrolytic, polished	-34	T	0.006
Copper	molten	1100-1300	T	0.13-0.15
Copper	oxidized	50	T	0.6-0.7

Copper	oxidized, black	27	T	0.78
Copper	oxidized, heavily	20	T	0.78
Copper	oxidized to blackness		T	0.88
Copper	polished	50-100	T	0.02
Copper	polished	100	T	0.03
Copper	polished, commercial	27	T	0.03
Copper	polished, mechanical	22	T	0.015
Copper	pure, carefully prepared surface	22	T	0.008
Copper	scraped	27	T	0.07
Copper dioxide	powder		T	0.84
Copper oxide	red, powder		T	0.70
Ebonite			T	0.89
Emery	coarse	80	T	0.85
Enamel		20	T	0.9
Enamel	lacquer	20	T	0.85-0.95
Fiber board	hard, untreated	20	SW	0.85
Fiber board	masonite	70	LW	0.88
Fiber board	masonite	70	SW	0.75
Fiber board	particle board	70	LW	0.89
Fiber board	particle board	70	SW	0.77
Fiber board	porous, untreated	20	SW	0.85
Gold	polished	130	T	0.018
Gold	polished, carefully	200-600	T	0.02-0.03
Gold	polished, highly	100	T	0.02
Granite	polished	20	LLW	0.849
Granite	rough	21	LLW	0.879
Granite	rough, 4 different samples	70	LW	0.77-0.87
Granite	rough, 4 different samples	70	SW	0.95-0.97
Gypsum		20	T	0.8-0.9

Ice: see water				
Iron, cast	casting	50	T	0.81
Iron, cast	ingots	1000	T	0.95
Iron, cast	liquid	1300	T	0.28
Iron, cast	machined	800-1000	T	0.60-0.70
Iron, cast	oxidized	38	T	0.63
Iron, cast	oxidized	100	T	0-64
Iron, cast	oxidized	260	T	0.66
Iron, cast	oxidized	538	T	0.76
Iron, cast	oxidized at 600°C	200-600	T	0.64-0.78
Iron, cast	polished	40	T	0.21
Iron, cast	polished	200	T	0.21
Iron, cast	unworked	900-1100	T	0.87-0.95
Iron and steel	cold rolled	70	LW	0.09
Iron and steel	cold rolled	70	SW	0.20
Iron and steel	covered with red rust	20	T	0.61-0.85
Iron and steel	electrolytic	22	T	0.05
Iron and steel	electrolytic	100	T	0.05
Iron and steel	electrolytic	260	T	0.07
Iron and steel	electrolytic, carefully polished	175-225	T	0.05-0.06
Iron and steel	freshly worked with emery	20	T	0.24
Iron and steel	ground sheet	950-1100	T	0.55-0.61
Iron and steel	heavily rusted sheet	20	T	0.69
Iron and steel	hot rolled	20	T	0.77
Iron and steel	hot rolled	130	T	0.60
Iron and steel	oxidized	100	T	0.74
Iron and steel	oxidized	125-525	T	0.78-0.82
Iron and steel	oxidized	1227	T	0.89
Iron and steel	oxidized strongly	50	T	0.88
Iron and steel	oxidized strongly	500	T	0.98
Iron and steel	polished	100	T	0.07
Iron and steel	polished	400-1000	T	0.14-0.38

Iron and steel	polished sheet	750-1050	T	0.52-0.56
Iron and steel	rolled, freshly	20	T	0.24
Iron and steel	rolled, sheet	50	T	0.56
Iron and steel	rough, plane surface	50	T	0.95-0.98
Iron and steel	rusted, heavily	17	SW	0.96
Iron and steel	rusted red, sheet	22	T	0.69
Iron and steel	rusty, red	20	T	0.69
Iron and steel	shiny, etched	150	T	0.16
Iron and steel	shiny oxide layer, sheet	20	T	0.82
Iron and steel	wrought, carefully polished	40-250	T	0.28
Iron galvanized	heavily oxidized	70	LW	0.85
Iron galvanized	heavily oxidized	70	SW	0.64
Iron galvanized	sheet	92	T	0.07
Iron galvanized	sheet, burnished	30	T	0.23
Iron galvanized	sheet, oxidized	20	T	0.28
Iron tinned	sheet	24	T	0.064
Krylon Ultra-flat black 1602	flat black	room temperature up to 175	LW	Ca. 0.96
Krylon Ultra-flat black 1603	flat black	room temperature up to 176	MW	Ca. 0.97
Lacquer	3 colors sprayed on Aluminum	70	LW	0.92-0.94
Lacquer	4 colors sprayed on Aluminum	70	SW	0.50-0.53
Lacquer	aluminum on rough surface	20	T	0.4
Lacquer	Bakelite	80	T	0.83
Lacquer	black, dull	40-100	T	0.96-0.98
Lacquer	black, matte	100	T	0.97
Lacquer	black, shiny, sprayed on iron	20	T	0.87
Lacquer	heat-resistant	100	T	0.92
Lacquer	white	40-100	T	0.8-0.95
Lacquer	white	100	T	0.92

Lead	oxidized, gray	20	T	0.28
Lead	oxidized at 200°C	200	T	0.63
Lead	shiny	250	T	0.08
Lead	unoxidized, polished	100	T	0.05
Lead red		100	T	0.93
Lead red, powder		100	T	0.93
Leather	tanned		T	0.75-0.80
Lime			T	0.3-0.4
Magnesium		22	T	0.07
Magnesium		260	T	0.13
Magnesium		538	T	0.18
Magnesium	polished	20	T	0.07
Magnesium powder			T	0.86
Molybdenum		600-1000	T	0.08-0.13
Molybdenum		1500-2200	T	0.19-0.26
Molybdenum	filament	700-2500	T	0.1-0.3
Mortar		17	SW	0.87
Mortar	dry	36	SW	0.94
Nextel Velvet 811-Black	Flat black	-60 - 150	LW	> 0.97
Nichrome	rolled	700	T	0.25
Nichrome	sandblasted	700	T	0.70
Nichrome	wire, clean	50	T	0.65
Nichrome	wire, clean	500-1000	T	0.71-0.79
Nichrome	wire, oxidized	50-500	T	0.95-0.98
Nickel	bright matte	122	T	0.041
Nickel	commercially pure, polished	100	T	0.045
Nickel	commercially pure, polished	200-400	T	0.07-0.09
Nickel	electrolytic	22	T	0.04
Nickel	electrolytic	38	T	0.06
Nickel	electrolytic	260	T	0.07
Nickel	electrolytic	538	T	0.10
Nickel	electroplated, polished	20	T	0.05

Nickel	electroplated on iron polished	22	T	0.045
Nickel	electroplated on iron unpolished	20	T	0.11-0.40
Nickel	electroplated on iron unpolished	22	T	0.11
Nickel	oxidized	200	T	0.37
Nickel	oxidized	1227	T	0.85
Nickel	oxidized at 600°C	200-600	T	0.37-0.48
Nickel	polished	122	T	0.045
Nickel	wire	200-1000	T	0.1-0.2
Nickel oxide		500-650	T	0.52-0.59
Nickel oxide		1000-1250	T	0.75-0.86
Oil, lubricating	0.025 mm film	20	T	0.27
Oil, lubricating	0.050 mm film	20	T	0.46
Oil, lubricating	0.125 mm film	20	T	0.72
Oil, lubricating	film on Ni base	20	T	0.05
Oil, lubricating	thick coating	20	T	0.82
Paint			LW	0.92-0.94
Paint	8 different colors and qualities	70	SW	0.88-0.96
Paint	aluminum, various ages	50-100	T	0.27-0.67
Paint	cadmium yellow		T	0.28-0.33
Paint	chrome green		T	0.65-0.70
Paint	cobalt blue		T	0.7-0.8
Paint	oil	17	SW	0.87
Paint	oil, black flat	20	SW	0.94
Paint	oil, black gloss	20	SW	0.92
Paint	oil, gray flat	20	SW	0.97
Paint	oil, gray gloss	20	SW	0.96
Paint	oil, various colors	100	T	0.92-0.96
Paint	oil based, average of 16 colors	100	T	0.94
Paint	plastic, black	20	SW	0.95
Paint	plastic, white	20	SW	0.84
Paper	4 different colors	70	LW	0.92-0.94

Paper	4 different colors	70	SW	0.68-0.74
Paper	black		T	0.90
Paper	black, dull		T	0.94
Paper	black, dull	70	LW	0.89
Paper	black, dull	70	SW	0.86
Paper	blue, dark		T	0.84
Paper	coated with black lacquer		T	0.93
Paper	green		T	0.85
Paper	red		T	0.76
Paper	white	20	T	0.7-0.9
Paper	white 3 different glosses	70	LW	0.88-0.90
Paper	white 3 different glosses	70	SW	0.7-0.78
Paper	white bond	20	T	0.93
Paper	yellow		T	0.72
Plaster		17	SW	0.86
Plaster	plasterboard, untreated	20	SW	0.90
Plaster	rough coat	20	T	0.91
Plastic	glass fiber laminate (printed circ. board)	70	LW	0.91
Plastic	glass fiber laminate (printed circ. board)	70	SW	0.94
Plastic	polyurethane isolation board	70	LW	0.55
Plastic	polyurethane isolation board	70	SW	0.29
Plastic	PVC, plastic floor, dull, structured	70	LW	0.93
Plastic	PVC, plastic floor, dull, structured	70	SW	0.94
Platinum		17	T	0.016

Platinum		22	T	0.03
Platinum		100	T	0.05
Platinum		260	T	0.06
Platinum		538	T	0.10
Platinum		1000-1500	T	0.14-0.18
Platinum	pure, polished	200-600	T	0.05-0.10
Platinum	ribbon	900-1100	T	0.12-0.17
Platinum	wire	50-200	T	0.06-0.07
Platinum	wire	500-1000	T	0.10-0.16
Platinum	wire	1400	T	0.18
Porcelain	glazed	20	T	0.92
Porcelain	white, shiny		T	0.70-0.75
Rubber	hard	20	T	0.95
Rubber	soft, gray, rough	20	T	0.95
Sand			T	0.60
Sand		20	T	0.90
Sandstone	polished	19	LLW	0.909
Sandstone	rough	19	LLW	0.965
Silver	polished	100	T	0.03
Silver	pure, polished	200-600	T	0.02-0.03
Skin	human	32	T	0.98
Slag	boiler	0-100	T	0.97-0.93
Slag	boiler	200-500	T	0.89-0.78
Slag	boiler	600-1200	T	0.76-0.70
Slag	boiler	1400-1800	T	0.69-0.67
Snow: see water				
Soil	dry	20	T	0.92
Soil	saturated with water	20	T	0.95
Stainless steel	rolled	700	T	0.45
Stainless steel	sandblasted	700	T	0.70
Stainless steel	sheet, polished	70	LW	0.14
Stainless steel	sheet, polished	70	SW	0.18
Stainless steel	sheet, untreated, somewhat scratched	70	LW	0.28
Stainless steel	sheet, untreated, somewhat scratched	70	SW	0.30
Stainless steel	type 18-8 suffet	20	T	0.16

Stainless steel	type 18-8, oxidized at 800°C	60	T	0.85
Stucco	rough, lime	10-90	T	0.91
Styrofoam	insulation	37	SW	0.60
Tar			T	0.79-0.84
Tar	paper	20	T	0.91-0.93
Tile	glazed	17	SW	0.94
Tin	burnished	20-50	T	0.04-0.06
Tin	tin-plate sheet iron	100	T	0.07
Titanium	oxidized at 540°C	200	T	0.40
Titanium	oxidized at 540°C	500	T	0.50
Titanium	oxidized at 540°C	1000	T	0.60
Titanium	polished	200	T	0.15
Titanium	polished	500	T	0.20
Titanium	polished	1000	T	0.36
Tungsten		200	T	0.05
Tungsten		600-1000	T	0.1-0.16
Tungsten		1500-2200	T	0.24-.31
Tungsten	filament	3300	T	0.39
Varnish	flat	20	SW	0.93
Varnish	on oak parquet floor	70	LW	0.90-0.93
Varnish	on oak parquet floor	70	SW	0.90
Wallpaper	slight pattern, light gray	20	SW	0.85
Wallpaper	slight pattern, red	20	SW	0.90
Water	distilled	20	T	0.96
Water	frost crystals	-10	T	0.98
Water	ice, covered with heavy frost	0	T	0.98
Water	ice, smooth	-10	T	0.96
Water	ice, smooth	0	T	0.97

Water	layer > 0.1 mm thick	0-100	T	0.95-0.98
Water	snow		T	0.8
Water	snow	-10	T	0.85
Wood		17	SW	0.98
Wood		19	LLW	0.962
Wood	ground		T	0.5-0.7
Wood	pine, 4 different samples	70	LW	0.81-0.89
Wood	pine, 4 different samples	70	SW	0.67-0.75
Wood	planed	20	T	0.8-0.9
Wood	planed oak	20	T	0.90
Wood	planed oak	70	LW	0.88
Wood	planed oak	71	SW	0.77
Wood	plywood, smooth, dry	36	SW	0.82
Wood	plywood, untreated	20	SW	0.83
Wood	white, damp	20	T	0.7-0.8
Zinc	oxidized at 400°C	400	T	0.11
Zinc	oxidized surface	1000-1200	T	0.50-0.60
Zinc	polished	200-300	T	0.04-0.05
Zinc	sheet	50	T	0.20

Appendix D

File format supported by common 3D modeler tools

In this section some exchanging file format are presented, in relation to the information they are able to import and export. These information are acquired from *RapidForm (3D Systems Inc, Korea)* manual.

File Format	Import			Export			Note
	Texture	Material	View	Texture	Material	View	
<i>MDL</i>	O	O	O	O	O	O	Rapidform's own model data format(Binary)
<i>ICF</i>	O	O	X	O	O	X	INUS' Compression Format
<i>PTS</i>	X	O	X	X	O	O	FCS format has a normal information of vertex rapidform's own vertex data format(ASCII)
<i>FCS</i>	X	O	X	X	O	O	FCS format has a normal information of vertex Rapidform's own face data

							format(ASCII)
TPL	X	X	X	X	X	X	Rapidform's own template data format
ASC (Ascii Points / Arius3D)	X	X	X	X	X	X	RGB colored points are supported
SURF (Binary Points)	X	X	X	Import only			General point cloud exchange format
3DS (3D Studio)	O	O	X	O	O	X	A shell can have no more than 65,535 faces
DXF (AutoCAD)	X	X	X	X	X	X	Import : PolyMesh, 3Dface Export : Point, PolyMesh, 3Dface, PolyLine (Curve)
PLY (Cyberware)	X	X	X	X	X	X	
IV (Open Inventor)	O	O	X	O	O	X	
STL	X	X	X	X	X	X	Import : Binary, ASCII Export : Binary, ASCII

WRL <i>(VRML 1.0 / 97)</i>	O	O	X	O	O	X	RGB colored points are supported
OBJ <i>(Wavefront)</i>	X	X	X	X	X	X	Point Cloud and Polygonal Mesh
ASE <i>(ASCII Scene Export)</i>	O	O	X	Import Only			
HYM <i>(HyMarc)</i>	X	X	X	Import Only			
VVD/CDM/CAM/CDK <i>(Minolta Vivid)</i>	O	X	X	Import Only			CDM: Vivid900, CAM: Vivid700, CDK: Vivid9i
AC <i>(Steinbichler)</i>	X	X	X	Import Only			
VIEW/CLOUD <i>(GOM)</i>	X	X	X	Import Only			
CBK/GRK/CWK <i>(Kreon)</i>	X	X	X	Import Only			
PMJ/PMJX <i>(RealScan)</i>	X	X	X	Import Only			
BRE <i>(Breuckmann)</i>	X	X	X	Import Only			RGB colored points are supported
XYZ/TXT <i>(EOIS)</i>	X	X	X	Import Only			
SAB/SAB2 <i>(3D SCANNERS)</i>	X	X	X	Import Only			
NRF	O	X	X	Import Only			RGB colored

(NEC range finder)							points are supported
PTS (Cyra)	X	X	X	Import Only			
STB (Scantech)	X	X	X	Import Only			Scantech Binary Exchange format v1.0
PIX (Roland PICZA)	X	X	X	Import Only			
XYZ (Opton)	X	X	X	Import Only			
SWL/BIN/SWB (Perceptron)	X	X	X	Import Only			
RTPI/XYZI /XYZRGB (DeltaSphere)	X	X	X	Import Only			
IGS/IGES	X	X	X	X	X	X	points 106, 116
VDA (VDAFS)	X	X	X	Import Only			curve / surface
STP/STEP	X	X	X	X	X	X	curve / surface
IGS/IGES	X	X	X	X	X	X	curve / surface
3DM (Rhino)	X	X	X	X	X	X	curve / surface (openNURBS)
POV (PovRay)	Export only			X	X	X	
MTS (MetaStream)	Export only			O	X	X	
Soi (Mensi)	X	X	X	Import Only			
3PI (Shape Grabber)	X	X	X	Import Only			
ICV (Solutionix)	X	O	X	Import Only			

<i>TFM</i> <i>(Wicks and</i> <i>Wilsons)</i>	X	O	X	Import Only	
--	---	---	---	-------------	--

Appendix E

Thermo camera datasheet

Specifications Flir ThermaCAM™ SC640

IMAGING PERFORMANCE	
	<u>Thermal:</u>
Field of view/min focus distance	24°x18° /0.3 m
Spatial resolution (IFOV)	0.65 mrad
Thermal sensitivity	60mK at 30°C
Image frequency	30 Hz non-interlaced
Focus	Automatic or manual
Electronic zoom / pan function	1 - 8 x continuous, including pan function
Detector type	Focal Plane Array (FPA), uncooled microbolometer 640 x 480 pixels
Spectral range	7.5 to 13µm
Digital image enhancement	Normal and enhanced
	<u>Visual:</u>
Built-in digital video	1.3 Mpixel, full color / built-in Target Illuminator / exchangeable lens
Standard lens performance	f=8 mm / FOV 32°
IMAGE PRESENTATION	
Video output	RS170 EIA/NTSC or CCIR/PAL composite video, IEEE-1394 FireWire, USB
Viewfinder	Built-in, tiltable, high-resolution color viewfinder (800 x 480 pixels)
External display	Built-in 5.6" LCD (1024 x 600 pixels)
MEASUREMENT	
Temperature range	-40°C to +1,500°C, in 3 ranges; up to + 2000°C, optional
Accuracy	±2°C, ±2% of reading
Measurement mode	Spots/Areas (Boxes, Circles), Isotherms (above, below, interval), Delta T
Menu controls	Palettes , load custom palletes, auto adjust (manual/continuous/based on histogram

	equilization), on screen live and reference image (PoP), image gallery, sequence storage, programmable storage
Alarm Functions	Automatic alarm on any selected measurement function, audible/visible alarm above/below,
Set-up controls	Date/time, Temperature °C/°F, language
Atmospheric transmission correction	Automatic, based on inputs for distance, atmospheric temperature and relative humidity
Optics transmission correction	Automatic, based on signals from internal sensors
Emissivity correction	Variable from 0.01 to 1.0 or select from listings in pre-defined materials list
Reflected ambient temperature correction	Automatic, based on input of reflected temperature
External optics/window correction	Automatic, based on input of optics/window transmission and temperature
IMAGE STORAGE	
Type	Removable SD-card (1 GB) Built-in RAM memory for radiometric real-time sequence storage
File formats - Thermal	Standard JPEG, 14 bit measurement data included
File formats - Visual	Standard JPEG, automatically associated with corresponding thermal image / possibility for visual marker
Voice annotation of images	30 sec. of digital voice "clip" stored together with the image wired headset
Text annotation of images	Predefined text selected and stored together with the image
VIDEO STORAGE	
Type	Recording of fully radiometric IR-video clips in camera, transferable to SD-card Recording of MPEG-4 non-radiometric video to SD-card
VIDEO STREAMING	
Type	Fully radiometric real-time 14-bit digital

	IR-video using FireWire MPEG-4, IP-link using FireWire or USB
LENSES (OPTIONAL)	
Field of view/min focus distance	12° x 9° / 0.9m telelens 45° x 34° / 0.1m wide angle lens Close-up 50µm 32 mm x 24 mm / 75 mm
Lens identification	Automatic
LASER POINTER	
Classification	Class 2
Type	Semiconductor AlGaInP Diode Laser: 1mW/635 nm red
BATTERY SYSTEM	
Type	Li-Ion, rechargeable, field replaceable
Operating time	3 hours continuous operation
Charging system	in camera (AC adapter or 12 V from car) or 2 bay intelligent charger
External power operation	AC adapter 110/220 V AC, 50/60 Hz or 12 V from car (cable with Std plug: optional)
Power saving	Automatic shutdown and sleep mode (user selectable)
ENVIRONMENTAL SPECIFICATION	
Operating temperature range	-15°C to +50°C
Storage temperature range	-40°C to +70°C
Humidity	Operating and storage 10% to 95%, non- condensing
Encapsulation	IP 54 IEC 529
Shock	Operational: 25G, IEC 68-2-29
Vibration	Operational: 2G, IEC 68-2-6
PHYSICAL CHARACTERISTICS	
Weight	1.7 kg incl. battery
Size	120 mm x 145 mm x 220 mm
Tripod mounting	1/4" - 20
INTERFACES	
FireWire	IEEE-1394 FireWire output (real-time radiometric or non-radiometric video / filetransfer to PC)

USB	Image (thermal and visual), measurement, voice and text transfer to PC
IrDA	Wireless communication
SD-card (2)	I/O slot; storage slot

Technical data Testo 882

INFRARED IMAGE OUTPUT	
Detector type	FPA 320 x 240 pixels, a.Si
Thermal sensitivity (NETD)	< 60 mK bei 30 °C
Field of view/min. focus distance	32° x 23° / 0,2 m
Geometric resolution (IFOV)	1,7 mrad
SuperResolution (pixel / IFOV) - optional	640 x 480 pixels / 1,1 mrad
Image refresh rate	33 Hz*
Focus	manual and motor focus
Spectral range	8 to 14 µm
IMAGE OUTPUT VISUAL	
Image size / min. focus distance	640 x 480 pixels / 0.4 m
IMAGE PRESENTATION	
Image display	3.5" LCD with 320 x 240 pixels
Display options	IR image only / real image only / IR and real image
Video output	USB 2.0
Color palettes	9 (iron, rainbow, cold-hot, blue-red, grey, inverted grey, sepia, Testo, iron HT
MEASUREMENT	
Temperature range	-20 °C to +100 °C / 0 °C to +350 °C (switchable)
High temperature measurement - optional	+350 °C to +550 °C
Accuracy	±2 °C, ±2% of m.v. ±3% of m. v. (+350 °C to +550 °C)
Emissivity / reflected temperature	0.01 to 1 / manual
MEASURING FUNCTIONS	

Display of surface moisture distribution (using manual input)	X
Humidity measurement with radio humidity probe** (automatic measurement value transfer in real time)	X
Solar mode	X
Analysis function	Up to 2 measurement points, Hot/Cold Spot Recognition, Isotherms, Min-/Max on Area
IMAGER EQUIPMENT	
Digital camera	X
Power LEDs	X
Motor focus	X
Standard lens	32° x 23°
Laser*** (laser classification 635 nm, Class 2)	X
Voice recording	wired headset
Video streaming (via USB)	X
IMAGE STORAGE	
File format	.bmt; export options in .bmp, .jpg, .csv, .xls
Storage device	SD card 2 GB (approx. 1,000 images)
POWER SUPPLY	
Battery type	Fast-charging, Li-ion battery can be changed on-site
Operating time	4 hours
Charging options	In instrument/in charging station (optional)
Mains operation	Yes
AMBIENT CONDITIONS	
Operating temperature range	-15 °C to +40 °C
Storage temperature range	-30 °C to +60 °C
Air humidity	20% to 80% non-condensing
Housing protection class (IEC 60529)	IP 54
Vibration (IEC 60068-2-6)	2G
PHYSICAL SPECIFICATIONS	
Weight	approx. 900 g

Dimensions (L x W x H) in mm	152 x 108 x 262
Tripod mounting	M6
Housing	ABS
PC SOFTWARE	
System requirements	Windows XP (Service Pack 3), Windows Vista, Windows 7, Interface USB 2.0
STANDARDS, TESTS, WARRANTY	
EU Directive	2004 / 108 / EC

References

- Artese G., De Napoli L., Rizzuti S. and Trecroci A., Calibrazione di un laser a scansione e confronto con tecniche fotogrammetriche e tastatore meccanico, Proc. of the 7th National Conference ASITA, ASITA:2003, Vol. 1, pp. 103-108, Verona, October 2003
- Barone S, Paoli A and Razonale A.V., A biomedical application combining visible and thermal 3D imaging, XVIII Congreso Internactional de Ingenieria Grafica, Sitges, 2006
- Barone S, Paoli A and Razonale A.V., Assessment of chronic wounds by three-dimensional optical imaging based on integrating geometrical, chromatic, and thermal data, Proc IMechE, Part H: J Engineering in Medicine, 225(2): 181–193, 2011
- Beraldin J. A., Basic theory on surface measurement uncertainty of 3D imaging systems, IS&T – Three – Dimensional Imaging Metrology Conference, San Jose, CA, USA, 18-22 January, 2009
- Bichinho G. L., Gariba M. A., Sanches I. J., Gamba H. R., Cruz F. P. F. and Nohama P., A Computer Tool for the Fusion and Visualization of Thermal and Magnetic Resonance Images, Journal of Digital Imaging, Vol 22, No 5 (October), pp 527 – 534, 2009
- Boehler W., Bordas Vincent M. and Marbs A., Investigating laser scanner accuracy, Proc. of XIXth CIPA Symposium at Antalya, Turkey, 30 Sept – 4 Oct, 2003
- Bondar J. L., Candoré J. C., Nicolas J. L., Szatanik G., Detalle V. and Vallet J. M., Stimulated infrared thermography applied to help restoring mural paintings, NDT&E International, 49, 40-46, 2012
- Botsaris P. N., Tsanakas J.A., Infrared thermography as an estimator technique of a photovoltaic module performance via operating temperature measurements,

Proc. of the 10th ECNDT Conference, 2010

Brioschi M. L., Sanches I. and Traple F., 3D MRI/IR Imaging Fusion: A New Medically Useful Computer Tool, Proceedings of InfraMation, 2007

Burleigh D. D., Kuhns D. R., Cowell S. D. and Engel J. E., Thermographic nondestructive testing (TNDT) of honeycomb composite structural parts of Atlas space launch vehicles, Proc. SPIE 2245, Thermosense XVI: An International Conference on Thermal Sensing and Imaging Diagnostic Applications, 152 – 163, March 21, 1994, doi:10.1117/12.171164

Burleigh D. D., Kuhns D. R., Cowell S. D., Engel J. E., Thermographic nondestructive testing (TNDT) of honeycomb composite structural parts of Atlas space launch vehicles, Proc. SPIE 2245, Thermosense XVI: An international Conference on Thermal Sensing and Imaging Diagnostic Applications, 152, March 21, 1994

Cabrelles M., Galcerá S., Navarro S., Lerma J. L., Akasheh T. and Haddad N., Integration of 3D laser scanning, photogrammetry and thermography to record architectural monuments, 22nd CIPA Symposium, Kyoto, Japan, 11-15 October, 2009

Candoré J. C., Bondar J. L., Szeftlinski A., Ibos L., Datcu S., Candau Y., Mattei S., Frichet J. C., Helps with the thermal diagnosis of the building: detection of defects of insulation by stimulated infrared thermography, Proc. of the 9th International Conference on Quantitative InfraRed Thermography, July 2-5, Krakow, Poland, 2008

Chen Z., Jiang G., Zheng F., Liu H. and Zhu B., A Correction Method of Medical Thermography's Distortion, Proceedings of the 2005 IEEE, Engineering in Medicine and Biology 27th Annual Conference, Shanghai, China, September 1-4, 2005

Coleman H. W. and Steele W. G. Jr, Experimentation and uncertainty analysis for engineers, John Wiley and Sons ed., 1989

Curuni S.A., Santopuoli N., Pompei via dell'Abbondanza: ricerche, restauri e nuove tecnologie, Skira, 2007

Danese M., Demsar U., Masini N. and Charlton M, Investigating material decay of historic buildings using visual analytics with multi-temporal infrared thermographic data, Archeometry, 52, 482-501, 2010

- De Crescenzo F., Fantini M., Lucchi F., Persiani F., Santopuoli N. and Seccia L., Ricostruzione 3D ed indagini non distruttive di un bassorilievo marmoreo nel suo contesto architettonico, Proc. of Aiar 2010, Pavia, ISBN 978-88-555-3181-8, 2010
- De Crescenzo F., Fantini M., Persiani F., Santopuoli N., Seccia L., Virgilli V., Monitoring of the conservation state of the internal wall surfaces of Room with Golden Vault in the Domus Aurea, International Workshop – SMW08 in sit monitoring of monumental surface, pp 77-86, Firenze 27-29 October, 2008, a
- De Crescenzo F., Fantini M., Persiani F., Santopuoli N., Seccia L., Virgilli V., Rilievo e ricostruzione integrata di opere d'arte e ambienti architettonici, Atti del V° congresso nazionale di Archeometria, Scienza e Beni Culturali, Siracusa, 26-29 febbraio, 2008, b
- Endsley A., Brooks C., Harris D., Ahlborn T., and Vaghefi K., Decision support system for integrating remote sensing in bridge condition assessment and preservation, Proc. SPIE 8345, Sensors and Smart Structures Technologies for Civil, Mechanical, and Aerospace Systems 2012, 834548, April 26, 2012, doi:10.1117/12.915640
- Fantini M., Benazzi S., De Crescenzo F., Persiani F. and Gruppioni G., Virtual Reconstruction of a Dismembered Andean Mummy from CT Data, in Short & Project Papers Proceedings of the 6th International Symposium on Virtual Reality, Archaeology and Intelligent Cultural Heritage, M. Mudge, N. Ryan and R. Scopigno (eds.), Pisa, 8-11 novembre 2005, pp. 61-66, 144, 2005
- Fantini M., De Crescenzo F. and Ciocca L., Design and manufacturing of customized surgical devices for mandibular rehabilitation, International Journal on Interactive Design and Manufacturing (IJIDeM), 1-11 , November 10, 2012
- Fantini M., De Crescenzo F. and Ciocca L., Design and Rapid Manufacturing of anatomical prosthesis for facial rehabilitation, International Journal on Interactive Design and Manufacturing (IJIDeM), 7: 51-62 , February 01, 2013
- Flir Technical Manual: www.flir.com
- Gaiani M. and Beraldin J. A., Evaluating the performance of close range 3D active vision systems for industrial design applications, in Videometrics VIII, Proceedings SPIE, Bellingham, vol. 5665, 2005, pp. 11,2005

- Gaussorgues G., *Infrared Thermography*, Chapman & Hall, pp. 508, 1994
- Ghosh K. K., Karbhari V. M., Use of infrared thermography for quantitative non-destructive evaluation in FRP strengthened bridge systems, *Materials and Structures*, 44, 169-185, 2011
- Gibson I., *Advanced manufacturing technology for medical applications – Reverse engineering, Software conversion and Rapid Prototyping*, Wiley, 2005
- Glaverbel website: www.glaverbel.com
- Griffith B., Türler D. and Goudey H., *Infrared Thermography Systems*, The Encyclopedia of Imaging Science and Technology, ed. John Wiley and Sons, 2000
- Guidi G., Remondino F., Morlando G., Del Mastio A., Uccheddu F. and Pelagotti A., Performances evaluation of a low cost active sensor for cultural heritage documentation, 8th Optical 3D, Zurich, 9-12 July 2007
- Guidi G., Russo M. and Beraldin J-A., *Acquisizione 3D e modellazione poligonale*, McGraw-Hill, pp.466, 2010
- Guidi G., Russo M., Magrassi G. and Bordegoni M, Performance Evaluation of Triangulation Based Range Sensors, *Sensors*, 10, 7192-7215, doi:10.3390/s100807192, 2010
- GUM, ISO ENV 13005, *Guide to the expression of uncertainty in measurement*, 1993
- Hoyano A., Asano K. and Kanamaru T., Analysis of the sensible heat flux from the exterior surface of buildings using time sequential thermography, *Atmospheric Environment*, 33, 3941-3951, 1999
- Ibarra-Castanedo C., Galmiche F., Darabi A., Pilla M., Klein M., Ziadi A., Vallerand S., Pelletier J-F. and Maldague X., Thermographic nondestructive evaluation: overview of recent progress, *Proc. SPIE 5073, Thermosense XXV*, 450, April 3, 2003
- Iwai D. and Sato K., Optical superimposition of infrared thermography through video projection, *Infrared Physics and Technology*, 53, 162-172, doi:10.1016/j.infrared.2009.11.001, 2010
- Izumi Y., Sakagami T., Kubo S., Accuracy improvement of self-referenced lock-in thermography methods and its application to detection of fatigue cracks in steel

- bridges, Proc. Of SPIE Thermosense XXXII, 7661, 76610D, 2010
- J. G. Webster, De Measurement instrumentation, und Sensors - Handbook, (editor in Chief) CRC Piress LLC, 1999
- J. R. Taylor, Introduzione all'analisi degli errori. Lo studio delle incertezze nelle misure fisiche, Zanichelli, 2004.
- Ju X., Nebel J. C. and Siebert J. P., 3D Thermography Imaging Standardization Technique for Inflammation Diagnosis, Proc. of SPIE, Photonics Asia, Beijing (China), p 5640–5646, 2004
- Kolokotsa D., Maravelaki-Kalaitzaki P., Papantoniou S., Vangeloglou E., Saliari M., Karlessi T., Santamouris M, Development and analysis of mineral based coatings for buildings and urban structures, Solar Energy, 86, 1648-1659, 2012
- Lagüela S., Armesto J., Arias P. and Herráez J., Automation of thermographic 3D modelling through image fusion and image matching techniques, Automation in Construction, 27, 24–31, 2012
- Lahiri B. B., Bagavathiappan S., Jayakumar T. and Philip J, Medical applications of infrared thermography: a review, Infrared Physics and Technology, 55, 221-235, 2012
- Laser Scanner Konica Minolta Vivid-9i - User Manual
- Ludwig N., Rosina E., Caglio S., Gargano M. and Redaelli V., Heat Diffusion in Klinker Facade: The Study Case of a Gio Ponti Building, Optical Technologies Volume, 2012
- Maldague X, Non destructive evaluation of materials by infrared thermography, Springer-Verlag, London, 1993
- Maldague X. P. V., *Theory and practice of Infrared Technology for Nondestructive Testing*, A Wiley-Interscience publication, John Wiley & Sons, Inc., pp. 684, 2001
- Maldague X., Introduction to NDT by active infrared thermography Materials Evaluation, 6(9),1060–1073, 2002
- Meola C., Carlomagno G. M., Recent advances in the use of infrared thermography, Measurement Science and Technology, 15, p. R27-R58, 2004
- Meola C., Di Maio R., Roberti N. and Carlomagno G. M., Application of infrared

- thermography and geophysical methods for defect detection in architectural structures, *Engineering Failure Analysis*, 12, 875-892, 2005
- Minkina W. and Dudzik S., *Infrared thermography, Errors and Uncertainties*, ed. John Wiley and Sons, 2009, p190
- P. M. Azzoni, *Strumenti di misura per l'ingegneria meccanica*, Hoepli, 2006.
- Persiani F., Seccia L., De Crescezio F., Fantini M., Virgilli V., Balzani M., Fabbri M., L'Ebe di Antonio Canova nella pinacoteca civica di Forlì studio di fattibilità per l'applicazione di tecnologie avanzate di rilievo, prototipazione e realtà virtuale, *Economia della cultura restauro, Salone dell'Arte del Restauro e della Conservazione dei Beni Culturali e Ambientali*, Ferrara, Marzo 2007
- R. Scopigno, 3D scanning: potenzialità e limiti delle tecnologie di acquisizione automatica, in CD-ROM DDD (Disegno Digitale e Design), edita da Poli.Design, n.5, Gennaio – Marzo 2003
- R. Scopigno, Gestione Efficiente dei Dati Prodotti dai Sistemi di Scansione Tridimensionale, Laser Scanner e GPS: Paesaggi Archeologici e Tecnologie Digitali, pp 41–68, 2005
- Ristić S., Polić-Radovanović S., Popović-Živančević M., and Jegdić B., Some examples of thermography application in detecting earthquake damages to buildings of cultural heritage protection, *Buildings and Materials Structures*, 54, 3, 83-96, 2011
- Sansoni G., Trebeschi M. and Docchio F., State-of-the-art and applications of 3D imaging sensors in industry, cultural heritage, medicine and criminal investigation, *Sensors*, 9, 568-901; doi:10.3390/s90100568, 2010
- Satzger W., Zenzinger G. and Carl V., Quantitative 3D-Thermography, *Proceedings of the 8th International Conference of Quantitative Infrared Thermography QIRT*, Padova, Italy, 2006
- Sham J. F. C., Lo T. Y. And Memon S. A., Verification and application of continuous surface temperature monitoring technique for investigation of nocturnal sensible heat release characteristics by building fabrics, *Energy and Buildings*, 53, 108-116, 2012
- Sun N., Rosin P., Martin R. and Langbein F. C., Noise analysis and synthesis for 3D

- laser depth scanners, *Graphical Models* , 71, 34-48, 2009
- Tan J. H., Ng E. Y. K., Acharya U. R., Chee C., Infrared thermography on ocular surface temperature: a review, *Infrared Physics and Technology*, 52, 97-108, 2009
- Testo Technical Manual: www.testo.com
- Tkáčová M, Hudák R, Foffová P. and Živčák J., An importance of camera – subject distance and angle in musculoskeletal applications of medical thermography, *Acta Electrotechnica et Informatica*, Vol. 10, No. 2, 57–60, 2010
- Voltolini F., Rizzi A., Remondino F., Girardi S. and Gonzo L., Integration of non-invasive techniques for documentation and preservation of complex architectures and artworks, *Proc. of 2nd ISPRS International Workshop 3D-ARCH 2007*, ETH Zurich, Switzerland, 12-13 July 2007
- Wu D. and Busse G., Lock-in thermography for nondestructive evaluation of materials, *Revue générale de thermique*, 37, 693-703, 1998
- Xi F., Liu Y. and Feng H. Y., Error compensation for three-dimensional line laser scanning data, *The International Journal of Advanced Manufacturing Technology*, 18, 211-216, 2001
- Yilmaz H.M., Yakar M. and Yildiz F., Documentation of historical caravansaries by digital close range photogrammetry, *Automation in Construction*, 17, 489-498, 2008

